Photoinduced Chemistry of Biomolecular Building Blocks and Molecules in Space



Dennis Milešević
St Hugh's College
University of Oxford

A thesis submitted for the degree of
Doctor of Philosophy
Michaelmas Term 2023

What the young scientist didn't realise was that she had just agreed to embark on an epic quest.

– Rutger Bregman

Acknowledgments

Firstly, I want to thank my supervisor, Professor Claire Vallance, for her guidance, positivity, and countless ideas. In addition to the terminology 'robust discussions', you have taught me a lot as a researcher and chemist, which I am very grateful for.

I want to express my sincere gratitude to the mechanical and electronics workshops. Your consistent assistance and problem-solving have been invaluable throughout this project. Without your support, many aspects of this work wouldn't have been achievable. I greatly appreciate the collaboration with Pete and Andy in redesigning the desorption source, Steve's efforts in installing components for the femtosecond laser beamline, Kevin's contributions to the interlock system, and Tim, Phil, and John's adeptness in resolving electronics-related challenges. Your assistance has been incredibly meaningful to me.

During my time in the Vallance group, I have worked alongside various people who have contributed positively to this work. Divya, thank you to for teaching me the ropes of the experiment. David, thank you to for the large amount of data analysis code we use routinely in the group and for always being keen to help. Patrick, thank you for the many fruitful scientific discussions and your supervision, I have learned a lot from you. Alex, thank you for the many very enjoyable

runs after work (let us avoid the construction work next time). I would also like to thank Zhihao and Paul, who worked closely with me and contributed greatly to the desorption source characterization. Furthermore, I want to thank Annabel and Liwen for being such good co-workers. It has been a pleasure working with everyone of you. Beyond that, I would like to thank Jo for getting me up to speed with CASSCF calculations.

I am very grateful to my friends, who have supported me during this journey. In particular, I would like to thank Andreea, Rodney, Lawrence, Ioanna and Kostas. I could not have asked for better flatmates. In particular, I want to thank Lawrence and Kostas. You were there for me through thick and thin, and I could always count on you. Thank you to Issabella for always making time and supporting me. Furthermore, I thank Max, Leyla, and Theresa for being amazing friends.

Lastly, I would like to thank my brother, Alex, and my parents, Petra and Goran, for their unwavering support and unconditional love for me. Now you can read about how to break 'stable molecules' apart.

List of Publications

1. D. Milesevic, D. Popat, P. Robertson, C. Vallance, "Photodissociation of *N,N*-dimethylformamide at 225 nm and 245 nm", *Phys. Chem. Chem. Phys.* **2022**, *24*, 28343-28352.

2. J. W. McManus, T. Walmsley, K. Nagaya, J. R. Harries, Y. Kumagai, H. Iwayama, M. N.R. Ashfold, M. Britton, P. H. Bucksbaum, B. Downes-Ward, T. Driver, D. Heathcote, P. Hockett, A. J. Howard, E. Kukk, J. W. L. Lee, Y. Liu, D. Milesevic, R. S. Minns, A. Niozu, J. Niskanen, A. J. Orr-Ewing, S. Owada, D. Rolles, P. A. Robertson, A. Rudenko, K. Ueda, J. Unwin, C. Vallance, M. Burt, M. Brouard, R. Forbes and F. Allum, "Disentangling sequential and concerted fragmentations of molecular polycations with covariant native frame analysis", *Phys. Chem. Chem. Phys.* **2022**, *24*, 22699-22709.

3. P. A. Robertson, D. Heathcote, D. Milesevic, C. Vallance, "Imaging the Dynamics of the Electron Ionization of C_2F_6", *J. Phys. Chem. A* **2022**, *126*, 7221-7229.

4. I. Gabalski, F. Allum, I. Seidu, M. Britton, G. Brenner, H. Bromberger, M. Brouard, P. H. Bucksbaum, M. Burt, J. P. Cryan, T. Driver, N. Ekanayake, B. Erk, D. Garg, E. Gougoula, D. Heathcote, P. Hockett, D. M. P. Holland, A. J. Howard, D. Kumar, J. W. L. Lee, S. Li, J. McManus, J. Mikosch, D. Milesevic, R. S. Minns, S. Neville, A-Tul-Noor, C. C. Papadopoulou, C. Passow, W. O. Razmus, A. Röder, A. Rouzee, A. Simao, J. Unwin, C. Vallance, T. Walmsley, J. Wang, D. Rolles, A. Stolow, M. S. Schuurman, R. Forbes, "Time-Resolved X-ray Photoelectron Spectroscopy: Ultrafast Dynamics in CS_2 Probed at the S 2p Edge", *J. Phys. Chem. Lett.* **2023**, *14*, 7126-7133.

5. J. Unwin, F. Allum, M. Britton, I. Gabalski, H. Bromberger, M. Brouard, P. H. Bucksbaum, T. Driver, N. Ekanayake, D. Garg, E. Gougoula, D. Heathcote, A. J. Howard, P. Hockett, D. M. P. Holland, S. Kumar, C. Lam, J. W. L. Lee, J. McManus, J. Mikosch, D. Milesevic, R. S. Minns, C. C. Papadopoulou, C. Passow, W. O. Razmus, A. Röder, A. Rouzée, M. Schuurman, A. Simao, A. Stolow, A. Tul-Noor, C. Vallance, T. Walmsley, D. Rolles, B. Erk, M. Burt, R. Forbes, "X-ray induced Coulomb explosion imaging of transient excited-state structural rearrangements in CS_2", *Commun. Phys.*, **2023**, *6*, 309.

6. D. Milesevic, J. Stimson, D. Popat, P. Robertson, C. Vallance, "Photodissociation dynamics of tetrahydrofuran at 193 nm", *Phys. Chem. Chem. Phys.* **2023**, *25*, 25322–25330.

7. D. Milesevic, D. Popat, P. Gellersen, Z. Liu, J. Stimson, P. Robertson, C. Vallance, "Design and characterization of an optical-fiber-coupled laser-induced desorption source for gas-phase dynamics experiments", *Rev. Sci. Instrum.* **2023**, *94*, 114105.

Contents

Acknowledgments **v**

1 Introduction **1**

1.1 Electronic structure theory 3

1.1.1 Born-Oppenheimer approximation 4

1.1.2 Potential energy surfaces 4

1.1.3 Optical transitions 7

1.2 Molecular relaxation processes 9

1.2.1 Intramolecular vibrational energy redistribution 9

1.2.2 Internal conversion and fluorescence 10

1.2.3 Intersystem crossing and phosphorescence 11

1.2.4 Photodissociation 12

1.3 Scattering distributions 12

1.3.1 Angular distributions 13

1.3.2 Radial distributions 16

1.4 Spectroscopy and imaging techniques 17

1.4.1 Velocity-map imaging 18

1.4.2 Doppler spectroscopy 21

1.4.3 Resonance-enhanced multiphoton ionization 22

1.4.4 Photoelectron spectroscopy 23

1.4.5 Transient absorption spectroscopy . . . 24
1.5 Molecule preparation techniques . . . 25
1.5.1 Gases and liquids . . . 25
1.5.2 Solids . . . 26
1.6 Overview of thesis . . . 28

2 Methods **33**
2.1 Experimental . . . 33
2.1.1 Spectrometer . . . 33
2.1.2 Vacuum system . . . 34
2.1.3 Pulsed molecular beam . . . 35
2.1.4 Laser systems . . . 38
2.1.5 Ion lens . . . 43
2.1.6 Time-of-flight . . . 45
2.1.7 Detector . . . 46
2.1.8 Camera . . . 48
2.2 Theoretical calculations . . . 49

3 Image processing **51**
3.1 Centroiding . . . 52
3.2 Inversion methods . . . 54
3.2.1 Abel inversion . . . 54
3.2.2 Basis function based inversion . . . 56
3.3 Energy calibration . . . 58
3.4 Covariance analysis . . . 61
3.4.1 TOF-TOF covariance . . . 63
3.4.2 Recoil-frame covariance . . . 65
3.4.3 Partial and contingent covariance . . . 67

4 Ultraviolet photodissociation of tetrahydrofuran **69**

4.1 Introduction . . . 69

4.2 Methods . . . 72

4.2.1 Experimental methods . . . 72

4.2.2 Computational methods . . . 74

4.3 Results . . . 75

4.3.1 Time-of flight spectrum . . . 75

4.3.2 Product speed and angular distributions . . . 77

4.3.3 Channel 1a: THF $\rightarrow$ OCH_2 + C_3H_6 . . . 80

4.3.4 Channel 1b: THF $\rightarrow$ $HOCH_2$ + CH_2CHCH_2 . . . 82

4.3.5 Channel 2: THF$\rightarrow$ OCH_2CH_2 + CH_2CH_2 . . . 83

4.4 Conclusions . . . 84

5 Ultraviolet photodissociation of *N,N*-dimethylformamide **89**

5.1 Introduction . . . 89

5.2 Methods . . . 92

5.3 Results and discussion . . . 95

5.3.1 Ultraviolet absorption spectrum of *N,N*-dimethylformamide 95

5.3.2 Photolysis of *N,N*-dimethylformamide at 225 nm . . . 96

5.3.3 Photolysis of *N,N*-dimethylformamide at 245 nm . . . 106

5.4 Conclusions . . . 111

6 Ultraviolet photodissociation of the *N,N*-dimethylformamide cation **115**

6.1 Introduction . . . 115

6.2 Methods . . . 117

6.2.1 Experimental set-up . . . 117

6.2.2 Theoretical calculations . . . 119

6.3 Theoretical results . . . 119

6.4 Experimental results . . . 123
6.4.1 118 nm ionization of neutral *N*,*N*-dimethylformamide . . . 123
6.4.2 Photolysis of *N*,*N*-dimethylformamide$^+$ at 225, 245, and 280 nm . . . 124
6.4.3 Comparison with literature . . . 129
6.5 Conclusions . . . 131

7 Set-up and characterization of a femtosecond beamline 133
7.1 Laser system . . . 135
7.2 Beamline . . . 136
7.2.1 Beam path . . . 136
7.2.2 Pulse timings . . . 138
7.3 Characterization . . . 140
7.3.1 Pulse length . . . 140
7.3.2 Focusing conditions . . . 144
7.3.3 Intensity . . . 145
7.4 Conclusion and Outlook . . . 147

8 Development and characterization of a laser-based thermal desorption source 149
8.1 Introduction . . . 149
8.2 Source requirements and design . . . 150
8.3 Methods . . . 154
8.3.1 Sample preparation . . . 154
8.3.2 Time of flight mass spectrometry and velocity-map imaging measurements . . . 155
8.4 Results and discussion . . . 156
8.4.1 Time-of-flight spectra and velocity-map images for uracil, adenine, and phenylalanine . . . 156

8.4.2 Dependence of signals on desorption laser power 162
8.5 Conclusion 166

9 Dissociative ionization of polycyclic aromatic hydrocarbons 169
9.1 Introduction 169
9.2 Methods 171
9.3 Triphenylene 174
9.3.1 Time-of-flight spectra 174
9.3.2 Velocity-map images 176
9.4 Perylene and Benzo[a]pyrene 191
9.5 Conclusions 196

10 Conclusion and Outlook 199
10.1 Conclusion 199
10.2 Outlook 203
10.2.1 Experimental upgrades 203
10.2.2 Coulomb-explosion imaging 204
10.2.3 Laser-induced desorption source 205

Bibliography 207

List of Abbreviations 229

List of Symbols 231

A Appendix: electronic structure theory A-1
A.1 Electron correlation methods A-1
A.2 Multi-configuration self-consistent field A-2

B Appendix: Figures A-7

C Appendix: Tables A-13

List of Figures

1.1 PESs of a diatomic molecule A−B. 6

1.2 Vibronic transition according to the Franck-Condon principle. 8

1.3 Jablonski diagram 10

1.4 Product scattering distributions for the dissociation of the parent molecule AB into the products A and B. 12

1.5 Anisotropic scattering distributions. 14

1.6 Working principle of VMI for a pump-probe experiment. 19

1.7 Schematic (1+1′) REMPI scheme and (2+1′) REMPI scheme. 22

2.1 Schematic of the custom-built VMI spectrometer. 33

2.2 CAD of the custom-built vacuum chamber from the side view. . . . 35

2.3 Schematic of the Parker Hannifin pulsed valve used in the present work. 36

2.4 Temporal profile of the molecular beam obtained via the ionization of N_2 with the 800 nm Titanium:Sapphire laser. 38

2.5 Schematic of the tunable dye laser with beamline to the experiment. 39

2.6 Schematic of the excimer laser beamline to the experiment. 41

2.7 Schematic of the Nd:YAG laser and its beam path to the experiment. 42

2.8 Two-dimensional side-view of the ion lenses used in this thesis. . . . 43

2.9 DMF^+ parent ion distribution under VMI conditions following single-photon ionization at a wavelength of 118 nm. 44

2.10 Schematic illustration of an ion imaging detector. 46

3.1 Schematic illustration of an inverted velocity-map ion image. 55

3.2 Inverted velocity-map images for the ^{35}Cl atomic products from the photodissociation of Cl_2 as a function of repeller potential. 60

3.3 TOF-TOF covariance map of a fictitious ion AB^{2+} dissociating into $A^+ + B^+$. 64

3.4 Simulated velocity-map images and the recoil-frame covariance image for the dissociation reaction $AB^{2+} \longrightarrow A^+ + B^+$. 66

3.5 Simulated velocity-map images and covariance images of the reaction $ABC^{2+} \longrightarrow A^+ + B^+ + C$. 66

4.1 Reaction scheme for THF following 193 nm excitation. 71

4.2 Background-subtracted TOF mass spectrum for the 193 nm photolysis products of THF. 75

4.3 Symmetrized velocity-map images for the observed photodissociation products of THF. 76

4.4 Speed distributions $P(v)$, recoil anisotropy distributions $\beta(v)$, and TKER distributions for the the three photodissociation channels of THF. 78

4.5 Optimized structures and $S_1 \leftarrow S_0$ transition dipoles for the C_2 and C_S conformers of THF. 81

5.1 Schematic cuts through the ground state and first two excited singlet and triplet state PESs of DMF along the N−CO stretch coordinate. . 91

5.2 UV absorption spectrum of liquid DMF. 95

5.3 TOF mass spectra of the photofragments formed following photoexcitation of DMF at 225 nm and 245 nm 96
5.4 Symmetrized and Abel-inverted velocity-map images and speed and angular distributions for fragments observed following 225 nm photolysis of DMF. 98
5.5 TKER distribution for the N−CO and N−CH_3 bond fission channels following 225 nm photolysis of DMF. 102
5.6 Symmetrized and Abel-inverted velocity-map images and speed and angular distributions for fragments observed following 245 nm photolysis of DMF. 107
5.7 TKER distribution for the N−CO and N−CH_3 bond fission channels following 245 nm photolysis of DMF. 110

6.1 Equilibrium geometries of the DMF cation and neutral optimized on a UMP2/aug-cc-pVTZ level of theory. 120
6.2 Excitation energies to the first ten ionic states of the DMF cation. . . 121
6.3 Background-subtracted TOF spectrum of DMF following ionization at 118 nm. 123
6.4 Background-subtracted TOF mass spectra produced by ionizing DMF at 118 nm followed by photolysis of the ion at 225, 245, and 280 nm. 124
6.5 Abel-inverted velocity-map images obtained from DMF following ionization at 118 nm and photolysis at 225, 245, and 280 nm and their resulting kinetic energy release distributions. 128

7.1 Schematic of the laser system used to produce femtosecond laser pulses. 135
7.2 Schematic showing the femtosecond laser beamline. 137
7.3 Schematic of the trigger system when working with the femtosecond laser. 138

7.4 Schematic of the FROG autocorrelator used to measure the laser pulse length. 142

7.5 Laser pulse length inside the chamber as a function of the Solstice compression setting. 143

7.6 Schematic defining the parameters used to calculate the beam waist diameter $2\omega_0$ inside the interaction region. 145

7.7 Ionization mechanisms as predicted by the Keldysh parameter γ. . . 146

8.1 Operating principle of the LID source and schematic of the VMI spectrometer for which the LID source was designed. 150

8.2 The LID source used in this work. 153

8.3 TOF spectra of the 118 nm photoionization products of uracil, adenine, and phenylalanine prepared with the LID source. 157

8.4 Velocity-map images recorded for the phenylalanine parent ion and the three fragment ions: $HC_2NH_2OOH^+$, $C_7H_7^+$, and $C_7H_7CHNH_2^+$. . 160

8.5 Velocity-map images recorded for uracil parent ions with foil–repeller distances of 2, 5, and 10 mm. 161

8.6 Uracil parent ion signals as a function of the desorption laser power and the direct comparison of the signals from 'thin' and 'thick' samples. 162

9.1 Schematic HACA mechanism for the formation of naphthalene from benzene. 170

9.2 Structures of the PAHs studied in this Chapter. 171

9.3 Background-subtracted TOF spectra of triphenylene following the irradiation with the 800 nm femtosecond laser beam. 174

9.4 Inverted velocity-map images and their kinetic energy release distribution for each fragment ion following the irradiation of triphenylene with the 800 nm femtosecond laser beam. 177

9.5 Reaction scheme illustrating possible acetylene (C_2H_2) loss pathways following the single or double ionization of triphenylene via irradiation with the 800 nm femtosecond laser beam. 178

9.6 Recoil-frame covariance maps of all possible combinations of signal and reference ions following the irradiation of triphenylene at a laser beam intensity of $5 \cdot 10^{14}$ W cm^{-2}. 181

9.7 Recoil-frame covariance maps of all possible combinations of signal and reference ions following the irradiation of triphenylene at a laser beam intensity of $9 \cdot 10^{14}$ W cm^{-2}. 182

9.8 Experimental momentum distributions of the signal ions from the (signal ion, reference ion) recoil-frame covariance images. 183

9.9 Simulated momentum distributions of the signal ions for various (signal ion, reference ion) ion pairs. 185

9.10 Fragmentation pathway showing the dissociation of doubly charged triphenylene molecules into a reference and a signal ion, followed by sequential C_2H_2 ejection from the signal ion and the expected momentum distributions of the signal ion in the covariance maps. . 186

9.11 Momentum distributions of the signal ions from the (signal ion, $C_5H_x^+$) recoil-frame covariance images. 187

9.12 Momentum distributions of the $C_{13}H_x^+$ signal ions from the ($C_{13}H_x^+$, reference ion) recoil-frame covariance images. 188

9.13 Recoil-frame covariance maps of various combinations of signal and reference ions following the irradiation of triphenylene at a laser beam intensity of $9 \cdot 10^{14}$ W cm^{-2}. 190

9.14 Background-subtracted TOF spectra of perylene following the irradiation with the 800 nm femtosecond laser beam. 192

9.15 Recoil frame covariance maps of all possible combinations of signal and reference ions following the irradiation of perylene at a laser beam intensity of $5 \cdot 10^{14}$ W cm^{-2}. 193
9.16 Background-subtracted TOF spectra of benzoapyrene following the irradiation with the 800 nm femtosecond laser beam 194
9.17 Possible mechanism for the loss of C_2H_2 from the benzoapyrene cation. 195
9.18 Recoil-frame covariance images of the (C_6^+, C_6^+) ion pair resulting from the irradiation of perylene and benzoapyrene with the 800 nm femtosecond laser beam at a laser beam intensity of $9 \cdot 10^{14}$ W cm^{-2}. 196

A.1 HF orbital energies for OCS and a possible way of diving them into active and inactive orbitals. A-3

B.1 Rigid PEC of the DMF cation along the N−CO stretch coordinate, the N−CH_3 coordinate on the side of the oxygen atom, and the remaining N−CH_3 bond calculated on a CASSCF(11,12) level of theory. A-8
B.2 Schematic illustration of the decay of triply charged triphenylene, C_{18}^{3+} into C_{16}^{2+} + C_2^+. A-9
B.3 Recoil-frame covariance maps of all possible combinations of signal and reference ions following the irradiation of perylene at a laser beam intensity of $9 \cdot 10^{14}$ W cm^{-2}. A-10
B.4 Recoil-frame covariance maps of all possible combinations of signal and reference ions following the irradiation of benzoapyrene at a laser beam intensity of $5 \cdot 10^{14}$ W cm^{-2}. A-11
B.5 Recoil-frame covariance maps of all possible combinations of signal and reference ions following the irradiation of benzoapyrene at a laser beam intensity of $9 \cdot 10^{14}$ W cm^{-2}. A-12

List of Tables

2.1 Laser dye concentrations in the pre-amplifier and amplifier cell to generate the wavelengths used in this work. 40

3.1 Radius of the inverted Cl ion image following the dissociation of $Cl_2 \longrightarrow Cl + Cl$ for different repeller voltages. 60

5.1 Recoil anisotropy parameters β averaged over the speed distributions for the photolysis products formed from DMF following irradiation at 225 and 245 nm, respectively. 98

5.2 Theoretical and experimental vertical excitation energies from the electronic ground state to the first three excited singlet states and the first two excited triplet states of neutral DMF. 100

6.1 Vertical excitation energies (V_E) from the electronic ground state of neutral DMF to the ionic ground state and excited states. 121

6.2 Ratio of the integrated peak intensity of each fragment ion to the overall intensity following ionization of DMF at 118 nm and photolysis at 225 nm, 245 nm, or 280 nm. 125

9.1 Central momentum and full width half maximum (FWHM) of the moment distributions shown in Figure 9.11 obtained by fitting a Gaussian distribution to the curves. 187

C.1 Internal coordinates for the DMF monocation and neutral optimized on a UMP2/aug-cc-pVTZ level of theory. A-13
C.2 Central momentum and full width half maximum (FWHM) of the signal ion in the recoil-frame covariance image of an ion pair obtained by fitting a Gaussian distribution to the momentum distribution. A-15
C.3 Central momentum and full width half maximum (FWHM) of the signal ion in the recoil-frame covariance image of an ion pair obtained by fitting a Gaussian distribution to the momentum distribution. A-15

Abstract

The interactions between light and matter are ubiquitous in the universe and initiate many fundamental chemical processes, such as photosynthesis and vitamin D production. Therefore, gaining a better understanding of how light interacts with molecules and how light-induced reaction mechanisms develop from reactants to products is of great interest.

This work uses a velocity-map imaging time-of-flight spectrometer to study the unimolecular photodissociation dynamics of molecules in the gas phase. The observables of the experiment are the product scattering distributions, which are a fingerprint of the chemical reaction, and the product time-of-flight, which reveals the fragment identities. The experiments aim to understand which chemical bonds break, how the system evolves on the potential energy surfaces involved in the reaction, and how the available energy is distributed over the product degrees of freedom.

The first part of this thesis studies the photodissociation of tetrahydrofuran at 193 nm, *N*,*N*-dimethylformamide at 225 nm and 245 nm, and the *N*,*N*-dimethylformamide cation at 225 nm, 245 nm, and 280 nm. Tetrahydrofuran is a model for the DNA backbone molecule ribose, and *N*,*N*-dimethylformamide is a model for the peptide bond, which forms the backbone of proteins. Both molecules reveal complex

dissociation dynamics, in which population transfer to lower electronic states is possible after the initial excitation. This population transfer probably plays an important role in the photoprotection of molecules in biological species. The great majority of the available energy is distributed into the internal product modes rather than product kinetic energy. This observation is pronounced in the *N*,*N*-dimethylformamide cation study, in which a change in photon energy of more than 0.5 eV leads to the same product kinetic energy release.

The second part of the thesis describes the design and characterization of a novel femtosecond laser beamline to the experiment which allows us to conduct Coulomb explosion imaging experiments, and a fibre-coupled laser-induced thermal desorption source capable of introducing non-volatile samples into the spectrometer. In a study combining both techniques, we investigate the fragmentation pattern of three singly and doubly charged polycyclic aromatic hydrocarbons: triphenylene, perylene, and benzo[a]pyrene. All three molecules display a common fragmentation pattern in which the summed number of carbon atoms in the fragment ions deviates from the carbon number of the parent molecule by a multiple of two, which we interpret in terms of a fragmentation mechanism involving sequential loss of neutral acetylene (C_2H_2) units. We also show that loss of the neutral acetylene units occurs preferably from the heavier fragment ion after an initial charge separation step.

1 Introduction

Large parts of chemistry focus on converting reactants into products efficiently via a chemical reaction, in which chemical bonds are broken and formed. Goals often include to increase the yield and selectivity under milder conditions using lower cost and more environmentally friendly starting materials. The yield and selectivity of a reaction is often tested using different catalysts at a range of temperatures and pressures. However, temperature and pressure are statistical quantities averaged over numerous events. They do not provide direct insight into how the products are formed, as that information is washed out by intermolecular energy redistribution following collisions of the products with other molecules. If we want to study chemical reactivity on a more fundamental level, we ideally follow the reaction in real time and measure the products directly as they are created. That is the goal of experiments in the field of chemical reaction dynamics.

We study reactions in the gas phase under single molecule conditions. The experiments are conducted under ultra-high vacuum ($\approx 10^{-7}$mbar). At such pressures, the mean free path is so long that products do not collide, and remain isolated post formation, allowing us to measure properties of the nascent products as they are formed in the reaction. The molecule of interest (parent molecule) is introduced into the experiment as a neutral and is intersected by a laser beam. Absorption of a photon leads to dissociation of the parent molecule into two or more fragments,

with the process satisfying conservation of energy and momentum. Summing the scattering patterns of the photoproducts over many events yields 3D scattering distributions, which provide a large amount of direct information on the reaction mechanism.[1–4] The scattering distribution for a given process can be seen as a unique fingerprint, providing insight into the forces acting on the nuclei during the reaction, which are in turn determined by the potential energy surfaces (PESs) involved. Therefore, our experimental goal is to measure the product scattering distributions. In this work, we use time-of-flight velocity-map imaging (TOF-VMI)[5,6], a popular spectroscopic technique in the field.

Within the Born-Oppenheimer approximation[7] (see Section 1.1.1), the electrostatic interactions within a molecule in a given electronic state depend only on the nuclear geometry. Therefore, the potential energy of the system can be represented as a multidimensional PES, which is a function of the internal coordinates. Within these coordinates, each electronic configuration/state has its own distinct PES.

Ultraviolet (UV) photons often have enough energy to lead to electronic excitation when absorbed by a molecule, where at least one electron is promoted to an orbital higher in energy. The subsequent forces acting on the nuclei are wholly governed by the PESs of the system, as relaxation to the electronic ground state competes with fragmentation into the photofragments. Here, we are only interested in excitations leading to the dissociation of the molecule. The scattering distributions of the products directly link to the nuclear trajectories on the PESs. By measuring the scattering distributions, we aim to answer the following questions:

1. Which chemical bonds are cleaved and formed?

2. Which PESs are involved in the reaction? What states can we access at a given photon energy?

3. What are the possible pathways from our electronically excited state to the photoproducts?

4. How is the available energy distributed among the translational, vibrational, and rotational degrees of freedom of the photoproducts?

Laser pump-probe experiments are two-laser experiments in which the pump laser initializes the reaction of interest, usually leading to neutral products. After a short period of time, the probe laser is used to interrogate the products, in our case ionizing the fragments for detection. In such experiments, the input energy is well-defined and corresponds to the photon energy of the pump beam. Furthermore, we can adjust the delay between the pump and probe laser. This delay cannot be arbitrary and is limited by the pulse length of the lasers. When using nanosecond lasers, the delay is typically a few nanoseconds long, in order to capture all the products. However, most chemical reactions occur on the sub-nanosecond timescale. Therefore, they are already over when the probe laser ionizes the products. With the increasing availability of femtosecond lasers, researchers can adjust the delay between pump and probe lasers on timescales short enough to follow the reaction in real time, leading to molecular movies.[8–11]

In the remainder of this Chapter we will discuss the various experimental and theoretical methods relevant to the work in the thesis, before giving an overview of the systems studied and techniques developed within the thesis.

1.1 Electronic structure theory

In chemical reaction dynamics, the link between experiments and theory is inherently strong. Lack of information on excitation energies, transition dipole moments,

and the topology of the PESs limits the interpretation of experimental data significantly and makes it very challenging. In this section we will discuss PESs, optical transitions, and the fates of an excited state molecule.

1.1.1 Born-Oppenheimer approximation

The Born-Oppenheimer[7] approximation is essential for solving the Schrödinger equation (SE). Electrons move on much shorter timescales than nuclei, since they are orders of magnitude lighter, and can therefore adapt to any change in the nuclear framework almost instantly. Consequently, one can ignore the coupling between the motion of nuclei and electrons, allowing the overall molecular wavefunction $\Phi(\mathbf{x}, \mathbf{R})$ to be to be separated into a nuclear state function $\chi(\mathbf{R})$ and an electronic state function $\Psi(\mathbf{x}; \mathbf{R})$

$$|\Phi(\mathbf{x}, \mathbf{R})\rangle = |\Psi(\mathbf{x}; \mathbf{R})\rangle|\chi(\mathbf{R})\rangle, \tag{1.1}$$

where $\mathbf{x}$ and $\mathbf{R}$ are the electronic and nuclear coordinates, respectively. Now, the electronic wavefunction depends only parametically on the nuclear coordinates. The nuclei themselves move on PESs, which are solutions of the electronic SE. While for most systems the Born-Oppenheimer approximation introduces only small errors, it breaks down if two or more solutions of the electronic SE come close to each other energetically.[12]

1.1.2 Potential energy surfaces

PESs describe the molecule's potential energy as a function of the internal coordinates and are key towards understanding both nuclear motion and the evolution

of the electronic structure of the molecule over time. Each electronic state has a characteristic PES. The dimensionality of the PESs is equal to the number of internal coordinates in the molecule. Linear molecules have $3N-5$ internal coordinates and non-linear molecules have $3N-6$, where N is the number of nuclei. The high dimensionality makes PESs calculations computationally expensive and challenging to visualize for anything more than a diatomic. To tackle this issue, scientists often visualize the potential energy as a function of only one or two internal coordinates whilst keeping all remaining coordinates fixed. Such cuts through the PES are called potential energy curves (PECs). PECs also allow one to look at an internal coordinate of interest that is particularly important for the description of nuclear dynamics, such as a dissociating bond.

How do PESs govern nuclear motion? Let us imagine a molecule with a well-defined geometry where the initial momenta of the nuclei are zero. The subsequent dynamics are fully governed by the force acting on the nuclei. For a set of N atoms with the nuclear coordinates $\mathbf{R} = \{\boldsymbol{R}_1, \boldsymbol{R}_2, \ldots, \boldsymbol{R}_N\}$ the force $\boldsymbol{F}(\mathbf{R})$ is defined by the gradient of the PES,

$$\boldsymbol{F}(\mathbf{R}) = -\nabla V(\mathbf{R}), \tag{1.2}$$

with $\nabla = \left(\frac{\partial}{\partial \boldsymbol{R}_1}, \frac{\partial}{\partial \boldsymbol{R}_2}, \cdots, \frac{\partial}{\partial \boldsymbol{R}_N}\right)$ being the gradient operator and $V(\mathbf{R})$ being the potential of the system. With knowledge of the PES and the initial position and momentum of each nucleus, we can predict the subsequent nuclear motion.[13] Molecules prepared in an identical state with identical geometries undergo the same trajectory across the surface and will exhibit identical dynamics.

Figure 1.1 shows the first three electronic states of a fictitious diatomic molecule A−B. The electronic ground and first excited states, shown in black and red, respectively, are bound. If the total energy of the system does not exceed the exit barrier towards dissociation, the molecule will stay bound. The blue surface is re-

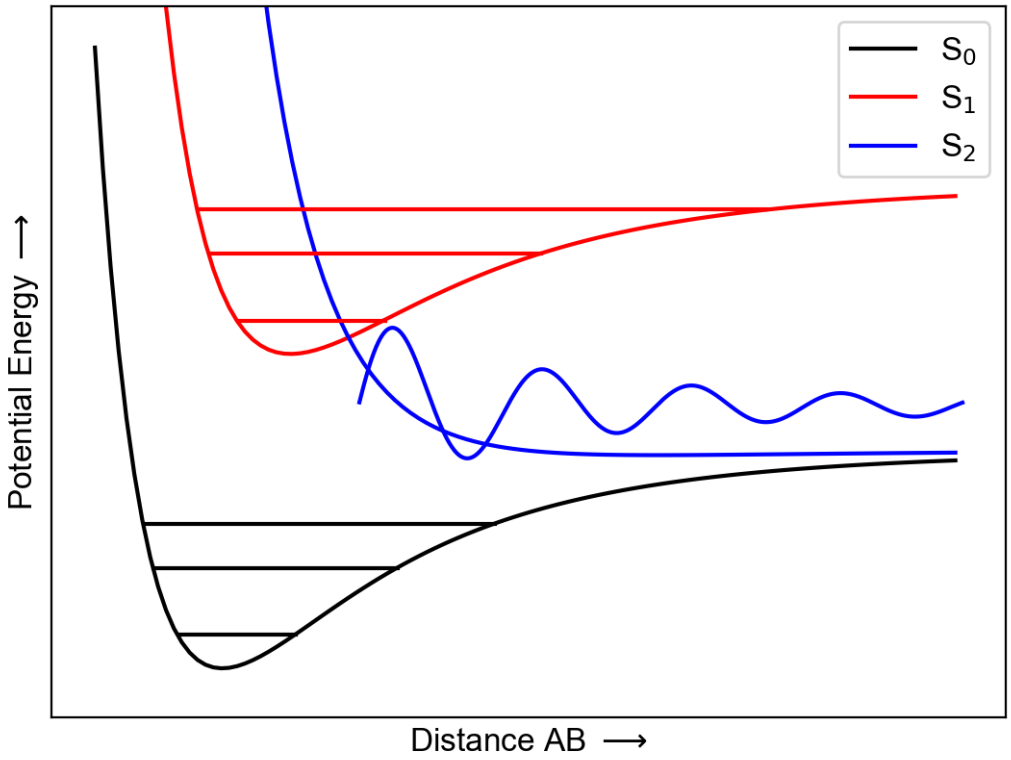

Fig. 1.1: PESs of a diatomic molecule A−B. S_0 (black) and S_1 (red) are bound, S_2 (blue) is repulsive. In the dissociation limit, S_0 and S_2 form A + B in the ground state, while S_1 leads to electronically excited A + B. A diatomic only has one vibrational mode, whereas polyatomic molecules have multiple modes of vibration.

pulsive, i.e. the molecule minimizes energy by increasing the internuclear distance $R_{\mathrm{A-B}}$. This is the driving force for dissociation. The population of this state leads to dissociation into the constituent atoms A + B.

Within each electronic state is a manifold of vibrational states in which numerous rotational states can be populated. Ignoring rovibronic couplings, the internal energy is simply a sum of these constituent energies,

$$E_{\mathrm{int}} = E_{\mathrm{elec}} + E_{\mathrm{vib}} + E_{\mathrm{rot}} \tag{1.3}$$

with E_{elec}, E_{vib}, and E_{rot} being the electronic, vibrational, and rotational energy contributions, respectively.

1.1.3 Optical transitions

Electronic transitions involve a change in electron density as population is transfered from one PES to another. Generally, such optical excitations do not only lead to electronic but also vibrational excitation. Simultaneous electronic and vibrational excitations are called vibronic transitions. The Franck-Condon (FC) principle[14,15] is an approximation commonly used to describe such transitions.

Mathematically, electronic transitions are described by the transition dipole moment $\boldsymbol{\mu}_{\mathrm{if}}$ defined as follows,

$$\boldsymbol{\mu}_{\mathrm{if}} = \langle \Phi_{\mathrm{f}}(\mathbf{x}, \mathbf{R}) | \hat{\boldsymbol{\mu}} | \Phi_{\mathrm{i}}(\mathbf{x}, \mathbf{R}) \rangle, \tag{1.4}$$

where $\hat{\boldsymbol{\mu}} = \hat{\boldsymbol{\mu}}_{\mathrm{e}} + \hat{\boldsymbol{\mu}}_{\mathrm{M}}$ is the electric dipole moment operator, which depends on the charges and positions of the electrons ($\hat{\boldsymbol{\mu}}_{\mathrm{e}}$) and the nuclei ($\hat{\boldsymbol{\mu}}_{\mathrm{M}}$), and $\Phi_{\mathrm{f}}(\mathbf{x}, \mathbf{R})$ and $\Phi_{\mathrm{i}}(\mathbf{x}, \mathbf{R})$ are final and initial wavefunctions, respectively. Both of these are functions of the electronic coordinates $\mathbf{x}$ and nuclear coordinates $\mathbf{R}$. Using the Born-Oppenheimer approximation[7] as defined in equation 1.1, we obtain

$$\begin{aligned}
\boldsymbol{\mu}_{\mathrm{if}} &= \langle \Psi_{\mathrm{f}}(\mathbf{x}; \mathbf{R}) \chi_{\mathrm{f}}(\mathbf{R}) | (\hat{\boldsymbol{\mu}}_{\mathrm{e}} + \hat{\boldsymbol{\mu}}_{\mathrm{M}}) | \Psi_{\mathrm{i}}(\mathbf{x}; \mathbf{R}) \chi_{\mathrm{i}}(\mathbf{R}) \rangle \\
&= \langle \Psi_{\mathrm{f}}(\mathbf{x}; \mathbf{R}) | \hat{\boldsymbol{\mu}}_{\mathrm{e}} | \Psi_{\mathrm{i}}(\mathbf{x}; \mathbf{R}) \rangle \langle \chi_{\mathrm{f}}(\mathbf{R}) | \chi_{\mathrm{i}}(\mathbf{R}) \rangle + \underbrace{\langle \Psi_{\mathrm{f}}(\mathbf{x}; \mathbf{R}) | \Psi_{\mathrm{i}}(\mathbf{x}; \mathbf{R}) \rangle \langle \chi_{\mathrm{f}}(\mathbf{R}) | \hat{\boldsymbol{\mu}}_{\mathrm{M}} | \chi_{\mathrm{i}}(\mathbf{R}) \rangle}_{=0},
\end{aligned} \tag{1.5}$$

where $\Psi(\mathbf{x}; \mathbf{R})$ is the electronic wavefunction and $\chi(\mathbf{R})$ is the nuclear wavefunction. The second term becomes zero because the initial and final states are orthogonal to each other for any nuclear geometry $\mathbf{R}$. In the remaining term, we have separated nuclear and electronic wavefunctions, assuming $\hat{\boldsymbol{\mu}}_{\mathrm{e}}$ is independent of the

nuclear geometry $\mathbf{R}$. The remaining expression,

$$\boldsymbol{\mu}_{\mathrm{if}} = \underbrace{\langle \Psi_{\mathrm{f}}(\mathbf{x};\mathbf{R}) | \hat{\boldsymbol{\mu}}_{\mathrm{e}} | \Psi_{\mathrm{i}}(\mathbf{x};\mathbf{R}) \rangle}_{\approx \text{const.}} \underbrace{\langle \chi_{\mathrm{f}}(\mathbf{R}) | \chi_{\mathrm{i}}(\mathbf{R}) \rangle}_{=S_{\mathrm{i,f}}} \tag{1.6}$$

contains an approximately constant integral and the overlap integral $S_{\mathrm{i,f}}$. Thus, the transition dipole moment increases with an increasing overlap of the nuclear wavefunctions of the initial and final states. Figure 1.2 schematically illustrates this principle.

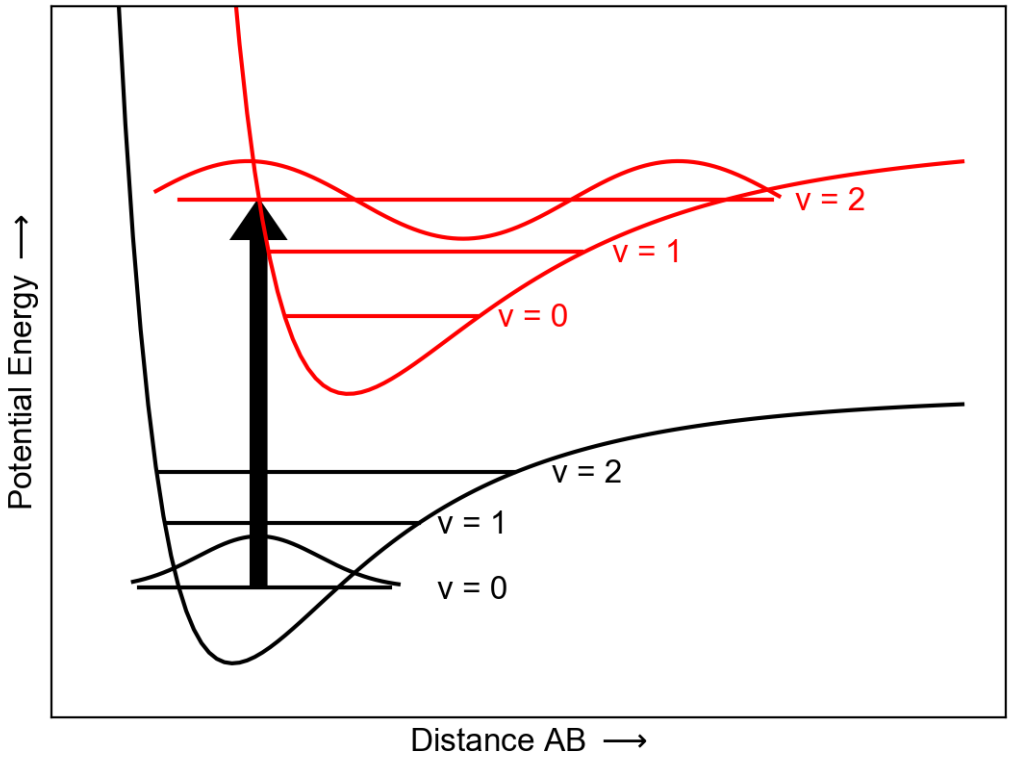

Fig. 1.2: Vibronic transition from the vibrational ground ($\mathrm{v} = 0$) state of the lower electronic state to $\mathrm{v} = 2$ in the higher electronic state. The transition is vertical, according to the FC-principle. The nuclear wavefunction remains almost unchanged.

In most cases, transitions to a number of different vibrational levels are possible, and we can assign probabilities to each of them by analyzing the respective overlap integrals.[16] The transition rate W_{if} from an initial state i to a discrete final state f

is defined as follows,

$$W_{\mathrm{if}} = B_{\mathrm{if}}\rho_{\mathrm{R}}(\nu_{\mathrm{if}}) = \frac{|\boldsymbol{\mu}_{\mathrm{if}}|^2}{6\epsilon_0\hbar^2}\rho_{\mathrm{R}}(\nu_{\mathrm{if}}), \tag{1.7}$$

where B_{if} is the Einstein coefficient of stimulated absorption and $\rho_{\mathrm{R}}(\nu_{\mathrm{if}})$ is the energy density of radiation states.[16] As a result, photoinduced excitation can only occur if the transition dipole moment is non-zero ($\boldsymbol{\mu}_{\mathrm{if}} \neq 0$). Consideration of the symmetry properties of the transition dipole moment leads to several optical selection rules that are summarized in reference 16. We have now discussed optical transitions. Next, we are going to explore the evolution of the newly populated excited state.

1.2 Molecular relaxation processes

Understanding the fate of an excited molecule is the goal of many of our experiments. While dissociation can occur on the initially populated state, often a shift of optical density leads to population of other states. A Jablonski diagram[17] in Figure 1.3 summarizes the processes involving a change of state.

1.2.1 Intramolecular vibrational energy redistribution

Intramolecular vibrational energy redistribution (IVR)[18–20] is a non-radiative intramolecular energy redistribution from an initial set of excited modes into a larger number of internal modes. While IVR is an isoenergetic process in the gas-phase, in the liquid phase it allows molecules to repopulate the vibrational ground state of an excited electronic state after a vibronic excitation as energy is transferred to other molecules. IVR is an ultrafast process ($10^{-14} - 10^{-11}$ s) and conserves the electronic state.

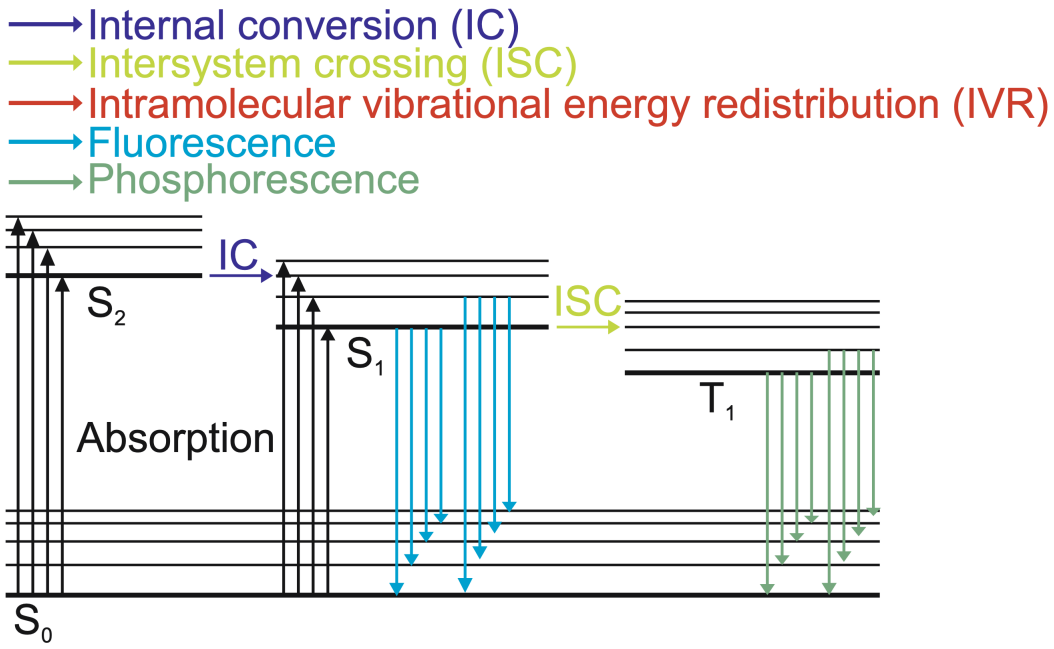

Fig. 1.3: Jablonski diagram, which illustrates radiative and non-radiative transitions between different electronic states in a molecule.

1.2.2 Internal conversion and fluorescence

Internal conversion (IC) is a non-radiative transition between states of the same spin multiplicity, for example $S_2 \rightarrow S_1$. The nuclear kinetic energy operator mixes different electronic states leading to non-adiabatic coupling between them. IC usually occurs at the crossing point of two surfaces with appropriate spin multiplicity and on the ultrafast timescale ($10^{-14} - 10^{-11}$ s). The rate constant can vary significantly depending on the molecule of interest, because it depends on the matrix elements of vibronic coupling and the energy gap between the initial and final state. A smaller energy gap leads to faster IC, a phenomenon known as the energy gap law.[21,22] IC can also provide a non-adiabatic deactivation pathway to the electronic ground state S_0.

In contrast, fluorescence[23] describes the radiative deactivation pathway between states of the same spin multiplicity, e.g. $S_1 \rightarrow S_0 + h\nu$. Fluorescence occurs on the nanosecond timescale ($10^{-9} - 10^{-7}$ s) or faster and, according to Kasha's rule[24],

usually from the lowest excited state of a given multiplicity and in accord with the FC principle. The emission spectrum is shifted to longer wavelengths relative to the absorption spectrum, as some energy has usually been converted into nuclear motion via IVR prior to photon emission.

1.2.3 Intersystem crossing and phosphorescence

Intersystem crossing (ISC) describes transitions between two electronic states with different spin-multiplicities, for example $S_1 \rightarrow T_1$. ISC results from the spin-orbit coupling operator, which mixes the electronic states. Spin-orbit coupling is a relativistic effect that arises from the Dirac equation[25] and scales with Z^4, where Z is the nuclear charge. Therefore, ISC can proceed more readily if heavy atoms are involved, for example in metal clusters.[26] Traditionally, ISC was believed to occur on longer timescales ($10^{-8} - 10^{-3}$ s) than IC. An increasing amount of evidence suggests that it can also occur on the sub-picosecond timescale for molecules involving only first period atoms.[27–30] Furthermore, according to El-Sayed's rule[31], ISC occurs more readily if the transition involves a change in orbital symmetry. For example, the transition ${}^3\mathrm{n},\pi^* \leftarrow^1 \pi,\pi^*$ is faster than the transition ${}^3\pi,\pi^* \leftarrow^1 \pi,\pi^*$. This is a consequence of the symmetry of the spin-orbit operator that couples the states.

Molecules undergoing ISC from S_1 to populate T_1 often become trapped in that state since radiative decay to the S_0 ground state is spin forbidden. In most cases, the triplet state T_1 is energetically lower than its singlet counterpart S_1, in agreement with Hund's rules, but it cannot decay easily to the electronic ground state S_0. The radiative transition $T_1 \rightarrow S_0 + h\nu$ is called phosphorescence and – although spin-forbidden – occurs on the millisecond timescale ($> 10^{-3}$ s).[32] Phosphorescence occurs according to the FC principle.

1.2.4 Photodissociation

Photodissociation describes the photo-induced cleavage of chemical bonds, leading to two or more fragments. Dissociation can only occur if the available energy exceeds the bond dissociation energy. As explained earlier, the driving force behind the dissociation is the reduction of potential energy. We can imagine different pathways towards dissociation. The most straightforward one involves excitation to a repulsive electronic state. The potential energy is reduced as the nuclei separate, leading to bond cleavage. Alternatively, if the state has an exit barrier towards dissociation, the molecule can dissociate by overcoming the barrier or skirting around it. Fragmentation does not have to occur solely in the initially populated state. IC or ISC can lead to the population of other excited states on which dissociation can occur.

1.3 Scattering distributions

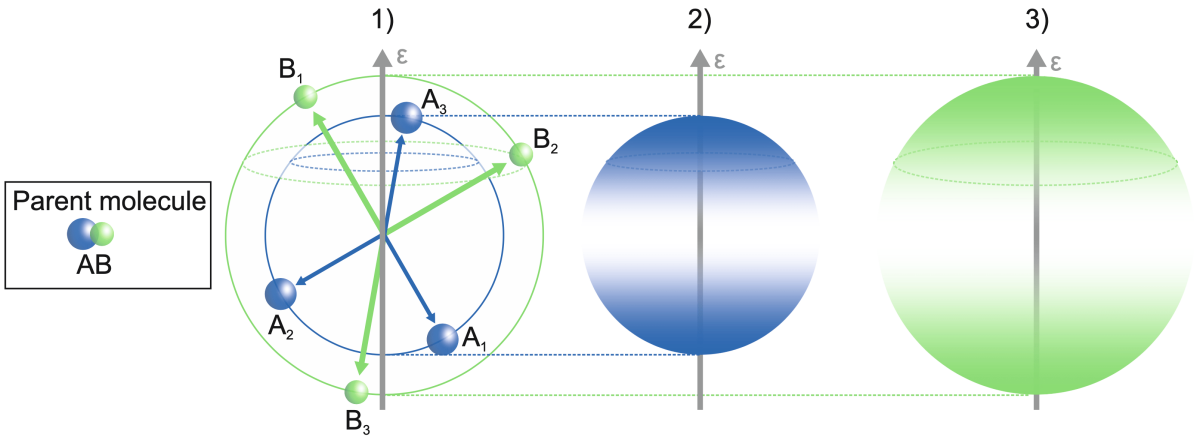

Fig. 1.4: Product scattering distributions for the dissociation of the parent molecule AB into the products A and B, where $m_{\mathrm{A}} > m_{\mathrm{B}}$. (1) shows three individual dissociation events. The laser polarization axis ϵ is vertical in the paper plane. A and B are formed with equal and opposite momenta. Due to the difference in mass, fragment B has a higher kinetic energy than fragment A, hence the greater radius. For a large number of events, the scattering distributions of either fragment exhibit a surface pattern, as shown in (2) for fragment A and (3) for fragment B. In this example, both scattering distributions show a $\cos^2(\theta)$-distribution, indicating a parallel transition.

A general photo-induced two-body dissociation event can be represented by the reaction equation:

$$\mathrm{AB} + \mathrm{h}\nu \rightarrow \mathrm{A} + \mathrm{B}. \tag{1.8}$$

Each fragment produced in a dissociation event has a well defined recoil velocity and direction. For a large number of events, the fragment velocities build up three-dimensional scattering distributions that can be characterized by their angular and radial distribution. This build up is shown schematically in Figure 1.4. The radius of the scattering distribution depends on the product recoil velocity, the shape depends on the electronic states involved in the excitation step and the transition dipole moment that couples them as well as on the dissociation mechanism. Thus, scattering distributions provide a large amount of direct information on the reaction mechanism.[1–4] Here, we will discuss the types of information we can extract from them.

1.3.1 Angular distributions

The product recoil direction, usually described as is the direction in which fragments are flying relative to the electric vector of the photolysis light, is not random but correlated with the transition dipole moment $\boldsymbol{\mu}_{\mathrm{if}}$ of the photoexcitation. We already know that the absorbed photon carries the energy needed to electronically excite the reactant by moving an electron from one molecular orbital (MO) to another. This change in electron density occurs more readily if the electric vector ϵ of the photolysis laser aligns with the movement of electron density. The probability P_{if} of an optical transition is defined as follows,

$$P_{\mathrm{if}} = |\boldsymbol{\mu}_{\mathrm{if}} \cdot \boldsymbol{\epsilon}|^2 = \boldsymbol{\mu}_{\mathrm{if}}^2 \cdot \boldsymbol{\epsilon}^2 \cdot \cos^2(\theta_{\boldsymbol{\mu}_{\mathrm{if}}\boldsymbol{\epsilon}}), \tag{1.9}$$

where $\theta_{\boldsymbol{\mu}_{\mathrm{if}}\boldsymbol{\epsilon}}$ is the angle between $\boldsymbol{\mu}_{\mathrm{if}}$ and $\boldsymbol{\epsilon}$. The probability of excitation is maximized if $\boldsymbol{\mu}_{\mathrm{if}}$ and $\boldsymbol{\epsilon}$ are parallel to each other and becomes zero if $\boldsymbol{\mu}_{\mathrm{if}}$ and $\boldsymbol{\epsilon}$ are perpendicular to each other. Therefore, in a randomly oriented sample some molecules are more likely to absorb a photon than others. Assuming dissociation is fast relative to the molecular rotation, this anisotropy is carried over into the product recoil distribution.

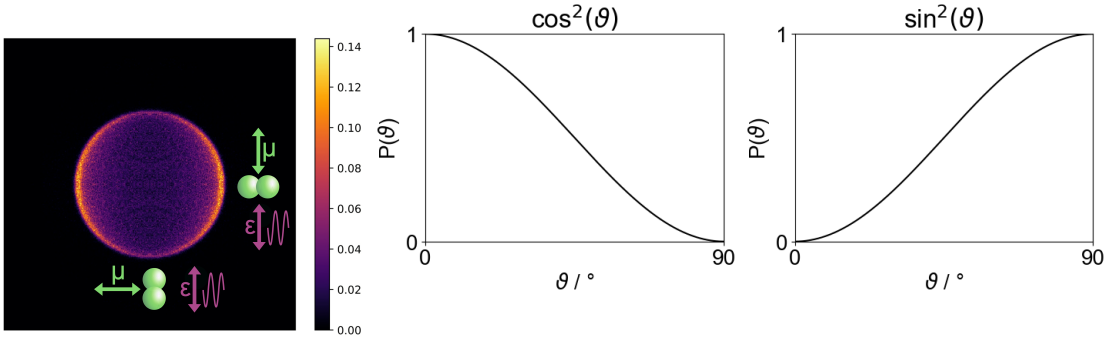

Fig. 1.5: Left: Crushed velocity-map image of the Cl atoms produced during the dissociation of Cl_2, following the optical transition $^1\Pi_{1u} \leftarrow^1 \Sigma_{0_g^+}$ at 355 nm.[33,34] Electron density is moved perpendicular to the bond axis hence the transition dipole moment is perpendicular to the bond axis, resulting in a $\sin^2(\theta)$ angular distribution. Centre: Photofragment angular distribution arising from a parallel transition; the angular dependence is described by a $\cos^2(\theta)$-distribution. Right: Photofragment angular distribution arising from a perpendicular transition; the angular dependence is described by a $\sin^2(\theta)$-distribution.

The normalized angular distribution of the photofragments can be described as follows[35,36],

$$I(\vartheta_{k\epsilon}) = \frac{1}{4\pi}[1 + \beta P_2(\cos\vartheta_{k\epsilon})] \qquad \text{with}: P_2 = \frac{1}{2}[3\cos^2(\vartheta) - 1] \tag{1.10}$$

where $\vartheta_{k\epsilon}$ is the angle between the recoil direction k and the electric vector $\boldsymbol{\epsilon}$, $P_2(\cos\vartheta_{k\epsilon})$ is the second Legendre polynomial, and β is the product recoil-anisotropy parameter ($-1 \leq \beta \leq +2$). The limiting value of $\beta = +2$ is reached for an ideal 'parallel' transition, where $\boldsymbol{\mu}_{\mathrm{if}}$ lies parallel to the breaking bond. In that case, the angular distribution can be described by a $\cos^2(\vartheta)$ distribution, as shown in the central panel in Figure 1.5. $\beta = -1$ is reached for an ideal 'perpendicular' transition,

where $\boldsymbol{\mu}_{\text{if}}$ lies perpendicular to the breaking bond. In that case, the angular distribution can be described by a $\sin^2(\vartheta)$ distribution, as shown in the right panel in Figure 1.5. One example of a perpendicular transition is found in the ${}^1\Pi_{1u} \leftarrow {}^1\Sigma_{0_g^+}$ transition of Cl_2 excited at 355 nm, which results in dissociation of Cl_2 into two chlorine atoms. This is shown in the left panel in Figure 1.5. Measuring the scattering distribution therefore indicates the direction of $\boldsymbol{\mu}_{\text{if}}$ in the molecule, as first demonstrated by Solomon[37]. This helps us to determine to which state the molecules are excited.

For polyatomic molecules, the limiting cases of parallel and perpendicular transitions usually do not apply, and instead β lies somewhere between its limiting values of -1 and $+2$. In that case, the angular distribution can be expressed as a linear combination of parallel and perpendicular distributions,

$$I(\vartheta_{v\epsilon}) = \underbrace{\frac{1+\beta}{4\pi}}_{A} \cos\vartheta_{v\epsilon}^2 + \underbrace{\frac{1-\frac{1}{2}\beta}{4\pi}}_{B} \sin\vartheta_{v\epsilon}^2 \tag{1.11}$$

where A and B are the weighting coefficients. The observed β-parameter also depends on the lifetime of the system. In the rapid dissociation limit, the correlation between the recoil direction and the transition dipole moment is fully conserved. We obtain $\beta = 2P_2(cos\vartheta)$ for a parallel transition.[38] However, if the parent molecule's lifetime exceeds its rotational period, it has time to reorient in space, and the correlation between k and $\boldsymbol{\mu}_{\text{if}}$ is reduced. In a semiclassical model, Jonah[39] showed that for a parallel transition in the limiting case of an infinitely large lifetime, the angular distribution converges to $\frac{1}{4}(1 + \cos^2\vartheta)$. Hence, the molecules always retain some information on the transition dipole moment.

1.3.2 Radial distributions

Dissociation events are fundamental physical processes and conserve energy and momentum. For the dissociation in equation 1.8, the conservation of energy can be quantified as follows,

$$\underbrace{E^0_{\mathrm{AB}} + \mathrm{h}\nu}_{E_{\mathrm{AB}^*}} = \underbrace{E^0_{\mathrm{A}} + E_{\mathrm{kin,A}} + E_{\mathrm{int,A}}}_{E_{\mathrm{A}}} + \underbrace{E^0_{\mathrm{B}} + E_{\mathrm{kin,B}} + E_{\mathrm{int,B}}}_{E_{\mathrm{B}}}, \tag{1.12}$$

where E^0_{AB} is the initial energy of the parent molecule, $\mathrm{h}\nu$ is the energy of the absorbed photon, and E_{A} and E_{B} are the energies of the products A and B, respectively, which consist of the ground state energy E^0, the kinetic energy E_{kin} and the internal energy E_{int}. One terminology often used in reaction dynamics is the available energy, which is the energy difference between photoexcited AB^* and the energy of the ground state products $E^0_{\mathrm{A}} + E^0_{\mathrm{B}}$. Making use of the bond dissociation energy D_0, we can express the available energy as follows:

$$E_{\mathrm{avail}} = E^0_{\mathrm{AB}} + \mathrm{h}\nu - D_0 = E_{\mathrm{kin,A}} + E_{\mathrm{int,A}} + E_{\mathrm{kin,B}} + E_{\mathrm{int,B}} \tag{1.13}$$

Hence, the available energy comprises the energy distributed into the product degrees of freedom. For an individual dissociation event, the products A and B will be formed with distinct kinetic and internal energy. The higher the amount of internal energy of the products, the lower their kinetic energy and vice versa. If the products are formed in their rovibronic ground state, then all of the available energy is released into translation, i.e. $E_{\mathrm{avail}} = E_{\mathrm{kin,A}} + E_{\mathrm{kin,B}}$.

By conservation of momentum, the translational kinetic energies of our products are correlated with each other. In a two-body event, the products A and B are

formed with equal and opposite momenta,

$$p_{\mathrm{A}} = -p_{\mathrm{B}}. \tag{1.14}$$

The total kinetic energy release (TKER) is the sum of the kinetic energies of A and B. In terms of momentum, it can be expressed as follows,

$$\begin{aligned} E_{\mathrm{kin,tot}} &= E_{\mathrm{kin,A}} + E_{\mathrm{kin,B}} \\ E_{\mathrm{kin,tot}} &= \frac{p_{\mathrm{A}}^2}{2m_{\mathrm{A}}} + \frac{p_{\mathrm{B}}^2}{2m_{\mathrm{B}}}, \end{aligned} \tag{1.15}$$

where m_{A} and m_{B} are the masses of A and B, respectively. Combining equations 1.14 and 1.15 allows us to express the energy of A or B as a function of the TKER,

$$E_{\mathrm{kin,A}} = \frac{m_{\mathrm{B}}}{m_{\mathrm{AB}}} E_{\mathrm{kin,tot}} \qquad E_{\mathrm{kin,B}} = \frac{m_{\mathrm{A}}}{m_{\mathrm{AB}}} E_{\mathrm{kin,tot}}. \tag{1.16}$$

Thus, if only the momentum distribution of fragment A is measured, we can reconstruct the TKER by assuming an ideal two-body dissociation.

As noted earlier, our experiments aim to record scattering distributions for all of the products formed in a photodissociation event. The experimental techniques employed to achieve this are explained in the following sections.

1.4 Spectroscopy and imaging techniques

The development of spectroscopy and imaging techniques has been key to probing the energetics and forces driving chemical reactions. We have mapped out four key questions at the beginning of this chapter. These can be answered by measuring the product scattering distribution. Ideally, we would measure the three-dimensional

scattering distribution of every photoproduct as a function of the radial coordinate r, the polar scattering angle ϕ, and the azimuthal angle φ. The state-of-the-art approach towards measuring the product scattering distribution is velocity-map imaging (VMI), which we will discuss in detail in this section. Afterwards, we will also cover other spectroscopy techniques that provide slightly different information from that attainable using VMI.

1.4.1 Velocity-map imaging

The first ion imaging experiment was reported by Chandler and Houston[5] in 1987.

In the interaction region, which is the region of intersection between the molecular beam and the lasers, CH_3I was photolysed by a 266 nm pump laser beam, producing CH_3 and I. Subsequently, CH_3 was ionized using (2+1) multiphoton absorption with a ∼330 nm probe laser beam. Detection of neutrals is possible[40] but generally much more challenging than detecting ions. When ionizing the neutral photoproducts, their velocity remains approximately unchanged since the ejected electron removes almost the entire kinetic energy. The resulting CH_3^+ ions were accelerated towards a position-sensitive detector by a linear electric field. The detector measured the intensity distribution.

One constrain of the technique developed by Chandler and Houston is the limited spatial resolution. The interaction region between the molecules and lasers is not infinitely small but has a finite volume, leading to the blurring of the recorded ion images. As a result, it can be challenging to draw quantitative conclusions from the recorded ion image.

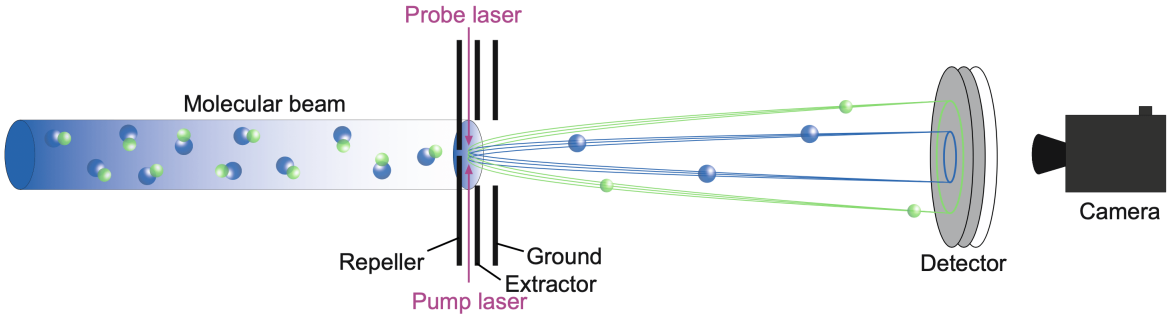

Fig. 1.6: Schematic showing the working principle of VMI for a pump-probe experiment. The parent molecules AB enter the interaction region, where a photolysis laser dissociates them into A and B, which are subsequently ionized by the probe laser. The electric field created by the ion lens maps the product ions onto the detector so that ions of the same identity with the same velocity strike the same detector position. The molecular beam diameter is significantly smaller than drawn with a diameter of ∼2 mm.

VMI is a measurement technique developed by Eppink and Parker[6] that allows mapping the product scattering distribution onto a position-sensitive detector with high spatial resolution. VMI uses a curved electric field rather than a uniform one, improving the image resolution significantly. Figure 1.6 schematically illustrates the working principle of VMI for a prototypical photoinduced reaction. The field is created by applying potentials to an ion lens comprising three open electrodes, usually referred to as the repeller (R), extractor (E), and ground (G) plates, respectively. Daughter ions with the same velocity and identity are mapped onto the same position on the detector, regardless of their origin within the interaction volume between the molecular beam and the lasers. The radius of the recorded ion image is proportional to the product velocity in the detector plane, giving a direct correlation between the position on the detector and the kinetic energy of the products. However, efficient velocity mapping only works for an interaction volume of a few millimetres. If the interaction volume becomes too large, the spatial resolution decreases.

In the original paper describing VMI, Eppink and Parker also demonstrated that spatial-map imaging (SMI) can be achieved with the same ion lens by retuning the lens potentials. In SMI, the ion positions on the detector depend on where the

ions are created in the interaction region but not on their velocity or mass. For example, if a focused laser beam intersects the molecular beam at a given height, we observe a line-shaped signal on the detector, corresponding to the ions formed along the laser track. While SMI cannot be used to extract velocity information on the scattering distribution, it is a powerful tool in the laboratory to visualize the laser path, which significantly facilitates finding spatial overlap for two-color pump-probe experiments.

VMI has become a standard technique in experimental chemical reaction dynamics and has been used to investigate a variety of reaction types, such as molecule-molecule scattering,[41,42], electron-molecule scattering[43–45] and photoinduced reactions[46,47]. One caveat of using the three-electrode ion lens is that the three-dimensional product scattering distribution cannot be preserved and is instead 'crushed' along the time-of-flight (TOF) axis and pancaked onto the two-dimensional imaging detector. We speak of 'crushed VMI'. The velocity information along the TOF axis is lost. The three-dimensional scattering distribution can be reconstructed from the two-dimensional image if an axis of cylindrical symmetry is present. This process, known as image inversion, is detailed in Chapter 3.2.

The three-dimensional scattering distribution can also be measured directly using 'sliced VMI'. In sliced imaging, additional lens elements enable VMI conditions to be obtained while simultaneously stretching the scattering distribution along the TOF axis. The three-dimensional scattering distribution is measured directly by time-gating the detector in order to record a narrow slice of the distribution along the TOF axis. First introduced by Gebhardt *et al.*[48] and two years later improved by Townsend *et al.*[49], the discovery of H-atom roaming in the decomposition of formaldehyde is one of the most notable contributions using sliced imaging.[50] Sliced imaging has the advantage of measuring the three-dimensional scattering

distribution directly. It also allows for the application of covariance imaging (see Chapter 3.4) in three dimensions.[51] On the downside, stretching or retaining the scattering distribution along the TOF axis worsens the mass resolution, which becomes a limiting factor when performing multi-mass imaging of fragments with close or adjacent mass-to-charge ratios. As the mass resolution in most experiments is a significant limiting factor, crushed VMI remains the more commonly used technique.

1.4.2 Doppler spectroscopy

The Doppler effect describes the change in frequency heard by a listener depending on the velocity between the sound source and the listener. This concept also applies to the absorbtion of light waves by an atom or molecule. By measuring the Doppler shift associated with a given transition, we can determine the velocity component of the molecule along the direction of photon propagation. The frequency of the absorbed light ν_{abs} depends on the velocity v of the molecule relative to the source as follows,

$$\nu_{\mathrm{abs}} = \nu_0 \left(1 - \frac{v}{\mathrm{c}}\right), \tag{1.17}$$

where ν_0 is the frequency of the absorbed light when the molecule is stationary and c is the speed of light.[38] Doppler spectroscopy allows one to reconstruct the three-dimensional velocity distribution[52] and enables state-selective probing, for example in combination with resonance-enhanced multiphoton ionization (REMPI) or laser-induced fluorescence (LIF). Prominent early examples include the studies by Schmiedl *et al.*[53] and Philipps *et al.*[54]. In order to detect all fragments with equal efficiency, the absorption frequency has to be scanned between the boundaries $v_{\mathrm{abs}}^{\mathrm{min}}$ and $v_{\mathrm{abs}}^{\mathrm{max}}$, which are associated with product recoil velocity v. The central frequency of this scan is v_0. In this thesis, Doppler spectroscopy is used for the

energy calibration experiment on Cl_2 in Chapter 3.3.

1.4.3 Resonance-enhanced multiphoton ionization

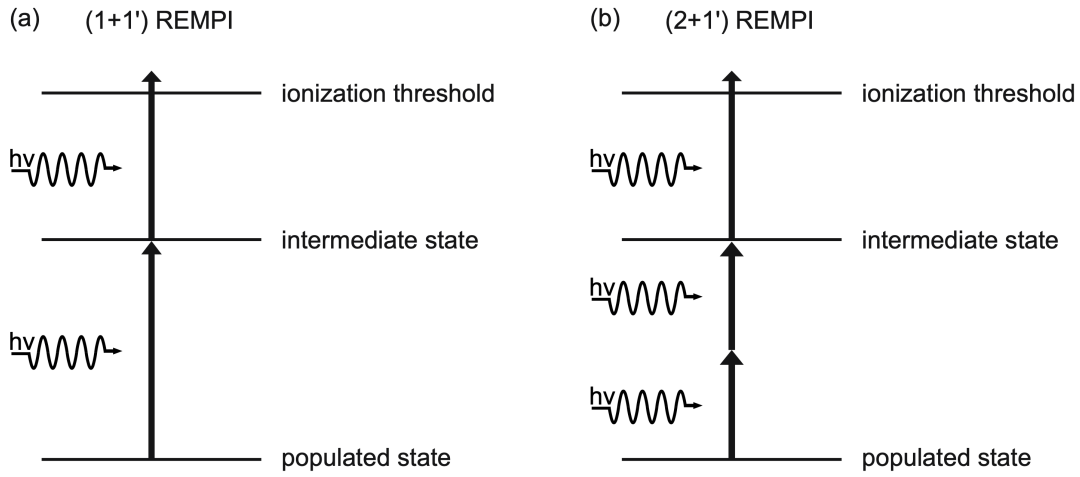

Fig. 1.7: Schematic (1+1′) REMPI scheme (a) and (2+1′) REMPI scheme (b). From the initial state, the product is first excited to an intermediate state by one (a) or two photons (b). The intermediate state is a true state of the product. Afterwards a photon of a different frequency lifts the product above the ionization threshold.

REMPI is a product-selective soft ionization technique in which a neutral species is ionized via multiphoton absorption via an excited electronic state of the molecule. REMPI methods are conventionally labelled according to the number of photons involved in reaching this 'intermediate' state and in the subsequent ionization step. Figure 1.7 shows the (1+1′) and (2+1′) REMPI processes schematically. In the (1+1′) process, excitation excitation to the intermediate state is achieved by a single photon, with a second photon of a different color causing ionization from this state. In the (2+1′) REMPI scheme, we require two photons for the excitation step, with a photon of a different wavelength to excite the product from the intermediate state to the ionization threshold. The change in wavelength is denoted by the ′ superscript. Compared with non-resonant multiphoton ionization, the intermediate state is a real electronic state of the system, making REMPI significantly more efficient. REMPI is commonly used with other techniques, such as Doppler spectroscopy and

VMI.[55,56] However, REMPI requires a high level of knowledge of the energy levels of the system in order to identify suitable wavelength(s). Due to its quantum-state selectivity, it is not suitable as a universal ionization technique.

1.4.4 Photoelectron spectroscopy

Photon absorption by the parent molecule does not always have to lead to neutral photoproducts. If the photon energy exceeds the ionization potential, we excite the molecule to an ionic state rather than a neutral state. Furthermore, if the available energy exceeds the bond dissociation energy of the ion, dissociation can occur in the ionic state, leading to two or more fragments. However, at least one of these fragments is now already ionized. Instead of measuring the product scattering distribution, we can measure the kinetic energy of the electron emitted in the ionization step. This is known as photoelectron spectroscopy.

Photoelectron spectroscopy is used to study the valence or core electronic structure of solids, liquids, or gases.[57–60] It yields direct information on quantities such as electron detachment energy[61]. The kinetic energy of the emitted electron also aids in determining the ionic state to which the molecule is excited. If the photon energy and the electron's kinetic energy are known, we know how much energy remains in the molecule's nuclear framework[62]. However, it does not reveal the product identities or how the remaining energy is distributed in the products' degrees of freedom. Therefore, it does not address the questions we want to answer in this thesis.

1.4.5 Transient absorption spectroscopy

Transient absorption spectroscopy investigates the change in optical density upon photoexcitation. In transient absorption spectroscopy, a fraction of molecules is in a first step photoexcited to an excited state. Subsequently, after a variable time, white light is used to measure the time-dependent absorption spectrum of this excited state. The transient absorption spectrum is generated by subtracting the excited state spectrum from the ground state spectrum.

The spectrum contains direct information on the fates of the excited state. Absorption is observed from the initially populated excited state and other excited states that are populated post-excitation. Let us assume we initially excite a molecule to the S_2 state. The initial absorption spectrum from S_2 will exhibit optical transitions to S_3, S_4,..., S_n. However, over time the population density can shift. Following the IC from S_2 to S_1, we will observe additional features corresponding to transitions from S_1 to S_2, S_3,..., S_n. These features will occur at higher energies (shorter wavelengths) than the transitions from S_2. Other transitions, such as ISC to triplet states, can also occur. If the excited state leads to dissociation into two or more fragments, the absorption spectrum of the fragments will also be measured. Changing the delay between the initial photoexcitation and measuring the absorption spectrum allows for following the change in population density in real-time. From the spectrum, the time constant for the individual redistribution processes can be extracted. That is the overall goal of transient absorption spectroscopy.

While transient absorption spectroscopy has been used in gas-phase experiments[63,64], it is more commonly used to investigate liquids or solids[65–67] due to the higher number density. For that reason, transient absorption spectroscopy is not suitable for us.

1.5 Molecule preparation techniques

One major part of the experiment is the introduction of the molecules to be studied into the gas phase. For gases and high-vapour-pressure liquids, a pulsed valve can be used, which separates the vacuum chamber from the sample gas via a small orifice that is periodically opened and closed. However, under standard conditions, only small molecules are gases or high-vapour-pressure liquids. The introduction into the gas phase is less straightforward for solids. Here we will introduce the pulsed valve and alternative techniques for the preparation of solids.

1.5.1 Gases and liquids

Most gas-phase experiments rely on supersonic expansion through a pulsed valve, a technique to introduce internally cold molecules with a narrow speed distribution into the experiment. Pulsed valves exist in many different versions, varying in operating pressure, duration, density, and frequency range.[68–73] The molecule of interest is seeded in an inert gas, which is usually helium or argon. When triggered, the pulsed valve opens temporarily, allowing the gas mixture to expand from the high-pressure to the low-pressure region. The molecules undergo numerous collisions with each other as they pass through the orifice and in the region immediately beyond, and only those for which the collisions convert their internal energy into kinetic energy along the beam axis normal to the orifice are expanded into the vacuum before the orifice shuts again. The result is an internally cold, highly dense molecular beam with a narrow speed distribution. While rotational cooling through collisions is quite efficient, vibrational cooling occurs with a lower probability. Hence, not all molecules in the beam will be in their vibrational ground state.

The mean terminal velocity $\langle v \rangle$ of the molecules in the molecular beam can be expressed as follows[74],

$$\langle v \rangle = \sqrt{\frac{2\mathrm{R}T_0\gamma}{m(\gamma-1)}} \qquad \gamma = \frac{C_\mathrm{p}}{C_\mathrm{v}} \tag{1.18}$$

where $\mathrm{R}, T_0, m, C_\mathrm{p}, \text{ and } C_\mathrm{v}$ are the gas constant, room temperature, the mass of the molecules, molar heat capacity at constant pressure, and molar heat capacity at constant volume, respectively.

1.5.2 Solids

Despite the popularity of the molecular beam approach, preparation of molecules in a pulsed expansion is limited to species with a sufficiently high vapour pressure at room temperature, typically gases or high-vapour-pressure liquids.* The range of molecules that can be prepared in a molecular beam can be increased by heating the pulsed valve; for example, the Even-Lavie valve[76,77] can operate at temperatures up to 250 °C, and has been used to generate seeded molecular beams of molecules such as small polycyclic aromatic hydrocarbons (PAHs)[78], indole[79], and adamantane[80], all of which are solids at room temperature. However, Even-Lavie valves are expensive (>£20,000). Furthermore, for many samples prolonged heating leads to decomposition rather than successful generation of a molecular beam[81], so care is needed when using this approach.

For some classes of molecule, laser ablation offers an effective means of desorbing non-volatile species into a beam of carrier gas[82,83]. This approach has been employed successfully for a variety of large systems, including polypeptides[84,85] and metal clusters[86,87]. However, the direct interation of the ablation laser beam with

*Some of the material in this section appears in the introduction of reference 75 and has been reproduced from (DOI: 10.1063/5.0170080), with the permission of AIP Publishing

the sample means that it is not suitable for studies on light-sensitive samples, for which signficant fragmentation is often observed[88].

Biomolecules are often particularly challenging to prepare in the gas phase without thermal decomposition. Several techniques have been developed to prepare such samples in ionic form, the two most common methods being electrospray ionization (ESI)[89,90] and matrix-assisted laser desorption/ionization (MALDI)[91,92]. Both have been used extensively in combination with TOF-mass-spectrometry to investigate non-volatile, thermally sensitive species. However, they cannot easily be used to prepare neutral species in a form suitable for spectroscopic or dynamics studies. One technique that can prepare neutral species is laser-induced acoustic desorption (LIAD)[93,94]. The sample is coated onto the front face of a thin metal foil, and the rear side of the foil is irradiated by a pulsed laser beam. While the detailed desorption mechanism is still not completely established[95–97], the general idea is that thermal and acoustic waves induced by the laser travel through the foil to the sample, leading to desorption of a plume of neutral molecules. Sample photostability does not need to be considered since the laser beam does not interact directly with the sample, and laser focus and pulse characteristics can be adjusted to give control over desorption rate and pulse timing. LIAD has been used to prepare a range of samples, including biochromophores[98], other large biomolecules[99], and human red blood cells[100].

Closely related to LIAD is the laser-induced thermal desorption (LID) technique. First reported by Poully *et al.*[101], the LID source is essentially identical to a LIAD source, with the distinction that a continuous-wave (CW) laser is employed in place of a pulsed nanosecond laser. Replacing the pulsed laser system with a CW diode laser substantially reduces the cost of the source, as well as reducing the level of technical expertise required by the user. As a result of the continuous irradi-

ation of the foil, the desorption mechanism within a LID source is purely thermal. However, unlike the situation within a heated pulsed nozzle, the fact that the thin layer of sample is heated under vacuum results in sublimation into the gas phase being favoured over thermal decomposition. Molecular species for which LID has been employed successfully include the four deoxyribonucleic acid (DNA) nucleosides[101], uracil[102], 4-, 5- and 6-hydroxyindole[103], 5,6-dihydroxyindole[104], 5-fluorouracil[105], uridine[106], phenylalanine[107], and other biomolecules[108,109].

The LIAD and LID techniques have recently been compared by Wang et al.[110] Unsurprisingly, molecules prepared via these techniques are found to have a slower, broader velocity distribution than molecules prepared within a supersonic expansion[98], but both approaches are able to generate high-density plumes of intact sample molecules.

We have now covered the theoretical and experimental methods relevant to the work in this thesis. The remainder of this Chapter provides an overview of the systems studied and techniques developed over the course of the work described in this thesis.

1.6 Overview of thesis

Photoinduced processes occur readily in nature. The most famous example is photosynthesis, a light-induced series of chemical reactions, which allow plants to store the sun's energy.[111] Another well-known example is DNA damage directly or indirectly induced by UV radiation[112–115] which can result in mutations or cell death. DNA consists of a combination of nucleotide bases bonded to the

backbone molecule deoxyribose.[**] Tetrahydrofuran (THF) (c-C_4H_8O) is a cyclic ether which has been considered previously as a model compound for the DNA backbone constituent ribose[117–123]. THF also plays a vital role in polymerisation reactions[124,125], and is used as a polar solvent for organic synthesis. As a prototypical oxygen-containing heterocycle, investigations into the photostability and photofragmentation behaviour of THF are also of more general interest, and the molecule has previously been the subject of studies involving excitation at a variety of different wavelengths.[126,127] In Chapter 4 we present an experimental study into the photodissociation of THF at 193 nm in which we employ multi-mass VMI to characterize the scattering distributions of the photofragments. We also report calculated transition dipole moments for the $S_1 \leftarrow S_0$ transition originating from the two possible ground-state conformers, and consider the relationship between these transition dipole moments, which provide significant insight into the angular dependence of the scattering distributions.

Proteins are another class of molecules highly prevalent in biological systems. [†] Peptide bonds form the backbone of proteins and are of key interest for biochemical processes. Understanding the photostability and photofragmentation of such bonds provides insight into UV radiation damage to biological systems. Monopeptides have been considered previously as useful model compounds for investigating the peptide bond fragmentation dynamics in a variety of experimental[129–135] and theoretical[136–139] studies. *N*,*N*-dimethylformamide (DMF) is the simplest tertiary amide, a planar molecule[140–143] (apart from the hydrogen atoms on the two methyl groups), and its amide bond offers an ideal candidate to model the photodissociation dynamics of peptide bonds. Additionally, DMF has been postulated to play an important role in the formation of adenine in astrochemical environ-

[**]Some of the material in this section appears in the introduction of reference 116 and has been reproduced from DOI: 10.1039/D3CP01974H with permission from the Royal Society of Chemistry.

[†]Some of the material in this section appears in the introduction of reference 128 and has been reproduced from DOI: 10.1039/D2CP02662G with permission from the Royal Society of Chemistry.

ments.[144] In Chapter 5 we report data from a multi-mass VMI study into the photofragmentation dynamics of DMF at excitation wavelengths of 225 nm and 245 nm. This work is complementary to a previous study from our group into the dynamics at 193 nm[135]. In order to investigate the influence of charge on the dissociation dynamics of the peptide bond, Chapter 6 presents a VMI study into the photofragmentation dynamics of the DMF cation formed by ionization of neutral DMF at 118 nm. Photolysis wavelengths of 225 nm, 245 nm, and 280 nm have been investigated.

To properly understand the influence of side chains on the photostability and fragmentation behaviour of peptide bonds, the next step would be the investigation of di- and tri-peptides. However, one main limitation continues to be the intact preparation of such molecules in the gas phase. Gases or high-vapour-pressure liquids are usually introduced into the experiment as a molecular beam that is internally cold and has a narrow speed distribution, following expansion through a pulsed valve. This technique is incompatible with non-volatile molecules such as di- and tri-peptides, because their vapour pressure is not high enough. Thus, we require an alternative method of preparing non-volatile molecules in the gas phase. As noted in Section 1.5.2, several techniques exist to achieve this goal, with one being the LID method. We have designed and characterized our own custom-built fibre-coupled LID source, capable of preparing intact, neutral parent molecules with high molecular densities suitable for VMI experiments (see Chapter 8).

Another limitation of the experiment has been that thus far we have only been equipped with nanosecond lasers. We have recently extended the experimental capabilities in this regard, and now have access to a shared femtosecond laser system to conduct one-color femtosecond experiments. The characterization of the femtosecond laser beamline can be found in Chapter 7.

To showcase the new experimental capabilities arising from these two upgrades, in the work described in Chapter 9, we use the LID source in conjunction with the femtosecond laser to conduct experiments into the dissociative ionization of PAHs. PAHs are a class of aromatic molecules consisting of two or more fused benzene rings. They are often classified into 'light PAHs' (< 5 aromatic rings) and 'heavy PAHs' (≥ 5 aromatic rings). The high degree of conjugation gives PAHs unique chemical properties, such as high chemical and photostability. However, as a consequence PAHs are known to pollute the environment and are dangerous to environmental and human health due to their toxic, carcinogenic, and mutagenic effects.[145,146] The United States Environmental Protection Agency has designated 16 PAHs as priority pollutants, including benzo[a]pyrene, which is one of the compounds studied in Chapter 9. While there are natural emission sources of PAHs, such as volcanic eruptions and wildfires, incomplete industrial combustion of wood, petroleum and coal is the primary emission source.[147,148]. PAHs are hydrophobic due to the large conjugated system, making them robust towards natural decomposition, which is why man-made PAHs have been found even in remote locations on Earth, including in Arctic ice[149,150], deep-sea sediments[151], and high-altitude mountain lakes[152]. Soil systems are particularly affected, and act as PAH sinks because the organic components in the soil can bind PAHs effectively.[153,154] Microorganisms metabolize carcinogenic PAHs from the soil, posing a risk to marine and terrestrial flora and fauna.[155,156] From the environment, PAHs can be transferred to foods consumed by humans.[157–160] Food consumption is associated with over 70 % of PAH exposure for non-smokers[161], highlighting how PAH pollution links to global human health. PAHs are also highly abundant in the interstellar medium (ISM) and are thought to be responsible for 10 to 15 % of all galactic carbon.[162,163] It is commonly accepted that PAHs cause the unidentified infrared emission features.[164–166] Definite assignment requires the measurement of gas-phase spectra of the relevant PAHs, which recently allowed Campbell *et al.*[167] to

assign the interstellar bands at 9577 Å and 9632 Å to C_{60}^{+}. The most common growth mechanism for PAHs in space is the hydrogen abstraction and acetylene or carbon addition (HACA) mechanism[168,169], in which sequential hydrogen abstraction and radical formation followed by acetylene (C_2H_2) addition leads to stepwise growth to large aromatic systems.[170] Previously, Lee *et al.*[78] have observed that doubly charged fluorene, phenanthrene, and pyrene dissociate in a 'reverse HACA' fashion by sequential ejection of acetylene units. The experiments used single photon extreme ultraviolet (XUV) ionization. In Chapter 9 we investigate the dissociation pathways of triphenylene, perylene, and benzo[a]pyrene following strong-field or multiphoton ionization using 800 nm photons from the Titanium:Sapphire laser.

2 Methods

This Chapter describes the experimental and theoretical methods used in this thesis. The theoretical part is brief, as details of specific calculations are given in the respective results Chapters. In the experimental part, we will discuss the custom-built VMI spectrometer and the laser systems used to acquire the data in this work.

2.1 Experimental

2.1.1 Spectrometer

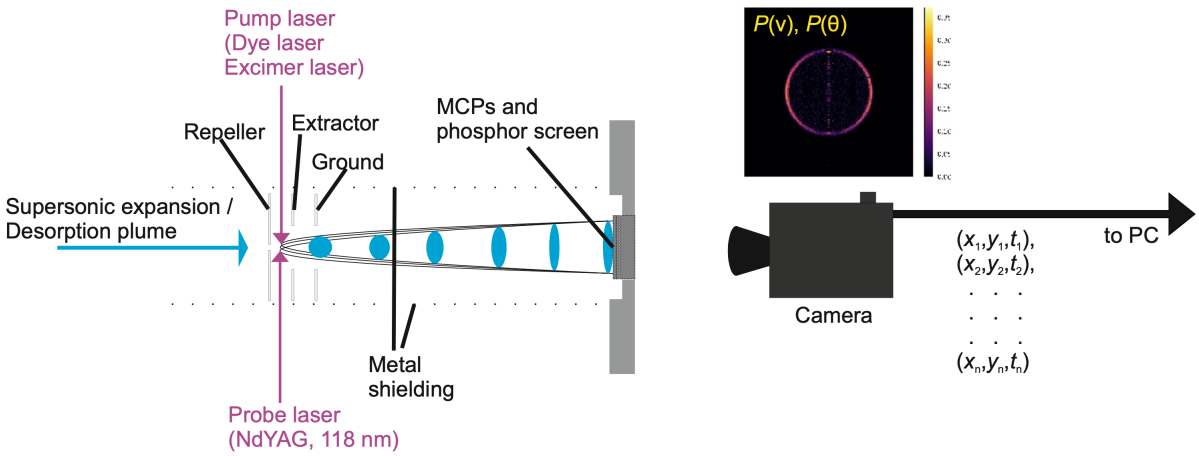

Fig. 2.1: Schematic of the custom-built VMI spectrometer.

Figure 2.1 shows a schematic of the custom-built VMI spectrometer used to record the experimental data presented in this thesis. Sample molecules are prepared in a supersonic expansion and pass through a skimmer before entering the velocity-mapping ion lens. In the interaction region, the molecules are first intersected by a photolysis laser, which electronically excites the molecules leading to the production of two or more neutral fragments. We use a dye laser or an excimer laser for this step. Subsequently, after a short delay of 15−20 ns, the products are ionized by the 118 nm (10.49 eV) ninth-harmonic of a neodymium-doped yttrium aluminium garnet (Nd:YAG) laser. The electric field maintained within the ion lens maps the product scattering distribution onto the position sensitive-detector, yielding a 2D projection of the full 3D scattering distribution. The various different components of the experiment are described in more detail in the following.

2.1.2 Vacuum system

Figure 2.2 shows a computer assisted design (CAD) drawing of the VMI spectrometer. The vacuum system comprises source, imaging, and detection chambers. The source chamber consists of a six-way cross. The bottom flange is used to mount a turbo pump (Pfeiffer Vacuum, HiPace1800, 1450 L/s) backed by a rotary pump (Edwards, E2M18). The base pressure in the source chamber is $\sim 10^{-8}$ mbar.

The source and imaging chamber are separated from each other by a metal face plate, on which the skimmer is mounted when a molecular beam is used (see Section 2.1.3). A high vacuum in the imaging chamber is achieved using another turbo pump (Pfeiffer Vacuum, HiPace700, 685 L/s) backed by a rotary pump (Edwards, E2M18). The base pressure in this chamber is $\sim 10^{-7}$ mbar.

The detection chamber is directly connected to the imaging chamber, and the two

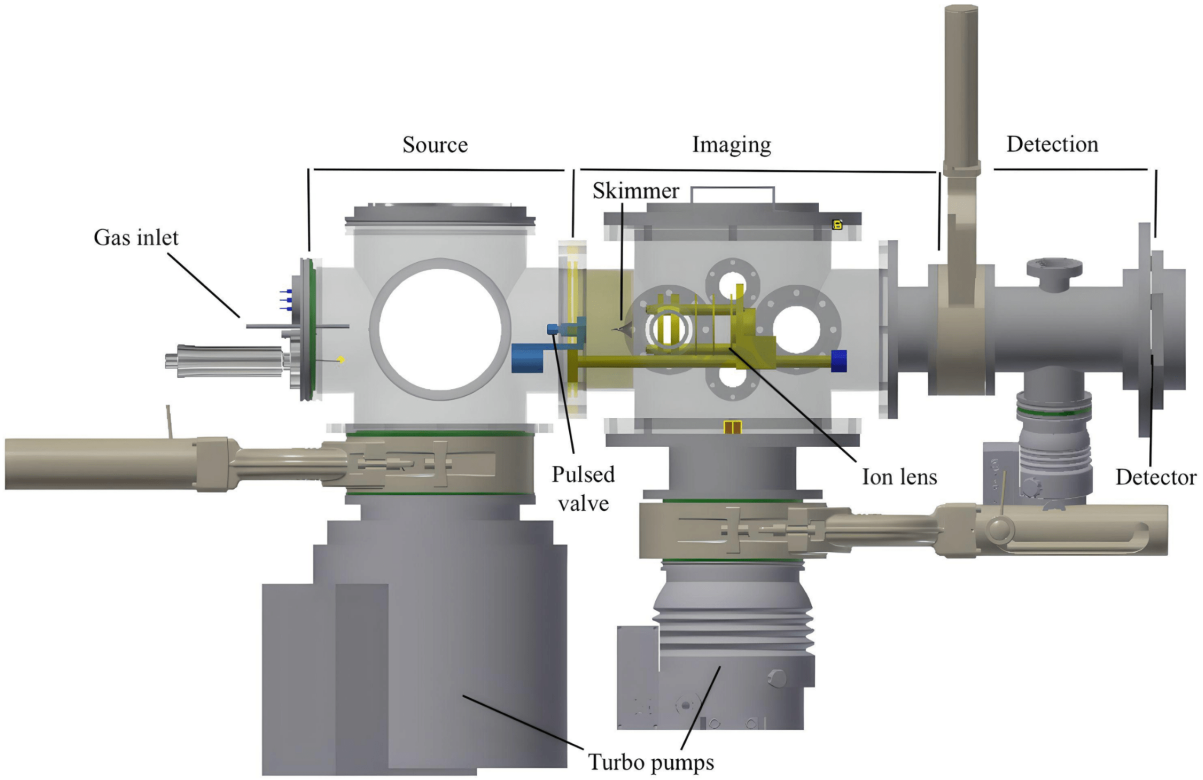

Fig. 2.2: CAD of the custom-built vacuum chamber from the side view. The chamber can be divided into three parts: source chamber, imaging chamber, and detection chamber. Gate valves on the experiment are shown in grey. Rotary pumps and the tubing between the gas inlet and the pulsed valve are invisible.

chambers can be isolated from each other by closing a gate valve. The chamber is pumped by another turbo pump (Pfeiffer Vacuum, HiPace80, 67 L/s) backed by a rotary pump (Edwards, RV12). In isolation, the base pressure is $\sim 10^{-6}$ mbar. During image acquisition, the detector and imaging chambers are connected, with a combined base pressure of $\sim 10^{-7}$ mbar.

2.1.3 Pulsed molecular beam

The liquids DMF (Sigma-Aldrich, 99.8 %) and THF (Sigma-Aldrich, ≥99.99 %), and the gas chlorine were introduced into the vacuum experiment via supersonic expansion through a pulsed valve. For the liquids, helium (BOC, 99.9 %, 1 bar back-

ing pressure) was bubbled through the sample in a mini-bubbler, yielding gaseous sample seeded in helium. Chlorine (BOC, 99.5 %) is already a gas and was seeded in Helium at a 10:90 ratio with a total pressure of 2 bar. Metal tubing connects the gas mixture to a pulsed solenoid valve (Parker Hannifin, Series 9, 10 Hz) located within the source chamber.

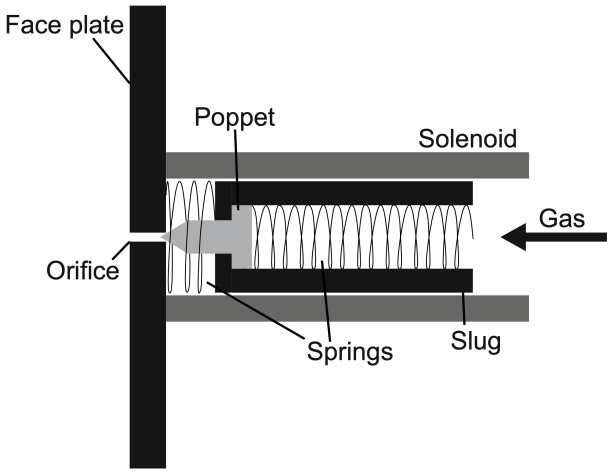

Fig. 2.3: Schematic of the Parker Hannifin pulsed valve used in the present work. The solenoid (grey) is magnetized when a current is passed through, which pulls the steel slug (black) back. The slug houses a Teflon poppet, which is retracted, opening the orifice to the gas. Once the current stops, a spring mechanically pushes the poppet back into the orifice, terminating the gas flow.

Figure 2.3 shows a schematic of the pulsed valve used in this work. The solenoid contains the steel slug, which houses the poppet. When current flows through the solenoid, the resulting magnetic force pulls the slug back, opening the orifice. Gas expands through the pulsed valve. When the current flow stops, a spring seals the orifice by mechanically pushing the poppet back into place.

There are several adjustments that can be made to optimize the performance of the pulsed valve. Firstly, we can change the opening duration of the pulsed valve by adjusting the period over which current is applied to the solenoid. This period is generally on the timescale of hundreds of µs. For the Parker Hannifin valve, the minimum opening time is about 250 µs, as this is the time needed for the mechanical opening and closing of the valve. Longer opening times increase the amount

of gas consumed and increase the amount of background gas. They also lead to lower molecular beam densities.

Secondly, we can adjust the force with which the slug is pulled back by changing the amount of current passing through the solenoid. The current should be high enough to open the orifice fully. However, it needs to be low enough to prevent multiple oscillations through bouncing of the springs.

Lastly, we optimize how tightly the pulsed valve body is screwed onto the face plate, which determines the pressure exerted by the two springs. This is an essential step, as the pulsed valve malfunctions otherwise. If it is screwed on too tight, the pulsed valve cannot open properly. If it is too loose, it cannot seal properly, in which case the temporal profile of the molecular beam exhibits an effusive tail. We make this adjustment when the experiment is at atmospheric pressure with the valve mounted in situ within the source chamber. Proper operation is confirmed when a small piece of lens tissue held in front of the valve is deflected by the gas pulses.

The molecular beam passes through a 1.5 mm skimmer before entering the interaction region in the imaging chamber.

Figure 2.4 shows a temporal profile of the molecular beam for neat N_2 detected via multi-photon ionization. The laser pulse has a temporal width of tens of femtoseconds, which is several orders of magnitude shorter than the molecular beam. Thus, the observed time profile is governed by the molecular beam and varying the delay between laser pulse and molecular beam allows us to measure the molecular beam density as a function of time. The observed beam profile is a normal distribution with a standard deviation of $\approx 250\,\mu s$. The pulse length applied to the solenoid was 250 µs.

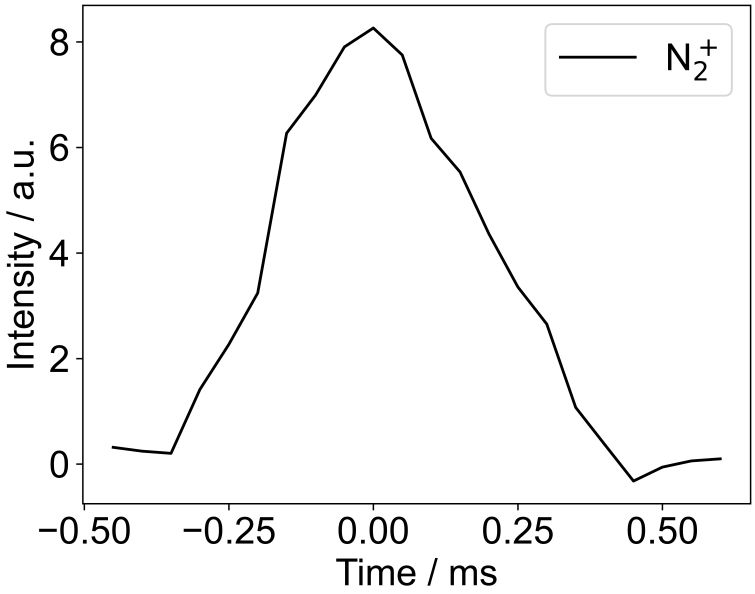

Fig. 2.4: Temporal profile of the molecular beam obtained via the ionization of N_2 with the 800 nm Titanium:Sapphire laser. The observed intensity is proportional to the number of molecules in the interaction region. Thus, varying the delay between laser pulse and molecular beam allows us to measure the molecular beam in time. The intensity is obtained by integrating the N_2^+ signal over time for each delay.

If the number of gas molecules introduced into the source chamber substantially exceeds the number of molecules pumped out, the skimmer can act as an effusive 'virtual' source. Consequently, the molecular beam exhibits an effusive tail in the temporal profile of the molecular beam. The pulse in Figure 2.4 does not show such a tail, confirming a well-defined, internally cold supersonic molecular beam.

2.1.4 Laser systems

Tunable Dye Laser

The Sirah Cobra-Stretch tunable dye laser is used to produce UV laser pulses with wavelengths between 215 and 280 nm. Figure 2.5 shows a schematic of the laser and its beam path to the experiment. The dye laser is pumped by the third harmonic of a Continuum Surelite II Nd:YAG laser (355.67 nm, 167 mJ per pulse, 7 ns,

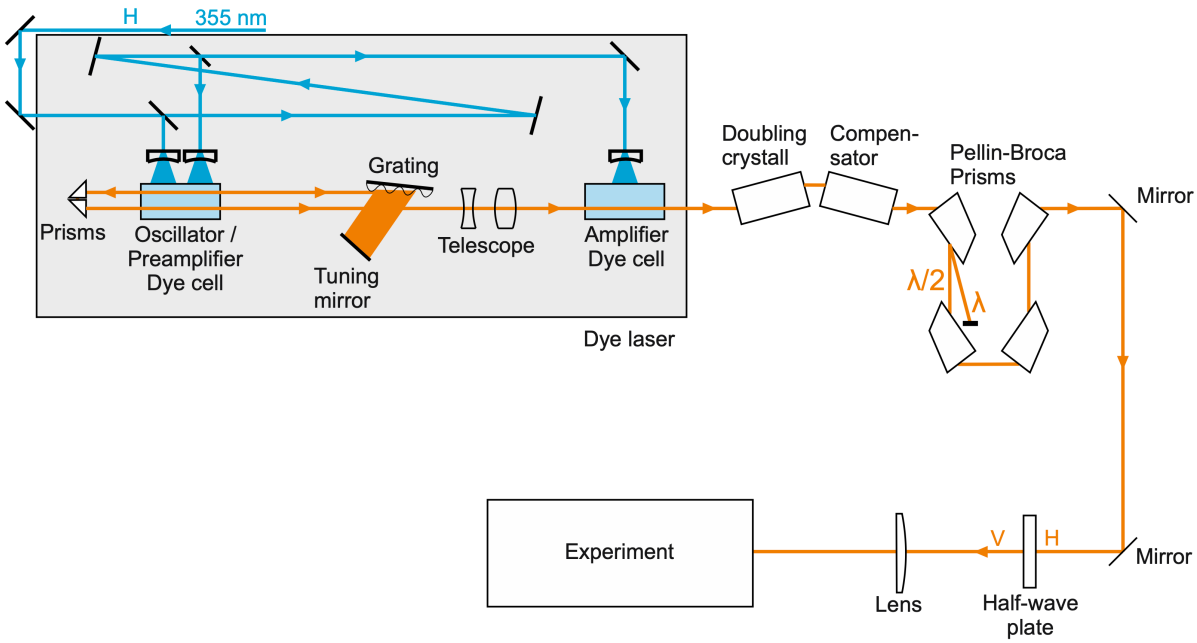

Fig. 2.5: Schematic of the tunable dye laser with beamline to the experiment. The laser dye, solvent, and grating angle determine the output wavelength of the laser. For details, refer to the text.

10 Hz). The pump beam is split into three parts and utilized at the oscillator, pre-amplification, and amplification steps. Starting with the oscillator beam, the 355.67 nm pump beam is focused into the laser dye in the preamplifier dye cell, causing population inversion of the laser dye. The dye molecules relax to the electronic ground-state via fluorescence. The resulting wavelengths depend on the laser dye and solvent used.

During the oscillator stage, laser action occurs within the cavity formed between the grating and the end mirror at the wavelength selected by the grating angle. The coherent oscillator beam emerging from the cavity then passes through the preamplifier and undergoes its first stage of amplification. The oscillator and preamplifier stages both occur within the oscillator cuvette, but are separated vertically in space.

Finally, the preamplified laser beam passes through the main amplifier, consisting of another dye cell that is pumped by the 355.67 nm light. The resulting out-

put passes through a beta barium borate (BBO) crystal, which frequency doubles the light. A set of four Pellin-Broca prisms subsequently separates the frequency-doubled light from the fundamental wavelength. Subsequently, the frequency doubled light is guided into the experiment. A tunable half-wave plate (HWP) converts the horizontally polarized light (perpendicular to the imaging plane) into vertically polarized light (vertical in the imaging plane). A plano-convex lens (ultra violet fused silica (UVFS), see Table 2.1 for focal length) focuses the light into the interaction region.

Tab. 2.1: Laser dye concentrations in the pre-amplifier and amplifier cell to generate the wavelengths used in this work. The focal length refers to how the laser light was focused into the experiment.

Wavelength / nm	Laser Dye	Solvent	c^*/gL^{-1}	$c^\dagger/\mathrm{gL}^{-1}$	Focal length / cm
225	Coumarin 2	Ethanol	0.200	0.067	45.0
245	Coumarin 307	Ethanol	0.400	0.133	50.0
280	Coumarin 153	Ethanol	1.600	0.533	50.0

* Mass concentration in the oscillator/pre-amplifier dye cell
† Mass concentration in the amplifier dye cell

The laser dye and solvent determine the range of wavelengths over which the dye laser can be tuned. We chose the dye and solvent according to the Sirah Lasertechnik specifications sheet. Table 2.1 summarizes the laser dye and solvent concentrations used. The dye laser was used as a photolysis laser to investigate the dissociation dynamics of DMF in Chapter 5 and the DMF cation in Chapter 6.

Excimer Laser

A Neweks excimer laser was used to produce pulses of 193.3 nm light at a repetition rate of 10 Hz, employing a 0.2 % Fluorine, 3.75 % Argon, 96.05 % Helium gas mixture as the gain medium. While the ground state PES for the ArF molecule is repulsive, the electronically excited state surface is bound. The molecule therefore

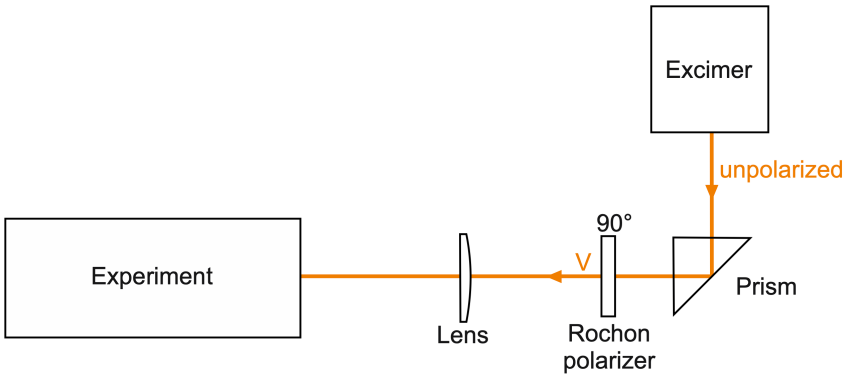

Fig. 2.6: Schematic of the excimer laser beamline to the experiment.

only exists in the excited state, and is known as an exciplex ('excited-state complex'). Within the laser, ArF exciplexes are formed in an electric discharge. Since no stable ground state exists, the population inversion is complete, and subsequent stimulated emission creates the 193.3 nm light.

The laser beam path is shown in Figure 2.6. The laser beam is steered by UVFS prisms. The unpolarized light is afterwards polarized by a (90°) Rochon polarizer, creating a vertically polarized beam (vertical in the imaging plane), which is focused into the interaction region by a UVFS lens (25 cm focal length). We utilized the excimer laser as a photolysis laser for the experiments on THF presented in Chapter 4.

Nd:YAG Laser

We use the ninth-harmonic of a Continuum Surelite I Nd:YAG laser to ionize the photofragments. The laser and the beam path to the experiment are shown schematically in Figure 2.7. A flashlamp produces several-microsecond-long laser pulses, which pump the Nd:YAG gain medium and achieve population inversion. Within the cavity consisting of two mirrors, the short pulses of several nanoseconds are generated via Q-switching, a technique controlling the quality factor of

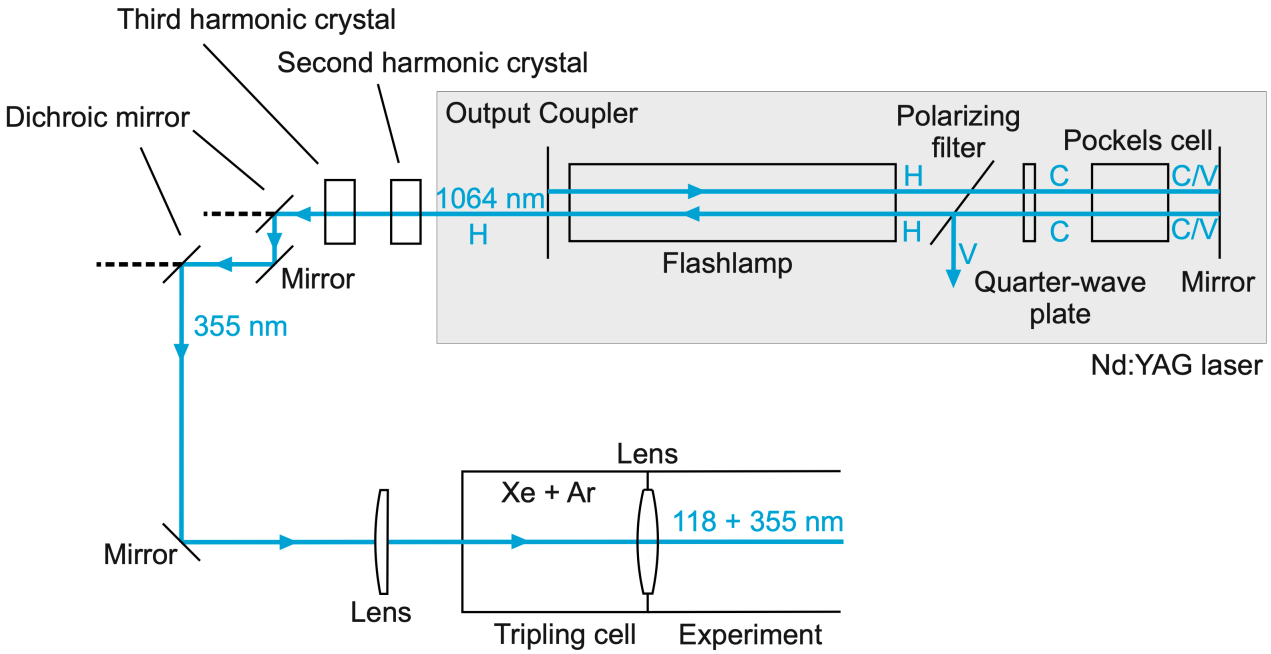

Fig. 2.7: Schematic of the Nd:YAG laser and its beam path to the experiment. The output power of the laser is controlled via Q-switching. The ouput light has a fundamental of 1064 nm. We use the ninth-harmonic of the fundamental as probe laser in the experiment.

the optical resonator. The Q-switching setup consists of a polarization filter, a quarter-wave plate, and a Pockels cell. If current is applied to the Pockels cell, the light is horizontally polarized, and the polarization filter is transmissive to the light. If the current stops, the light is vertically polarized in the polarization filter, and subsequently reflected out of the cavity. As a result, the microsecond pump beam is converted into a nanosecond laser beam. Changing the delay between the flashlamp and Q-switch also allows for electrical control of the energy of the laser pulses.

The output light is horizontally polarized and has a fundamental wavelength of 1064 nm. This light travels through the second harmonic generation (SHG) and triple harmonic generation (THG) stages to create a mixture of 355 nm, 532 nm, and 1064 nm wavelengths. Dichroic mirrors separate out the 355 nm light, which is guided through a plano-convex lens (UVFS, 200 mm focal length), into a tripling cell.

The tripling cell contains a phase-matched gas mixture of 27 mbar xenon (BOC, 99.9 %) and 298 mbar argon (BOC, 99.9 %), which frequency triples the 355 nm light to create 118 nm light.[171–174]. The 118 nm light (ninth harmonic of the fundamental, 10.49 eV) is focused into the interaction region by a plano-convex lens (MgF_2, 75 mm focal length), which also acts as a window between the tripling cell and the high-vacuum chamber. Under these focusing conditions, the 355 nm light focuses well away from the interaction region. The 118 nm pulse energy can be tuned to be on the order of tens to hundreds of nanojoules. The ionization potentials of most organic compounds are between 8−11 eV, enabling the 118 nm light to ionize them via single-photon absorption, making it a near universal ionization technique. The 118 nm light was used in the probe step for the experiments described in Chapters 4−6 and Chapter 8.

2.1.5 Ion lens

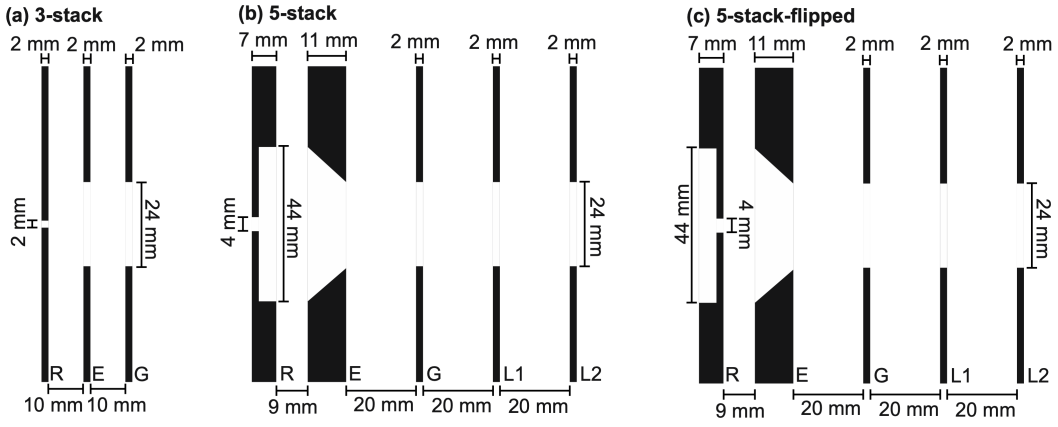

Fig. 2.8: Two-dimensional side-view of the ion lenses used in this thesis. Dimensions are indicated in the Figure. The 3-stack, shown in (a), is the simplest design suitable for crushed VMI, and consists of repeller, extractor, and ground plate. The 5-stack is suitable for crushed VMI, or sliced-imaging[49]. The 5-stack flipped is similar to (b), but the repeller plate is flipped.

VMI is achieved by using the electric field generated by an appropriate ion lens to map the ions onto the detector. For the work described in this thesis, we used three different ion lenses, to investigate how the performance of the LID source

developed in this thesis varies with the distance from the repeller plate hole to the interaction region. Figure 2.8 shows cross-sections through the ion lenses, labelled with dimensions. Each ion lens consists of a minimum of three lens elements, referred to as the repeller (R), extractor (E), and ground (G) plates. For velocity mapping the ratio of potentials applied to the plates are approximately $V_{\mathrm{R}} : V_{\mathrm{E}} : V_{\mathrm{G}} = V_{\mathrm{R}} : 0.73V_{\mathrm{R}} : 0$. For the 5-stack and 5-stack-flipped, the additional two electrodes were grounded. The exact lens potentials were optimized daily and depended on the distance between the point of ionization and the detector. The repeller voltage V_{R} is adjusted to fit the ion distribution on the detector with sufficient spatial resolution. If V_{R} is too small, the product scattering distribution has too much time to expand, and the ion distribution does not fit fully on the detector. Fast and light ions are particularly affected. If V_{R} is too large, the scattering distribution is mapped onto only a small area on the detector, decreasing the spatial resolution of the image. This tends to affect particularly slow and heavy ions. SMI requires potential ratios of approximately $V_{\mathrm{R}} : V_{\mathrm{E}} : V_{\mathrm{G}} = V_{\mathrm{R}} : 0.90V_{\mathrm{R}} : 0$.

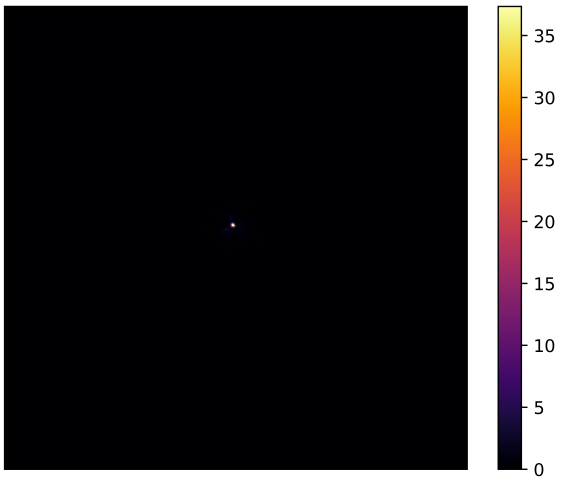

Fig. 2.9: DMF^+ parent ion distribution under VMI conditions following single-photon ionization at a wavelength of 118 nm. Due to the very small recoil velocity imparted by the departing electron, this is essentially an image of the transverse velocity distribution within the molecular beam.

VMI conditions are optimized by focusing the parent ion to a small spot on the detector, as shown for DMF^+ in Figure 2.9. The parent ions appear as a spot because

they have little to no kinetic energy in the imaging plane. If the voltage ratios are not optimized, the parent distribution will appear as a line, reflecting the shape of the interaction region between the molecular beam and the probe laser beam.

2.1.6 Time-of-flight

Upon ionization, the electric field of the ion lens accelerates the ions towards the detector. Electrostatic potential energy is converted into kinetic energy of the ions,

$$\frac{1}{2}m{v_\parallel}^2 = zV, \tag{2.1}$$

where m is the ion mass, $v_\parallel$ is the velocity along the TOF-axis, z is the charge of the ion, and V is the potential of the electric field. The ion velocity can be expressed by the TOF length d, i.e. the distance between the ionization point and the detector, and the time of flight t,

$$v_\parallel = \frac{d}{t}. \tag{2.2}$$

Substituting equation 2.2 into equation 2.1 and solving for t gives

$$t = \underbrace{\frac{d}{\sqrt{2V}}}_{k}\sqrt{\frac{m}{z}}, \tag{2.3}$$

where k is a constant for a given potential. Therefore, the arrival time t is proportional to $\sqrt{\frac{m}{z}}$. As the scattering distributions are travelling towards the detector, they separate according to their m/z. Lighter ions with higher charges travel faster than heavy, low charge ions. If two peaks in the mass spectrum are known, this allows mass-calibration of the TOF spectrum, in which t is converted to m/z, revealing information on the fragment identity and charge state of the ion.

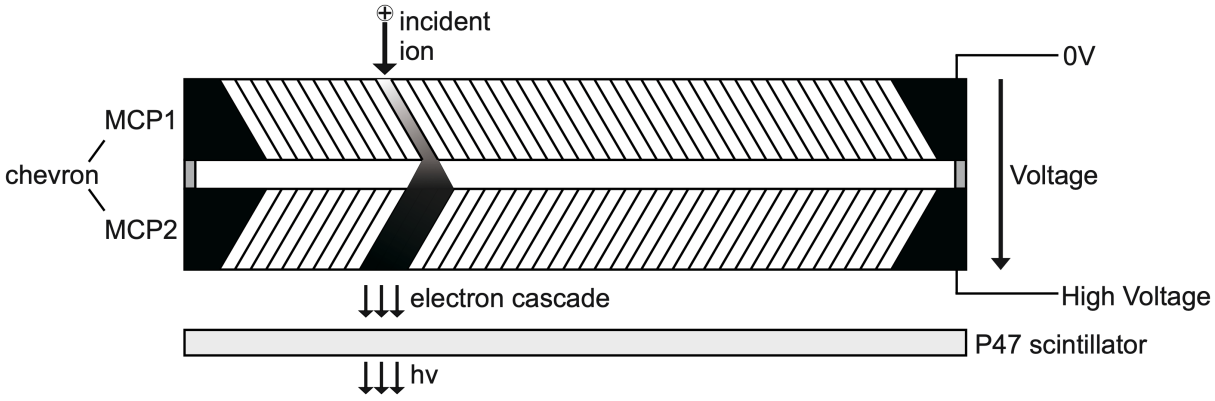

Fig. 2.10: Schematic illustration of an ion imaging detector. The incident ion hits the front of a pair of two chevron-stacked MCPs. A gradiant potential accelerates the produced electron cascade to a P47 phosphor scintillator, which converts the electrical signal and an optical signal.

The potential, V, with which the scattering distributions are accelerated, is mainly determined by the repeller potential V_{R}. Thus, a low voltage V_{R} gives the scattering distributions more time to separate, improving the mass resolution. High voltages worsen the mass resolution, as the scattering distributions have less time to separate. Ions that are close in their m/z might not fully separate, as the scattering distributions for the different ions overlap partially.

2.1.7 Detector

Finally, we need to be able to record the arrival position of the ions with a position-sensitive detector. The detector needs to convert the incoming ion into a detectable signal. In our case, we convert incoming product ions into light, which is subsequently captured by a camera. The detector needs to be sensitive to the ionized photolysis products independent of their identity and velocity. Secondly, it needs to have a high time resolution to resolve the signal of products with adjacent mass-over-charge ratios. Furthermore, the wavelength and intensity of the emitted photons have to match the requirements of the camera. Lastly, the detector needs to be able to operate continuously for long periods without a decrease in performance.

Figure 2.10 shows a schematic of the detector used for the work described in this thesis. The incident ion strikes a microchannel plate (MCP). MCPs consist of an array of small channels which act as electron multipliers. The channels are parallel to one another and at a small bias angle to the input surface. If an ion strikes the wall in one of these amplifiers, several electrons are released, which are accelerated down the microchannel and can strike the channel wall themselves, leading to emission of further electrons. In this way, each ion produces an electron cascade. MCPs can be stacked to yield larger charge amplifications, with amplification factors of $10^4 - 10^7$. The time resolution of MCPs is typically < 100 ps[175], making them suitable for applications in TOF mass-spectrometry. One downside is that ions are only detected if they strike a microchannel. Thus, the detection efficiency depends highly on the open area ratio of the MCP, which is the area of the detector surface comprising the entrances to microchannels divided by the total area of the surface. The open area is usually around 60 %[176,177] but can be increased to higher values.[178]

The next step is to convert the charge output from the MCPs into light. The main technique used in chemical reaction dynamics to achieve this conversion are scintillators. Scintillators are absorbing materials that convert the energy of incident charged particles into optical signals.[179] The most commonly used scintillator in the field is a P47 (Y_2SiO_5:Ce) phosphor, with a decay lifetime of 69.3 ± 0.8 ns. Alternatives with a shorter decay lifetime include various Exalite laser dyes, which have decay lifetimes of around 4 ns.[180] Short lifetimes are beneficial as they improve the time resolution and therefore the mass resolution of the experiment.

Our ion detector works as shown schematically in Figure 2.10. It comprises a pair of chevron-stacked MCPs (Photonis, 31849) with an active diameter of 40 mm and an open area ratio of 55 %. The front of the MCP stack is grounded to ensure that

the flight tube is a field-free region. The back has a potential of 1.9 kV applied in order to accelerate the electron cascade from the front to the back of the MCPs. The emitted electrons are incident on a P47 scintillator coated on conductive glass. We apply a voltage of 4.4 kV to the glass to accelerate the electrons into the scintillator.

The potentials applied to the back of the MCP stack and the phosphor were chosen for the following reasons. Firstly, the ion signal has to be distinguishable from camera noise, i.e. it has to illuminate multiple adjacent pixels on the camera. Secondly, the potentials need to result in suitable centroiding conditions, a data processing step explained in Section 3.1. Lastly, the ion signal should not be too high in order to avoid damage to the detector. We found that for our detector the above potentials were suitable.

2.1.8 Camera

The camera needs to record and store the optical signal emitted by the detector. The requirements are high spatial resolution and the capability to record multiple different fragment ions in one acquisition cycle. The two most commonly used multi-mass imaging sensors are the Pixel Imaging Mass Spectrometry (PImMS) sensor[181–183] and Timepix[184,185]. In this work a PImMS 2 sensor is used. The camera has an array of 324 $\times$ 324 pixels, and each pixel can record up to four ion hits per acquisition cycle with a time resolution of 25 ns. The sensor records an (x, y, t) data point for each incident ion, where (x, y) is the position on the detector and t is the arrival time of the ion. Prior to data acquisition, the camera lens is adjusted to focus on the phosphor screen. The set-up is optimized so that the P47 scintillator takes up as many pixels as possible while still being captured fully by the camera, thereby maximizing the spatial resolution. The camera is controlled by

a custom LABVIEW code, which allows one to view the images in 'real-time' on a shot-by-shot basis.

Once summed over a sufficient number of acquisition cycles, the ion hits form ion images, which are the raw data from the experiment. In the next Chapter, we will describe how the images are processed post-experiment to obtain meaningful information from the data. We will see that the conclusions we draw directly link to the questions we want to answer about our chemical systems.

2.2 Theoretical calculations

An introduction into electron correlation methods is provided in Appendix A. For a general introduction to electronic structure theory or a more detailed explanation, the reader is referred to the standard literature[186,187].

The experiments described in Chapter 4 on THF and Chapter 6 on DMF^+ are supported by electronic structure calculations. Geometry optimizations were conducted using the Gaussian09[188] software program. Frequency calculations confirmed a finding of a global minimum. For THF, the transition dipole moment for the $S_0 - S_1$ photoexcitation was also calculated using Gaussian. For DMF^+, rigid PESs were calculated along the relevant internal coordinates using the Molcas software package[189]. The respective results Chapters contain specific details on the calculations.

3 Image processing

Here, we will cover data analysis techniques routinely used to obtain information on the photoproducts of our chemical system from the experimental data. During the experiments, data sets are collected for both 'signal' and 'background'. The details of both measurements will be described in the relevant Chapters. The first stage of image processing is often a background subtraction. Note that this does not apply for data sets that will be subjected to covariance analysis (described in Section 3.4).

The camera output to the computer is a list of (x, y, t, i, j) data points, in which each data point corresponds to a detected ion. (x, y) are the spatial coordinates, t is the arrival time, i is the acquisition cycle number, and j is the time stamp register in which the ion hit was stored.

Integrating the data set over the spatial coordinates (x, y), as well as over i and j, yields the TOF spectrum of the photolysis products. A mass calibration of the spectrum, as explained in Section 2.1.6, reveals the fragment identities, linking to our initial question of which chemical bonds break in the molecule during the dissociation.

Integrating the data set over the relevant ranges of the time coordinate yields the velocity-map images for each detected species. This chapter gives an overview

of the steps necessary to extract kinetic energy release information from the ion images. It also discusses covariance analysis, a commonly used data analysis technique in the field used to obtain information on correlated ions originating from the same parent molecule. Both, the kinetic energy distribution of the products and the covariance analysis yield great insight into the fragmentation mechanism.

3.1 Centroiding

The detector runs under conditions such that an incident ion illuminates multiple adjacent pixels of the camera rather than a single pixel, with the advantage of distinguishing camera noise from the real signal. However, the spatial resolution suffers as each ion is recorded as a pixel cluster, and the precise position of the ion on the detector is therefore not sharply defined. Furthermore, different ions are recorded with different intensities depending on where they strike the detector relative to a pore of the MCP. Care must be taken not to overcount ions leading to large clusters while undercounting ions leading to smaller ones. To achieve this, we apply a centroiding algorithm.

Centroiding[190] is a data processing technique used to improve the spatial and temporal resolution of the data and to count every ion hit only once. First, we remove camera noise from the data. Camera noise typically triggers single pixels, while ion hits trigger multiple pixels. Thus, we remove the camera noise by discarding all one-pixel hits from the data. The number of ion hits lost by this process is negligible compared to the signal-to-noise improvement of the data. Next, the algorithm determines the centre of mass of the pixel cluster and assigns the ion to the pixel closest to that centre with an intensity of one.

Centroiding also needs to be conducted in time, as an ion hit is usually detected in several adjacent time bins as a consequence of the decay time of the P47 scintillator exceeding the time resolution of the camera. A pixel is triggered once the signal intensity exceeds the user-defined rising edge threshold. For pixels closer to the centre of mass of the recorded signal cluster, the signal exceeds the rising edge threshold earlier compared with pixels further away. Thus, adjacent pixels might be triggered in different time bins by the same ion hit. Therefore, we include a time spread into the centroiding algorithm as it searches for clusters of pixels. This time spread has to be long enough to capture all pixels of an ion hit but short enough to separate different ion hits from each other. We assign the arrival time as the earliest time bin in the cluster: since the ion cannot be detected before it has arrived, the earliest time must be the most accurate one. For the data in this thesis, a time spread of six time bins (150 ns) is used. Centroiding in time improves the mass resolution and can help to distinguish ions with different m/z that hit the detector close to each other in time.

To employ the centroiding algorithm, the data must be acquired under conditions such that the pixel clusters corresponding to individual ion hits are separated in space and do not overlap. Before each measurement, we checked that this was the case, reducing the signal levels if required. Centroiding stops being feasible once the number of events per experimental cycle is so high, that the pixel of different ions overlap in space and time and the centroiding algorithm cannot distinguish them anymore. However, this limit depends on the specific experimental conditions, in particular the detector area that is struck by the ions.

3.2 Inversion methods

Crushed VMI is a technique in which the scattering distributions are crushed along the TOF-axis in order to improve the mass resolution of the experiment. We record a 2D projection of the 3D scattering distribution. Hence, we lose information on the scattering distribution along the TOF-coordinate. The product velocity distribution cannot be directly obtained from the 2D projections, since the radial distribution of the 2D image differs from that of the original 3D distribution. For example, if fragments recoil along the TOF-axis, they will land in the image centre, implying a recoil velocity of zero. However, their recoil velocity might have been significant, but since the image is crushed along the TOF-axis we lose the velocity information. We recover it by reconstructing the 3D scattering distribution from the 2D image. This process is called image inversion and yields the central slice of the original (cylindrically symmetric) 3D distribution, as shown in Figure 3.1. The inverted image can be used to extract quantitative information on the velocity distribution of the product fragments. For the scattering distributions recorded in our experiments, the axis of cylindrical symmetry is the electric vector ϵ of the photolysis laser, which is vertical in the imaging plane (see Figure 3.1). The inverted image contains the symmetry axis. Hence, by rotating the inverted image about the axis of cylindrical symmetry, the 3D scattering distribution is obtained. The most common inversion technique is the inverse Abel transform.

3.2.1 Abel inversion

The inverse Abel transform[191,192] is a mathematical procedure used to recover the 3D scattering distribution from the 2D image. Here we provide a short derivation based on previous work by Eppink *et al.*[193]

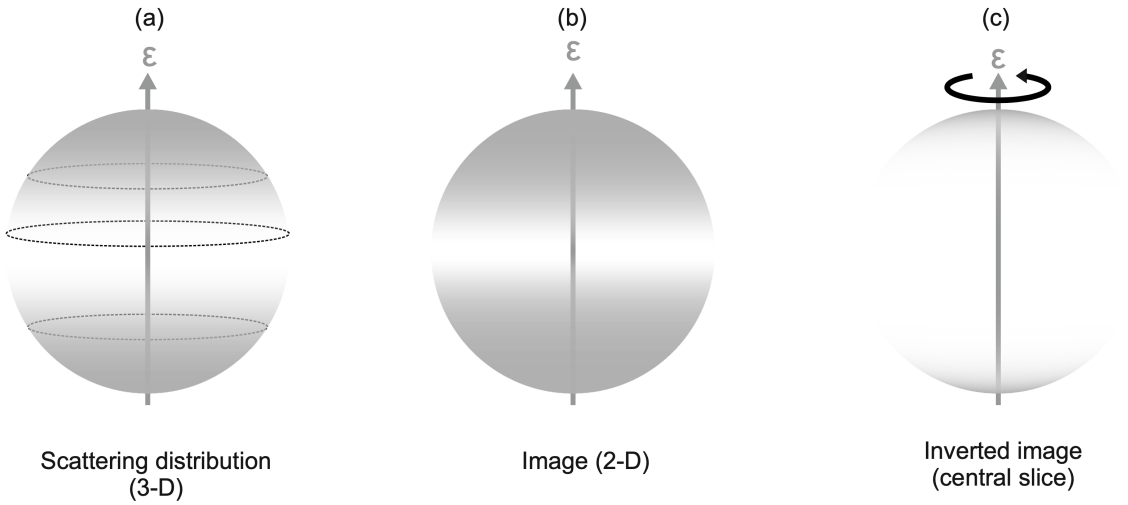

Fig. 3.1: Schematic illustration of an inverted velocity-map ion image. The 3D scattering distribution (a) is crushed along the TOF-axis. We record the 2D projection (b) of the 3D sphere. This image is cylindrically symmetric about the laser polarization axis, ϵ, which is vertical in this case. Making use of the symmetry, the 2D image is inverted. The result is the inverted image (c), which is the central slice of the 3D distribution.

Let us consider a 3D scattering distribution $i(x, y, z)$ in Cartesian coordinates, where the TOF-axis is parallel to the z axis, the detector is in the x, y plane, and the y axis is the axis of cylindrical symmetry. Recording the 2D projection of the 3D image corresponds to integrating over z,

$$p(x, y) = \int_{-\infty}^{\infty} i(x, y, z)\, dz, \tag{3.1}$$

where $p(x, y)$ is the 2D image. If we now consider one row in the image at a height $y = y_0$, we obtain

$$f(x) = p(x, y_0) = \int_{-\infty}^{\infty} s(x, z)\, dz = 2 \int_{0}^{\infty} s(x, z)\, dz, \tag{3.2}$$

where $s(x, z) = i(x, y_0, z)$ is a slice of the distribution perpendicular to the axis of symmetry in the x, z-plane. Here, we have already used the symmetry properties of the scattering distributions by defining z_0 as a point on the axis of cylindrical symmetry so that the integrals over positive and negative z values are equal. To recover the 3D distribution, we want to obtain $s(x, z)$. Since this function is cylindrically

symmetric, we can express the 2D function $f(x)$ in polar coordinates,

$$f(x) = 2\int_x^\infty \frac{s(r)r}{\sqrt{r^2 - x^2}}\, dr, \tag{3.3}$$

where $r^2 = x^2 + z^2$. To now obtain $s(r)$ from the measured distribution $f(x)$, the Fourier transform convolution theorem can be applied, yielding

$$s(r) = \frac{1}{\pi}\int_r^\infty \frac{\frac{df(x)}{dx}}{\sqrt{x^2 - r^2}}\, dx. \tag{3.4}$$

Solving this equation for every row, i.e. for every y value, yields our original scattering distribution. However, this method also has limitations. For $r \to x$, finding an analytical solution to equation 3.4 is challenging since we cannot divide by zero. Furthermore, the method is sensitive to noise. For $x \to 0$, the noise is amplified significantly, leading to a central line of noise in the image in Cartesian Coordinates. Lastly, the method assumes a symmetrical input, which is never perfectly fulfilled for experimental data.

3.2.2 Basis function based inversion

Inversion can also be achieved by expanding the experimental image in a set of basis functions, each of which has a known inverse function. The weighting coefficients of the basis functions directly yield the information necessary to invert the image. The recorded 2D image, $I(r, y)$, is described by a set of basis functions, $\{ f_0(r, y), \ldots, f_{K-1}(r, y) \}$, according to

$$I(r, y) = \sum_{k=0}^{K-1} a_k \cdot f_k(r, y), \tag{3.5}$$

where a_k is the weight of the k-th basis function $f_k(r, y)$ and y is the axis of cylindrical symmetry in the 3D scattering distribution. The weighting coefficients are obtained directly by minimizing the difference between the experimental data and the fit with Equation 3.5. In addition, regularization methods can applied to avoid overfitting the data. One commonly used regularization method is the Tikhonov regularization[194], which penalizes large weighting coefficients by a user-defined factor.

Different basis function methods deviate in the shape of the basis function used. The basis function type and width depends on the data and is usually chosen to smooth the data to a reasonable extent while retaining sharp features in the data. Basis set expansion (BASEX)[195], the most commonly used basis function method, uses functions as follows,

$$\rho_k(r) = \left(\frac{e}{k^2}\right)^{k^2} \left(\frac{r}{\sigma}\right)^{2k^2} e^{-\left(\frac{r}{\sigma}\right)^2} \approx e^{-2\left(\frac{r}{\sigma - k}\right)^2}, \tag{3.6}$$

with σ being the standard deviation of the basis function. These are almost identical to Gaussian functions but can be integrated analytically, yielding the basis functions used for the fitting,

$$f_k(r) = 2\sigma\rho_k(r)\left[1 + \sum_{l=1}^{k^2}\left(\frac{x}{\sigma}\right)^{-2l}\prod_{m=1}^{l}\frac{(k^2+1-m)\left(m-\frac{1}{2}\right)}{m}\right]. \tag{3.7}$$

Other commonly used basis function methods are pBASEX[196] and lin-BASEX[197]. In this work, we use the BASEX method for image inversion, unless specified otherwise. Advantages of basis function fitting methods include that the user can choose the type of basis function used and the basis function width to fit the data as well as possible. Furthermore, this method is generally fast, as basis functions and their inverse functions are calculated and stored in advance.

3.3 Energy calibration

The inverted image can be used for quantitative analysis of the product kinetic energy. By defining the centre of the image and integrating over the angular coordinate, we obtain the radial distribution of the products. However, we need to convert the radial distribution (in pixel coordinates) into a kinetic energy distribution via an energy calibration.

The radius is proportional to the product velocity in the imaging plane $v_\perp$, perpendicular to the TOF-axis, which can be expressed as follows,

$$v_\perp = \frac{r}{t}, \tag{3.8}$$

where r is the radius and t is the TOF. From equation 2.3, the kinetic energy depends on the radius as follows,

$$E_{\text{kin}} = \frac{1}{2} m \left(\frac{r}{t}\right)^2 = zV \tag{3.9}$$

$$= \underbrace{\frac{V}{d^2}}_{s} zr^2. \tag{3.10}$$

The conversion is independent of the product mass, i.e. the identity of the product, as it is governed by the experimental constant s. The longer the TOF length d and the lower the potential of the ion lens V, the more time the scattering distribution has to expand and the larger the radius for a given product recoil energy. The product kinetic energy increases with r^2. Since the relationship is quadratic rather than proportional, a Jacobian has to be applied to the intensity when converting radial distributions to kinetic energy distributions. The integral of the intensity

before and after conversion has to be equal,

$$\int_0^\infty I(E_{\text{kin}})\, dE_{\text{kin}} = \int_0^\infty I(r)\, dr. \tag{3.11}$$

Solving the equation for $I(E_{\text{kin}})$ yields

$$I(E_{\text{kin}}) = \frac{I(r)}{2szr}. \tag{3.12}$$

Thus, the intensity increases in inverse proportion to the radius. An analogous conversion from radius to velocity or momentum can be conducted.

The objective of the energy calibration is to determine the scaling constant s, which depends solely on the field strength V and the distance d between the interaction region and the detector. This can be determined either through calibration experiments or simulations. We conducted calibration experiments on the photodissociation of Cl_2 at a wavelength of 355 nm. At this wavelength, the Cl_2 parent molecules are predominantly excited from the bound electronic ground state to a repulsive electronically excited state via the perpendicular transition $^1\Pi_{1u} \leftarrow ^1\Sigma_{0_g^+}$.[33,34] Each dissociating molecule absorbs an energy of 3.50 eV. The dissociation energy of the Cl−Cl bond is 2.52 eV.[198] Thus, the system has a total available energy of 0.98 eV. This energy can only go into product translation, as the two Cl atoms formed do not have internal modes. Therefore, we know that the TKER is 0.98 eV. Furthermore, the Cl atoms are formed with equal and opposite momenta. Hence, their kinetic energy is equal and the total kinetic energy is evenly distributed to the two Cl atoms. Thus, both Cl atoms recoil with a kinetic energy of 0.49 eV and a velocity of

$$v_{\text{Cl}} = \sqrt{\frac{2E_{\text{Cl}}}{m_{\text{Cl}}}} = 1.6 \cdot 10^3 \text{ ms}^{-1}. \tag{3.13}$$

For the experiment, a 10 % mixture of Cl_2 seeded in Helium is prepared in a super-

sonic expansion, leading to ground-state $Cl_2(^2P_{3/2})$ in the interaction region. The molecule is photoexcited by the third harmonic of an Nd:YAG laser and breaks apart into two Cl atoms. The resulting fragments are ionized via (2+1) REMPI with the tunable dye laser, whose frequency was scanned from 236.1790 to 236.1890 nm to capture the complete Doppler width of the recoiling fragments.

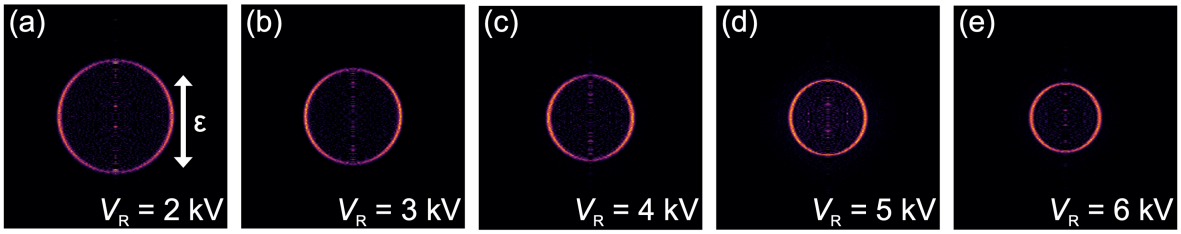

Fig. 3.2: Inverted velocity-map images for the ^{35}Cl atomic products from the photodissociation of Cl_2 as a function of repeller potential V_R. The electric vector of the photolysis laser is vertical in the images.

The resulting TOF spectrum (not shown) shows two peaks, which we assign to the two isotopes ^{35}Cl and ^{37}Cl. By integrating only over the ^{35}Cl peak, we eliminate the effects ^{37}Cl has on the energy calibration. Figure 3.2 shows the resulting inverted velocity-map images of the ^{35}Cl photoproducts. Each image comprises a well-defined ring, corresponding to the single allowed product recoil velocity . As explained above, the radius of the ring increases with decreasing repeller potential.

Tab. 3.1: Radius of the inverted Cl ion image following the dissociation of $Cl_2 \longrightarrow Cl + Cl$ for different repeller voltages.

Repeller voltage / V	2000	3000	4000	5000	6000
Radius / pixels	129	106	91	82	75

Table 3.1 summarizes the radius of the Cl atoms for the different repeller voltages. Fitting a second degree polynomial over the radius as a function of the repeller voltage yields,

$$r_{Cl}(V) = 2.199921 \cdot 10^{-6} V^2 - 2.843602 \cdot 10^{-2} V + 1.5233975 \cdot 10^{2}. \tag{3.14}$$

For a product ion arriving at the radius r_p within the imaging plane, the corresponding kinetic energy E_p is given by

$$E_p = E_{\mathrm{Cl}} \left(\frac{r_p}{r_{\mathrm{Cl}}} \right)^2 . \tag{3.15}$$

Therefore, we can obtain the kinetic energy of each product ion from the experiment. This relates directly to the question of how the available energy is distributed among the available degrees of freedom, which we set out at the beginning of this work. The product kinetic energy links directly to the reaction mechanism. For example, if the reactant undergoes significant geometrical rearrangement before fragmentation the kinetic energy release (KER) will tend to be low, as most of the available energy becomes dispersed into internal degrees of freedom. Next, we will discuss covariance analysis, a technique used to obtain information on ion pairs originating from the very same parent molecule.

3.4 Covariance analysis

Covariance is a statistical parameter that quantifies the correlation between two variables, X and Y. Mathematically, covariance is defined as follows,

$$\mathrm{Cov}(\mathrm{X}, \mathrm{Y}) = \langle (\mathrm{X} - \langle \mathrm{X} \rangle)(\mathrm{Y} - \langle \mathrm{Y} \rangle) \rangle \tag{3.16}$$

$$= \langle \mathrm{XY} \rangle - \langle \mathrm{X} \rangle \langle \mathrm{Y} \rangle, \tag{3.17}$$

where $\langle\ \rangle$ indicates the mean of the contained expression. Correlation between two variables means that the value of the first variable affects the value of the second variable. Positive covariance describes the correlation in which X being greater than its mean increases the probability of Y to be larger than its mean. Negative

covariance means the opposite, where if X is greater than its mean, the probability of Y to be larger than its mean is decreased. One example of positive covariance is the correlation between the consumption of processed meats and the prevalence of coronary heart disease and diabetes mellitus. People who eat processed meats regularly are more likely to get coronary heart disease or diabetes mellitus.[199] On the other hand, people who do not consume processed meats regularly are less likely to get the disease. An example of uncorrelated events is rolling two dice. The outcome of the first die does not affect on the outcome of the second die. Thus, they are not covariant with each other.

Since its first use in TOF mass-spectrometry[200], covariance analysis has established itself as a powerful tool capable of combining the advantages of multi-mass imaging with correlation information, which is inherent in the data set[201]. In our experiments, products coming from the same parent molecule are covariant with each other. However, products stemming from different parent molecules do not show covariance. Therefore, covariance analysis can look at product channels leading to the selected product pair while being blind to all other co-fragments. Since the product ions need to originate from the same parent molecule, measuring the respective ions in the same acquisition cycle is vital, highlighting the advantages of using a multi-mass imaging camera such as the PImMS camera.

In our application, we use either TOF-TOF covariance or recoil-frame covariance. The former uses the TOF-information, t, of the ions, and the latter uses the positional information, x, y.

3.4.1 TOF-TOF covariance

TOF-TOF covariance investigates the covariance between the arrival times of different ions. The product TOF is defined in equation 2.3 and depends on the product m/z. However, when the product is formed, it gains an additional momentum kick from the dissociation. If this momentum vector points towards the detector, the ion will arrive earlier at the detector. If it points in the opposite direction, it will arrive later. Mathematically, the relationship between the arrival time t and the product momentum p is defined as follows[202],

$$t = t_0 + kp\cos\theta, \tag{3.18}$$

where t_0 is the arrival time of the product if there was no additional momentum kick, k is a constant, and θ is the angle between the momentum vector and the TOF-axis.

Now, let us consider the following two-body channel: $AB^{2+} \longrightarrow A^+ + B^+$. If the A^+ ion experiences a momentum kick towards the detector, B^+ will experience a momentum kick in the opposite direction, as momentum has to be conserved. A^+ will arrive earlier and B^+ later than their respective means. Conversely, if A^+ experiences a momentum kick away from the detector and B^+ towards the detector, A^+ will arrive later, and B^+ will arrive earlier. In both cases, the daughter ions are covariant with each other, as they stem from the same parent molecule. Figure 3.3 shows the TOF-TOF covariance map for this example. The diagonal line from the bottom left to the top right is the variance of the signal and an axis of symmetry of the map. The covariance signal between the ion pair (A^+, B^+) is shown in red. The slope of this signal is $m = -1$, as this is a two-body channel. Higher-body channels lead to slopes between -1 and zero, $-1 \leq m \leq 0$. The covariance intensities for a

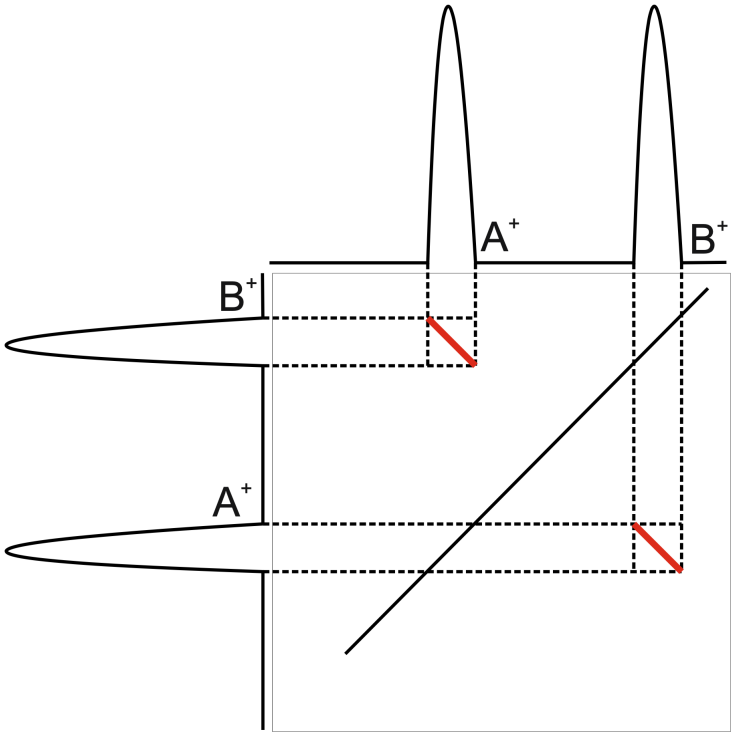

Fig. 3.3: TOF-TOF covariance map of a fictitious ion AB^{2+} dissociating into $A^+ + B^+$. The black diagonal is a symmetry axis of the map, the red lines are the covariance signal.

given ion pair in the map should also correlate directly with the branching ratios to form the ion pair, even though, to the author's knowledge, this has not been explored yet.

The main use of TOF-TOF covariance maps is to see which ion pairs display covariance with each other, i.e. which ion pairs can be formed as partner fragments from the same parent ion. While the slope contains some information on the dissociation mechanism, most mechanistic insight is obtained from recoil-frame covariance images.

3.4.2 Recoil-frame covariance

Recoil-frame covariance looks at the correlation between the velocity vectors of the two correlated ions. Again, the daughter ions need to originate from the same parent molecule. The recoil-frame covariance map visualizes the velocity vector of a selected signal ion relative to the velocity of a reference ion. Thus, the technique uses the x, y coordinates of the ions. Here, we discuss briefly the key points of this covariance technique. A comprehensive introduction is given in Dr David Heathcote's DPhil thesis[203].

In recoil-frame covariance, the variables X and Y from equation 3.17 correspond to the spatial coordinates $(x_{\mathrm{R}}, y_{\mathrm{R}})$ of the ion R^+ and $(x_{\mathrm{S}}, y_{\mathrm{S}})$ of the ion S^+. With a total of four variables involved, the resulting covariance is four dimensional, making it challenging to visualize. To reduce the dimensionality of the problem, we assign the ions R^+ and S^+ to be reference and signal ion, respectively. The goal is now to describe the velocity vector of S^+ relative to R^+. Next, we rotate the R^+ velocity vector, which so far could have been anywhere in the xy plane, to point along a pre-defined reference direction. The S^+ velocity vector is rotated accordingly. In that way, the four dimensional problem has been reduced to a two dimensional problem. The resulting recoil-frame covariance map shows us the velocity distribution of the signal ion relative to the reference direction, i.e. the distribution of relative velocities of the two ions.

Figure 3.4 shows a simulation of the recoil-frame covariance image corresponding to a diatomic molecule dissociating: $AB^{2+} \longrightarrow A^+ + B^+$. We have defined B^+ as the reference ion, and A^+ as the signal ion. In the covariance image we see A^+ is recoiling at an angle of 180° from the reference direction since momentum has to be conserved. The 'tail' towards the image centre arises because we are calculating

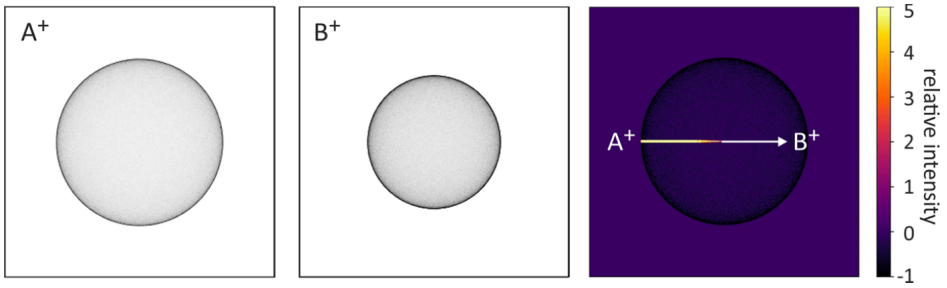

Fig. 3.4: Simulated velocity-map images (left and middle) and the recoil-frame covariance image (right) for the dissociation reaction $AB^{2+} \longrightarrow A^+ + B^+$. A+ is the signal ion, B+ is the reference ion. The reference direction is pointing to the right. The figure is adapted with permission from reference [202]. Copyright 2023 American Chemical Society.

the covariance between a pair crushed velocity-mapped images. Unfortunately, we cannot determine the covariance form Abel-inverted images, as the inversion process destroys any information on correlations between individual ions.

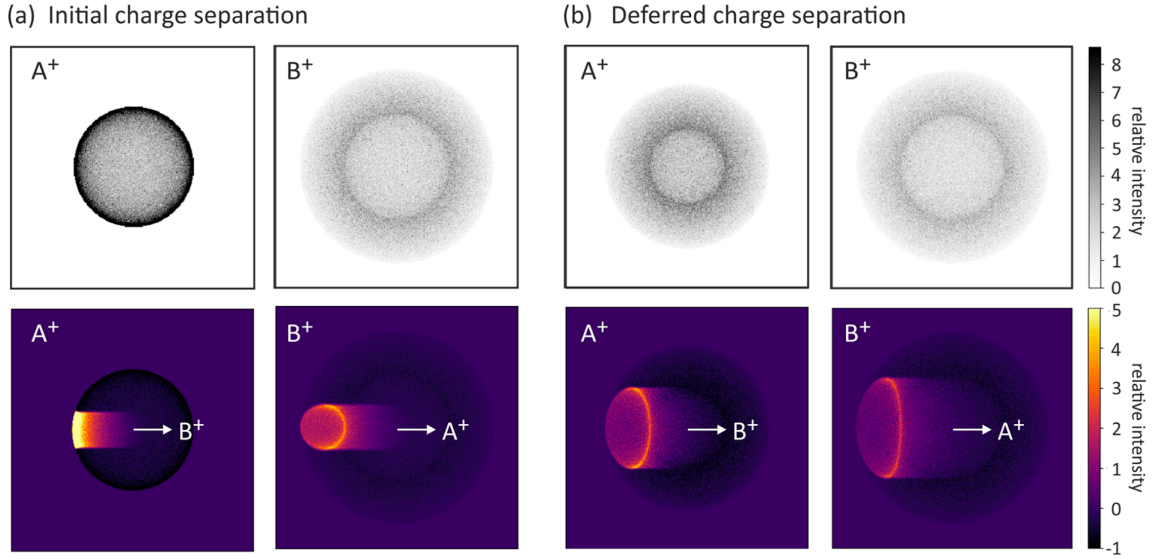

Fig. 3.5: Simulated velocity-map images and covariance images of the reaction $ABC^{2+} \longrightarrow A^+ + B^+ + C$ following via (a) initial charge separation and (b) deferred charge separation. A+ is the signal ion, B+ is the reference ion. The reference direction is pointing to the right. The figure is adapted with permission from reference [202]. Copyright 2023 American Chemical Society.

For higher-body dissociations, the resulting recoil-frame covariance images are more complex, and do not exhibit signals solely opposite the reference direction. Figure 3.5 shows simulated recoil frame covariance images for two ions resulting from the reaction $ABC^{2+} \longrightarrow A^+ + B^+ + C$. These simulations were performed by Dr David Heathcote, and appeared in reference [202]. Case (a) assumes an 'initial

charge separation' mechanism $ABC^{2+} \longrightarrow A^+ + BC^+ \longrightarrow A^+ + B^+ + C$, while case (b) assumes a 'deferred charge separation', $ABC^{2+} \longrightarrow AB^{2+} + C \longrightarrow A^+ + B^+ + C$. The covariance images for the two mechanisms differ significantly, showing that the covariance images exhibit a great amount of information on the dissociation mechanism.[202] This highlights how powerful covariance analysis can be in revealing the fragmentation dynamics of an individual dissociation pathway.

Recoil frame covariance has also been used in conjunction with Coulomb explosion imaging (CEI) to distinguish between different stereoisomers[204,205] and as a tool for structural determination,[206–208] and covariance analysis remains an evolving field of research. Recent developments include investigating the correlation between three[209] or more ions[210] and native-frame covariance[211,212], in which the second dissociation step from a two-step three-body channel is recreated in momentum space. Very recently, our group has developed a method for inverting recoil-frame covariance maps in an analogous way to the inversion of crushed velocity-map images by the inverse Abel transform.[213]

3.4.3 Partial and contingent covariance

Changes in the overall signal level in an experiment can lead to 'false covariances', where two uncorrelated ions display covariance with each other. Reasons for these fluctuations include changes in the laser power on a shot-by-shot basis, or changes in the number of parent molecules in the interaction region. For example, if the molecular beam or laser intensity gradually drifts with time, all of the ion signals will increase or decrease simultaneously, and every signal will become covariant with every other signal. This can lead to artefacts in the TOF-TOF-covariance maps and recoil-frame covariance maps, making it challenging to distinguish true covariance from false covariance. Partial covariance and contingent covariance are

techniques that mitigate the false covariance contribution.[214]

In contingent covariance[215], the experimental cycles are ordered according to their total signal level. Afterwards, the data are split into even 'chunks'. For example 100,000 frames split into 10 chunks would result in a chunk size of 10,000. In each subset, the covariances are calculated and then summed to yield the overall covariances. In each chunk, the changes in the overall signal level are significantly lower. Therefore, the false covariance contribution can be significantly reduced.

Partial covariance is an alternative to contingent covariance, but rather than sorting the signal level in increasing order, this technique subtracts off the false covariances caused by correlations with a third variable I. We obtain[216,217],

$$\mathrm{pCov(X,Y;I)} = \underbrace{\mathrm{Cov(X,Y)}}_{A} - \underbrace{\frac{\mathrm{Cov(X,I)Cov(I,Y)}}{\mathrm{Cov(I,I)}}}_{B}, \tag{3.19}$$

where A is the standard covariance between X and Y, and B is a correction term to remove the false covariance contributions. In our application, we define I as the total signal intensity in each acquisition cycle, which is a good approximation for any variations in the molecular beam or laser intensities.

We have covered a wide range of analysis tools that we can use to extract useful information from our experimental data, which links directly to the questions set out in the Introduction Chapter. With this knowledge, we will now move on to describe a series of studies into the photoinduced dissociation dynamics of THF, DMF, and DMF^+.

4 Ultraviolet photodissociation of tetrahydrofuran

This Chapter describes a photodissociation study of THF at 193 nm. The work has previously been published in reference 116. Here, we reproduce the article in full (DOI: 10.1039/D3CP01974H) with permission from the Royal Society of Chemistry. Some of the data has also appeared previously in Dr. Divya Popat's DPhil thesis[218] and Joseph Stimson's Part II thesis[219].

4.1 Introduction

As noted in Section 1.6 of Chapter 1, THF provides a useful small-molecule model of the ribose backbone unit of DNA. Several authors have reported gas-phase absorption spectra of THF[220–223]. The lowest energy ($S_1 \leftarrow S_0$) absorption band lies between 180 and 200 nm, and has been assigned to a $3s \leftarrow n$ transition involving promotion of one of the oxygen lone-pair electrons. The transition has been shown to form part of an s-type Rydberg series converging to the ground state of the ion at 9.41 eV[222]. Giuliani and co-workers[224] have probed the absorption spectrum in this region at high resolution, revealing separate but overlapping con-

tributions to the band from the two near-degenerate ground-state conformers of THF, which have C_2 and C_S symmetry, respectively (see Figure 4.5 for geometry-optimized structures of the two conformers). While the global energy minimum of ground-state THF is generally considered to correspond to the C_S conformer[225–229], interconversion between the two near-degenerate conformers is almost barrierless via pseudorotation through a C_1 conformation[228,230–232].

When excited at the shorter wavelength of 160 nm, Röder *et al.*[233] assigned a $3d \leftarrow n$ transition followed by a $3d \rightarrow 3p \rightarrow 3s$ Rydberg cascade. The authors reported cuts through excited-state PESs of THF along the C−O, C_α−H, and C_α−C_β stretch coordinates. The S_1 state of THF is bound along both the C_α−H, and C_α−C_β coordinates. However, along the C−O stretching coordinate, the S_1 state is repulsive and changes its electronic character from Rydberg (3s) in the Franck-Condon region to valence ($n\pi^*$) at larger C−O separations, leading eventually to a conical intersection with the S_0 ground state along the ring-opening coordinate. In addition to direct dissociation on S_1, the conical intersection provides a non-adiabatic pathway for populating excited vibrational levels of the electronic ground state, from which fragmentation can also occur. A similar picture of $S_1 \leftarrow S_0$ excitation, C−O bond elongation, and IC to the ground-state followed by fragmentation has also been observed in oxetane[234] and oxirane[235]. Asymmetric ring expansion leading to coupling of excited-state and ground-state surfaces has also been explored in other systems such as furan[236,237], thiophene[238,239], and tetrahydrothiophene[240].

The ring opening described above implies that THF dissociates in a stepwise manner following photoexcitation to the S_1 state. Figure 4.1 summarizes the main observed fragmentation pathways in THF following excitation at 193 nm. Ring opening forms the linear diradical C_4H_8O, which then dissociates along either the C_α−C_β ('Channel 1a') or the C_β−C_γ ('Channel 2') bond coordinate, leading to the

product pairs C_3H_6 + OCH_2 and C_2H_4 + OCH_2CH_2, respectively[241]. It is interesting to note that Kramer[242] observed these same two channels by inducing decomposition of THF on the S_0 surface via infrared multiphoton dissociation. The C_3H_6 product of the first channel has the stable isomers propylene and cyclopropane. However, the diradical C_2H_4O product of the first channel, formed initially as the $O{-}CH_2{-}CH_2$ isomer, rapidly rearranges via a hydrogen-atom transfer to internally excited $(CH_3{-}CHO)\cdot$, which decomposes into HCO and CH_3 on the subnanosecond timescale[243] in the absence of collisions to stabilize the excited intermediate. An intramolecular H atom migration can accompany the $C_\alpha{-}C_\beta$ cleavage ('Channel 1b'), leading to the products $HO{-}CH_2$ + CH_2CHCH_2.

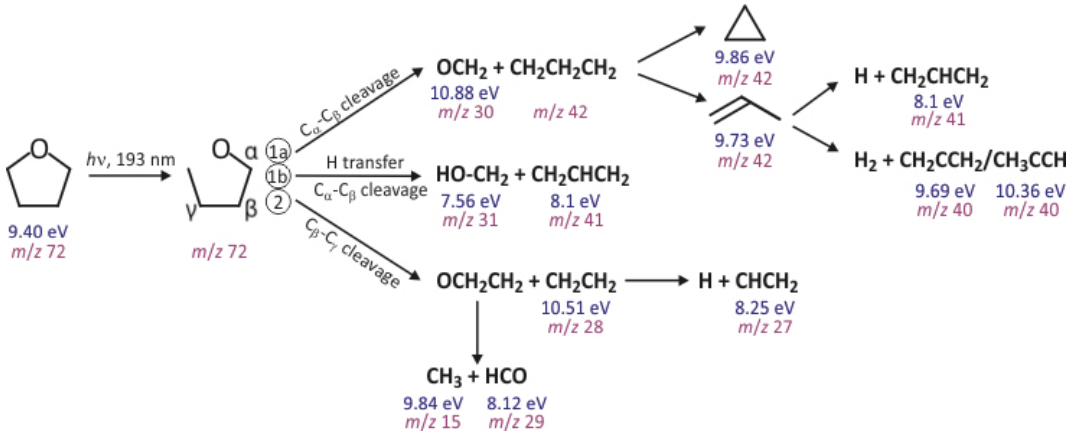

Fig. 4.1: Reaction scheme for THF following 193 nm excitation. Absorption of a 193 nm photon leads to rapid cleavage of one of the C−O bonds to form the ring-opened diradical $OCH_2CH_2CH_2CH_2$. The diradical dissociates over a longer timescale via cleavage of either the $C_\alpha{-}C_\beta$ or $C_\beta{-}C_\gamma$ bond to form C_3H_6 + OCH_2 (Channel 1a) and C_2H_4 + OCH_2CH_2 (Channel 2) products, respectively. An internal H-atom migration can accompany the $C_\alpha{-}C_\beta$ cleavage (Channel 1b). Several of the primary dissociation products undergo isomerization and/or further dissociation, e.g. by loss of H or H_2. Shown beneath each chemical species is the respective ionization energy and mass-to-charge ratio.

Lee[244] investigated the photofragmentation of THF following photoexcitation via the $S_1 \leftarrow S_0$ transition at 193.3 nm, the same wavelength employed in the present study. Based on an analysis of the photofragment TOF distributions, Lee determined branching ratios and TKERs for five different fragmentation channels. The three dissociation channels with significant branching ratios were those described

above, leading to C_2H_4 + HCO + CH_3, C_3H_6 + OCH_2, and C_3H_5 + $HOCH_2$. The photofragment angular distributions were all reported to be nearly isotropic, which is somewhat surprising given that the fragmentations are believed to occur on the sub-picosecond timescale[126,233]. Lee offered two possible explanations for the lack of angular anisotropy: (i) that the non-planar structure of THF causes the fragmentation products to recoil at angles near to the magic angle[245] of 54.7° to the transition dipole; or (ii) that internal rotations within the diradical intermediate result in the dissociation products recoiling over a wide range of angles.

In the following, we present an experimental study into the photodissociation of THF at 193 nm in which we employ multi-mass VMI to characterize the scattering distributions of the photofragments. We also report calculated transition dipole moments for the $S_1 \leftarrow S_0$ transition originating from the two possible ground-state conformers, and consider the relationship between these transition dipole moments, the angular dependence of the observed product scattering distributions, and the lifetime of the intermediate diradical C_4H_8O.

4.2 Methods

4.2.1 Experimental methods

The TOF-VMI mass spectrometer used in this work has been described in detail in Chapter 2 and elsewhere[246]. Briefly, helium (BOC, 99.9 %) at a pressure of 1 bar was bubbled through liquid tetrahydrofuran (Sigma-Aldrich, ≥99.9 %). The resulting gas mixture underwent supersonic expansion through a pulsed Solenoid Valve (Parker Hannifin, Series 9, 10 Hz) before being collimated by a 1.5 mm diameter skimmer and entering the interaction region, where the UV photolysis beam

and vacuum ultraviolet (VUV) probe beam intersected the molecular beam at right angles.

The 193.3 nm (from hereon referred to as 193 nm) UV photolysis beam was generated by a Neweks PSX-100 ArF excimer laser (7 ns, ∼1.5 mJ pulses). A Rochon polarizer was used to polarize the photolysis beam linearly along a polarization axis parallel to the detector plane (perpendicular to the TOF axis). The pulse energy of the photolysis light at the entrance to the vacuum chamber after passing through the polarizer and beam steering optics was measured to be between 0.1 and 0.6 mJ, and the beam was focused down to a diameter of around 5-10 microns at the interaction region. The estimated fluence is therefore in the range $\sim 1 \times 10^5$ to 3×10^6 mJ cm^{-2}.

After a delay of 20 ns, the neutral photofragments were ionized by the 118.2 nm (10.49 eV) VUV probe beam, generated by frequency tripling the third harmonic of a Nd:YAG laser (Continuum Surelite I) in a phase-matched mixture of 298 mbar argon (BOC, 99.9 %) and 27 mbar xenon (BOC, 99.9 %)[171–174]. The probe laser beam was linearly polarized along the TOF axis (perpendicular to the imaging plane) to ensure that all anisotropy observed in the measured photofragment angular distributions results from the photolysis step. However, preliminary experiments performed with the probe laser polarized either parallel or perpendicular to the imaging plane revealed no differences in the recorded images.

The ionized photoproducts were accelerated towards the detector by the electric field maintained within the VMI ion lens, which projects the three-dimensional scattering distribution for each ion mass-to-charge (m/z) ratio into a two-dimensional image on the detector plane[5,6]. The detector, consisting of a pair of MCPs coupled to a P47 phosphor screen, generates an optical signal on the phosphor for each incident ion. A PImMS2 camera[181–183] records an (x, y, t)-data point for each incident

ion. The full multi-mass imaging data set was acquired over 80,000 pump-probe cycles.

In addition to the two-colour pump-probe signals, one-laser signals (pump only and probe only) were recorded. In the raw data sets the signal from a single ion generally extends over several adjacent pixels and time bins, so to improve the spatial and temporal resolution as well as to reduce the size of the data set, the signal from each ion was centroided to a single (x, y, t) point before further analysis. The one-laser signals were then subtracted from the pump-probe signals in order to obtain the true pump-probe signal. The resulting data set can then be integrated over the (x, y) coordinates to yield the product TOF spectrum, and velocity-map images can be generated for each photofragment by integrating over the relevant range of arrival times. The photofragment scattering distributions are cylindrically symmetric about the photolysis laser polarization axis, allowing us to Abel invert the images for each fragment ion using a Python version of the Basex software package[195]. From the inverted images, we extracted radial and angular distributions and converted the radial distributions into kinetic energy distributions using a pixel-to-velocity calibration determined in previous measurements on the 355 nm photolysis of Cl_2.

4.2.2 Computational methods

The geometries of the C_2 and C_S ground-state conformers of THF were optimized in a B3LYP/aug-cc-pVQZ calculation using the Gaussian09 software package[188]. Transition dipole moments for the $3s \leftarrow n$ transition to the S_1 state were calculated for each conformer using EOM-CCSD/aug-cc-pVTZ.

4.3 Results

4.3.1 Time-of flight spectrum

Figure 4.2 shows the mass-calibrated two-colour pump-probe TOF spectrum of THF and its photofragments following excitation at 193 nm and probe laser irradiation at 118 nm. The one-laser contributions have been subtracted from the two-colour signal, which leads to a negative peak in the TOF spectrum for the parent ion. This arises due to the depletion of neutral THF through dissociation by the pump laser, with the result that fewer intact molecules are available to be ionized by the probe laser in the pump-probe experiments than in the probe-only experiments. Note that because the parent ion velocites are essentially those of the neutral molecules in the molecular beam, the parent ions all arrive in a small spot at the centre of the detector (rather than being spread across the detector as in the case of fragment ions with non-zero kinetic energies) and often saturate the signal response of the MCP to some extent. We therefore do not expect to observe a quantitative match between the intensity of this negative peak and the summed intensity of the fragment peaks.

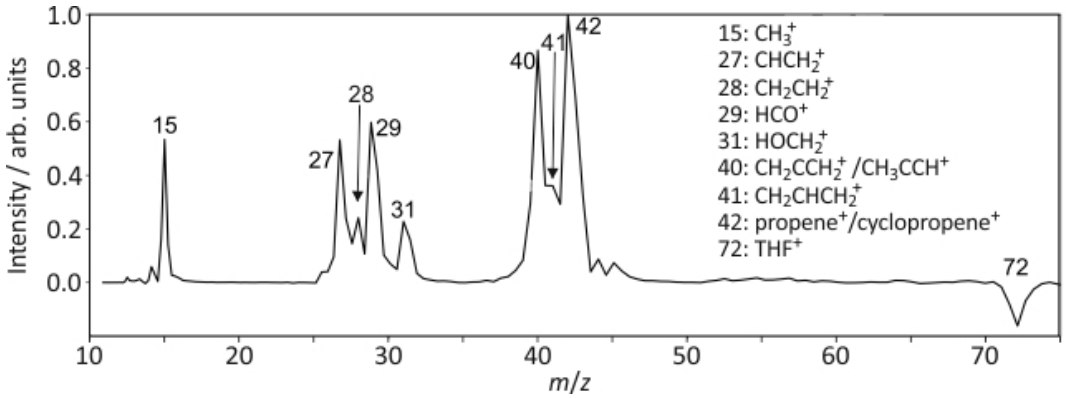

Fig. 4.2: Background-subtracted TOF mass spectrum for the 193 nm photolysis products of THF.

Based on the 10.49 eV photon energy of our probe laser and the ionization energies

given for the various molecular fragments in Figure 4.1, we might expect to observe the following species from each of the three main dissociation channels:

1. Channel 1a: propene (m/z 42), cyclopropane (m/z 42), CH_2CHCH_2 (m/z 41), and CH_2CCH_2/CH_3CCH (m/z 40);

2. Channel 1b: HO$-CH_2$ (m/z 31) and CH_2CHCH_2 (m/z 41);

3. Channel 2: CH_3 (m/z 15), HCO (m/z 29), possibly CH_2CH_2 (m/z 28), and $CHCH_2$ (m/z 27).

Inspecting the TOF spectrum in Figure 4.2, we indeed see peaks at all of the predicted m/z values, indicating that we observe the same three major dissociation channels as reported by previous authors[242,244] and discussed in the Introduction. We do not see evidence in the TOF spectrum for cleavage of both C$-$O bonds as reported by SenGupta and co-workers[247], although we note that the atomic oxygen formed in such a process would not be ionized by our probe laser and would therefore not be detected in our experiment.

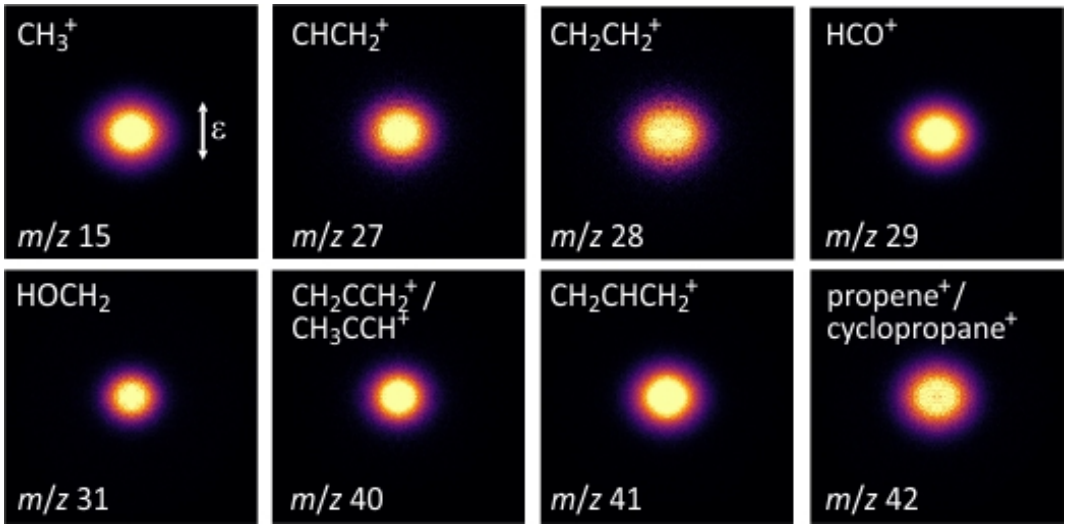

Fig. 4.3: Symmetrized velocity-map images for the observed photodissociation products of THF. The direction of linear polarization of the 193 nm photolysis laser is indicated by the double-headed arrow in the first panel.

4.3.2 Product speed and angular distributions

Our multi-mass VMI detection system enables us to record scattering distributions for all of the reaction products appearing in the TOF spectrum. The measured velocity-map images are shown in Figure 4.3. As explained in Section 4.2, Abel inversion of the images allows the speed and angular distributions to be determined for each fragment.

Inspection of the reaction scheme in Figure 4.1 allows us to determine how the measured scattering distributions can best be used to probe the dynamics of the three dissociation channels. The most straightforward channel from this point of view is Channel 1b, which forms two momentum-matched products, HO−CH_2 and CH_2CHCH_2, neither of which undergo any further fragmentation or rearrangement. The HO−CH_2 product is uniquely assigned to m/z 31, and we can therefore use the corresponding image to determine the speed and angular distributions for the products of this channel. These are shown in Figure 4.4(b).

The CH_2CHCH_2 product, appearing at m/z 41 in the TOF spectrum, is not unique to Channel 1b, since it is also formed as a secondary H-atom loss product in Channel 1a. The m/z 41 signal therefore contains contributions from both of these pathways [*]. However, as noted above, the component arising from Channel 1b is momentum matched with the HO−CH_2 product, allowing the components arising from the two channels to be disentangled: after appropriate correction for the branching ratios and ionization efficiencies using data from Lee[244], the momentum-matched distribution arising from Channel 1b can simply be subtracted from the total signal to leave the component arising from Channel 1a.

[*]We note that within the mass resolution of our experiment, there may also be some contributions to the 'm/z 41' signal from the higher velocity components of the m/z 40 and 42 signals. However, given the analysis we are about to describe, we do not believe that this is likely to introduce any significant error to the TKER and $\beta(v)$ distributions reported for this channel, and does not change any of our conclusions.

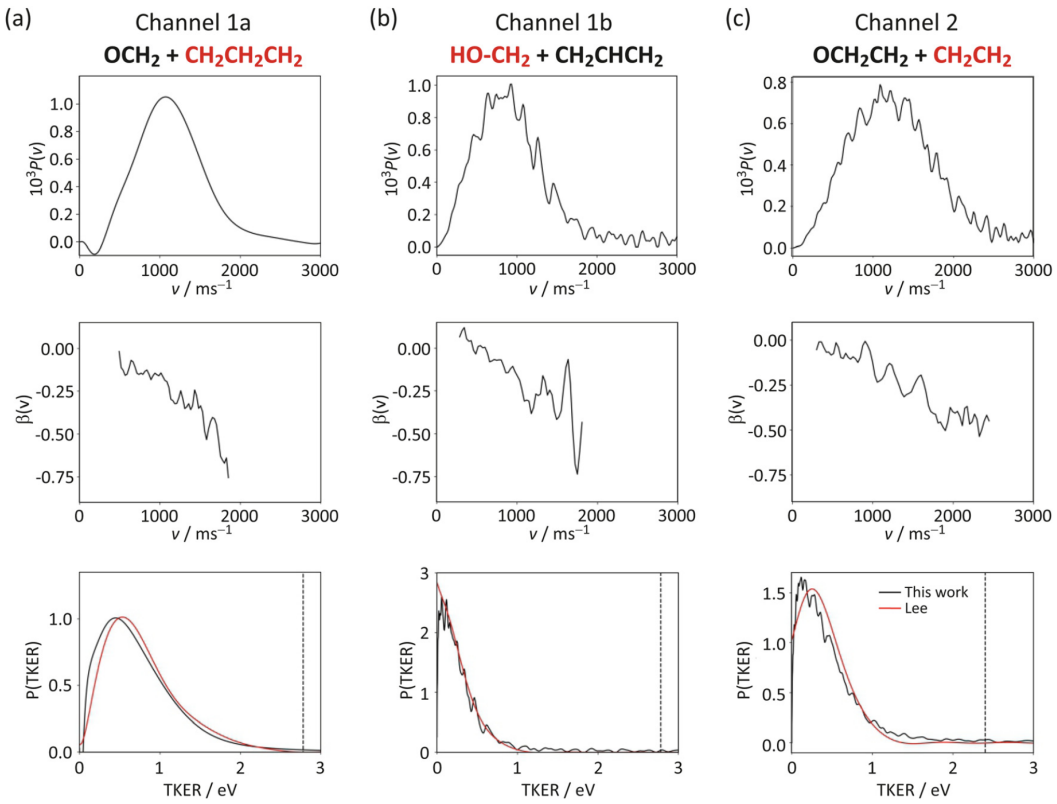

Fig. 4.4: Speed distributions, $P(v)$, and recoil anisotropy distributions, $\beta(v)$, for the dissociation products of (a) Channel 1a, (b) Channel 1b, and (c) Channel 2. Speed and recoil anisotropy distributions are for the primary products indicated in red text, determined as explained in the text. The kinetic energy distributions determined in the present work are compared with the equivalent result from Lee[244], and the maximum accessible kinetic energy is indicated by a dashed line.

Moving now to Channel 1a, the O−CH_2 product is unique to this channel and its scattering distribution would provide all of the required information on the dynamics of this channel. Unfortunately, this scattering distribution is not available to us, since the ionization energy of O−CH_2 lies above the 10.49 eV photon energy of our ionization laser. Instead, we must consider the $CH_2CH_2CH_2$ product. The initially formed linear $CH_2CH_2CH_2$ primary product of C_α−C_β bond cleavage is unstable, rearranging on the femtosecond timescale[248,249] to either propene or cyclopropane[242]. The propene product of this rearrangement can undergo H_2 elimination to form CH_2CCH_2/CH_3CCH or loss of a single H atom to produce CH_2CHCH_2. The scattering distribution of the primary $CH_2CH_2CH_2$ product is unchanged by unimolecular rearrangement to propene or cyclopropane, so we do not

lose any information in the isomerization step. Additionally, the fact that linear momentum must be conserved during H or H_2 loss from propene, coupled with the much lighter mass of H/H_2 relative to the partner fragment, means that any kinetic energy released in the secondary dissociation step will almost all be carried away by the H or H_2 product, leaving the velocity distributions of the partner fragments unchanged to a very good approximation. As a result, summing the velocity distributions recorded for the m/z 40, 41, and 42 products of Channel 1a (noting that for the m/z 41 fragment we use the Channel 1a component described earlier), yields a very good approximation to the velocity distribution of the nascent primary $CH_2CH_2CH_2$ product. The speed and angular distributions determined using this approach are shown in Figure 4.4(a).

Finally, we consider Channel 2. As noted earlier, the OCH_2CH_2 product (m/z 44) of this channel is known from previous work[243] to dissociate rapidly into CH_3 + HCO under the collision-free conditions of our experiment, consistent with the fact that we see virtually no signal at m/z 44. We therefore cannot use this product to learn about the primary dissociation step. Some of the partner fragment, CH_2CH_2, also dissociates further via H atom loss to give H + $CHCH_2$. However, as noted above, the recoil momentum imparted to the $CHCH_2$ product by the departing H atom is very small, and is expected to have an almost negligible effect on its velocity distribution. We can therefore sum the velocity distributions for the CH_2CH_2 and $CHCH_2$ products to give a good approximation to the velocity distribution of the nascent primary CH_2CH_2 product [**] The resulting speed and angular distributions associated with Channel 2 are shown in Figure 4.4(c).

[**]Interestingly, but not surprisingly, comparison of the velocity-map image for the $CHCH_2$ and CH_2CH_2 products reveals more intensity in the centre of the image for the H-loss product. This implies that the slower-moving, more highly internally excited primary products are more likely to undergo H loss than the faster moving, less internally excited products.

4.3.3 Channel 1a: THF $\rightarrow$ OCH_2 + C_3H_6

The velocity distribution for the products of Channel 1a (see Figure 4.4(a)) appear relatively broad, indicating that significant energy is released into translation and that a broad range of internal (rotational and vibrational) states are populated in the products. The recoil anisotropy parameter $\beta(v)$ is close to zero for slow products with the highest degree of internal excitation, and decreases to a value of around -0.75 as the recoil velocity increases.

Previous TOF measurements carried out by Lee[244] as a function of photolysis laser polarization suggested that the average β parameter is close to zero, so our results do not agree with the conclusions drawn from these earlier measurements. The $\beta(v)$ distributions measured in the present experiments lead to only a small asymmetry in the images. However, we have checked carefully that this anisotropy is real and is not caused by any artefacts of the experiment or the data processing. For example, we have made measurements on the same instrument of scattering distributions which by symmetry must be isotropic, and confirmed that they give rise to β values of zero across the full range of product velocities, as well as checking that we obtain β parameters in line with literature reports for processes such as the 355 nm photolysis of Cl_2. Having carried out these checks, and given that we are using VMI detection and can therefore clearly resolve β as a function of product recoil velocity, we believe our values are accurate, and that the discrepancy arises from the different velocity resolution achievable in our VMI measurements and Lee's TOF measurements. If we project our images along the x and y axes, equivalent to Lee's measurements with the photolysis laser linearly polarized parallel and perpendicular to the TOF axis, there is a small but clear difference in the widths of the resulting distributions. The velocity-dependent anisotropy we measure is therefore easily resolved within the spatial resolution of our velocity-map

images, but would be very difficult to resolve with the typical temporal resolution achievable in a TOF measurement. This is consistent with the fact that while our $\beta(v)$ distribution does not agree with that reported by Lee, our translational kinetic energy distribution for the products of Channel 1a is in excellent agreement.

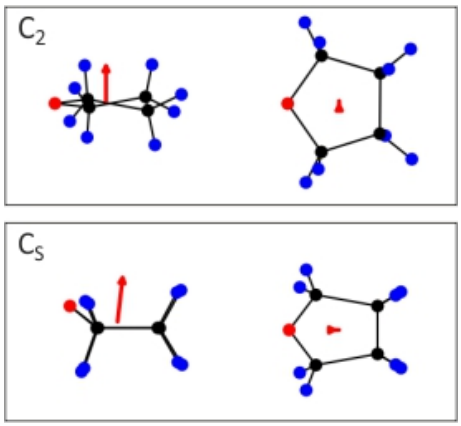

Fig. 4.5: Optimized structures and $S_1 \leftarrow S_0$ transition dipoles (red arrows) for the C_2 (top) and C_S (bottom) conformers of THF. For visualization purposes the transition dipole moments have been elongated by factors of five and four for the C_2 and C_S conformers, respectively.

Figure 4.5 shows geometry-optimised structures for the C_2 and C_S conformers of ground-state THF, which we expect to be present at similar number densities within our molecular beam, together with the transition dipole moments (red arrows) associated with the $S_1 \leftarrow S_0$ transition in each conformer. For both conformers the transition dipole moment lies perpendicular to the plane of the ring. In the axial recoil limit, both the ring-opening step and the subsequent C−C bond cleavage occur in the molecular plane. We therefore expect the products to recoil in this same plane, perpendicular to the transition dipole moment, giving rise to a β parameter close to its limiting value of -1.

While the highest velocity products do have β parameters close to -1, we observe a strong dependence of β on the product recoil velocity. The slowest products have near-zero values, which decrease monotonically to a near-limiting value at the highest velocities. We ascribe this behaviour to the finite lifetime of the C_4H_8O diradical formed in the initial ring-opening step and to the distribution of internal energies

with which the diradical is formed, noting from the discussion in Section 4.1 that dissociation can occur either directly on S_1 or following internal conversion to S_0. Following photoexcitation, the repulsive character of the S_1 surface leads to rapid C−O bond cleavage to form the diradical. When the ring-opened diradical dissociates on a timescale that is short relative to intramolecular vibrational relaxation and rotation, most of the available energy will be released into product translation. In this case the product recoil velocity is high and β approaches its limiting value determined by the perpendicular orientation of the transition dipole moment relative to the molecular plane, as described above. As the lifetime of the diradical increases, perhaps following IC to S_0, the molecule has more time to undergo rotation and for energy to be redistributed into internal modes. This leads to a decrease both in the photofragment velocities and in the correlation between the transition dipole moment and the ejection direction of the photoproducts, explaining the reduction in β for slower fragments. The TKER distribution is consistent with this picture. The distribution peaks at low kinetic energies, indicating that a significant portion of the excess energy is partitioned into internal degrees of freedom in the photofragments. Taken together with the behaviour of $\beta(v)$ described above, this is consistent wtih dissociation of the diradical over a relatively broad range of timescales.

4.3.4 Channel 1b: THF → $HOCH_2$ + CH_2CHCH_2

Formation of $HOCH_2$ + C_3H_5 products requires H-atom transfer to the oxygen atom, in addition to C−O and C−C bond cleavage. According to Lee[244], this subchannel generally exhibits lower TKERs when compared with the pathway forming C_3H_6 + H_2CO. This is entirely consistent with our own observations; the kinetic energy release distribution obtained from our velocity-map images is in excellent

agreement with that reported by Lee, and peaks at significantly lower energies than that measured for Channel 1a. A plausible explanation for this behaviour is that internal H atom migration requires the C_4H_8O species to distort its geometry such that hydrogen and oxygen atoms are near each other, which becomes more likely at long C_4H_8O lifetimes following redistribution of energy into internal modes. The $\beta(v)$ distribution shows almost identical behaviour to that measured for Channel 1a, with slow products exhibiting isotropic scattering and the fastest products having β values of around -0.75.

4.3.5 Channel 2: THF$\rightarrow$ OCH_2CH_2 + CH_2CH_2

The photofragment speed distribution for the products of Channel 2 is very similar to that observed earlier for the products of Channels 1a and 1b, comprising a broadly-peaked distribution extending out to maximum speeds of around 3000 m s^{-1}. As for the other channels, we can infer that the products are formed in a range of rotational and vibrational states. We also see similar behaviour for the velocity-dependence of the recoil anisotropy parameter β, which has values close to zero at low velocities (high internal excitation), but decreases monotonically to a value of around -0.5 at the highest velocities. We believe the explanation for this behaviour to be analogous to that for Channels 1a and 1b. Following the initial ring-opening step, dissociation of the diradical intermediates with the shortest lifetimes retains the highest degree of correlation between the transition dipole moment, which lies perpendicular to the plane of the ring, and the photofragment velocities, which lie in the plane of the ring. Dissociation on longer timescales degrades the correlation through rotational and vibrational motions prior to C$-$C bond cleavage, leading to a reduction in β for the slower products. The limiting value of β observed for Channel 2 of around -0.5 is significantly lower than the

value of around -0.75 determined for Channels 1a and 1b. This perhaps implies a longer lifetime for C_4H_8O intermediates dissociating via Channel 2, which would be consistent with the higher barrier to dissociation for this channel reported by Scala *et al.*[126], and also with the lower branching ratio for Channel 2 relative to Channels 1a and 1b determined by Lee[244]. The velocity-averaged value for β of -0.23 is again in disagreement with the near-zero value determined by Lee[244].

The TKER distribution for the primary dissociation products of Channel 2 is again in excellent agreement with that reported by Lee[244]. The distribution peaks at around 0.15 eV and tails off by around 1 eV, intermediate between the behaviour for Channel 1a and Channel 1b, and well below the available energy of 2.30 eV. This is consistent with the lifetime arguments evoked above to explain the behaviour of β in the two channels. The longer lifetimes associated with dissociation via Channel 2 result in a greater degree of energy redistribution into internal modes, and therefore a smaller fraction of energy released into translation.

4.4 Conclusions

We have presented the results of a VMI study into the 193 nm photodissociation of tetrahydrofuran. Excitation of THF at this wavelength leads to population of the S_1 state via an $3s \leftarrow n$ transition involving a lone-pair electron on the oxygen atom. The associated transition dipole lies perpendicular to the plane of the ring for both the C_2 and C_S conformers of THF. The S_1 state is repulsive along the C−O bond stretching coordinate, resulting in rapid bond scission to form a ring-opened diradical intermediate species. The diradical undergoes further dissociation over a broad range of timescales via cleavage of either the C_α−C_β bond to form OCH_2 + C_3H_6 or $HOCH_2$ + C_2H_5 products (denoted Channel 1a and Channel 1b, respectively)

or cleavage of the $C_\beta - C_\gamma$ bond to form OCH_2CH_2 + C_2H_4 (Channel 2). The C_3H_6 products of Channel 1a isomerise rapidly to cyclopropane and propene, the latter of which undergoes secondary decay via loss of H or H2. The OCH_2CH_2 products of Channel 2 are also unstable on the timescale of our experiment, and dissociate to form CH_3 and CHO, while some of the CH_2CH_2 products decay via H loss to give $CHCH_2$.

The translational kinetic energy releases measured in the present work for all three channels are in excellent agreement with previous measurements by Lee[244]. However, Lee reported near-zero angular anisotropy for both channels, whereas we observe a recoil anisotropy parameter β that has near-zero values for products formed with low velocities, but decreases to around -0.75 for Channels 1a and 1b and -0.5 for Channel 2, respectively, for products formed with the highest recoil velocities. We attribute this behaviour to the extent of internal excitation of the C_4H_8O diradical intermediate and the range of lifetimes over which it survives prior to cleavage of a C−C bond. Diradicals which dissociate on a rapid timescale have the highest translational energies and retain the strongest correlation between the transition diople moment for the $S_1 \leftarrow S_0$ excitation and the recoil velocities of the photofragments. Since the transition dipole lies perpendicular to the plane of the ring and the recoil velocities of the photofragments lie preferentially in the plane of the ring, this results in negative β parameters which approach the limiting value of -1. In contrast, diradicals with longer lifetimes undergo both rotation and redistribution of energy into internal degrees of freedom prior to dissociation, both of which reduce both the magnitude of the photofragment velocities and their correlation with the transition dipole moment. The highest values of β observed for Channel 2 are significantly lower than those observed for Channels 1a and 1b, which is consistent with the higher barrier to dissociation via Channel 2 leading to dissociation on a slower timescale than via Channels 1a and 1b.

Our work on the UV photolysis of THF implies that the backbone of DNA may be susceptible to UV-induced ring opening and fragmentation. However, as a building block of DNA, the photostability and photodissociation dynamics might differ, as DNA has probably 'evolved' to be resistant to UV damage. Similarly, the DNA bases and base pair have a well known photoprotection mechanism involving ultrafast IC to the non-reactive electronic ground-state.[250–253]

Another class of molecules highly prevalent in biological system are proteins, which consist of various side chains bound to a backbone of peptide linkages. The next Chapter presents a UV photodissociation study of DMF, a tertiary amide that can be seen as a model compound for the peptide bond.

Statement of Authorship for joint/multi-authored papers for PGR thesis

To appear at the end of each thesis chapter submitted as an article/paper

The statement shall describe the candidate's and co-authors' independent research contributions in the thesis publications. For each publication there should exist a complete statement that is to be filled out and signed by the candidate and supervisor **(only required where there isn't already a statement of contribution within the paper itself).**

Title of Paper	Photodissociation dynamics of tetrahydrofuran at 193 nm
Publication Status	✗Published □ Accepted for Publication □Submitted for Publication □Unpublished and unsubmitted work written in a manuscript style
Publication Details	D. Milesevic, J. Stimson, D. Popat, P. Robertson, C. Vallance, "Photodissociation dynamics of tetrahydrofuran at 193 nm", *Phys. Chem. Chem. Phys.*, **2023**, *25*, 25322-25330.

Student Confirmation

Student Name:	Dennis Milesevic		
Contribution to the Paper	Generated data, performed data analysis, interpreted data, wrote initial manuscript.		
Signature	D. Milešević	Date	22 November 2023

Supervisor Confirmation

By signing the Statement of Authorship, you are certifying that the candidate made a substantial contribution to the publication, and that the description described above is accurate.

Supervisor name and title:	Prof. Claire Vallance		
Supervisor comments	I confirm that Dennis has done the bulk of the work on this project, as described above.		
Signature	C. Vallance	Date	24 November 2023

This completed form should be included in the thesis, at the end of the relevant chapter.

5 Ultraviolet photodissociation of *N,N*-dimethylformamide

This Chapter includes a photodissociation study of DMF at 225 nm and 245 nm. The work has previously been published in reference 128. Here, we reproduce the article in full (DOI: 10.1039/D2CP02662G) with permission from the Royal Society of Chemistry. This data has also previously been used in Dr. Divya Popat's DPhil thesis[218].

5.1 Introduction

As noted in Section 1.6 of Chapter 1, DMF is a useful model compound for the peptide backbone of proteins. Experimental and theoretical studies of DMF have focused primarily on dynamics following excitation at wavelengths below 200 nm. Summarizing first the theoretical studies, a number of authors have reported PESs for the ground and electronically excited states. Based on experimental gas-phase spectra of DMF[254,255], Serrano-Andrés and Fülscher[256] used the complete active space with second order perturbation (CASPT2) theory to determine vertical excitation energies from the ground state. Liu *et al.*[136] discussed the photolysis mech-

anism of DMF following excitation at 193 nm based on Complete Active Space Self-Consistent Field (CASSCF) calculations of the relevant PESs. Eckert-Maksić and Antol[137] also performed CASSCF calculations in the context of understanding DMF photolysis, and were able to characterize several significant points such as energy minima, saddle points, and conical intersections and to determine how the geometry of DMF changes to reach those points. Lipciuc *et al.*[135] determined transition dipole moments for excitations to the first three valence singlet states via CASSCF calculations, and generated cuts through the PESs along N−CO and N−CH_3 bonds based on CASPT2 calculations. The arguably most comprehensive theoretical study on DMF has been conducted by Shastri *et al.*[139]. These authors correlated the electronic absorption spectrum over the wavelength range 125 nm − 221 nm with results from density functional theory (DFT) calculations, providing an in-depth discussion of relevant molecular orbitals, vibrational frequencies, and electronically excited singlet and triplet states. They reported PECs for the first five excited states of DMF, including valence and Rydberg states, as a function of bond length. These PECs guide the interpretation of the results reported in this paper, and are summarized in Figure 5.1. Note that we include in this Figure the $2^1A''$ Rydberg state, which was not found in the valence-state calculations carried out by Lipciuc *et al*[135]. This now becomes the S_2 state in place of the higher-lying $2^1A'$ state that was identified as such by Lipciuc *et al*. Note that the first two excited singlet states exhibit energy barriers along the N−CO bond, impeding prompt dissociation along that coordinate.

There are comparatively fewer experimental studies on DMF. Forde *et al.*[129,130] performed photodissociation studies at 193 nm and recorded recoil translational energy distributions and angular distributions for the dissociation products. The studies indicated two main dissociation channels: cleavage of the N−CO amide bond to form HCO and $N(CH_3)_2$; and fission of one of the two N−CH_3 bonds,

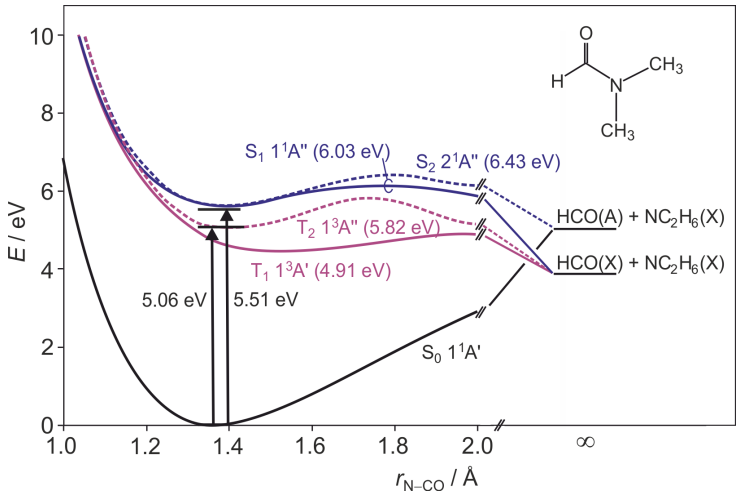

Fig. 5.1: Schematic cuts through the ground state and first two excited singlet and triplet state PESs of DMF along the N−CO stretch coordinate using time-dependent DFT and basis sets augmented with diffuse functions like aug-cc-pVTZ, adapted from reference[139]. Barrier heights for each surface are given in parentheses after the state labels, and the dissociation limit for each surface is indicated.

forming $HCONCH_3$ and CH_3. Cleavage of the N−CO bond was found to lead to formation of ground state HCO($\tilde{X}$) with either ground state $N(CH_3)_2(\tilde{X})$ or electronically excited $N(CH_3)_2(\tilde{A})$. The products were measured to have a recoil anisotropy of $\beta = 1.2 \pm 0.2$, implying a rapid bond dissociation to a state for which the transition dipole from the ground state lies predominantly parallel to the breaking bond.

Lipciuc *et al.*[135] investigated the 193 nm photolysis of DMF using VMI. They observed the same N−CO and N−CH_3 bond breaking channels as Forde *et al.*, and measured complete scattering distributions for each observed photoproduct. For products associated with the N−CO bond breaking channels the β-parameter was found to show a strong dependence on the fragment velocity, with faster products exhibiting larger values of β. This was attributed to excitation of out-of-plane vibrations on the same timescale as dissociation. Excitation is primarily to the $3^1A'$ state, via a transition with a transition dipole almost parallel to the N−CO bond. Dissociation occurs either on this state or following population transfer to the $1^1A''$ or $2^1A'$ states. All three excited states have non-planar minima. For molecules

dissociating rapidly from near-planar geometries with little out-of-plane nuclear motion, most of the available energy is released into product translation, leading to near-limiting values of β in good agreement with the axial recoil approximation. Conversely, molecules in which out-of-plane motions are excited will experience forces during dissociation that lead to rotational and vibrational excitation of the products, reducing their translational energy, and also to deviations from axial recoil, reducing β.

Previous experimental studies on the photoexcitation of DMF have neglected possible excitation to Rydberg states. However, DMF and related molecules exhibit sharp excitation bands corresponding to transitions to these states[257–260]. The relevance of Rydberg and Rydberg/Valence surfaces for amides has been discussed in detail elsewhere[261–263]. The experimental studies described above have focused either on multi-photon absorption[133] or on photolysis at wavelengths below 200 nm[129,130,135], perhaps because experiments at wavelengths longer than 200 nm are more challenging due to the lower UV absorption cross-section of the molecule[254,255]. In the present study, we report data from a multi-mass VMI study into the photofragmentation dynamics of DMF at excitation wavelengths of 225 nm and 245 nm. This work is complementary to our previous study of the dynamics at 193 nm[135].

5.2 Methods

The experimental set-up has already been discussed in Chapter 2 and is similar to that described by Hopkins *et al.*[246] Briefly, helium (BOC, 99.9 %) at a pressure of 1 bar was bubbled through liquid DMF (Sigma-Aldrich, 99.8 %) to generate a ≈0.5 % mixture of DMF in helium. The gas mixture underwent a supersonic ex-

pansion through a pulsed solenoid valve (Parker Hannifin, Series 9, 10 Hz), which was collimated by a 1.5 mm skimmer before passing through the repeller plate of the ion optics assembly into the interaction region of a TOF-VMI mass spectrometer. Here the molecular beam was intersected at right angles by the UV photolysis laser beam and VUV probe beam.

The 225 nm or 245 nm photolysis beam used to initiate photolysis was generated using a tuneable, pulsed, frequency-doubled dye laser (Sirah Cobra Stretch), pumped by the third harmonic of a Nd:YAG laser (Continuum Surelite II). The beam was linearly polarized in the imaging plane (perpendicular to the TOF axis). Following a short time delay of 15−18 ns, the neutral photofragments were ionized by the 118 nm VUV probe laser beam. The 118 nm radiation was produced by frequency tripling the third harmonic of a Nd:YAG laser (Continuum Surelite I) in a phase-matched mixture[171] of 27 mbar xenon (BOC, 99.9 %) and 298 mbar argon (BOC, 99.9 %).[172–174] The probe beam was linearly polarized along the TOF axis (perpendicular to the imaging plane) to ensure that any anisotropy observed in the velocity-map images is caused by the photolysis laser polarization.

The VMI ion lens used to map the ionized photofragments onto the detector consists of repeller, extractor, and ground electrodes. The repeller plate has a 4 mm diameter hole in the centre through which the molecular beam is admitted to the interaction region. The extractor and ground electrodes have 24 mm holes in the centre to transmit the expanding product scattering distributions. The ratio of potentials applied to the extractor and repeller plates is tuned to achieve velocity-mapping conditions[5,6], mapping the three-dimensional scattering distribution of the nascent photofragments via a 56 cm flight tube onto a two-dimensional position sensitive ion detector. The ion detector comprises a pair of chevron-mounted MCPs coupled to a P47 phosphor screen. Each incoming ion generates an optical signal on

the phosphor, which is captured by a second-generation PImMS camera.[181–183] The photofragment scattering distributions are read out from the camera in the form of an (x, y, t) data point for each detected ion. The data sets can be integrated over the (x, y) coordinates to obtain product TOF spectra, or over the relevant arrival time ranges to generate velocity-map images for each photofragment.

Data sets were acquired under pump–probe conditions, and also, for the purposes of background subtraction, under pump-only and probe-only conditions. This allowed any one-laser signals to be subtracted from the overall signal in order to obtain the true pump–probe signal. Each ion signal generally excites multiple pixels and time bins within the PImMS sensor, which is corrected by running the data set through a centroiding algorithm. The velocity-map images are two-dimensional projections of the full three-dimensional scattering distribution for each photoproduct. The scattering distributions are cylindrically symmetrical about the polarization vector of the photolysis laser, such that an inverse Abel transform can be used to obtain the central slice through each distribution, which contains all of the information required in order to extract product speed and angular distributions. The Abel inversion was performed using the Basex software package[195]. From the inverted images we extracted radial and angular distributions, converting the radial distributions into kinetic energy distributions using a calibration determined in previous measurements on the 355 nm photolysis of Cl_2.

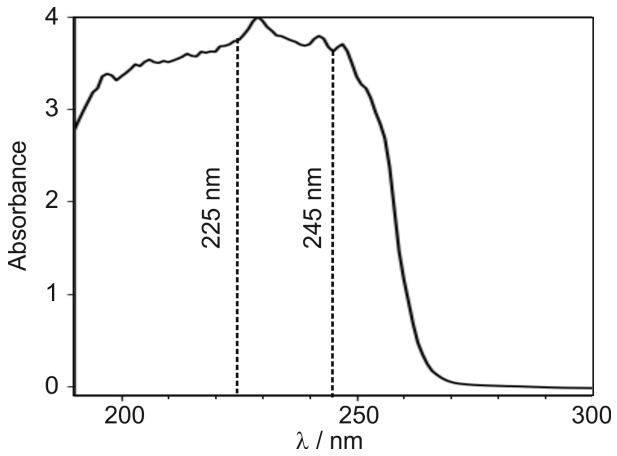

Fig. 5.2: UV absorption spectrum of liquid DMF, recorded on a Thermo Fisher Scientific Evolution 220 spectrometer. Dashed vertical lines indicate the photolysis wavelengths of 225 nm and 245 nm chosen for the VMI experiments.

5.3 Results and discussion

5.3.1 Ultraviolet absorption spectrum of *N*,*N*-dimethylformamide

Several authors have reported UV/VIS spectra of DMF.[139,254,255] However, these studies mainly reported results at shorter wavelengths, where the excitation cross-section is larger. A liquid-phase UV absorption spectrum of the DMF used in the present study, recorded over the wavelength range 190–350 nm on a Thermo Fisher Scientific Evolution 220 spectrometer, is shown in Figure 5.2.

The absorption spectrum exhibits a peak between 220–230 nm with a wide shoulder on the red-edge extending to wavelengths of about 245 nm. We decided to investigate pump wavelengths of 225 nm, which is in the centre of the absorption peak, and 245 nm, marking the end of the shoulder, at which significant absorption is observed, while minimizing potential contribution from the 225 nm feature.

5.3.2 Photolysis of *N,N*-dimethylformamide at 225 nm

Fragmentation pathways

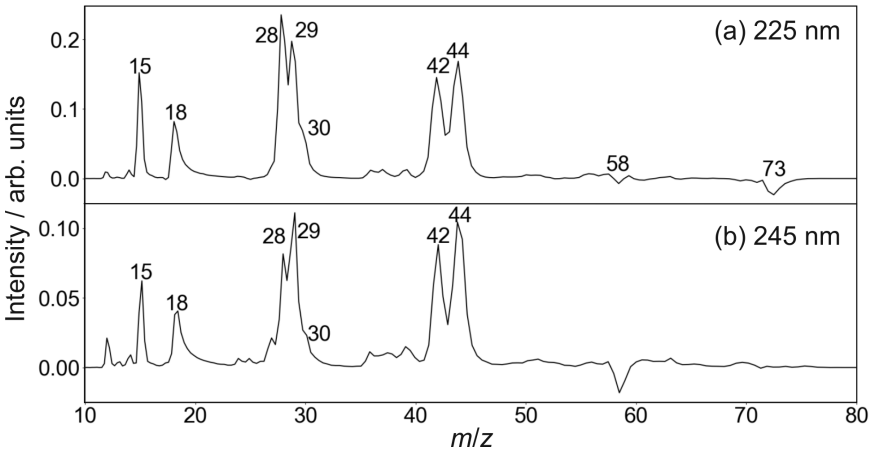

Fig. 5.3: TOF mass spectra of the photofragments formed following photoexcitation of DMF at 225 nm (upper panel) and 245 nm (lower panel).

The TOF mass spectrum for the products of 225 nm photolysis of DMF is shown in the upper panel of Figure 5.3, and reveals the important fragmentation pathways for DMF at 225 nm. The one-laser contributions have been subtracted from the pump–probe signal. While the TOF resolution of our instrument is not sufficient to completely separate all mass-adjacent fragments, we see clear peaks at mass-to-charge (m/z) ratios of 15, 18, 28, 29, 30, 42, and 44, which can be assigned to the ionized photoproducts CH_3^+ , NH_4^+ , CO^+, HCO^+, $C_2H_6^+$ or $HCOH^+$ or $HNCH_3^+$, $NC_2H_4^+$, and $NC_2H_6^+$, respectively. The same products were observed in our previous study of DMF photolysis at 193 nm.[135] The small negative peaks at $m/z = 58$ and 73 correspond to $HCONCH_3^+$ and the parent ion, respectively. These ions are formed efficiently through one-laser dissociative ionization of neutral DMF by the 118 nm probe laser, and are reduced in intensity in the pump–probe signal due to depletion of neutral DMF via photolysis. The result is a negative signal intensity for these peaks when the probe-only signal is subtracted from the pump–probe signal.

Cleavage of the N–CO amide bond generates HCO and NC_2H_6 products, and we therefore expect to see signal arising from this pathway at $m/z = 44$ and 29. We do indeed see signal at these two m/z values. However, dissociative ionization of the nascent fragments in the probe step, as well as neutral predissociation of some of the nascent HCO products[135,264], has the result that we see signal associated with the NC_2H_6 products at $m/z = 44$ ($NC_2H_6^+$), 43 ($NC_2H_5^+$), 42 ($NC_2H_4^+$) and 18 (NH_4^+), and signal associated with the HCO fragment at $m/z = 29$ (HCO) and 28 (CO^+). We note that formation of NH_4^+ has been confirmed in isotope labelling experiments, and involves significant structural rearrangement of nascent internally excited $N(CH_3)_2^+$ ions.[135] Since there is little kinetic energy release during this secondary reaction, the NH_4^+ products essentially inherit the speed and angular distribution of the $N(CH_3)_2^+$ ions from which they are formed, and the images resemble the central region of the images of these parent primary ions. The arrival time distribution for the NH_4^+ fragment has a significant tail extending to longer flight times, implying that the rearrangement and dissociation occur on a relatively long timescale, with the final products forming both within the interaction region of the experiment and along the flight tube between the interaction region and the detector.

Fission of either N–CH_3 bond in the parent DMF molecule generates the fragments CH_3 and $HCONCH_3$. Only the former is ionizable using one 118 nm photon,[135] appearing at $m/z = 15$ in the mass spectrum. Low intensity signals, presumably associated with H-atom loss either from neutral or ionized CH_3, can be observed at $m/z = 12, 13$, and 14.

Based on its mass-to-charge ratio, the small signal at $m/z = 30$, observed as a shoulder on the much larger signals at $m/z = 28$ and 29, may correspond either to $C_2H_6^+$, $HCOH^+$, or $HNCH_3^+$. While formation of $C_2H_6^+$ would require significant

molecular rearrangement, the latter two ions can be formed via quite plausible mechanisms. Whatever its identity, this minor fragment is not considered further in the following.

Product speed and angular distributions

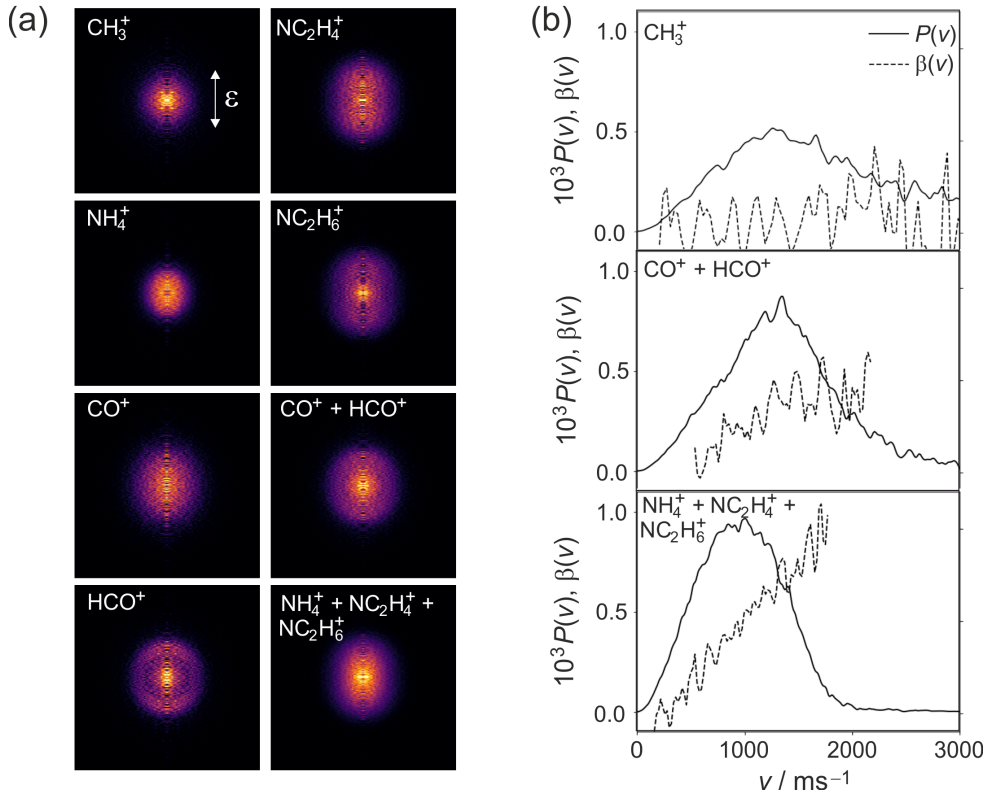

Fig. 5.4: (a) Symmetrized and Abel-inverted velocity-map images for fragments observed following 225 nm photolysis of DMF; (b) speed and angular distributions for each product channel as explained in the text.

Tab. 5.1: Recoil anisotropy parameters β averaged over the speed distributions for the photolysis products formed from DMF following irradiation at 225 and 245 nm, respectively. The quoted uncertainties are one standard deviation of the noise on the $\beta(v)$ distributions, determined from the residual of $\beta(v)$ and a polynomial fit through the distribution.

Species	m/z	$\beta_{225\text{nm}}$	$\beta_{245\text{nm}}$
CH_3^+	15	0.07 ± 0.17	-0.05 ± 0.33
$NH_4^+ + NC_2H_x$	18/42/42/44	0.52 ± 0.07	0.30 ± 0.09
$CO^+ + HCO^+$	28/29	0.20 ± 0.09	0.17 ± 0.13

Figure 5.4(a) shows the symmetrized and Abel-inverted velocity-map images recorded

for the ionized DMF photolysis products CH_3^+, NH_4^+, CO^+, HCO^+, $NC_2H_4^+$, and $NC_2H_6^+$. As noted above, several of these fragments arise from dissociative ionization and/or predissociation of the nascent HCO and NC_2H_6 products (the velocity-map images imply, for example, that the more highly internally excited/lower-velocity HCO^+ ions experience H loss to form CO^+). As a result of momentum conservation, loss of one or two H atoms from the neutral or ionized products has only a very small effect on the velocity distributions. We have also shown previously[135] that formation of NH_4^+ from $NC_2H_6^+$ is associated with only very small kinetic energy release. As a result, we can sum the velocity and angular distributions for the $m/z = 18$, 42, 43, and 44 products and for the $m/z = 28$ and 29 products in order to obtain very good approximations to the distributions for the nascent products. The resulting speed and angular distributions – expressed in terms of the recoil anisotropy parameter β – for the CH_3, HCO, and NC_2H_6 photofragments are shown in Figure 5.4(b). The values of β for each fragment, averaged over the velocity distribution, are shown in Table 5.1.

We note that the velocity distributions are all fairly broad, implying population of a wide range of rotational and vibrational states in the recoiling fragments. The β parameter for the CH_3 fragments is close to zero, while the HCO and NC_2H_6 fragments exhibit non-zero β parameters that increase markedly with fragment velocity. These features of the speed and angular distributions will be discussed in more detail below.

Table 5.2 shows calculated vertical excitation energies to the three lowest lying electronic singlet states and two lowest lying triplet states of DMF, together with oscillator strengths for the associated transitions. Frequency calculations show the zero-point energies for the various states to be very similar, so we have not included these explicitly when considering the excitation energies. Two sets of val-

Tab. 5.2: Theoretical and experimental vertical excitation energies from the electronic ground state to the first three excited singlet states and the first two excited triplet states of neutral DMF.

Symmetry		Excitation energies / eV		Oscillator strength	
		DFT [a]	CASPT2 [b]	DFT [a]	CASPT2 [b]
$1^1A'$	(ground state)				
$1^1A''$	$(n \rightarrow \pi^*)$	5.59 (222 nm)	5.64 (220 nm)	< 0.001	0.001
$2^1A''$	$(4a'' \rightarrow 3s)$	5.62 (221 nm)	5.92 (209 nm)	0.021	0.005
$2^1A'$	$(16a' \rightarrow \pi^*)$	5.99 (207 nm)	6.48 (191 nm)	0.009	0.002
$1^3A'$	$(n \rightarrow \pi^*)$	4.73 (262 nm)	5.41 (229 nm)	-	-
$1^3A''$	$(\pi \rightarrow \pi^*)$	5.08 (244 nm)	5.06 (245 nm)	-	-

[a] B3LYP/aug-cc-pVTZ in Shastri *et al.*[139]
[b] central in Serrano-Andres *et al.*[256]

ues are given: the results of DFT calculations by Shastri *et al.*[139], and the results of CASPT2 calculations by Serrano-Andres *et al.*[256] The recent DFT calculations by Shastri *et al.* indicate that the $1^1A''$ and $2^1A''$ states are likely to be energetically accessible at 225 nm, with the CASPT2 calculations of Serrano-Andres *et al.* predicting that the states lie slightly higher in energy. The $(n \rightarrow \pi^*)$ transition to the first excited $1^1A''$ singlet state has a near-zero oscillator strength, making it unlikely to be populated directly by absorption of a 225 nm photon. In contrast, the $(4a'' \rightarrow 3s)$ transition to the second excited $2^1A''$ singlet state has a much higher oscillator strength, implying that this state is most likely to be populated in the absorption step.

The measured β parameters provide further insight into the excited states involved in the photodissociation. The transition dipole for the $\pi \leftarrow n(\sigma)$ excitation to the first excited $1^1A''$ singlet state lies perpendicular to the breaking N−CO bond. This would give rise to a negative value for β, which approaches a value of -1 for a pure perpendicular transition. In contrast, excitation to the second excited $2^1A''$ singlet state involves movement of electron density from the $n(\pi)$-orbital located at the nitrogen atom to the Rydberg 3s-orbitals on the CH_3 groups,[139], resulting

in a parallel transition and a correspondingly positive value of β between 0 and 2. As noted above, the measured values of β for both the HCO and NC_2H_6 products are positive. This is consistent with excitation to the second excited $2^1A''$ singlet state, in agreement with the predictions made above on the basis of the calculated oscillator strengths for the two transitions.

Having established that excitation at 225 nm is most probably to the $2^1A''$ singlet state, we now explore the subsequent processes leading to cleavage of the N−CO and N−CH_3 bonds and production of the observed photofragments.

N–CO bond cleavage

To understand the partitioning of the available energy amongst the various accessible translational and internal degrees of freedom, it is helpful to replot the HCO and NC_2H_6 velocity distributions in terms of the TKER. The total available energy is calculated from the 5.510 eV energy of a 225 nm photon and the N−CO bond dissociation energy of 3.89 eV[130]. For products formed in their electronic ground states, the available energy is 1.62 eV. When the HCO fragment is formed in its first electronically excited state the available energy becomes 0.47 eV[264]. The TKER distribution for the HCO + NC_2H_6 products is shown in Figure 5.5(a), with the energetic limits corresponding to formation of HCO in its ground and first-excited electronic states marked as dashed lines.

The TKER distribution peaks at low energies, implying that the majority of photofragments are formed with significant amounts of internal energy. The lower energy part of the distribution, below 0.47 eV, is consistent with formation of HCO in either its electronic ground or first excited state, with the excited state not accessible for products with TKER above this value. While product internal excitation is

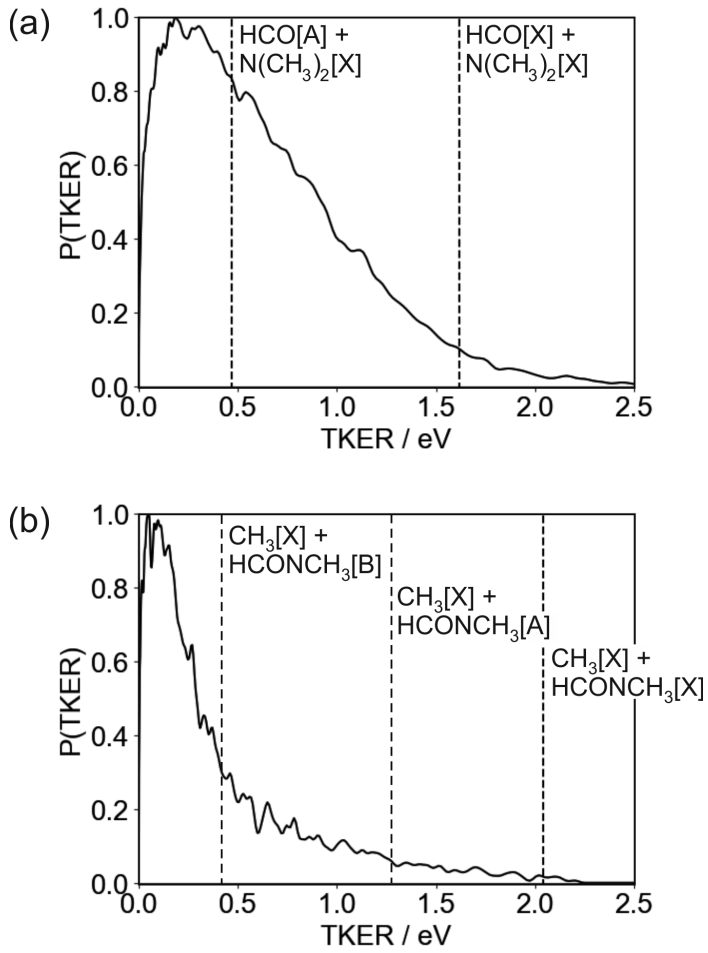

Fig. 5.5: TKER distribution for the (a) N−CO and (b) N−CH_3 bond fission channels following 225 nm photolysis of DMF. The total available energies for the possible product channels are indicated by dashed vertical lines.

clearly a key feature of the fragmentation dynamics, the long tail extending out to the maximum available energy indicates that for a significant proportion of products the majority of the available energy is released into relative translation of the recoiling fragments. A small proportion of fragments are formed with energies higher than the supposed maximum. A small amount of 'extra' energy can often be explained by the presence of a small fraction of vibrationally excited DMF in the molecular beam. However, in this case we believe the high energy tail extends too far above the nominal maximum available energy for this to be the explanation. Trajectory studies by Eckert-Maksic and coworkers[137] indicate that following excitation to low-lying excited singlet states, a significant fraction of trajectories become

trapped in minima on these states. We therefore postulate that in our experiment a small number of these 'trapped' excited-state molecules survive long enough to undergo dissociative ionization by the probe laser, and that this is the source of the high energy tail on the TKER distribution for the N−CO bond cleavage channel. While 'probe-only' dissociative ionization is removed from our signal during the background-subtraction process, this second dissociative ionization signal requires both pump and probe lasers, so is not removed when the one-laser signals are subtracted.

The high amount of internal excitation in the majority of products is explained by the topography of the excited state potential energy surface(s) over which the system evolves during dissociation. The $2^1A''$ surface to which DMF is initially excited correlates to $NC_2H_6(\tilde{X})$ + $HCO(\tilde{A})$ products, and exhibits a significant energy barrier of around 0.81 eV (see Figure 5.1) along the N−CO bond stretching coordinate[139], with the energy maximum corresponding to a bond length of ∼1.8 Å. In contrast to the planar structure of ground-state DMF, the energy minimum of the $2^1A''$ surface is non-planar. The dissociating molecules are therefore likely to follow a variety of trajectories across the PES. Some of these trajectories will surmount the barrier with little out-of-plane motion, in which case there will be few torsional forces acting and correspondingly little internal excitation of the products, with the majority of the energy being released into product translation. For these products the lack of out-of-plane motion also maintains the spatial relationship between the polarization vector of the excitation light and the axis of the dissociating bond (i.e. the axial recoil approximation holds), yielding relatively large positive values for the recoil anisotropy parameter β. Other trajectories will explore out-of-plane geometries that 'skirt around' the barrier. The torsional forces acting during dissociation in these cases lead to rotational and/or vibrational excitation of the photofragments, and therefore a correspondingly smaller amount of energy

released into translation. The out-of-plane motion also leads to breakdown of the axial recoil approximation and a corresponding reduction in β. The correlation between product internal excitation and breakdown of the axial recoil approximation explains the observed increase in β with increasing photofragment velocity. Similar behaviour has been seen previously in the dissociation of DMF on the higher-lying $3^1A'$ singlet surface following photoexcitation at 193 nm[135].

As noted above, the TKER distribution for the HCO + NC_2H_6 products is not consistent with dissociation only on the $2^1A''$ surface, since many of the HCO products must be formed in their electronic ground state in order to account for the products formed with TKER greater than 0.47 eV. Coupling between the $2^1A''$ and $1^1A''$ surfaces can lead to transfer of population to the lower excited singlet surface, which correlates to ground state products. The topographies of the two singlet surfaces are qualitatively similar, with a barrier along the N−CO stretching coordinate and a non-planar minimum-energy geometry, so we see a similar increase in β with increasing product velocity and decreasing product internal excitation. Population transfer from the $1^1A''$ first excited singlet state to the $1^1A'$ ground state is also possible via a conical intersection at highly non-planar geometries, as is ISC to the $1^3A'$ first excited triplet state[136]. In common with the second excited singlet state, the former of these pathways correlates to formation of ground state NC_2H_6 and electronically excited HCO, while the T_1 state correlates to ground state products.

N−CH_3 bond cleavage

Cleavage of one of the N−CH_3 bonds leads to the formation of CH_3 and $HCONCH_3$ products, of which only the former can be ionized by our 118 nm probe laser. We therefore see a significant signal in the TOF spectrum (see Figure 5.3) at $m/z = 15$, corresponding to the CH_3 fragment, but no signal at $m/z = 58$ corresponding to

the $HCONCH_3$ co-fragment. In contrast to the velocity-map images observed for the N−CO bond cleavage channel, the velocity-map image for the CH_3 fragment reveals a relatively isotropic angular distribution. As explained previously by Lipciuc *et al.*[135], the isotropic scattering distribution is simply a result of the molecular geometry. Excitation via a transition to the $2^1A''$ state, which has a transition dipole moment parallel to the N−CO bond, yields an ensemble of excited-state molecules with a $\cos^2\theta$ distribution of the N−CO axis about the polarization vector of the photolysis laser. In the case of the 193 nm photolysis studied by Lipciuc *et al.*, the excitation was via a parallel transition to the $3^1A'$ state rather than the $2^1A''$ state, but the same arguments apply. Ejection of CH_3 at an angle of approximately 60 degrees to the N−CO axis, as determined by the molecular geometry, combined with this $\cos^2\theta$ distribution of molecular orientations, yields an almost isotropic distribution of CH_3 velocity vectors relative to the photolysis polarization axis, as observed.

The TKER distribution for the N−CH_3 bond cleavage products is sharply peaked at low kinetic energy, indicating that the majority of the available energy is released into internal excitation. Following excitation to the $2^1A''$ state there are various possible pathways by which the molecule can evolve to the separated CH_3 + $NCOCH_3$ products. At 193 nm, the dissociation is thought to proceed via excitation to the $3^1A'$ state and subsequent coupling to and dissociation on the $2^1A'$ state. Couplings involving the $2^1A''$ state which is initially excited at 225 nm have not been comprehensively studied, but it is clear that several potential dissociation pathways are possible, involving either direct dissociation over a small barrier on the $2^1A''$ state to form electronically excited products, or coupling to a lower-lying state. Three product channels are energetically accessible at an excitation wavelength of 225 nm, corresponding to ground-state CH_3 partnered by $HCONCH_3$ in its electronic ground, first, or second excited state, respectively. None of these are ruled

out by the form of the TKER distribution, though the sharp peak at low kinetic energies below the energy cutoff for production of $CH_3[\tilde{X}]$ + $HCONCH_3[\tilde{B}]$ does perhaps suggest a significant contribution from this product channel. If this is the case then it is certainly not the only product channel, as the TKER distribution extends out to the energy thresholds of both of the lower energy channels. Given the geometry of the DMF molecule (see inset to Figure 5.1), it is also very likely that a considerable amount of the internal excitation is in rotational and vibrational modes of the products. Assuming the $N-CH_3$ bond cleavage is reasonably rapid, which it must be to compete with the N−CO bond dissociation pathway, the force exerted away from the centre of mass of the $HCONCH_3$ fragment is likely to result in considerable rotational excitation of this fragment. Significant excitation of the umbrella vibrational mode in CH_3 as well as other vibrational modes in both fragments is also highly likely.

5.3.3 Photolysis of *N*,*N*-dimethylformamide at 245 nm

Fragmentation pathways

The lower panel of Figure 5.3 shows the background-subtracted TOF spectrum for the ionized products of DMF photolysis at 245 nm. As for the 225 nm data, the one-laser signals have been subtracted from the pump-probe signal. Qualitatively, we observe the same products arising from N−CO and $N-CH_3$ bond cleavage as we saw following 225 nm photolysis, including the various products of dissociative ionization of the nascent neutral products. One notable observation is that on moving from 225 nm to 245 nm photolysis, the relative intensities of the $m/z = 28$ (CO^+) and 29 (HCO^+) peaks are reversed. This perhaps implies that HCO is formed with lower internal energy at the longer photolysis wavelength, leading to a smaller

degree of predissociation and/or dissociation following ionization by the 118 nm probe laser.

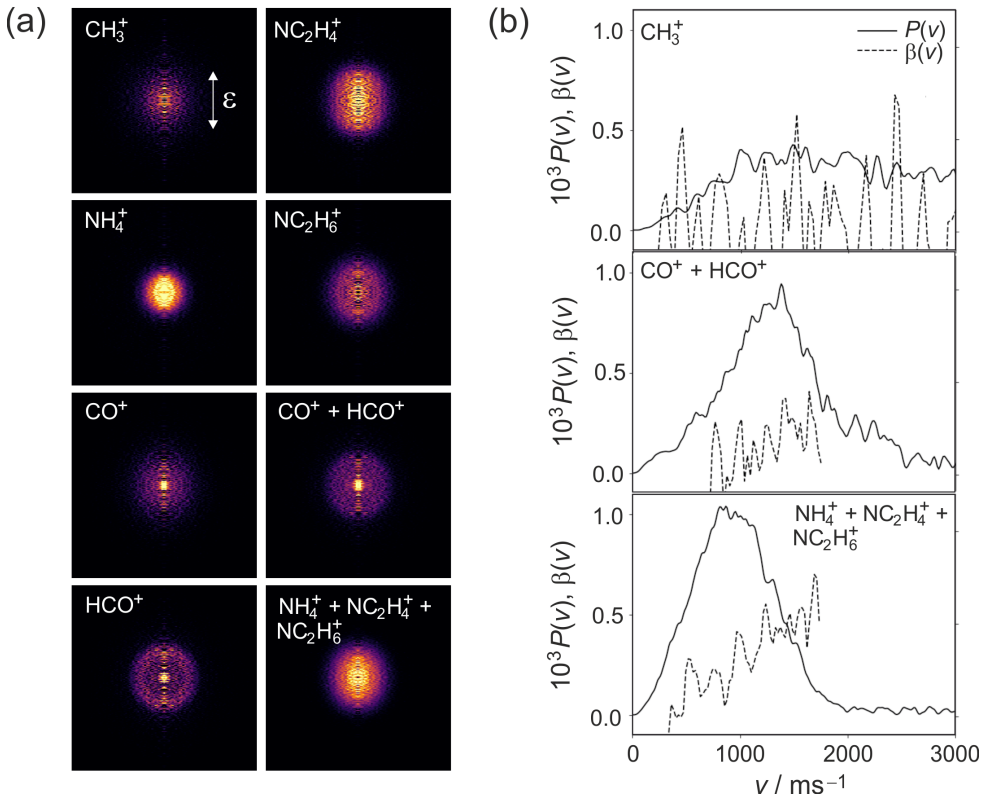

Fig. 5.6: (a) Symmetrized and Abel-inverted velocity-map images for fragments observed following 245 nm photolysis of DMF; (b) Speed and angular distributions for each product channel as explained in the text.

Figure 5.6(a) shows the symmetrized and Abel-inverted velocity-map images recorded for the ionized DMF photolysis products CH_3^+, NH_4^+, CO^+, HCO^+, $NC_2H_4^+$, and $NC_2H_6^+$. As before, we have summed the velocity and angular distributions for the $m/z = 18, 42, 43$, and 44 products and for the $m/z = 28$ and 29 products in order to obtain good approximations to the distributions for the nascent products, shown in Figure 5.6(b). The values of β averaged over the velocity distribution for each fragment are shown in Table 5.1.

N−CO bond cleavage channel

Qualitatively, the velocity-map images recorded at 245 nm for the N−CO bond cleavage products are similar to those observed at 225 nm, though the scattering distributions are somewhat less anisotropic at the longer wavelength, as reflected in the lower values of β. We see the same increase in β with photofragment velocity as previously, but the limiting values at high photofragment velocities are significantly reduced.

Referring to the excitation energies in Table 5.2 we see that for ground-state molecules at their equilibrium geometry all of the singlet states lie significantly higher in energy than the 5.06 eV energy of a 245 nm photon. However, the strong similarities between the scattering distributions observed at 225 and 245 nm, coupled with the very similar absorption intensities at the two wavelengths, lead us to believe that excitation is to the S_2 state in both cases. The apparent energy shortfall is explained by the fact that the 2.749 eV zero-point energy of ground-state DMF (calculated at UB3LYP/6-311++g(d,p) level) enables the molecule to explore a significant range of geometries away from the equilibrium geometry. Distortion of the geometry towards the equilibrium geometry of the S_2 state, which involves significant out of plane motion of the molecular backbone, reduces the excitation energy to the S_2 state considerably[137]. Based on the smaller β parameters observed at the longer wavelength, the geometrical distortion results in a rotation of the $S_0 \rightarrow S_2$ transition dipole away from the C−N bond axis. As noted above, though the maximum β parameters are roughly halved at 245 nm compared with photolysis at 225 nm, we see a similar increase in β with photofragment velocity. As before, we believe this arises as a result of dissociation from a range of molecular geometries. Dissociation from more planar geometries yields higher photofragment velocities and larger values of β, and dissociation from significantly non-planar geometries re-

sults in a higher degree of internal excitation and therefore lower photofragment velocities and β parameters.

It is also possible that excitation to the S_1 state plays a small role at molecular geometries away from the equilibrum structure. This state also becomes energetically accessible at such geometries, and the $S_0 \rightarrow S_1$ transition dipole lies perpendicular to the amide bond even at the equilibrium molecular geometry, which would result in a reduction in the observed value of β. However, the oscillator strength for the transition to S_1 is at least an order of magnitude lower than that for excitation to the S_2 state, so any involvement of this state is unlikely to account for the observed two-fold reduction in β. Shastri *et al.*[139] suggested based on the calculated vertical excitation energies that the two low-lying triplet states may also make a contribution to the absorption band under study. The excitations to the T_1 and T_2 states are respectively perpendicular and parallel in character relative to the amide bond, but on the basis of oscillator strength arguments any such contributions are likely to be minor. As noted previously for dissociation at 245 nm, involvement of the S_1, T_1, and S_0 states in the exit channel, accessed via IC or ISC, is certainly likely and has been proposed previously[136].

The TKER distribution for the HCO + NC_2H_6 products is shown in Figure 5.7(a). The calculated maximum kinetic energy is shown as a vertical dashed line on the plot. The TKER distribution measured at 245 nm is very similar to that observed following photolysis at 225 nm, peaking at low kinetic energies but with a long tail extending out beyond the nominal maximum available energy. As for the 225 nm data, we believe the high-energy tail to be caused by dissociative ionization of a small number of molecules that become trapped within minima on the low-lying singlet surfaces. As already noted, dissociation occurs from a range of molecular geometries, with dissociation from planar geometries yielding little internal exci-

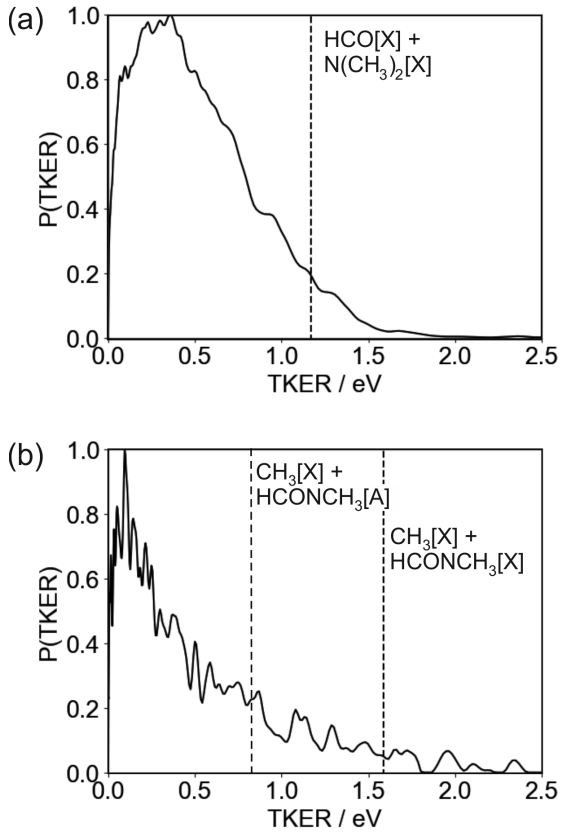

Fig. 5.7: TKER distribution for the (a) N−CO and (b) N−CH_3 bond fission channels following 245 nm photolysis of DMF. The total available energies for the possible product channels are indicated by dashed vertical lines.

tation and relatively fast products, and dissociation from non-planar geometries leading to a higher degree of photofragment internal excitation and correspondingly lower photofragment velocities.

N−CH_3 bond cleavage channel

As was the case at 225 nm, the CH_3 velocity-map image recorded at a photolysis wavelength of 245 nm (see Figure 5.6(a)) reveals an isotropic angular distribution and relatively slow products. The TKER distribution for this channel is shown in Figure 5.6(b). At the longer wavelength only two product channels are energetically accessible, corresponding to ground-state CH_3 partnered by $HCONCH_3$ in either

its ground or first-excited electronic state. Based on the TKER distribution we are unable to rule out either of these pathways. The signal-to-noise ratio for the CH_3 products is fairly low following 245 nm photolysis, and this somewhat limits what we can say about this pathway. However, while different states are almost certainly involved in the dissociation, we believe the general picture and the explanations for the isotropic angular distribution and low-peaking kinetic energy distribution are similar to those outlined previously for dissociation at 225 nm.

5.4 Conclusions

We have reported the results of a comprehensive experimental study on the photofragmentation dynamics of *N*,*N*-dimethylformamide following excitation at 225 nm and 245 nm, respectively. To our knowledge, this is the first study into the dissociation dynamics of DMF in this wavelength region. At both excitation wavelengths, we observe products corresponding to cleavage of both the N−CO amide bond and one of the N−CH_3 bonds, as well as products arising from secondary fragmentation or dissociative ionization of the primary products.

The velocity-map images allow us to determine speed and angular distributions for each fragment, as well as TKERs associated with each fragmentation channel. We have interpreted these data in light of complementary theoretical studies by Shastri *et al.*[139] and Serrano-Andres *et al.*[256], and by comparison with results from a previous study performed in our own group into the photolysis of DMF at 193 nm[135], in order to determine the electronic states involved in the photofragmentation at each wavelength. We conclude that excitation at both 225 nm and 245 nm is predominantly to the S_2 $2^1A''$ state via a parallel transition, with dissociation along the N−CO bond occurring either on this state or on a lower singlet surface fol-

lowing IC. At the shorter wavelength, the S_2 state is energetically accessible via a vertical transition from the equilibrium geometry of the molecule, while geometrical distortion of the molecular structure is required in order to access this state at the longer wavelength. Dissociation occurs either on the S_2 surface or following population transfer to S_1. Both singlet surfaces, as well as the low lying T_1 and T_2 triplet surfaces, share similar topographical features, exhibiting a barrier along the N−CO stretching coordinate, and possessing non-planar minimum-energy geometries. As a result, dissociation occurs from a variety of molecular geometries. Dissociation from planar geometries leads to little product internal excitation and correspondingly high photofragment velocities, with near-limiting values of the recoil-anisotropy parameter β. In contrast, dissociation from non-planar geometries leads to significant product internal excitation, with correspondingly lower photofragment velocities and breakdown of the axial recoil approximation to give reduced values of β.

Less detailed information is available on the potential energy curves along the N−CH_3 bond coordinate than for the N−CO coordinate. However, at both wavelengths we see an isotropic angular distribution for the CH_3 product, and a TKER distribution peaking at low kinetic energies, indicating significant internal excitation in the fragments. This is similar to the behaviour observed previously at 193 nm[135], and can be rationalised in terms of the geometry of the molecule and the orientation of the breaking bond relative to the transition dipole for the initial excitation.

Having now established the photochemical pathways involved in the cleavage of the model peptide bond in DMF at a number of different pholysis wavelengths, future work is likely to focus on investigating the effects of the various different amino acid side chains in the photofragmentation of a series of simple di- and

tri-peptides.

A further point worth considering is that proteins in solution can carry one or more positive charges, which impart important properties in terms of structure, solubility, and functionality. Both, the charge number and the charge distribution are likely to alter the dissociation dynamics of peptide bonds significantly. The following Chapter presents a gas-phase photodissociation study of the DMF cation at three different UV wavelengths.

Statement of Authorship for joint/multi-authored papers for PGR thesis

To appear at the end of each thesis chapter submitted as an article/paper

The statement shall describe the candidate's and co-authors' independent research contributions in the thesis publications. For each publication there should exist a complete statement that is to be filled out and signed by the candidate and supervisor **(only required where there isn't already a statement of contribution within the paper itself).**

Title of Paper	Photodissociation of *N,N*-dimethylformamide at 225 nm and 245 nm
Publication Status	☒ Published □ Accepted for Publication □ Submitted for Publication □ Unpublished and unsubmitted work written in a manuscript style
Publication Details	D. Milesevic, D. Popat, P. Robertson, C. Vallance, "Photodissociation of *N,N*-dimethylformamide at 225 nm and 245 nm", *Phys. Chem. Chem. Phys.*, **2022**, *24*, 28343-28352.

Student Confirmation

Student Name:	Dennis Milesevic		
Contribution to the Paper	Generated data, performed data analysis, interpreted data, wrote initial manuscript.		
Signature	D. Milešević	Date	16 August 2023

Supervisor Confirmation

By signing the Statement of Authorship, you are certifying that the candidate made a substantial contribution to the publication, and that the description described above is accurate.

Supervisor name and title:	Prof. Claire Vallance		
Supervisor comments	Dennis's description of his contributions to this paper are accurate.		
Signature	C. Vallance	Date	23 August 2023

This completed form should be included in the thesis, at the end of the relevant chapter.

6 Ultraviolet photodissociation of the *N,N*-dimethylformamide cation

6.1 Introduction

For many years scientists have used mass-spectrometric methods to understand the fragmentation patterns of peptide cations in the gas phase.[265–267] These breakdown patterns are typically described using the mobile proton model[268–271], in which fragmentations are charge-directed, with the charge being close to the breaking bond. For example, if the charge of a peptide is tightly located in an amino acid side chain rather than on the peptide backbone, breaking the peptide chain requires additional energy to move the charge from the side chain to the backbone in addition to the bond dissociation energy. The fragmentation pathways of peptides depend on where the charge is situated within the molecule.[272,273]

As discussed in the previous Chapter, DMF can be considered a model compound for investigating the peptide bond fragmentation dynamics.[128–139] We have already presented a comprehensive study into the UV photodissociation of neutral DMF. The photodissociation dynamics of the DMF cation will be inherently different from those of neutral DMF since the electronic wavefunction changes upon ioniza-

tion, leading to a new set of PESs with different energy spacing and topology.

In an electron ionization study on isotopically labelled DMF, Li *et al.*[274] provided an unambiguous product ion assignment and reported appearance energies for the various observed product ions. The authors also proposed fragmentation pathways leading to the formation of each fragment ion. One channel involves cleavage of the N−CO amide bond. However, in contrast to the dissociation of neutral DMF, this bond cleavage can also occur simultaneously with an intramolecular hydrogen shift from the carbonyl side of the molecule to the nitrogen atom, as initially proposed by Loudon and Webb[275]. Li *et al.* also suggested that a similar hydrogen transfer occurs during the cleavage of an N−CH_3 bond. Fragmentation of the DMF ion can also lead to the formation of NCH_4^+, a fragment ion not observed in the dissociation of neutral DMF with a significant abundance. This pathway requires cleavage of one N−CH_3 bond and the N−CO bond and hydrogen transfer to the nitrogen atom. Thus, intramolecular hydrogen transfer appears to be a characteristic pattern for DMF cation dissociations.

The photo-induced fragmentation dynamics of the DMF cation have not been studied previously, and can provide insight into the amide bond stability and fragmentation dynamics on a fundamental level. In this Chapter, we aim to achieve this in a multi-mass VMI study into the photofragmentation dynamics of the DMF cation formed by ionization of neutral DMF at 118 nm. Photolysis wavelengths of 225 nm, 245 nm, and 280 nm have been investigated.

6.2 Methods

6.2.1 Experimental set-up

A general description of the spectrometer is given in Chapter 2. Here, we only describe the details specific to the data in this Chapter. We bubbled helium (BOC, 99.9 %, 1 bar) through DMF (Sigma-Aldrich, 99.8 %) to generate a ≈0.5 % mixture of DMF in helium. The gas mixture underwent a supersonic expansion through a pulsed solenoid valve (Parker Hannifin, Series 9, 10 Hz), and the resulting beam was collimated by a 1.5 mm skimmer before passing through the repeller plate of the ion optics assembly into the interaction region of a TOF-VMI mass spectrometer. Here the molecular beam was intersected at right angles by the VUV ionizing laser beam and the UV photolysis laser beam.

The VUV laser beam used to ionize the sample molecules was generated by frequency tripling the third harmonic of a Nd:YAG laser (Continuum Surelite I) in a phase-matched mixture[171] of 27 mbar xenon (BOC, 99.9 %) and 298 mbar argon (BOC, 99.9 %).[172–174] In addition to the beamline shown in Figure 2.7, we added a Glan-Taylor polarizer at a 90° angle relative to the laser beam and a HWP at an angle of 45°. As a result, the light was vertically polarized in the imaging plane (perpendicular to the TOF axis).

Following a short time delay of approximately 15 ns, the molecular beam was intersected by the UV photolysis laser beam at wavelengths of 225 nm, 245 nm, and 280 nm generated using a tuneable, pulsed, frequency-doubled dye laser (Sirah Cobra Stretch), pumped by the third harmonic of a Nd:YAG laser (Continuum Surelite II). The beam was linearly polarized in the imaging plane (perpendicular to the TOF axis).

The VMI ion lens maps the ionized photofragments onto the detector. It consists of repeller, extractor, and ground electrodes. The repeller plate has a 4 mm diameter hole in the centre, which admits the molecular beam to the interaction region. The extractor and ground electrodes have 24 mm holes in the centre to transmit the expanding product scattering distributions. The ratio of potentials applied to the extractor and repeller plates is tuned to achieve velocity-mapping conditions[5,6], mapping the three-dimensional scattering distribution of the nascent photofragments via a 56 cm flight tube onto a two-dimensional position-sensitive ion detector. The ion detector comprises a pair of chevron-mounted MCPs coupled to a P47 phosphor screen. Each incoming ion generates an optical signal on the phosphor, which is captured by a second-generation PImMS camera.[181–183] The camera records an (x, y, t) data point for each detected ion. The data set can be integrated over the (x, y) coordinates to obtain the product TOF spectrum or over the relevant arrival time ranges to generate velocity-map images for each photofragment.

Data sets were acquired using both lasers and under UV-only and VUV-only conditions for background subtraction purposes, allowing any one-laser signals to be subtracted from the overall signals in order to obtain the two-colour signals. Each ion signal generally excites multiple pixels and time bins within the PImMS sensor, which is corrected by running the data set through a centroiding algorithm. The velocity-map images are two-dimensional projections of the full three-dimensional scattering distribution. The scattering distributions are cylindrically symmetrical about the polarization vector of the lasers (vertical in the imaging plane), such that an inverse Abel transform can be used to obtain the central slice through each distribution, which contains all of the information required to extract the product speed and angular distributions. The Abel inversion was performed using the Basex software package.[195] From the inverted images, we extracted the radial and angular distributions and converted the radial distributions into kinetic energy dis-

tributions using a calibration determined in previous measurements on the 355 nm photolysis of Cl_2.

6.2.2 Theoretical calculations

The ground state geometries of neutral DMF and the DMF cation were optimized at UMP2/aug-cc-pVTZ level using the Gaussian09[188] software package. Vertical excitation energies to the first ten ionic states were calculated at the two equilibrium geometries at UB3LYP/aug-cc-pVTZ level of theory using Gaussian09. Starting from the optimized geometry of neutral DMF, rigid PECs along the N−CO and both N−CH_3 stretch coordinates were calculated. The PECs were generated using the CASSCF(11,12) method with the ANO-R2(6-311G** sized) basis-set in the software program Molcas[276] and reveal the product pair formed upon cleavage of the selected bond. Furthermore, the energy of each product channel was calculated by optimizing the geometry of each fragment at UMP2/aug-cc-pVTZ level using the Gaussian09[188] software package. All calculations were conducted in C_1 symmetry.

6.3 Theoretical results

Figure 6.1 shows the equilibrium geometries of the ground state DMF monocation (a) and neutral (b). Neutral DMF is planar due to the partial double bond character of the N−CO bond associated with conjugation of the nitrogen lone pair into the amide bond. The initial photon energy of 10.49 eV (118 nm) removes an electron from either of the two highest molecular orbitals. The Highest Occupied Molecular Orbital (HOMO) corresponds predominantly to the nitrogen lone pair.

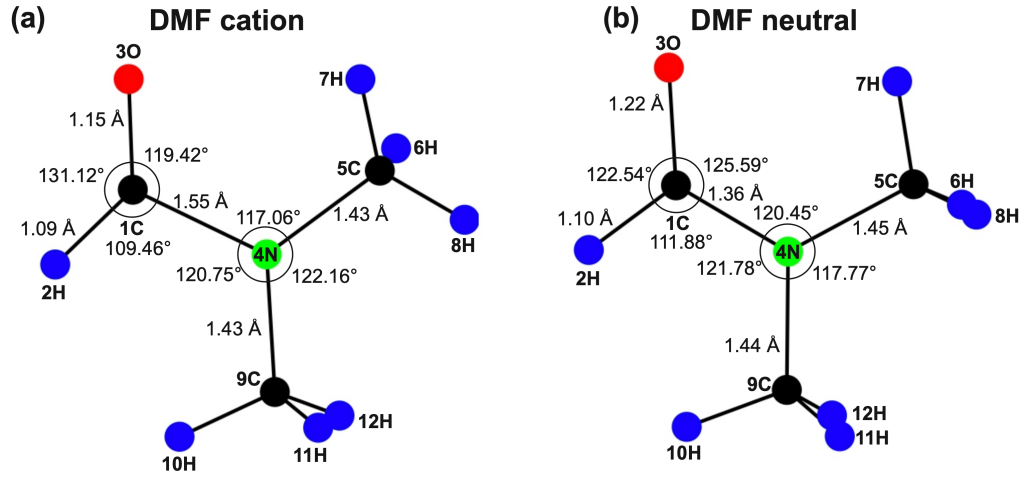

Fig. 6.1: Equilibrium geometries of the DMF cation (a) and neutral (b) optimized on a UMP2/aug-cc-pVTZ level of theory. Carbon atoms are shown in black, the oxygen atom in red, the nitrogen atom in green, and the hydrogen atoms in blue. The main bond lengths and angles are highlighted in the Figure. A full list of the internal coordinates is provided in Table C.1 in the Appendix.

Upon ionization from the HOMO, the double bond character of the N−CO amide bond vanishes. Perhaps surprisingly, the optimized structure of the ion is also almost planar (except for the hydrogen atoms). Starting the geometry optimization from a variety of non-planar geometries yields the same geometry, and frequency calculations confirmed that this is the global minimum structure.

Table C.1 in the Appendix lists the internal coordinates of the DMF cation and neutral at their equilibrium geometries. The N−CO and C=O bond lengths change most upon ionization. The N−CO bond elongates from 1.36 Å to 1.55 Å, which we attribute to the loss of the partial double bond character. Furthermore, the C=O equilibrium bond length reduces from 1.22 Å to 1.15 Å. The large change in the N−CO stretch coordinate might indicate that the bond is prone to cleavage in the ion.

In order to understand which electronic states are involved in the photolysis, we calculated the vertical excitation energies from neutral ground state DMF to the first ten ionic states. The results are shown in Table 6.1, which also summarizes

Tab. 6.1: Vertical excitation energies (V_E) from the electronic ground state of neutral DMF to the ionic ground state and excited states. The geometries and energy of the neutral and ionic ground state were optimized/calculated on a UMP2/aug-cc-pVTZ level of theory. The vertical excitation energies of the excited states were calculated using on the UB3LYP/aug-cc-pVTZ level of theory. For the first six ionic states, the resulting product pair upon cleavage of either the N−CO bond or either of the N−CH_3 bonds is shown.

State	V_E / eV [a]	V_E / eV [b]	N−CO	N−CH_3
$1^2A'$ (ground state)	10.16	9.71	HCO + $NC_2H_6^+$	$HCONCH_3^+$ + CH_3
$2^2A'$	10.57	11.41	HCO + $NC_2H_6^+$	$HCONCH_3^+$ + CH_3
$3^2A'$	13.88	14.23	HCO^+ + NC_2H_6	$HCONCH_3^+$ + CH_3
$4^2A'$	13.88	14.59	HCO + $NC_2H_6^+$	$HCONCH_3$ + CH_3^+
$5^2A'$	14.46	14.66	HCO + $NC_2H_6^+$	$HCONCH_3^+$ + CH_3
$6^2A'$	14.70	14.92	HCO + $NC_2H_6^+$	$HCONCH_3^+$ + CH_3
$7^2A'$	14.70	15.15		
$8^2A'$	15.50	15.66		
$9^2A'$	16.13	16.06		
$10^2A'$	16.43	16.58		

[a] At the equilibrium geometry of neutral DMF
[b] At the equilibrium geometry of the DMF^+ ion

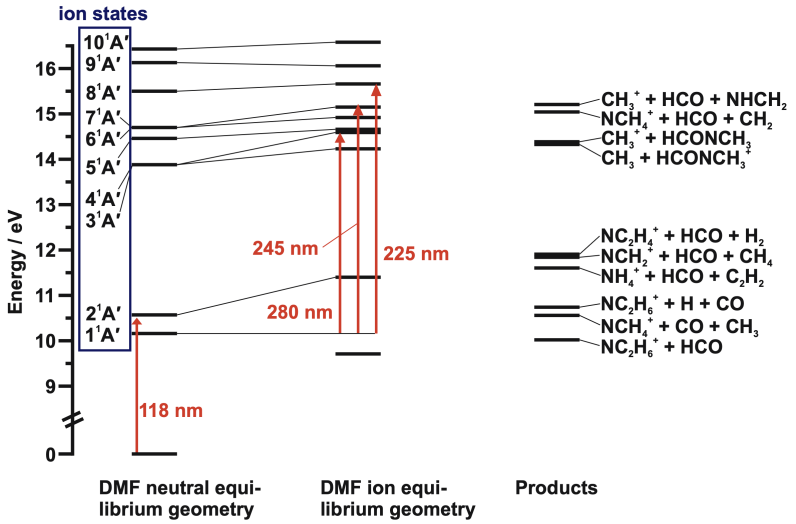

Fig. 6.2: DMF^+ excitation energies to the first ten ionic states at the ground state geometries of neutral DMF and of the DMF cation. The red arrows indicate the photoexcitation for ionization (118 nm) and photolysis (225 nm, 245 nm, and 280 nm). On the right are the energies for various product channels following dissociation of the ion into two or more fragments.

which product pair each state converges to upon cleavage of the N−CO or either of the N−CH_3 bonds. The product pair assignment was obtained from the PECs in Figure B.1 in the Appendix. Ionization at 118 nm (10.49 eV) populates almost

solely the $1^2A'$ ionic ground state (with the $2^2A'$ state also potentially accessible within the expected accuracy of the calculations). Absorption of 225 nm, 245 nm, and 280 nm photons, in addition to the 118 nm photon, leads to summed excitation energies of 16.01 eV, 15.56 eV, and 14.93 eV, respectively. The highest lying accessible states of the ion are the $7^2A'$ state (280 nm), the $8^2A'$ state (245 nm), and the $8^2A'$ state (225 nm). Figure 6.2 also shows the energies of the various possible fragmentation channels relative to the ionic state energies. The energy ordering of the channels agrees for the most part with the experimental appearance energies reported by Li *et al.*[274], except for the $HCONCH_3^+ + CH_3$ channel, for which our calculations predict the product energy to be relatively high. Given that we observe $HCONCH_3^+$ following dissociative ionization at 118 nm (see Section 6.4.1), we assume that we did not find the global energy minimum for the $HCONCH_3^+$ ion in our calculations.

It is worth noting that the NCH_4^+ ion can be formed via the following two reactions,

$$DMF \longrightarrow NCH_4^+ + HCO + CH_2 \tag{6.1}$$

$$DMF \longrightarrow NCH_4^+ + CO + CH_3, \tag{6.2}$$

which differ in that the hydrogen atom on the oxygen side of the molecule either remains bound to the carbon atom (reaction 6.1) or is transferred to the nitrogen atom (reaction 6.2). Interestingly, the intramolecular hydrogen transfer channel is significantly lower in energy, and accessible at all three photolysis wavelengths studied, while the simpler bond cleavage reaction is only energetically accessible at the 225 nm photolysis wavelength. The reason for the energy difference is that in reaction 6.2 CH_3 is produced rather than CH_2, which makes the channel energetically more feasible.

6.4 Experimental results

6.4.1 118 nm ionization of neutral *N,N*-dimethylformamide

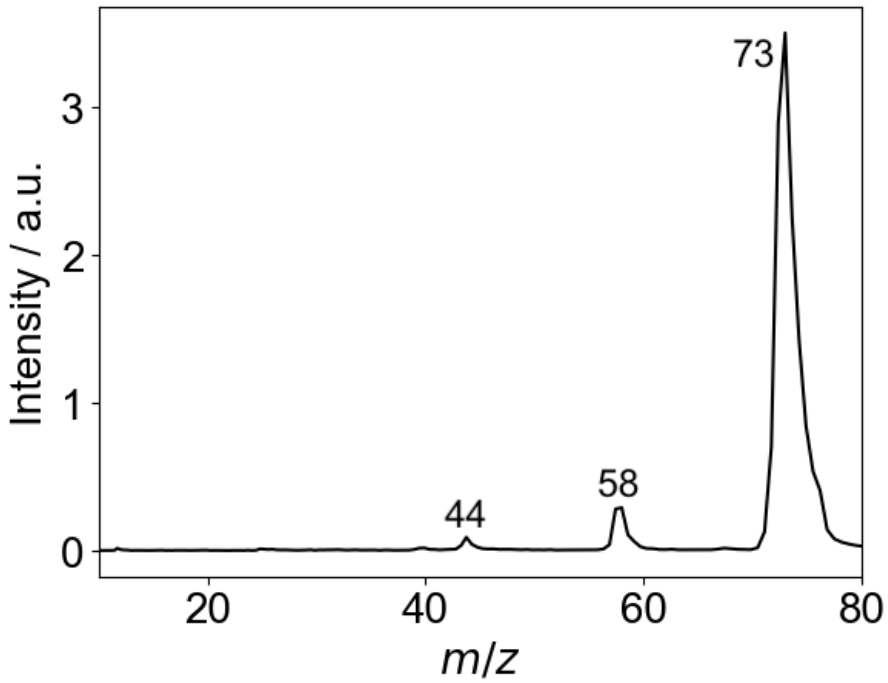

Fig. 6.3: Background-subtracted TOF spectrum of DMF following ionization at 118 nm.

Figure 6.3 shows the mass-calibrated TOF spectrum for the 118 nm ionization products of DMF. The most intense signal is the DMF^+ parent ion peak. However, we also observe significant fragment ion peaks at m/z values of 44 and 58, which we assign to $NC_2H_6^+$ and $HCONCH_3^+$. Based on the vertical excitation energies in Table 6.1, the fragment ions are produced on the ionic ground-state surface, which yields HCO + $NC_2H_6^+$ or $HCONCH_3^+$ + CH_3, depending on whether the N−CO or either of the N−CH_3 bonds break.

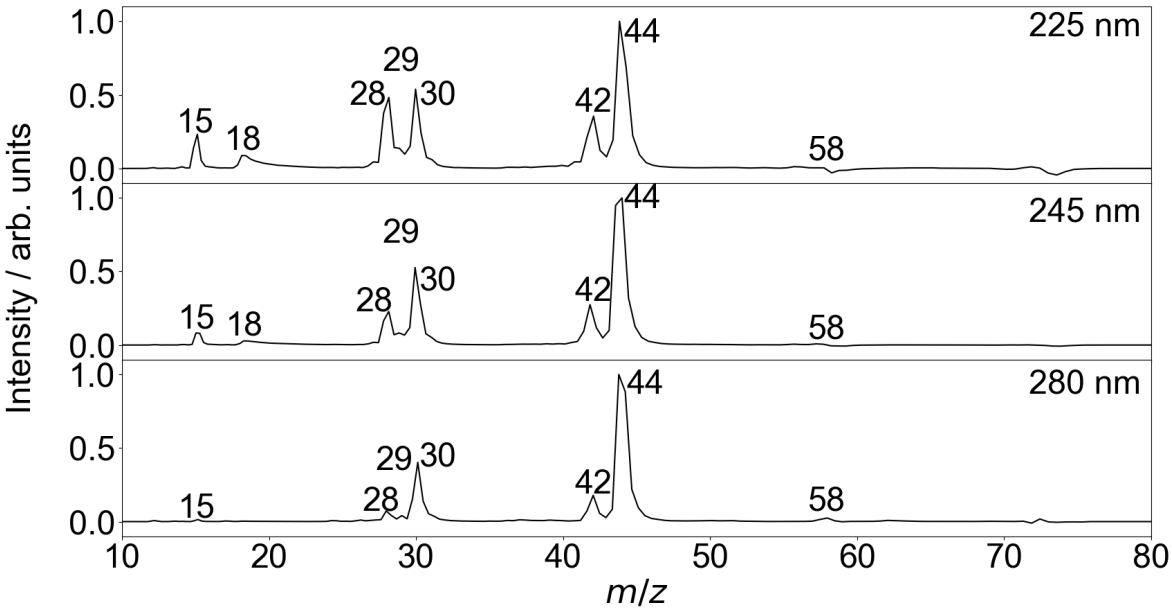

Fig. 6.4: Background-subtracted TOF mass spectra produced by ionizing DMF at 118 nm followed by photolysis of the ion at 225 nm (upper panel), 245 nm (central panel), and 280 nm (lower panel).

6.4.2 Photolysis of *N*,*N*-dimethylformamide$^+$ at 225, 245, and 280 nm

Primary dissociation pathways

Figure 6.4 shows the two-colour TOF spectra recorded following ionization of neutral DMF at 118 nm and photolysis of the resulting cation at 225 nm, 245 nm, and 280 nm. The single-laser signals have been subtracted off. The most intense peak at all three wavelengths is m/z 44, which we assign to the $NC_2H_6^+$ ion produced via N−CO bond fission in DMF^+ to form HCO + $NC_2H_6^+$. As shown in Table 6.1, nearly all low-lying electronic states yield the charge on the nitrogen-containing fragment following bond cleavage. Only the $3^2A'$ state produces HCO^+ + NC_2H_6. The HCO^+ peak at m/z 29 is low in intensity at all three photolysis wavelengths, indicating that the dissociation into HCO^+ + NC_2H_6 is a minor fragmentation path-

way. The $NC_2H_6^+$ ion is initially formed as $N(CH_3)_2^+$, but is known to isomerize into the more stable $H_2C{-}NH{-}CH_3^+$[277].

$N{-}CH_3$ methyl bond fission competes with $N{-}CO$ bond fission. If $N{-}CH_3$ bond cleavage occurs readily, we expect the $HCONCH_3^+$ fragment peak at m/z 58 to be high in intensity since all states but the $4^2A'$ state lead to the product pair $HCONCH_3^+$ + CH_3. However, the $CHONCH_3^+$ peak intensity is virtually zero at all three wavelengths. The $4^2A'$ state leads to $HCONCH_3$ + CH_3^+ and is energetically accessible at the 225 nm and 245 nm photolysis wavelengths. The CH_3^+ ion signal is observed at m/z 15, and increases in intensity as the photolysis photon energy increases. However, while $N{-}CH_3$ bond fission on the $4^2A'$ state cannot be ruled out, it is unlikely that the bond dissociation occurs solely on this state and not on lower-lying states. Instead, CH_3^+ probably results from the secondary dissociation of $NC_2H_6^+$, with $N{-}CO$ amide bond fission outpacing $N{-}CH_3$ bond cleavage in the DMF^+ cation.

Secondary dissociation pathways

Tab. 6.2: Ratio of the integrated peak intensity of each fragment ion to the overall intensity following ionization of DMF at 118 nm and photolysis at 225 nm, 245 nm, or 280 nm.

Ion	225 nm	245 nm	280 nm
CH_3^+	0.046	0.023	0.004
NH_4^+	0.063	0.029	0.005
NCH_2^+	0.163	0.082	0.035
HCO^+	0.014	0.014	0.006
NCH_4^+	0.160	0.198	0.193
$NC_2H_4^+$	0.171	0.115	0.092
$NC_2H_6^+$	0.393	0.539	0.650

Table 6.2 compares the relative fragment peak intensities for each wavelength. The CH_3^+(m/z 15), NH_4^+(m/z 18), NCH_2^+(m/z 28), and $NC_2H_4^+$(m/z 42) fragments ions

increase in relative abundance with an increasing photolysis energy. All of these ions result from the secondary dissociation of the $NC_2H_6^+$ fragment ion formed via cleavage of the N−CO amide bond from the DMF parent ion. Except for CH_3^+, the formation of these ions requires significant structural rearrangement of the $NC_2H_6^+$ ion, and is therefore likely to occur over relatively long timescales. The NH_4^+ ion peak exhibits a long exponentially decaying tail, characteristic of ion formation on long timescales outside the interaction region and along the TOF tube en route to the detector. This is consistent with our study on neutral DMF, in which the NH_4^+ ion peak exhibits an analogous tail. The secondary dissociations can either occur from the initially formed $N(CH_3)_2^+$ or from its more stable isomer $H_2C{-}NH{-}CH_3^+$.

NCH_4^+(m/z 30) is also likely to be a secondary dissociation product, and is highly abundant at all three photolysis wavelengths. In contrast to the other secondary dissociation products, its relative abundance does not increase with increasing photon energy. As discussed previously, at the two larger photolysis wavelengths the NCH_4^+ ion can only be formed if the N−CO amide bond cleavage is accompanied by intramolecular hydrogen transfer from the oxygen side of the molecule to the nitrogen atom (see Figure 6.2). This is in contrast to the other secondary dissociation products, which do not require the hydrogen transfer.

In line with the increasing intensity of the signals from secondary fragmentation products, the relative intensity of the $NC_2H_6^+$ ion signal decreases with increasing photon energy. Based on the arguments above, we can probably describe the formation of the various secondary ions in terms of a statistical decay of the $NC_2H_6^+$ ion, with the formation of a given secondary ion increasing in probability with increasing internal energy of the $NC_2H_6^+$ ion. The velocity-map images of the various fragment ions provide insight into whether the available energy is released as product

kinetic or internal energy.

Velocity-map images

Figure 6.5 shows the Abel-inverted velocity-map images of the fragment ions formed at all three photolysis wavelengths, together with the corresponding KER distributions. The integrals of the KER distributions are normalized to unit intensity.

Perhaps surprisingly, the kinetic energy distributions of the $NC_2H_6^+$ fragment ion recorded at the three energies are almost identical, extending out only to very slightly higher energies as the photolysis wavelength is reduced from 280 nm to 225 nm. The KER distributions peak at around 0.05 eV and extend to about 0.75 eV. Rather than being released into product translation, the vast majority of the excess energy is clearly released into internal excitation of the nascent ion. This is consistent with the clear increase in the extent of secondary fragmentation with reducing photolysis wavelength noted earlier when considering the TOF spectra.

The KER distributions for the secondary dissociation products show the same trend observed in $NC_2H_6^+$ and change only very slightly upon increasing the photon energy. The exceptions are CH_3^+ and NCH_2^+, whose KER distributions at 280 nm appear to extend to significantly higher kinetic energies. We believe this is an artefact resulting from the very low signal levels for these ions at 280 nm. As a result, the Abel-inverted image contains a great deal of centreline noise, which distorts the kinetic energy distribution. Moreover, the velocity-map images of the secondary dissociation products are very similar both to each other and to the $NC_2H_6^+$ ion images, even though there are differences in the intensities. This implies that very little energy is released into translation during the secondary dissociation processes, consistent with a lifetime long enough to enable statistical redistribution of energy

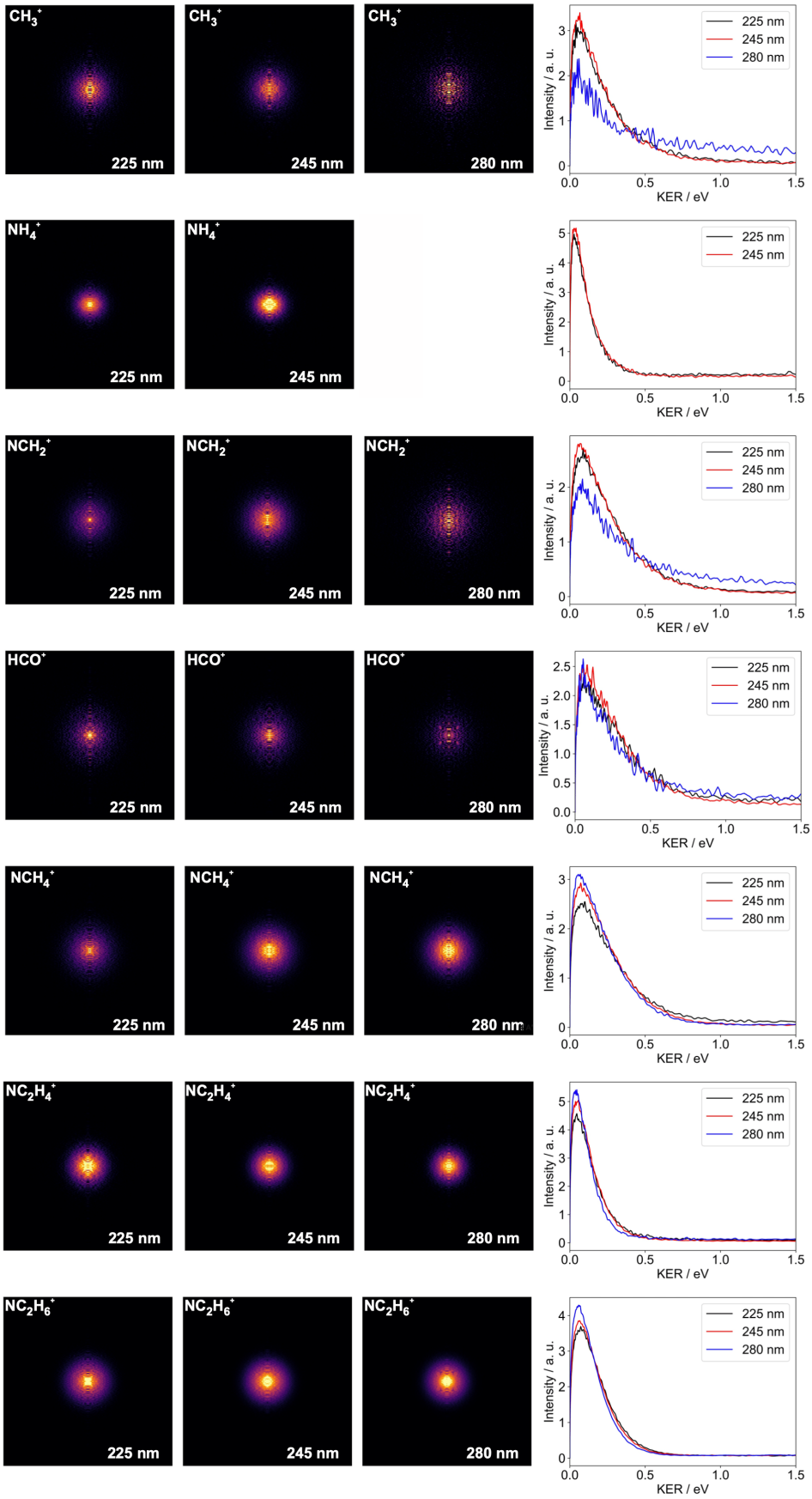

Fig. 6.5: Abel-inverted velocity-map images obtained from DMF following ionization at 118 nm and photolysis at 225, 245, and 280 nm and their resulting kinetic energy release distributions, whose integrals are normalized to one.

amongst all of the available internal modes until a given bond is sufficiently energized to break. The long lifetime is also in accord with the images being isotropic, as a result of molecular rotation prior to dissociation.

The observation that the velocity-map images are very similar to each other for the different photolysis wavelengths studied implies that dissociation may occur from the same ionic state at all three wavelengths. Based on the vertical excitation energies, the DMF^+ cation is excited to the $7^2A'$ state at 280 nm. Dissociation can either occur on this state or the $1^2A'$ state following IC. Even though excitation at 245 nm and 225 nm can lead to excitation up to the $8^2A'$ state, the population density is likely to transfer down to the $1^2A'$ and $2^2A'$ states on a timescale faster than the relatively slow dissociation. Dissociation occurring from the ionic ground and first excited state over the photolysis wavelength range studied is highly consistent with the lack of wavelength dependence in velocity-map images.

6.4.3 Comparison with literature

The TOF spectrum obtained at 225 nm is similar to the 70 eV electron ionization mass spectrum reported by Li *et al.*[274]. The fragment ions resulting from the secondary dissociation of $NC_2H_6^+$ have higher relative intensities in Li's work, probably due to the difference in internal energy transferred to the nuclear framework via the two different ionization mechanisms. Li *et al.* observe straightforward $N-CO$ or $N-CH_3$ bond cleavage and a channel involving $N-CO$ bond fission and simultaneous intramolecular hydrogen transfer from the HCO carbonyl end to the nitrogen atom, followed by loss of one of the methyl hydrogen atoms to form $NC_2H_6^+$. Interestingly, we see $N-CH_3$ bond cleavage as a result of the initial 118 nm photoionization step, but we do not see further $N-CH_3$ cleavage in the DMF cation on the absorption of a UV photon. As noted earlier, in contrast to

the electron ionization experiments, absorption of a UV photon by the DMF cation appears to lead almost exclusively to cleavage of the amide bond, which can be accompanied by simultaneous intramolecular hydrogen transfer, with the resulting $NC_2H_6^+$ ion able to decompose via a variety of pathways to yield our observed products. All of these, apart from CH_3^+, were observed and studied by Li *et al.* Many of these processes had also been studied earlier by Loudon and Webb[275] through analyzing metastable peak shapes within a commercial mass spectrometer, an analysis which provides insight into the initial and final masses and the conversion between them.

In a collisional activation study on $NC_2H_6^+$ and deuterium-labelled analogues, Levsen and McLafferty[277] passed $NC_2H_6^+$ ions prepared via dissociative electron ionization through a helium buffer gas. The internal energy of the $NC_2H_6^+$ ions was correlated with the electron energy used in the ionization step. The main secondary dissociation products observed were CH_3^+, NH_4^+, $NC_2H_4^+$, and $NC_2H_5^+$. Lowering the electron energy decreased the NH_4^+ and $NC_2H_4^+$ peak intensities while increasing the $NC_2H_5^+$ intensity. This is similar to the behaviour observed in our photolysis study as the photon energy is reduced, except that we do not see significant amounts of the $NC_2H_5^+$ product at any of the three wavelengths studied. Additionally, we also observe the formation of NCH_4^+, which Levsen and McLafferty did not observe. As stated above, the intramolecular hydrogen transfer is very likely the driving force behind NCH_4^+ formation, which cannot occur in Levsen and McLafferty's study, which uses a different precursor ion.

In addition to the activation mechanism, a second key difference between our experiments and those of Levsen and McLafferty relates to the timescales involved. Their collisional activation measurements are made around 10 µs after the formation of the $NC_2H_6^+$ ions as a result of the transport time of the ion beam to the

collision region. Over this timescale, all of the ions will have isomerized to their most stable structure, and any ions that have undergone fragmentation on a faster timescale than this will have been lost from the beam. Therefore, the products observed are those formed in collisions of only the most stable isomer of $NC_2H_6^+$ with helium. In our experiment, we extract ions from the interaction region on a much faster timescale, and therefore probably see dissociation products arising from more than one isomer.

6.5 Conclusions

This Chapter presents a comprehensive VMI study into the photodissociation of the DMF^+ cation. DMF was intersected with 118 nm (10.49 eV), producing mostly intact DMF^+ monocations. Afterwards, the ions were photolysed at 225 nm, 245 nm, and 280 nm. The initial ionization step produces predominantly DMF parent ions and small amounts of $N_2H_6^+$ and $HCONCH_3^+$ following N−CO or N−CH_3 bond cleavage. In the subsequent UV-induced photolysis, the N−CO amide bond breaks selectively, yielding HCO + $NC_2H_6^+$ on all low-lying ionic states, except the $3^2A'$ state, which produces HCO^+ + NC_2H_6. Virtually all the available energy is released into internal modes of the $NC_2H_6^+$ ion and its co-product(s), with only a few percent of the energy released into translation. In addition, N−CO bond cleavage can be accompanied by simultaneous intramolecular hydrogen transfer from the oxygen side of the molecule to the nitrogen atom, in which case NCH_4^+ can be formed. This channel is low in energy and observed efficiently at all three photolysis wavelengths.

The $NC_2H_6^+$ ion has lifetimes of at least tens of microseconds and is fluxional in structure, readily isomerizing from $N(CH_3)_2^+$ to $H_2C{-}NH{-}CH_3^+$. It can dissociate

via a number of different pathways to produce CH_3^+, NH_4^+, NCH_2^+, and $NC_2H_4^+$. The abundance of the various fragment ions increases with increasing photon energy, in line with the increased internal energy of the primary dissociation products. This is consistent with the velocity-map images, which look very similar in that they are fully isotropic and show little dependence on the photolysis photon energy over the range studied. The similarity of the velocity-map images could indicate that dissociation occurs from the same set of electronic states, most likely the ionic ground state ($1^2A'$) and first excited state ($2^2A'$).

Nanosecond pump-probe studies address some of the most fundamental questions in physical chemistry. They give insight into which chemical bonds break or are formed, the PESs involved in the reaction, and how the available energy is distributed among the degrees of freedom of the products. However, one major limitation remains the timescale on which reaction products are probed. In most cases, the reaction is already over when the reaction products are ionized. We therefore have knowledge of the system before and after the reaction but not during, as rotations occur on the picosecond timescale, and vibrations occur on the femtosecond timescale. If we want to follow the nuclei in real time, we need adequately short laser pulses, i.e. on the femtosecond timescale. In the following Chapter we will report on progress towards achieving this goal.

7 Set-up and characterization of a femtosecond beamline

In a pump-probe experiment employing femtosecond laser pulses, the pump laser pulse initiates the chemical reaction. After a series of well-defined time delays, the probe laser pulse generates an observable that provides insight into the evolving chemical system, allowing the recording of 'molecular movies'[278,279], which follow the evolution of reactants into products in real time. The first molecular movies were recorded by Ahmed Zewail[280,281], who pioneered the application of femtosecond laser pulses to probe molecular dynamics and was awarded the Nobel Prize in Chemistry in 1999 for his work.

The probe technique varies depending on the nature of the observable. In transient absorption spectroscopy, a technique covered in Chapter 1, the probe laser beam is usually of high bandwidth in order to capture as many transitions as possible to extract the maximum amount of information. The same applies to 2D spectroscopy, which provides a series of transient absorption spectra for different pump wavelengths.[282] While both techniques measure absorption spectra, they do not provide direct structural information on the system. Time-resolved X-ray diffraction is a commonly used technique capable of following nuclear motion in real-time. However, generating ultrashort X-ray pulses is challenging, and most experimen-

tal studies rely on X-ray free electron laser facilities rather than being conducted 'in-house'. This leaves space for alternative probing methods capable of following atomic motion. CEI has emerged as a potential method for filling that gap.

In CEI, interaction of a molecule with an intense ultrafast probe laser pulse leads to the ejection of multiple valence electrons, leaving the chemical system in a highly charged, unbound state. Upon dissociation, the molecule breaks apart into fragment ions, whose trajectories are determined predominantly by the Coulombic repulsion within the parent ion. During this Coulomb explosion, the atomic positions are mapped onto the final velocities of the ions. We can measure the final velocities using VMI, and use these to determine the initial atomic positions, and therefore the molecular geometry. Covariance analysis provides information on the relative velocities of the various co-fragments and greatly simplifies the determination of structures from the velocity map images. Zhou *et al.*[283] illustrated that CEI only works well as a structural determination technique if the number of charges in the system is greater or equal to the number of atoms. Only in this high-charge regime can the trajectories of the fragment ions be predicted accurately by considering the electrostatic repulsion between the charges in the system, as the ion trajectories are fully governed by the initial geometry and charge distribution. For lower charge states, electronic effects play a significant role in the dissociation mechanism, which makes the extraction of geometric information more challenging.

Although multiple studies[284–288] have employed a CEI probe step in combination with covariance analysis, it remains unclear to what extent quantitative structural information can be obtained in terms of bond angles and bond lengths. This can be studied systematically in one-laser femtosecond experiments by conducting CEI on the ground state of the molecule for different laser intensities.

Our group jointly owns a shared Spectra-Physics Solstice Ace laser system with the

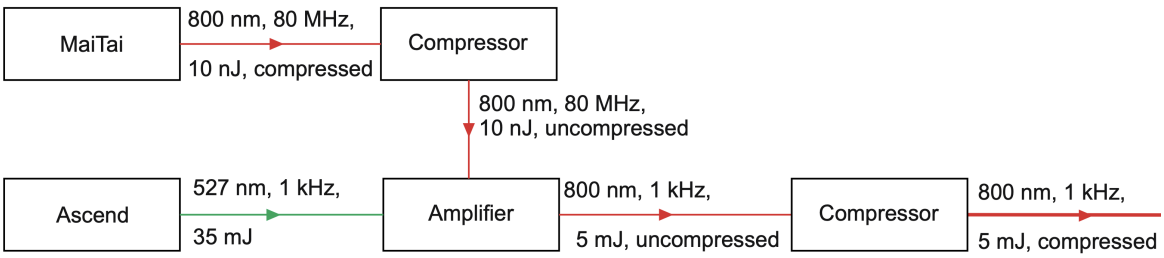

Fig. 7.1: Schematic of the laser system used to produce femtosecond laser pulses. The MaiTai is the oscillator of the system, and the Ascend is used as a pump laser during the chirped pulse amplification. A grating compressor recompressed the amplified pulse.

Brouard and Mackenzie groups in Oxford. The laser system is located in the B2 laboratory adjacent to our laboratory in the Chemistry Research Laboratory building. Part of my project involved building a beamline from the laser through the wall between the B1 and B2 laboratories to the experiment. This Chapter describes the beamline setup and provides a full characterization of the laser pulse at the chamber.

7.1 Laser system

The laser beam has a central wavelength of 800 nm, with a 60 nm bandwidth, a transform limited pulse length of 35 fs, and an average output power >5 W at an operating frequency of 1 kHz. Figure 7.1 schematically illustrates the working principle of the laser system.

The complete laser system comprises several individual lasers, including a MaiTai (Spectra-Physics), Ascend 40 (Spectra-Physics), and Solstice Ace (Spectra-Physics). The MaiTai comprises the oscillator of the laser system, and uses Titanium:Sapphire (Ti:Al_2O_3) as the gain medium. Femtosecond pulses are generated via mode locking[289], a technique that fixes the phase relationship between the different frequency components in the cavity. The MaiTai output has a central wavelength of

800 nm, with a 60 nm bandwidth at a frequency of 80 MHz and an average power of 10 nJ.

The MaiTai oscillator output needs to be amplified. The amplification of femtosecond laser pulses is not straightforward, as the high intensities can damage the gain medium in the amplifier. Our laser system uses chirped-pulse amplification[290,291], a technique that was awarded the Nobel Prize in Physics in 2018. The laser pulse is stretched in time, amplified, and afterwards recompressed. The regenerative amplifier uses another Titanium:Sapphire crystal as the gain medium. Population inversion of the gain medium is achieved by using the second harmonic (527 nm) of the Ascend laser (Nd:YLF) laser, which has a frequency of 1 kHz and a power of 35 mJ. The oscillator beam is stretched in time and subsequently introduced into the regenerative amplifier cavity, where the amplitude increases every round trip. The output beam has a power >5 kW, but the pulse is still elongated in time. In the last step, the pulse is recompressed by a motor-controlled grating compressor before leaving the laser system.

7.2 Beamline

7.2.1 Beam path

Figure 7.2 shows the femtosecond laser beam path to the experiment. The beam is split by a 15:85 beamsplitter (Eksma Optics, 042-7785PB), from which we use the transmitted fraction (15 %). The reflected portion (85 %) is used by other groups. Mirrors (Eksma optics, 072-7288 or 085-7288) guide the laser pulse through the wall into our laboratory, where the TOF-VMI spectrometer is located. The beam passes through a HWP (Eksma optics, 460-4215) and a polarization filter (Eksma optics,

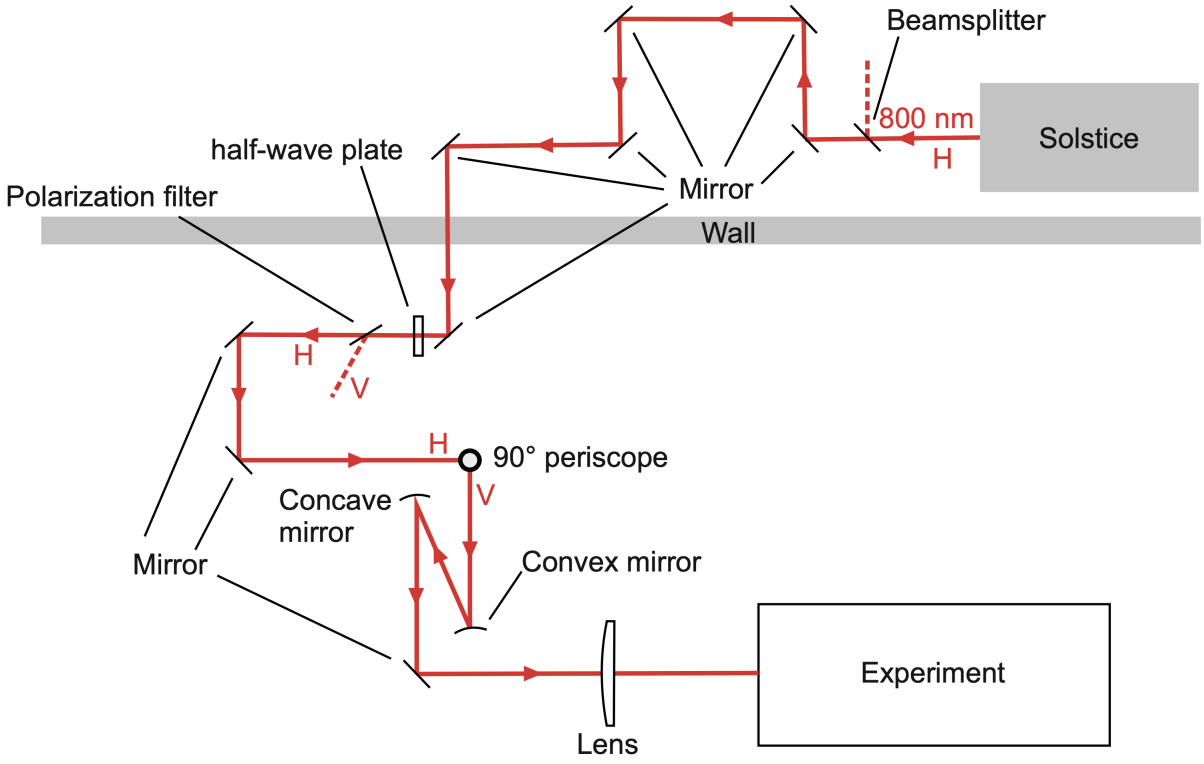

Fig. 7.2: Schematic showing the femtosecond laser beamline. The laser system is located in the adjacent lab. Mirrors guide it from there to the experiment. A combination of a half-wave plate and polarization filter allows for power control of the laser.

420-0526E) set at Brewster's angle. The reflected part (vertical polarization in the imaging plane) is dumped, and the transmissive contribution (horizontal polarization, perpendicular to the imaging plane) is guided into the experiment. Rotating the HWP changes the ratio of vertical to horizontal polarized light. Thus, the combination of the HWP and polarization filter allows us to control the laser power reaching the experiment. The transmitted beam passes through a 90° periscope, which lifts the laser beam to the appropriate height and flips the polarization from horizontal (perpendicular to the imaging plane) to vertical in the imaging plane. Afterwards, the laser beam passes through a telescope consisting of a convex mirror (Eksma optics, 095-0225R+400) and a matching concave mirror (Eksma optics, 095-0125R-800). The telescope magnifies the initial beam waist from 10 mm to 20 mm. The distance between the mirrors is set to collimate the expanded laser beam as well as possible. The expanded laser beam is subsequently focused into the interaction

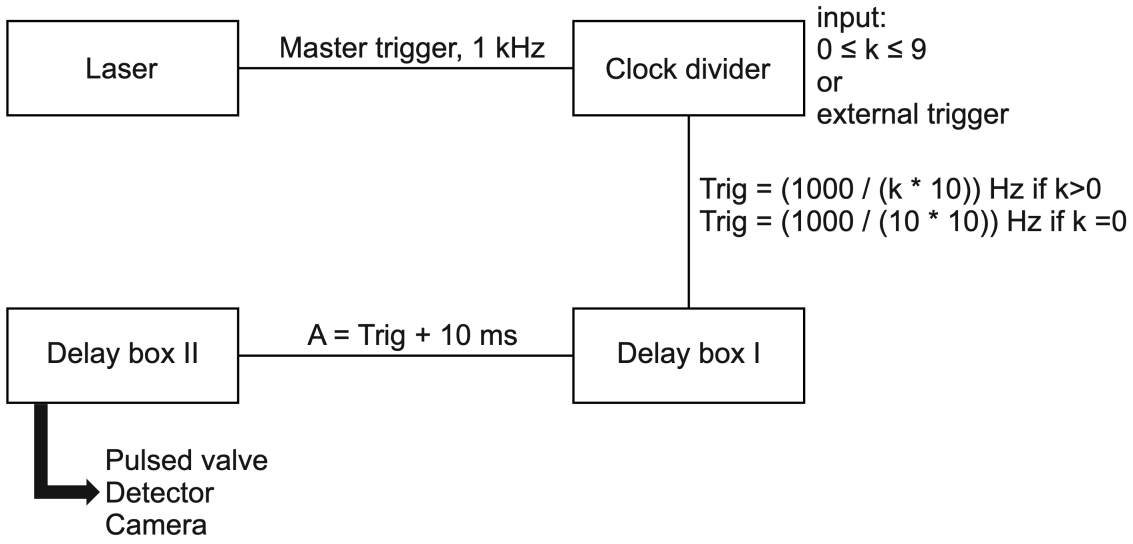

Fig. 7.3: Schematic of the trigger system when working with the femtosecond laser. The electrical signal from the laser is used as the master trigger. A pulse divider clock changes the frequency from 1 kHz to a target frequency. A combination of two delay boxes triggers the pulsed valve, detector, and camera relative to the laser shot.

region by a plano-convex lens (Eksma optics, 110-1519ET). We use a 2 mm-thick CaF_2 window as our chamber window (Crystran Ltd, CAFP35-2).

7.2.2 Pulse timings

When using the shared laser system, we use the electrical signal of the MaiTai as the master pulse to trigger the pulsed valve, MCPs, and camera of the VMI experiment. The laser system emits an electrical signal once the laser fires. However, the light will reach the experiment faster than the electrical pulse reaches the delay box. Furthermore, if used with a molecular beam, the pulsed valve is triggered before the laser fires. To solve this problem, we use the electrical signal of the ith laser pulse to trigger the pulsed valve, detector, and camera for the laser pulse of the $(i+1)^{\text{th}}$ shot. The electrical signal of the $(i+1)^{\text{th}}$ pulse is used to trigger the experiment for the $(i+2)^{\text{th}}$ laser pulse, and so on. That way, we can trigger the pulsed valve prior to the laser firing so that the molecular beam and the laser pulse

overlap in time in the interaction region.

Figure 7.3 summarizes the elements involved in the trigger system. The laser emits an electrical signal at a 1 kHz rate, which provides the master trigger for the rest of the experiment. The electrical pulse is guided to a clock divider box via Bayonet Neill-Concelman (BNC) cables. The clock divider reduces the frequency from 1 kHz to the target frequency at which the user wishes to operate the experiment, since the pulsed valve and camera cannot run at 1 kHz. It obtains the master trigger from the laser and a second signal either from a second external pulse, which runs at the target frequency, or from an internal clock. The frequency of the internal clock is defined by the input variable k, an integer defined as $0 \leq k \leq 9$. The clock divider only outputs a trigger if the master and external trigger arrive simultaneously. If an external trigger is used, the output frequency equals the frequency of the external pulse. If the internal clock is used, the output frequency is $\frac{1000}{k*10}$ Hz unless $k = 0$, which leads to a frequency of $\frac{1000}{10*10}$ Hz. Thus, $k = 5$ results in 20 Hz, and $k = 0$ in 10 Hz. We use a frequency of 20 Hz for experiments with the femtosecond laser.

The clock divider output pulse triggers Delay box I, which adds a delay of 10 ms before triggering Delay box II. Without the delay, Delay box II would get retriggered by the $(i + 1)^{\text{th}}$ shot before triggering the detector and camera in the i-th cycle. Delay box II then triggers the pulsed valve, detector, and camera. At a frequency of 20 Hz, the triggers for all three have delays of approximately 40 ms on Delay box II. Combined with the delay from Delay box I, this yields about 50 ms, corresponding to the delay between two laser pulses. For a frequency of 10 Hz, the delays on Delay box II would need to be around 90 ms.

One initial concern when using the electrical signal from the ith cycle for the $(i + 1)^{\text{th}}$ cycle is that there is a drift in time between the experiment being triggered

relative to when the light arrives at the chamber. However, this drift proved to be negligible.

7.3 Characterization

To characterize the laser beam, we need to determine its peak intensity. The laser intensity in the chamber is defined as follows[292],

$$I = \sqrt{\frac{\ln 2}{\pi}} \cdot \frac{P}{\nu \Delta_t \pi \omega_0^2}, \tag{7.1}$$

where P is the average power, ν is laser frequency, Δ_t is the pulse duration, and ω_0 is the beam waist in the interaction region at the point of tightest focus. The factor $\sqrt{\frac{\ln 2}{\pi}}$ arises from assuming a Gaussian shape for the laser pulse.

7.3.1 Pulse length

Equation 7.1 shows how the peak intensity of a Gaussian laser pulse is determined. It is inversely proportional to the pulse length in time. Measuring this length is essential. Not only do we need to know the pulse duration to calculate the peak intensity, but Coulomb explosions only work well in combination with short laser pulses. The goal of Coulomb explosions is to achieve very high charge states in the molecule while retaining the nuclear geometry, ideally for the whole duration of the laser-molecule interaction. However, nuclei move on the femtosecond timescale. For instance, the typical vibrational period of a covalent bond is tens to hundreds of femtoseconds long[293]. Thus, if the laser pulse is stretched in time, it will not measure the frozen geometry of the molecule, but geometries spreading over a

larger configurational space governed by the distance the nuclei can move during the interaction with the laser pulse.

Measuring the length of femtosecond laser pulses is challenging. The most common approach to characterizing a femtosecond laser in the time domain is to employ an autocorrelator, in which the laser pulse 'scans itself'. While autocorrelator designs can vary significantly[294,295], the underlying working principle remains the same. The input pulse is split into a reference and a scanning path. The path length of the reference arm is constant, and the scanning arm includes a motor controlled delay stage that enables the user to vary the scanning arm path length systematically. The scanning path is delayed relative to the reference arm. If both beams are incident on the doubling crystal at the same time then the intensity will be high enough to generate frequency-doubled light at 400 nm, whose intensity depends on the overlap of the reference and scanning arm in time. Scanning one beam relative to the other in time and measuring the intensity of 400 nm light therefore allows a beam temporal profile to be measured. The light can be captured by a photo multiplier tube (PMT) or spectrometer. Frequency-resolved optical gating (FROG)[296,297] devices combine the autocorrelator technique with a spectrometer to determine the intensity and phase of the laser pulse.

Figure 7.4 shows schematically the custom-built FROG autocorrelator used to measure the laser pulse length. It was designed and built by Dr. Chow-shing Lam and works as follows: the input beam is split by a partially reflective mirror into a reference and scanning arm. The reference arm consists solely of a 0° mirror that is fixed in place. The scanning arm also comprises a 0° mirror. However, this mirror is mounted on a motor-controlled delay stage. Both arms are subsequently reflected to the right side in the Figure, where they are offset. A set of two mirrors focuses both arms into a BBO doubling crystal, which frequency doubles the light.

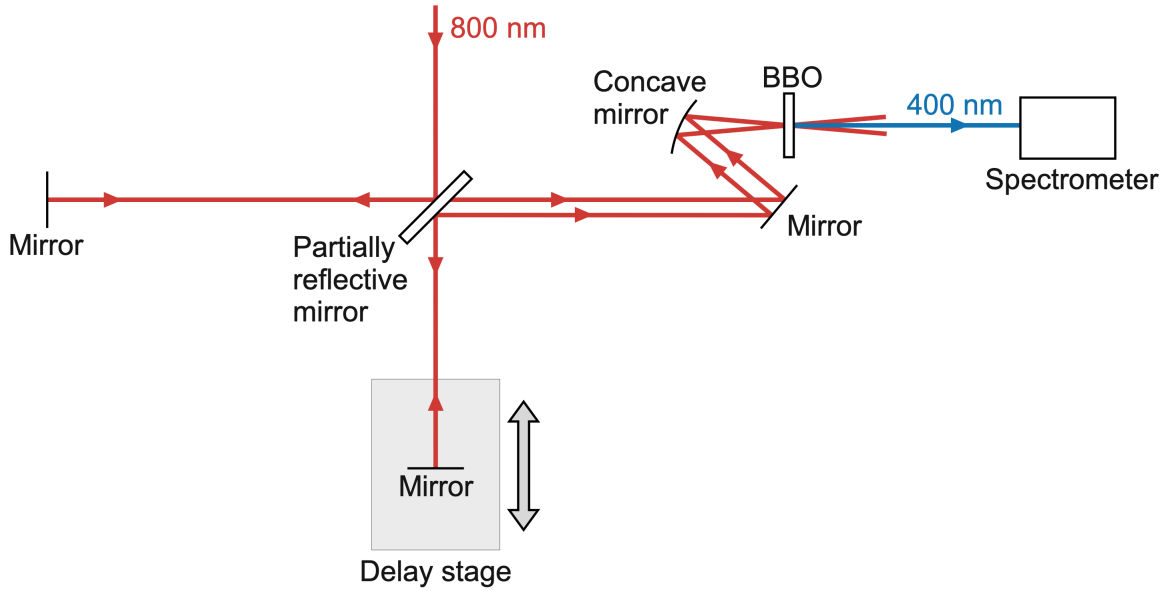

Fig. 7.4: Schematic of the FROG autocorrelator used to measure the laser pulse length.

The individual arms continue to diverge and are blocked by an iris (not shown in the Figure). In the middle, a third 400 nm arm arises, whose intensity depends on the overlap of the scanning and reference arm in time. The third arm is captured by a spectrometer.

The resulting signal is fit by a Gaussian distribution,

$$G(x) = A \cdot \mathrm{e}^{\frac{(x-\mu)^2}{2\sigma^2}}, \tag{7.2}$$

where x is the delay stage position in mm, A is the amplitude, μ is the delay stage position, where reference and scanning arm overlap in time, and σ is the standard deviation of the distribution. The full width half maximum (FWHM) can be obtained from σ as follows,

$$\mathrm{FWHM}_{\mathrm{mm}} = 2\sigma\sqrt{2\ln(2)}. \tag{7.3}$$

Lastly, we convert $\mathrm{FWHM_{mm}}$ to the pulse length Δ_t in fs,

$$\Delta_t = \underbrace{\frac{\mathrm{c} \cdot 10^{-15} 10^{3}}{2}}_{\mathrm{C}} \frac{\mathrm{FWHM_{mm}}}{\sqrt{2}}, \tag{7.4}$$

where C is a constant converting the delay stage distance from mm to fs. The factor of 2 arises from the light travelling the delay stage distance twice (backwards and forwards). The factor $\sqrt{2}$ stems from the convolution of reference and scanning arm, assuming Gaussian shapes.

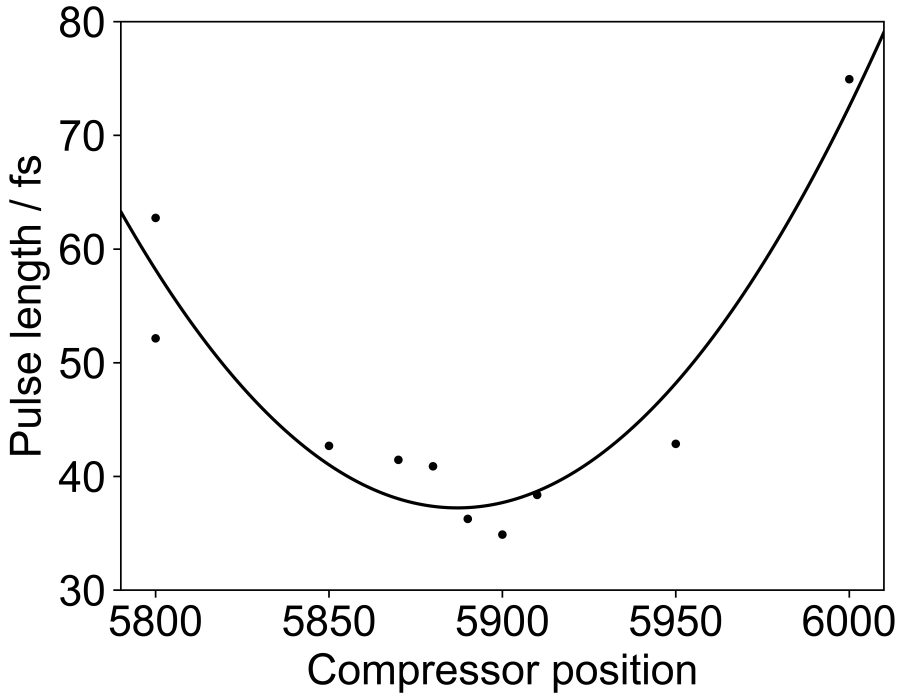

Fig. 7.5: Laser pulse length inside the chamber as a function of the Solstice compression setting, which determines the initial GDD of the laser pulse. The data points are indicated by the dots. The curve is a parabolic fit over the data.

Figure 7.5 shows the pulse length inside the chamber as a function of the Solstice compression setting. The Solstice compression setting is a quantity associated with adjusting the compression grating at the recompression stage. Thus, it is a measure of the initial group delay dispersion (GDD)-value at the laser output in arbitrary units. The data points can be described to first approximation by a parabolic curve, which has a minimum of 37 fs at a compression of 5887, which is only 2 fs above

the transform limit of 35 fs. Changing the Solstice compression either side of this value increases the pulse length.

The shortest possible pulse of 35 fs at the Solstice output is achieved at a compression setting of about 5840. In the experiment, this corresponds to a pulse length > 43 fs. Although the beamline is designed to minimize GDD, some pulse elongation is unavoidable due to the beamline length and the need for transmissive optics. At 800 nm, all optics used add positive GDD to the beam. Compression setting values greater than 5840 translate to the beam starting with negative GDD. At a compression setting of 5887, the initial negative GDD is perfectly compensated for in the beamline so that the pulse is close to its transform limit in the experiment. Minimizing the number of transmissive optics also reduces higher order dispersion, which is harder to compensate for. For this reason, we use a set of mirrors for the telescope instead of lenses.

7.3.2 Focusing conditions

A tight focus is essential when trying to achieve high laser intensities. As shown in equation 7.1, the laser intensity is proportional to ω_0^{-2}, where ω_0 is the beam waist of the laser, which is the beam radius at the focal point. The diameter of the focal spot is given by,

$$2\omega_0 = \frac{4M^2\lambda f}{\pi D}, \tag{7.5}$$

where M^2 is the quality parameter of the beam, λ is the wavelength, f is the focal length of the lens, and D is the $1/\mathrm{e}^2$ diameter of the Gaussian beam going into the lens. The laser focus is illustrated schematically in Figure 7.6. A shorter focal length and a larger initial beam diameter lead to a tighter focus inside the chamber.

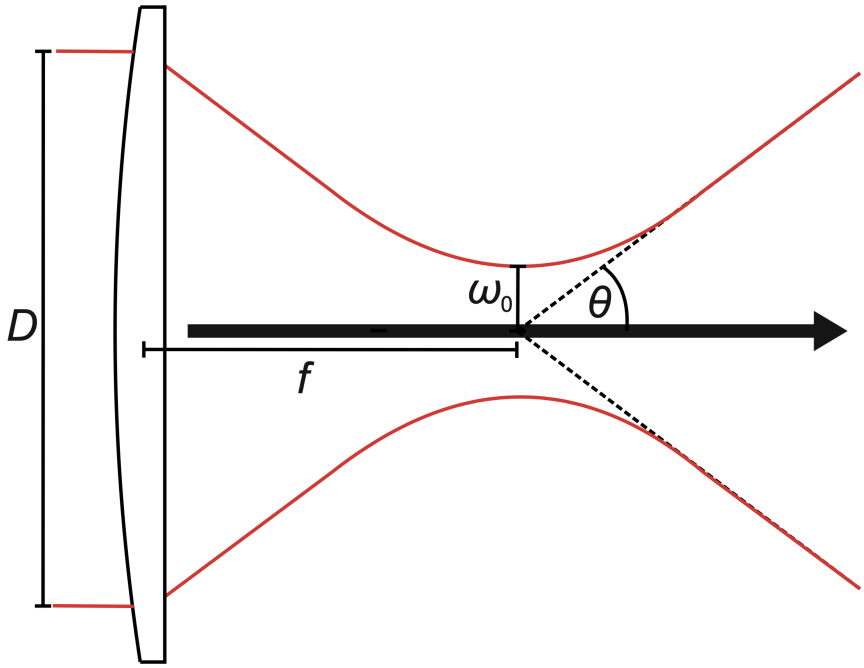

Fig. 7.6: Schematic defining the parameters used to calculate the beam waist diameter $2\omega_0$ inside the interaction region.

The focusing lens has a focal length of 300 mm, and the $1/e^2$ diameter is 20 mm. With a beam quality factor of 1.25, as stated on the SpectraPhysics website, we obtain $2\omega_0 = 19.1\,\mu m$. The tighter the focus, the higher the laser intensity in the interaction region. In addition, the focus is inversely proportional to the initial beam diameter D. The telescope magnifies the beam diameter by a factor of two, reducing the beam waist by a factor of two inside the chamber. That increases the laser intensity by a factor of four. Expanding the beam further cannot be achieved without modifications to the vacuum chamber, as the window port on the source chamber limits the beam diameter.

7.3.3 Intensity

The laser power at the experiment is between $0 - 280$ W, and can be adjusted by rotating the HWP, as mentioned previously. Therefore, the laser intensity inside the

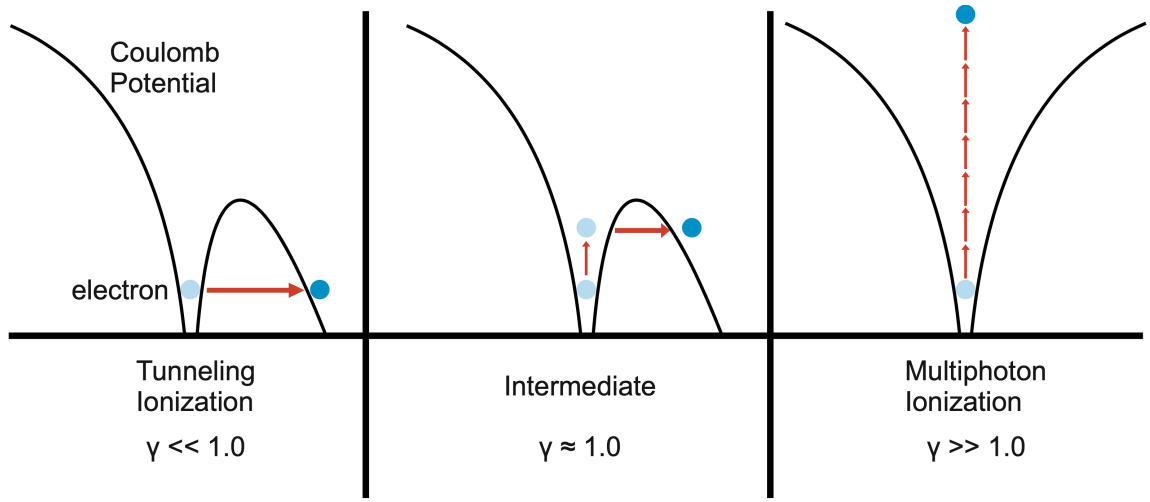

Fig. 7.7: Ionization mechanisms in the low intensity regime (left), intermediate regime (centre) and high intensity regime (right), as predicted by the Keldysh parameter γ.

chamber is between $0 - 5.59 \cdot 10^{15}$ W cm^{-2}, which is in the same order of magnitude as the intensities reported in the literature for one-colour CEI experiments.[298–302]

The ionization mechanism depends directly on the laser intensity. The two mechanisms at play are multiphoton absorption and strong-field ionization. Non-linear ionizations are commonly described by the Keldysh theory[303]. The Keldysh parameter is defined as follows,

$$\gamma = \sqrt{2mI_\mathrm{P}}\frac{\omega}{eE_0}, \tag{7.6}$$

where ω and E_0 are the frequency and amplitude of the electric field, m and e are the electron mass and charge, and I_P is the ionization potential. It defines two different ionization mechanism regimes, the multiphoton ionization regime ($\gamma >> 1$) and the tunnelling domain ($\gamma << 1$). Figure 7.7 illustrates the two regimes schematically. In the multiphoton ionization regime, ionization is achieved via the successive absorption of multiple photons, raising the energy above the ionization threshold of the system.[304] This regime dominates at low laser intensities. In the tunnelling regime, also known as the adiabatic regime, electrons tunnel through a

time-dependent barrier before being ejected from the molecule. This mechanism dominates at high laser intensities. In the intermediate regime, with $\gamma \approx 1$, both mechanisms are prevalent. For high laser powers, our laser intensities tend to be in the intermediate to tunnel ionization regime[305,306], where most molecules experience tunnel ionization, but multiphoton absorption cannot be excluded. Ultimately, the ionization mechanism is irrelevant to this work as long as we can access sufficiently high charge states.

7.4 Conclusion and Outlook

This Chapter describes the set-up and characterization of a Titanium:Sapphire femtosecond laser beamline for the VMI experiment. The beamline is designed to minimize pulse dispersion and maximize the laser intensity inside the interaction region. The laser intensities range from $0 - 5.59 \cdot 10^{15}$ Wcm^{-2} and are adjusted via rotation of the HWP in the beamline.

Access to the femtosecond laser greatly extends the types of experiments we can perform. In the future, the group is aiming to conduct systematic studies on CEI of a variety of molecules. Zhou *et al.*[283] defined low- and high-charge regimes in CEI. In the low-charge regime, electronic effects play a central role, making the dissociation mechanism complex and challenging to model. In the high-charge regime, the dissociation is governed by the geometry and charge distribution of the molecule. The subsequent ion trajectories are easier to model. However, it remains unclear where the quantitative boundaries between the two regimes for different molecules are. Furthermore, the high-charge regime is commonly used in femtosecond pump-probe studies to probe the nuclear geometry. However, to date there has been no systematic study into the extent to which quantitative informa-

tion can be obtained on the nuclear geometry. Establishing this is the second goal of the project.

Access to the femtosecond laser upgrades the spectrometer significantly in terms of the experiments that can be performed. As noted previously, another major limitation is that reliance on a molecular beam generation limits the types of molecules that can be investigated in the experiment. A pulsed valve is suitable for preparing gases and high vapour-pressure liquids in a supersonic expansion. However, non-volatile molecules such as solids are precluded. The next Chapter aims to extend our experimental capabilities in that regard and describes the design and characterization of a novel LID source.

8 Development and characterization of a laser-based thermal desorption source

This Chapter includes the design and characterization of a custom-built, fibre-coupled LID source. The work has previously been published in reference 75. Here, we reproduce the article in full (DOI: 10.1063/5.0170080), with the permission of AIP Publishing.

8.1 Introduction

Many gas-phase spectroscopic and chemical dynamics studies rely on the preparation of the molecule under study in a pulsed supersonic expansion. The molecule of interest is seeded into an inert gas, typically at a pressure of one to several bar, and expanded into vacuum through a small orifice. The resulting expansion is usually then passed through a skimmer, resulting in a narrow beam of molecules with a well-defined velocity and internal energy distribution. The flow of gas is usually controlled by means of a pulsed valve, and many designs for such valves have

been reported.[68–73,76,77,307] Despite the popularity of the molecular beam approach, preparation of molecules in a pulsed expansion is limited to species with a sufficiently high vapour pressure at room temperature, typically gases or high-vapour-pressure liquids. As detailed in Section 1.5.2 in Chapter 1, the LID technique is a soft thermal desorption technique capable of preparing non-volatile molecules in the gas phase. In the present work, we report the design and characterization of a fiber-coupled LID source designed specifically for use in VMI experiments.

8.2 Source requirements and design

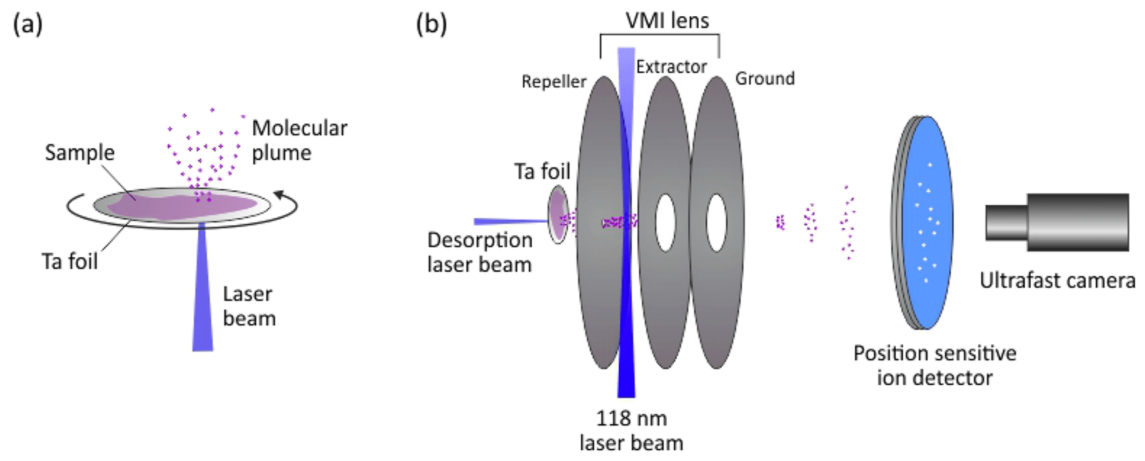

Fig. 8.1: (a) Operating principle of the LID source. Laser irradiation of the back of a thin metal foil coated in sample leads to desorption of a molecular plume. (b) Schematic of the VMI spectrometer for which the LID source was designed. See the text for explanation.

Figure 8.1 shows a schematic of the VMI instrument for which the source was designed.[246] Prior to design of the LID source, the experiment employed a pulsed supersonic molecular beam, which traveled along the axis of the instrument, entering the three-electrode velocity-mapping ion optics assembly through a small hole in the first ('repeller') plate. Between the repeller and extractor plates, the beam is intersected by one or more laser beams that initiate the chemistry of interest and ionize the products for detection if required. The electric field generated by the

velocity-mapping ion optics then accelerates the resulting ionized photofragments along a flight tube to a position-sensitive detector, where the position and arrival time are recorded for each ion in the form of an (x, y, t) data point. During this process, the three-dimensional scattering (velocity) distribution of the photofragments is projected onto the two-dimensional imaging plane of the detector. Integrating the resulting dataset over the spatial coordinates x and y yields the TOF distribution of the photofragments, which can be transformed into a mass spectrum in order to identify each fragment. Integrating the dataset over the arrival time period corresponding to an ion of interest yields a scattering distribution for that ion, which can be analyzed in order to gain insights into the detailed mechanism of the process that led to its formation.

The aim was to design a LID source that can be used in place of the pulsed molecular beam, in order to enable the study of non-volatile molecules in VMI experiments. We began by defining a number of key requirements as follows:

1. The source needed to desorb intact neutral molecules into the gas phase within a well-defined plume. The ability to localize the sample in space is a requirement for VMI experiments, which, as noted above, are more usually performed using a pulsed molecular beam.

2. The plume density needed to be comparable to the number density within a pulsed molecular beam, in order to give sufficient signal levels to perform VMI measurements on a reasonable experimental timescale.

3. The source needed to be sufficiently compact that it could be installed behind the repeller plate of the VMI ion optics assembly.

4. The desorption laser beam should be coupled into the vacuum chamber via an optical fiber, in order to enable facile and robust alignment with the foil

and to ensure that the plume remains localized behind the collimating hole in the repeller plate of the ion optics assembly.

5. We required the sample to have a long enough lifetime to perform a complete set of experiments without having to vent the vacuum system in order to renew the sample. This requires the ability to refresh the sample *in vacuuo*.

Satisfying the first two requirements requires that the sample heating is highly localized on the surface of the metal foil. This is achieved by using a thin foil of a metal with low thermal conductivity. When irradiated with a focused laser beam, the heat is transmitted primarily through the foil to the sample rather than being dispersed laterally across the foil, resulting in the desired highly localized heating. Suitable foil materials include stainless steel, tantalum, and titanium. In the present work, we chose to use a 12.5 µm thick tantalum foil (Goodfellow TA000300). Some simple thermal modeling of the source using the SimScale software package (`www.simscale.com`) indicated that the sample is likely to reach temperatures of around 450−500 K at the laser focus. The SimScale program uses the LID source tip geometry, sample identity and thickness, and laser power and focusing conditions to carry out a full heat transfer simulation.

The last three requirements are satisfied through a careful source design. Figure 8.2 shows a series of photographs of the source. The entire assembly is mounted on an xyz translator (not shown) in order that the LID plume can easily be aligned with the hole in the repeller plate of the VMI ion optics assembly. The assembly can also be retracted along the TOF axis in order to vary the distance between the tip of the LID source and the back face of the repeller plate.

The desorption laser is a 450 nm diode laser (Thorlabs L450P1600WW) with a tunable power up to 1285 mW. The laser output is collimated, focused by an aspheric

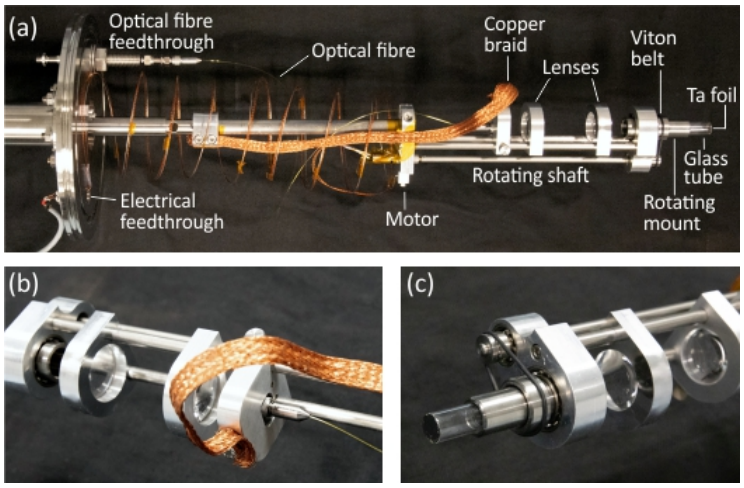

Fig. 8.2: (a) The LID source used in this work. See the text for a detailed description. (b) Close-up view of the optical fiber termination, showing the two lenses used to collimate and focus the beam onto the back of the tantalum foil. (c) Close-up view of the source tip, showing the tantalum foil, glass tube, and viton belt connecting the mount to the rotatable shaft in order to allow replenishment of the sample under vacuum.

lens (Thorlabs A280TM-A), and aligned into an SMA-connectorized fiber patch cable (Newport F-MBC-C-2SMA, 400 µm core diameter, numerical aperture 0.37). The laser light enters the vacuum chamber through a fiber feedthrough (Avantes FC-VFT-UVIR400, 400 µm core diameter, numerical aperture 0.22), where it is relayed to the LID source tip through a vacuum compatible optical fiber cable (Thorlabs MV41L1, 400 µm core diameter, numerical aperture 0.22). The fiber feedthrough is visible in Figure 8.2(a), and the fiber termination at the LID source tip is visible in Figure 8.2(a) and (b). A copper braid serves to transmit heat away from the fiber mount in order to prevent thermal damage to the end of the fiber. The laser light exiting the fiber is collimated by a bi-convex lens (BK-7, focal length 30 mm) and focused onto a ∼1 mm spot on the rear side of the tantalum foil by a plano–convex lens (BK-7, fl. = 50 mm). The maximum laser power achievable at the foil is 870 mW.

The foil comprises a 10 mm disk glued carefully onto the front end of a glass tube. The tube/foil assembly is easily demountable from the rest of the source to facilitate changing of samples. The glass tube inserts into a rotatable mount, which is

coupled by a viton rubber belt to a rotating shaft driven by a small vacuum compatible motor (Faulhaber Minimotor SA, Swiss Made 3115, 1810113). The point at which the foil is irradiated is purposely chosen to be away from the center of the foil, enabling replenishment of the sample simply by rotating the tip so that the laser irradiates a fresh region of the sample. We have fabricated a number of foil/tube source tips in order that samples can be queued. Changing to a new sample then simply requires removing the glass tube and replacing it with a new tip coated with the next sample to be studied.

8.3 Methods

8.3.1 Sample preparation

The three prototypical biomolecules uracil (Merck U0750, $\geq$99.0 %), adenine (Merck A8626, $\geq$99.0 %), and phenylalanine (Merck 147966, $\geq$99.0 %) were purchased from Merck and used without further purification. A number of methods were trialled for depositing samples on the surface, including recrystallization from solution, sedimentation, and spin coating. The performance of the source was found to be very similar for all methods tested, so one of the simplest sample preparation methods was adopted for the work described here. The solid sample was evenly spread on the foil and carefully pressed down with a spatula. A few drops of water (for uracil) or acetone (for adenine and phenylalanine) were added, which had the effect of evening out the layer of the sample. After evaporation of the solvent, the resulting sample layers were generally a few hundreds of microns thick, though thinner samples can also be prepared by the same method.

8.3.2 Time of flight mass spectrometry and velocity-map imaging measurements

The LID source was installed in our VMI spectrometer such that the foil was located a few millimeters behind the repeller plate of the VMI ion lens assembly. The ion lens comprises three 90 mm-diameter plates spaced 10 mm apart. The repeller (first) plate has a 2 mm hole in the center to admit the LID plume to the interaction region, and the extractor (second) and ground (third) plates have 24 mm apertures to transmit the expanding cloud of reaction products. In the experiments performed to characterize the performance of the LID source, the LID plume is intersected at right angles between the repeller and extractor plates by a focused (5−10 µm spot size) 118 nm (10.49 eV) laser beam, in order to ionize the molecules in the plume (the ionization potentials for uracil, adenine, and phenylalanine are 9.15, 8.20, and 8.65 eV, respectively[308]). The laser beam is the ninth harmonic of a Nd:YAG laser (Continuum Surelite II, repetition rate 10 Hz), generated by frequency tripling the 355 nm, ∼6.5 mJ third harmonic pulses in a phase-matched mixture of Xe and Ar gases.[171–174] The conversion efficiency from 355 to 118 nm light is not directly measurable in our experiments but has been found by other authors[309] to be around 10^{-5}, corresponding to a 118 nm pulse energy of around 65 nJ. The electric field within the ion optics can be tuned either to 'spatial mapping' or to 'velocity mapping' conditions, in which either the positions or the velocities, respectively, of the ions at their point of formation are mapped onto the detector.[5,6] In the present work, spatial mapping conditions were used for recording TOF spectra, in order to ensure that all ions had the same spatial distribution on the detector and were, therefore, detected with equal probability. Velocity mapping conditions were used to investigate the velocity distributions of the neutral molecules within the plume and of any fragments arising from dissociative ioniza-

tion by the 118 nm laser. After traversing a 61 cm flight tube, the ions are detected using a position-sensitive ion detector comprising two chevron-stacked MCPs (Photonis, 31849) coupled to a P47 phosphor screen. The resulting light emission from the phosphor is captured using a second-generation PImMS camera, which records an (x, y, t) data point for each incident ion.

Datasets were recorded with (signal) and without (background) irradiation of the foil by the desorption laser. Within each dataset, the ion hits were centroided in order to remove spatial and temporal blurring associated with the time and positional resolution of the P47 phosphor, and background subtraction was performed. As noted earlier, the resulting dataset can be integrated over x and y to yield the TOF mass spectrum or over an appropriate range of times in order to obtain velocity-map images for ions of interest.

8.4 Results and discussion

8.4.1 Time-of-flight spectra and velocity-map images for uracil, adenine, and phenylalanine

Figure 8.3 shows the TOF spectra recorded for the 118 nm photoionization products of the two nucleotide bases uracil and adenine and the amino acid phenylalanine, prepared with the LID source with desorption laser powers of 590 mW (uracil) and 458 mW (adenine and phenylalanine), respectively. We note that uracil has been prepared previously via LID by other authors.[102,106]

Our experimental setup is optimized for velocity-map imaging and has a rather low mass resolution of $m/\Delta m \approx 100$. At present, this is limited primarily by the

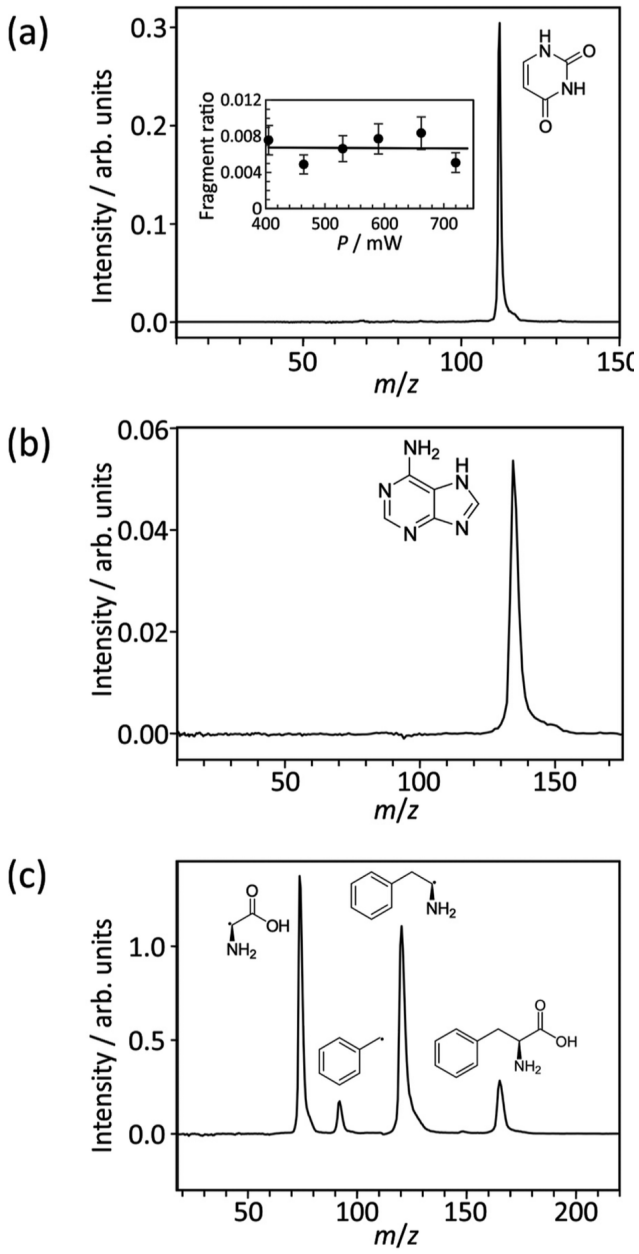

Fig. 8.3: TOF spectra of the 118 nm photoionization products of (a) uracil, (b) adenine, and (c) phenylalanine prepared with the LID source. The desorption laser power was 590 mW for the measurements on uracil and 458 mW for the measurements on adenine and phenylalanine. The inset of (a) shows that the small fraction of daughter ions detected at m/z 69 for uracil has no dependence on desorption laser power within our measurement uncertainty.

∼80 ns decay lifetime of the phosphor screen that forms part of the ion detector (which also leads to the appearance of a small shoulder on the high-mass side of some of the mass peaks) and the time resolution of the PImMS camera that records the ion signals. Planned upgrades in the form of a fast phosphor and increased

camera time resolution will improve on this substantially for future work, but our current mass resolution is more than sufficient for the purposes of the present demonstration.

The spectra for uracil and adenine are both dominated by the parent ion peaks, appearing at m/z 112 and 135, respectively. The uracil mass spectrum has a second very small peak at m/z 69, corresponding to the $C_3H_3NO^+$ fragment, which constitutes around 1 % of the overall signal. As shown in the inset of Figure 8.3(a), the relative intensities of the fragment and parent ion peaks remain constant within our measurement uncertainty as the desorption laser power, and therefore, the temperature at the LID source tip is increased. This indicates that the fragment is not the result of thermal decomposition of neutral uracil but rather a product of a small amount of dissociative ionization. This is consistent with the established ionization potential of 9.15 eV for uracil and the appearance potential of 10.95 eV for the $C_3H_3NO^+$ fragment,[310] which lies significantly above the 10.49 eV available from our ionizing laser. Even at the estimated desorption temperatures of 450−500 K, the internal energy of the desorbed molecules is expected to be less than 0.1 eV, so the observed fragmentation pathway is only likely to be accessible to a very small fraction of molecules in the plume that absorb more than one photon from the 118 nm laser pulse. We, therefore, conclude that we prepare intact uracil molecules in the laser-induced desorption process. The adenine mass spectrum shows only a single peak. Again, this is consistent with the ionization energy of 8.20 eV and relatively high appearance energies for any fragment ions; the lowest appearance energy is 11.56 eV for the $C_4H_4N_4^+$ ion.[310] We can again conclude that only intact neutral molecules are produced from the LID source.

In contrast to uracil and adenine, the mass spectrum for phenylalanine comprises a number of peaks in addition to the m/z 165 parent ion peak. The signals at m/z 120,

91, and 74 correspond to $C_7H_7CHNH_2^+$, $C_7H_7^+$, and $HC_2NH_2OOH^+$, respectively. The appearance energies for these fragments are 8.65 ± 0.02 eV, 9.31 ± 0.02 eV, and 8.95 ± 0.02 eV respectively.[311] These are all significantly lower than the 10.49 eV photon energy of the 118 nm laser, immediately making dissociative ionization the most likely explanation for their formation. Further evidence for this explanation is provided by the fact that the relative abundances of the various fragment ions are in good agreement with those reported by Gaie-Levrel *et al.*[311] in a photoionization study employing VUV synchrotron radiation at energies similar to ours. However, we should not immediately discount the possibility that neutral fragments are formed by the LID source via thermal decomposition and subsequently ionized by the 118 nm laser beam. We can investigate this further by inspecting the velocity-map images recorded for the parent and daughter ions. Any species emitted by the LID source must pass through the 2 mm hole in the repeller plate of the ion optics assembly in order to enter the interaction region. This places an upper limit on their transverse velocity component, determined both by the size of the hole and by the distance between the tantalum foil and the back face of the repeller plate. The resulting images will comprise a small spot in the center of the detector. In contrast, fragments formed via the dissociation of the parent ion following ionization will have a significant non-zero recoil velocity as a result of the dissociation process.

Figure 8.4 shows the velocity-map images recorded for the phenylalanine parent ion and the three fragment ions. The parent ion appears as a small spot, with a maximum radial velocity determined by the 2 mm hole in the repeller plate through which the neutral phenylalanine enters the interaction region. The three daughter ions all have considerably broader velocity distributions, which reduce in width as the fragment mass increases, indicating that they are formed within the interaction region via dissociative ionization rather than being emitted as neutrals from the

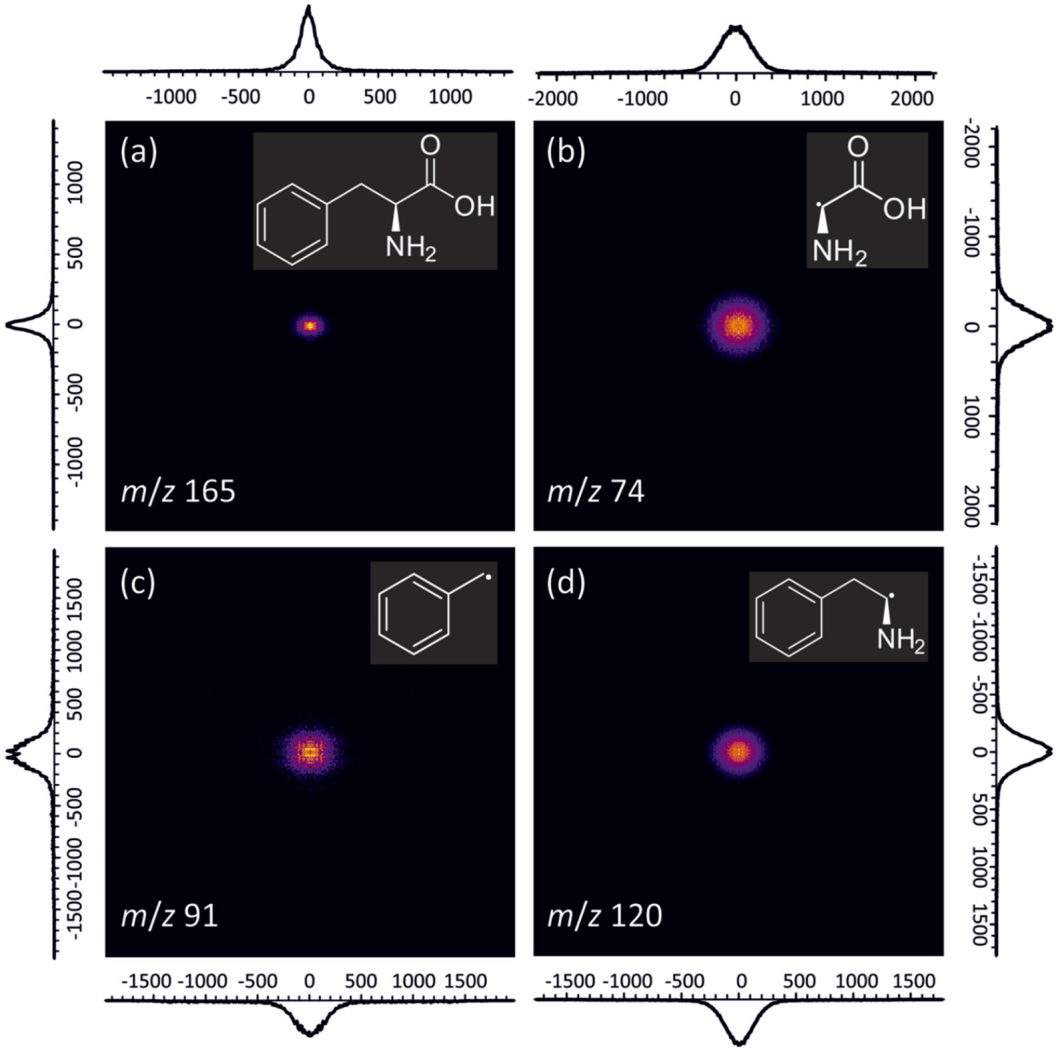

Fig. 8.4: Velocity-map images recorded for (a) the phenylalanine parent ion and the three fragment ions: (b) $HC_2NH_2OOH^+$ (m/z 74), (c) $C_7H_7^+$ (m/z 91), and (d) $C_7H_7CHNH_2^+$ (m/z 120). Projections onto each axis (labeled in units of m s^{-1}) are also shown.

LID source. We can, therefore, conclude that for all three samples tested, the LID source generates an intense plume of intact neutral parent molecules.

The velocity-map images shown in Figure 8.4 demonstrate that we have achieved our goal of designing a LID source compatible with the VMI technique. We note that the signal intensity, measured in terms of the total number of ion hits per experimental cycle, is comparable with that obtained in similar measurements employing a pulsed molecular beam (we provide a quantitative comparison at the end of Section 8.4.2). A key requirement for VMI is that the ions to be imaged are

formed within a relatively small region of space between the repeller and extractor plates of the VMI ion lens, known as the interaction region. Once the interaction region exceeds the dimensions of a few millimeters, the ability of the velocity-mapping electric field to correct for the spatial origins of the ions begins to break down, leading to blurring of the velocity-map images. In the present experiment, the size of the interaction region is determined by the (fixed) laser focus and by the dimensions of the LID plume entering the ion lens. As explained above, the latter is determined by the cone of acceptance defined by the 2 mm hole in the repeller plate through which the plume passes and by the distance between the LID foil and the back face of the repeller plate. The effect of changing this distance is shown in Figure 8.5. At foil–repeller distances of 5 and 10 mm, the interaction region is small enough (2.71 and 2.42 mm in diameter, respectively) to give good velocity mapping, while at a distance of 2 mm, the interaction region increases to around 3.25 mm in diameter, which appears to be large enough to lead to some blurring of the image. The foil–repeller distance also determines the maximum transverse velocity component of the molecules entering the interaction region. From the image projections onto the x and y axes, we estimate these to vary from around 40 m s^{-1} at a foil–repeller distance of 2 mm to around 15 m s^{-1} at a distance of 10 mm.

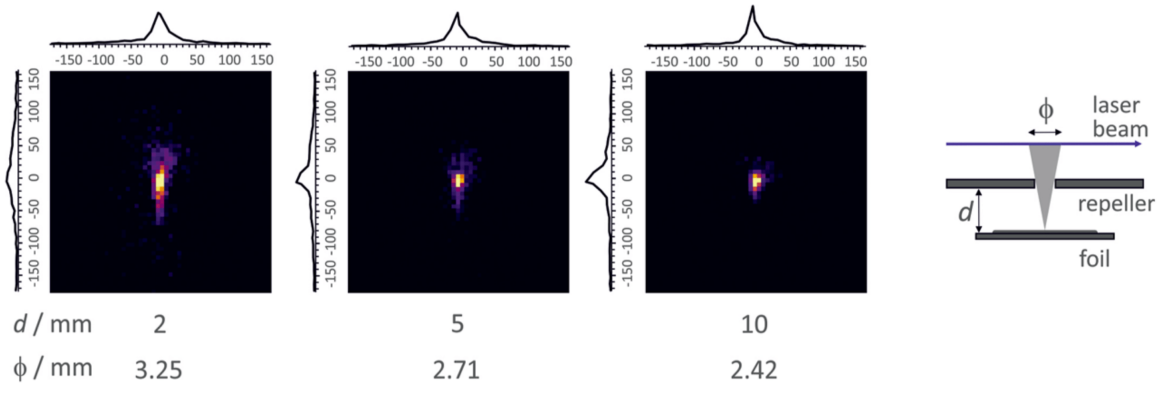

Fig. 8.5: Velocity-map images recorded for uracil parent ions with foil–repeller distances of 2, 5, and 10 mm (note: only the central 34×34 pixel^2 region is shown in each case). Projections onto each axis (labeled in units of m s^{-1}) are also shown. Plume diameters in the interaction region are given for each foil–repeller distance based on the cone of acceptance of the 2 mm hole in the repeller plate of the ion optics assembly.

We note that while increasing the foil–repeller distance reduces the plume diameter within the interaction region, significantly improving the velocity-mapping performance, it has little effect on the molecular density in the interaction region. Most of the signal arises from the position of the laser focus, which is much smaller than the plume diameter, and as a result, the total signal intensities are similar for the various foil–repeller distances investigated, varying by less than 20 %.

8.4.2 Dependence of signals on desorption laser power

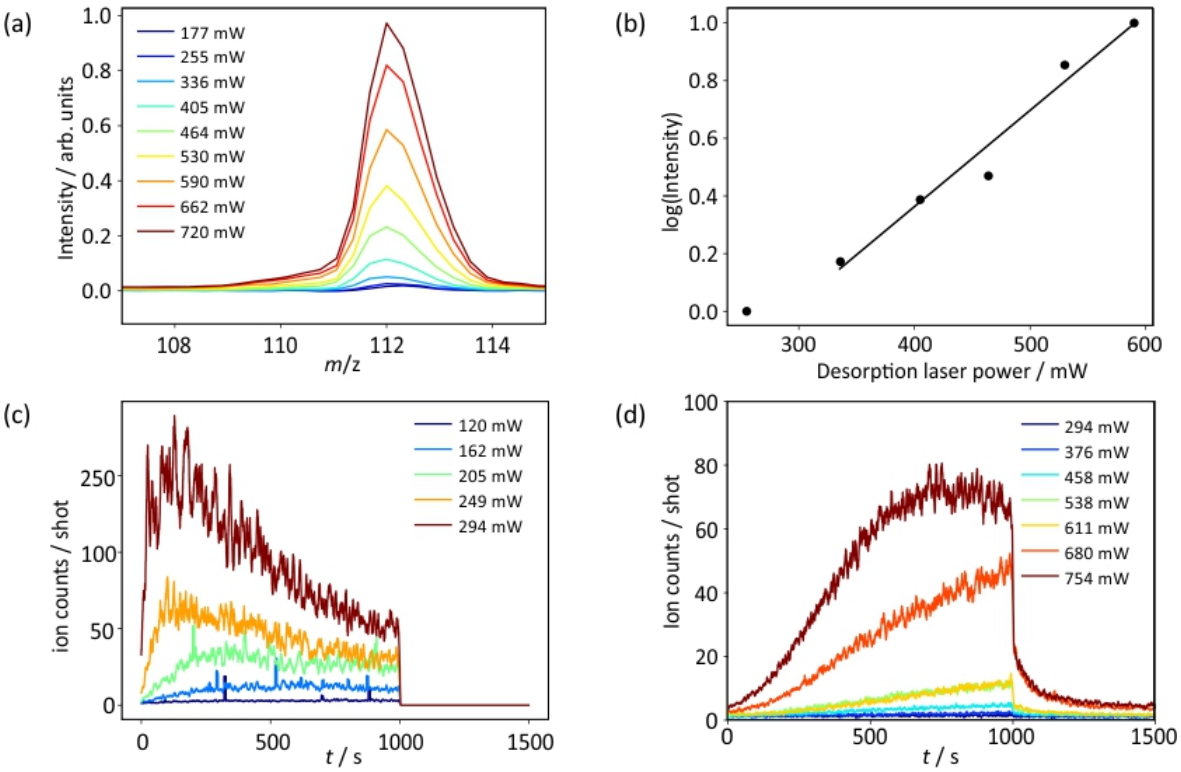

Fig. 8.6: (a) Uracil parent ion TOF signal as a function of desorption laser power. (b) Log plot of the total uracil signal as a function of desorption laser power. Total uracil signal as a function of time after switching on the desorption laser for (c) a 'thin' (tens of microns thickness) sample and (d) a 'thick' (hundreds of microns thickness) sample. The data shown in (c) and (d) have been smoothed using a 71- and 51-point moving average, respectively.

The temperature reached by the tantalum foil, and, therefore, the rate of desorption of sample molecules, depends strongly on the desorption laser power. The power incident on the foil from the 450 nm diode laser used in the LID source is tunable

over the range from 0 to 870 mW. However, in general, we use only the range below ~500 mW, since higher powers result in complete and uncontrolled desorption of large areas of the sample. Figure 8.6(a) shows the uracil parent ion TOF signal recorded at laser powers in the range from 177 to 720 mW. We see that the signal intensity is highly tunable through the appropriate choice of laser power. Since desorption is a thermally activated process, we expect the peak intensity to follow an Arrhenius-type temperature dependence. Assuming a linear proportionality between the energy input into the sample from the laser beam and the thermal energy RT, we, therefore, expect a log plot of the uracil signal against laser power to be linear.[110] This is, indeed, found to be the case, and the relevant plot is shown in Figure 8.6(b).

The final property of the LID source that requires characterization is the time dependence of the molecular emission after turning the desorption laser on or off. This is shown for various different laser powers in Figure 8.6(c) and (d). Figure 8.6(c) shows the total signal recorded as a function of time for a 'thin' sample of uracil, with a thickness on the order of tens of microns, while Figure 8.6(d) shows the equivalent signal recorded for a 'thick' sample, with a thickness of hundreds of microns. In both cases, the desorption laser was turned on at $t = 0$ s and turned off at $t = 1000$ s, and a single spot on the foil was irradiated, i.e. the tip of the source was not rotated. The time-dependent signals are seen to depend strongly on both the desorption laser power and the sample thickness. We note that the signal-to-noise ratio achievable in these experiments is determined primarily by the shot-to-shot stability of the 118 nm laser used to ionize the desorbed molecules rather than by variations in the emission from the LID source.

The signals recorded for the thin sample exhibit a short rise time, with hundreds of ion counts being obtained per TOF cycle within a few seconds of turning on the

desorption laser. Heat transfer to the front of the thin sample is fast, and once a sufficiently high temperature is reached, sublimation occurs rapidly. On continued heating, the signals plateau and then decrease as the sample is depleted. As the desorption laser power is decreased, the rate of desorption is reduced. In addition to yielding lower signals overall, this results in a slower rise time of the signal and a less marked decrease at longer times. In all cases, once the desorption laser is turned off, the signal drops rapidly to zero, indicating rapid cooling of the foil.

The signals recorded for the thick sample exhibit much longer rise times, reflecting the slower transfer of heat through the foil and sample to the top layer of sample molecules. At most of the laser powers investigated, the plateau region of the signal has not yet been reached within the 1000 s time window of the measurement. However, the plateau and a subsequent decrease in signal are apparent for the highest laser power of 754 mW. Again, the signal drops rapidly as soon as the desorption laser is turned off, though a 'tail' in the signal persists for some time after this, implying that cooling of the sample surface is slower for the thick sample than for the thin one.

We note that the detailed shapes of the time-dependent signal curves also strongly depend on the thermal properties of the sample. For some of the samples we have investigated (not included in this article), the plateau region had not been reached even after several hours of irradiation. We recommend that the time-dependent emission is characterized for each new sample as part of the general experimental setup in order that appropriate choices can be made in relation to optimum laser power, sample thickness, and sample irradiation time or frequency/speed of tip rotation. Among the samples we have explored to date, we have found that for some samples, the tip may not need to be rotated at all, and the samples can last for weeks, while for others, the tip should be rotated by a small angle in between

data acquisition runs, and the samples must be refreshed daily. We have not yet encountered a sample sufficiently volatile to require a rotation of the tip during an individual data acquisition run, but such a rotation would need to be performed very slowly in order to ensure that thermal equilibrium is maintained within the irradiated region of the sample.

Finally, we have used the dataset shown in Figure 8.6(d) to perform a quantitative comparison between the signal levels obtained using the LID source and a molecular beam. In the region between 700 and 800 s, the average number of ion counts per experimental cycle (reported with one-standard-deviation uncertainties) ranges from 1.5 ± 1.3 at the lowest desorption laser power of 294 mW to 72 ± 18 at the highest desorption laser power of 754 mW. For comparison, in a similar experiment using a pulsed molecular beam of TOF seeded in helium at a total pressure of $\sim$1 bar, the average number of ion counts per cycle was 79 ± 14, very close to that obtained with the LID source operating at the highest desorption laser powers. The very similar measurement uncertainties in the two cases reflect the fact that the uncertainty is dominated by the shot-to-shot variation in the 118 nm laser pulse used to ionize the molecules (which was the same in both sets of experiments) rather than by the stability of the molecular beam pulses or LID plume intensity. We note that the molecular density is tunable in both cases: when using a molecular beam source, the beam density can be tuned via the gas pressure inside the pulsed valve and/or the amplitude of the current pulse used to open the valve, while for the LID source, the plume density is tunable by varying the desorption laser power.

8.5 Conclusion

Robust and easy-to-use methods for preparing non-volatile molecules in the gas phase are required in order to fulfill the desire to study the spectroscopy and dynamics of increasingly large molecular systems in the gas phase. We believe that LID is a very good candidate method for many of these studies, and we have described the design and optimization of a novel optical-fiber-coupled LID source for use in VMI and other gas-phase experiments. Within the source, the samples are deposited on a thin metal foil and released into the gas phase following irradiation of the back of the foil by a CW diode laser beam. We have demonstrated the performance of the source for three prototypical biomolecules – uracil, adenine, and phenylalanine – showing that all three molecules are released intact into the gas phase in number densities that can be controlled simply by adjusting the desorption laser power. Signal levels observed in VMI experiments are comparable with those achieved using a pulsed supersonic expansion. We believe that the new source offers an appealing option for a wide variety of gas-phase measurements on non-volatile chemical species. The next Chapter utilizes the LID source to investigate the decay pathways of PAHs following ionization with a femtosecond laser beam.

Statement of Authorship for joint/multi-authored papers for PGR thesis

To appear at the end of each thesis chapter submitted as an article/paper

The statement shall describe the candidate's and co-authors' independent research contributions in the thesis publications. For each publication there should exist a complete statement that is to be filled out and signed by the candidate and supervisor **(only required where there isn't already a statement of contribution within the paper itself).**

Title of Paper	Design and characterization of an optical-fiber-coupled laser-induced desorption source for gas-phase dynamics experiments
Publication Status	✗Published □ Accepted for Publication □Submitted for Publication □Unpublished and unsubmitted work written in a manuscript style
Publication Details	D. Milesevic, D. Popat, P. Gellersen, Z. Liu, J. Stimson, P. Robertson, A. Green, C. Vallance, "Design and characterization of an optical-fiber-coupled laser-induced desorption source for gas-phase dynamics experiments", *Rev. Sci. Instrum.* **2023**, 94, 114105.

Student Confirmation

Student Name:	Dennis Milesevic		
Contribution to the Paper	Data curation (equal); Formal analysis (equal); Investigation (equal); Methodology (equal); Software (equal); Writing – original draft (lead)		
Signature	D. Milešević	Date	22 November 2023

Supervisor Confirmation

By signing the Statement of Authorship, you are certifying that the candidate made a substantial contribution to the publication, and that the description described above is accurate.

Supervisor name and title:	Prof. Claire Vallance		
Supervisor comments	I confirm that Dennis has done a large portion of the work on this project, as described above.		
Signature	C. Vallance	Date	24 November 2023

This completed form should be included in the thesis, at the end of the relevant chapter.

9 Dissociative ionization of polycyclic aromatic hydrocarbons

9.1 Introduction

PAHs are a class of aromatic, highly conjugated hydrocarbons which play an important role on Earth and in space, as detailed in Section 1.6 of Chapter 1. A key question in the scientific community centres around how PAHs are formed in outer space, as their sizes and abundances indicate the existence of highly efficient formation processes. The growth mechanism can be divided into two parts: benzene formation; and the subsequent growth to larger aromatic systems. The initial benzene ring may be formed in various ways, following the combination of at least two smaller reactants.[168,312–315] While the ensuing growth mechanism depends on the environmental conditions and carbon source, the HACA mechanism is one of the main mechanisms believed to be responsible for the formation of larger PAHs.[170]

Figure 9.1 illustrates the two recurring elementary steps of the HACA[168,169] growth mechanism. In the first step, a hydrogen atom is removed from the molecule, leading to the formation of a radical. In the second step, this radical combines with an acetylene molecule. The stepwise addition of acetylene units involves low energy

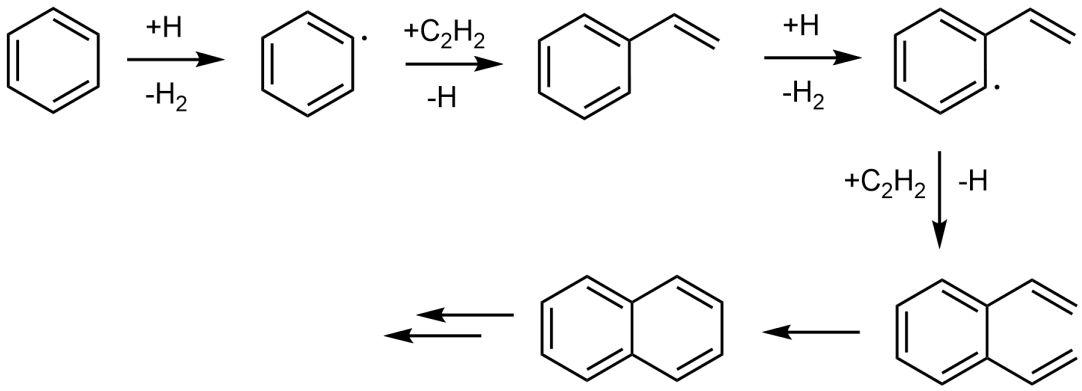

Fig. 9.1: Schematic HACA mechanism for the formation of naphthalene from benzene.

barriers[316] and is exothermic[317], which is important for multiple reasons. Firstly, lower energy barriers have higher reaction rates. Secondly, the temperature in interstellar space is very low (tens of Kelvin), so the barrier height for acetylene addition needs to be near zero for the reaction to occur at a significant rate. Since the forward reaction is endothermic, the reverse reaction is exothermic, encouraging the addition of multiple acetylene units rather than fragmentation back to the reactants at each step. In space, the mean free path of the molecules and therefore the time between collisions is relatively long. Thus, the intermediates need to be sufficiently low in energy to be stable and not undergo the reverse reaction by ejecting acetylene. Kislov[317] *et al.* report exothermicities of $120 - 160$ kJ mol^{-1} for non-aromatic products and $125 - 200$ kJ mol^{-1} for aromatic products for acetylene addition. Once the PAHs are formed, they are robust towards photo-induced or electron-induced dissociation. Multiple studies report ultrafast relaxation processes on the order of tens of femtoseconds back to the ground state following electronic excitation[78] or formation of the monocation[78,318] or dication[78], which are facilitated by conical intersections, as the Born-Oppenheimer approximation breaks down.[319,320] This protection mechanism is one reason for the high abundance of PAHs on Earth and in interstellar space.

In a study conducted at FLASH, Lee *et al.*[78] investigated the fragmentation path-

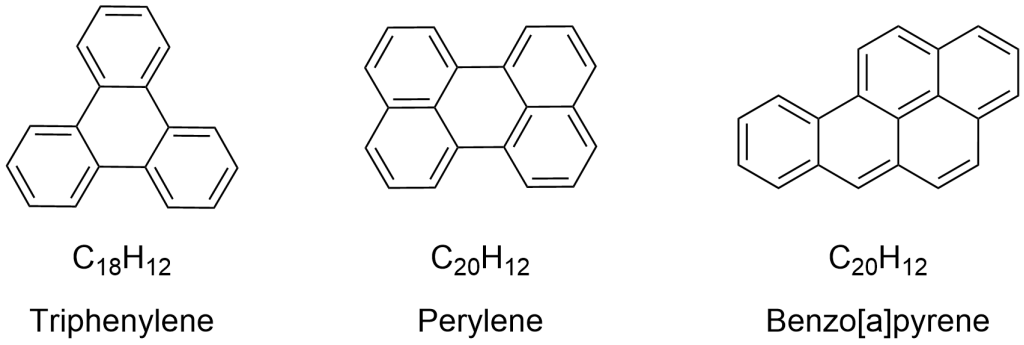

Fig. 9.2: Structures of the PAHs studied in this Chapter.

ways of multiply charged small PAHs (fluorene, phenanthrene, and pyrene) produced via x-ray core ionization. In addition to dissociation into two or more singly charged fragment ions, the authors were able to infer the ejection of one or more neutral C_2H_2 acetylene units, which can occur before or after the initial charge separation. Thus, the fragmentation follows a 'reverse HACA' pattern, in which C_2H_2 units are ejected from rather than added to the molecule. Based on these results, open questions include whether this fragmentation pathway is also observed in heavier PAHs and whether it depends on the ionization mechanism. In this Chapter, we aim to answer these two questions by conducting experiments into the photodissociation of triphenylene ($C_{18}H_{12}$), perylene ($C_{20}H_{12}$), and benzo[a]pyrene ($C_{20}H_{12}$). Figure 9.2 shows the molecular structure of the systems. The experiments combine novel experimental techniques described in Chapters 7 and 8.

9.2 Methods

The TOF-VMI mass spectrometer used in this work has been described in detail in Chapter 2 and elsewhere[246]. The three molecules studied are triphenylene (Merck, T82600, 98 %), perylene (Merck, P11204, $\geq$99 %), and benzo[a]pyrene (Merck, B1760, $\geq$96 %). The experimental methods are identical for the three sys-

tems. The sample was introduced into the experiment via the LID source described in Chapter 8. The solid sample was spread evenly onto the 12.5 µm thick tantalum foil (Goodfellow TA000300) and carefully pressed down with a spatula. Afterwards, a few drops of acetone were added, which evened out the sample layer and helped it bind to the metal substrate. After evaporation of the acetone, the sample layer is tens to hundreds of microns thick. The diode laser powers used to irradiate the foil were 205 mW for triphenylene and perylene and 120 mW for benzo[a]pyrene.

The distance from the foil to the repeller plate was ∼10 mm. The ion lens comprised the '3-stack' shown in Figure 2.8 in Chapter 2, which consists of a 2 mm thick, equally spaced repeller, extractor, and ground plate. The 2 mm hole in the repeller plate admits the molecular plume to the interaction region, where it is intersected by the 800 nm femtosecond laser beam (37 fs, 60 nm bandwidth, 200 Hz repetition rate) described in Chapter 7. The resulting ions are accelerated towards the detector by the electric field maintained within the VMI ion lens, which crushes the 3D scattering distribution of each fragment ion onto the 2D detector. The detector comprises a pair of chevron-stacked MCPs (Photonis, 31849) with an active diameter of 40 mm and an open area ratio of 55 %), and a P47 phosphor scintillator. The light emitted from the phosphor each time an ion is incident on the MCPs is captured by a second-generation PImMS camera. The camera records an (x, y, t) data point for each incident ion, where x, y is the position of the detector, and t is the product time-of-flight. The MCPs and camera run at an acquisition rate of 20 Hz, which is synchronised with the fs laser pulses. We recorded TOF spectra at various femtosecond laser powers between $0-50$ mW ($0-4\times10^{15}$ W cm^{-2}) in order to observe which fragment ions are formed at different laser intensities. For this measurement, we also recorded the background by measuring the TOF spectrum without irradiating the sample but under otherwise identical conditions. In a second set of

experiments, we recorded velocity-map images for the product ions formed at two selected laser powers of 5.5 mW (5×10^{14} W cm^{-2}) and 9.2 mW (9×10^{14} W cm^{-2}) for each sample. The data obtained in both sets of experiments were run through a centroiding algorithm. We smoothed the velocity-map images of each product ion by applying a Gaussian filter with a standard deviation of five pixels along the x and y axes. The velocity-map images were inverted using the rBasex method from the PyAbel package in order to obtain the central slice of the three-dimensional scattering distribution. From the inverted images, we extracted the radial and angular distributions before converting the radial distributions into kinetic energy distributions using a radius-to-energy calibration determined through SIMION ion trajectory simulations of the experiment.

To disentangle the complex dissociation pathways of multiply charged parent ions, we use partial covariance (see Section 3.4.3 in Chapter 3), with the total signal intensity in each acquisition cycle employed as our measure of experimental fluctuations. Recoil-frame covariances images were generated for each plausible ion pair, i.e. each pair whose atom sum does not exceed the maximum number of atoms in the parent molecule. From the recoil-frame covariance images, the momentum distribution of the signal ion was extracted, which in turn can be used to determine the kinetic energy release associated with a particular ion pair. The momentum distributions were obtained from the recoil-frame covariance images by discarding the forwards-scattered image half (which does not contain signal) and integrating the remaining half over the angular coordinate to obtain the radial distribution, which is converted into momentum space using the SIMION ion calibration mentioned above.

9.3 Triphenylene

9.3.1 Time-of-flight spectra

Since the mass resolution is insufficient to fully resolve the number of hydrogen atoms on each fragment ion, we focus on the carbon framework and integrate the signal from fragment ions with the same number of carbon atoms but different numbers of hydrogen atoms, e.g. C_2^+, C_2H^+, $C_2H_2^+$, $C_2H_3^+$ etc. will be treated as one signal with the label $C_2H_x^+$ (or C_2^+). The loss of a neutral hydrogen atom is unlikely to significantly affect the velocity distribution (and therefore the velocity-map image) of the much heavier co-fragment ion. Furthermore, this treatment reduces data complexity significantly for this first study and improves the signal-to-noise ratio.

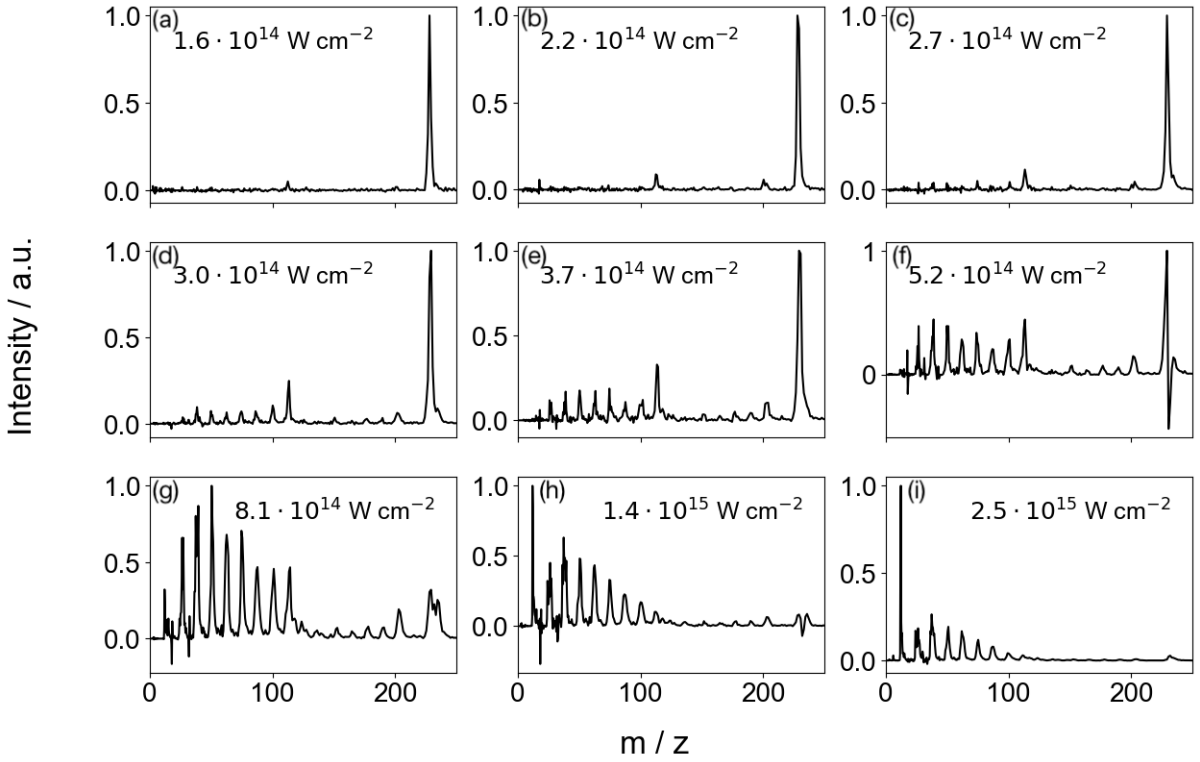

Fig. 9.3: Background-subtracted TOF spectra of triphenylene following the irradiation with the 800 nm femtosecond laser beam at different laser beam intensity. The laser beam intensities used are indicated in each plot.

Figure 9.3 shows the TOF spectra of the product ions formed from triphenylene following ionization with the 800 nm femtosecond laser beam, with data shown for nine different laser beam intensities. At a femtosecond laser beam intensity of 1.6×10^{14} W cm^{-2} (panel a), we observe the parent ion C_{18}^{+} and dication C_{18}^{2+} and the fragment ion C_{16}^{+}. The great majority of ions observed in panel (a) are parent ions, indicating that the LID source generates intact triphenylene. Hence, all observed fragment ions are assumed to result from dissociative photoionization of intact parent molecules within the LID plume. The C_{18}^{+} peak intensity is an order of magnitude larger than the C_{18}^{2+} peak intensity. The $C_{16}H^{+}$ ion is formed in the following reaction,

$$C_{18}H_x^{+} \longrightarrow C_{16}H_y^{+} + C_2H_2 \tag{9.1}$$

with a very low peak intensity, indicating that reaction 9.1 is inefficient. Previously, the loss of neutral acetylene, C_2H_2, was observed from fluorene monocations[321] and other small PAH monocations[322]. West *et al.*[322] postulated a common pathway for C_2H_2 loss, which involves the formation of an azulene-containing intermediate followed by contraction of the seven-membered ring and subsequent acetylene loss. A schematic illustration of this mechanism is shown in Figure 9.17 for C_2H_2 loss from benzo[a]pyrene ions. However, the additional benzene ring in triphenylene compared with phenanthrene probably prevents the formation of the five-membered ring to form a stable azulene-containing intermediate, since in the central benzene ring, all carbon atoms are bridging atoms. Therefore, C_2H_2 loss might occur from C_{18}^{+} via an alternative mechanism that is less efficient.

As the laser intensity increases, additional fragment ion peaks appear. At an intensity of 3.0×10^{14} W cm^{-2} (panel d), we observe fragment ions with carbon atom numbers between two and 16, i.e. C_2^{+}, C_3^{+}, ... , C_{16}^{+}. The fragment ions C_1^{+} and

C_{17}^+ are not observed at this laser beam intensity. Previously, ejection of CH_2 has been observed from 9,10-dihydrophenanthrene and 9,10-dihydroanthracene, following isomerization of the central benzene ring to a five-membered species.[323] As discussed previously, this isomerization is prohibited in triphenylene due to the additional benzene ring. Hence, the loss of a methyl unit is not observed. The relative intensity of the lighter fragment ions (< ten carbon atoms) is significantly higher than the intensity of heavier fragment ions ($\geq$ ten carbon atoms).

As the laser intensity is further increased, the relative peak intensities shift from high to low m/z ratios. For example, at an intensity of 8.1×10^{14} W cm^{-2} (panel g), C_4^+ is the most abundant ion. The parent ion peak has dropped in intensity since the laser tends to form more highly-excited monocations, which are more prone to fragmentation, or the laser removes multiple valence electrons from the molecule, leaving it in a highly charged, unbound state. At even higher intensities, predominantly C^+ ions are formed. In Section 9.3.2 we report results from a VMI study carried out at a femtosecond laser beam intensity of 5×10^{14} W cm^{-2} in order to probe the dissociation dynamics further.

9.3.2 Velocity-map images

Figure 9.4 shows the Abel-inverted velocity-map images and corresponding KER distributions for each fragment ion. The velocity-map images reveal a low-kinetic-energy-release signal close to the image centre and a high-kinetic-energy-release signal further away from the centre. These two contributions to the signal are most visible for the C_2^+, C_3^+, and C_4^+ fragment ions, but are also present in the images and associated KER distributions for many other fragment ions. The low kinetic energy signals stem from the dissociation of singly charged triphenylene ions, $C_{18}H_{12}^+$, while the signal at higher kinetic energies results from the fragmentation of doubly

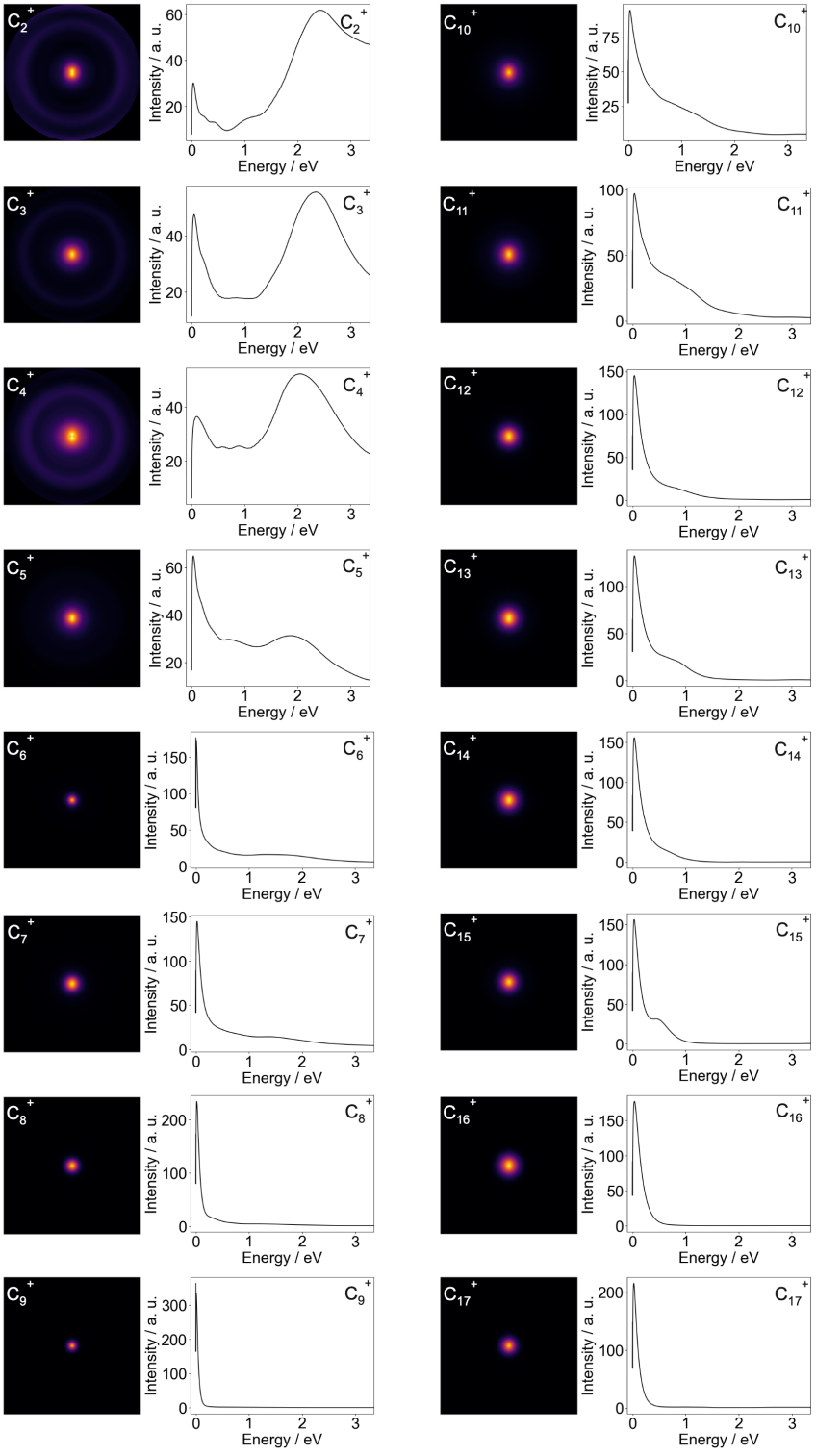

Fig. 9.4: Pairs of inverted velocity-map images and their kinetic energy release distribution for each fragment ion following the irradiation of triphenylene with the 800 nm femtosecond laser beam with an intensity of 5×10^{14} W cm^{-2}. The labels refer to the number of carbon atoms on the fragment ion and the charge of each fragment ion is assumed to be one, e.g. the label C_3^+ is short for the frgament ion $C_3H_x^+$.

charged triphenylene ions, $C_{18}H_{12}^{2+}$. Fragment ions stemming from doubly charged parent ions are born with higher kinetic energies due to the Coulombic repulsion between the two positive charges, which does not exist in singly charged parent ions. The difference in kinetic energy is higher in fragment ions with low m/z values because they carry away more kinetic energy from the dissociation than their heavier co-fragments.

The C_{18}^{+} parent ion appears to be quite stable and does not dissociate readily, as indicated by the high parent ion peak in panels (a-f) in Figure 9.3. Thus, dissociation of the parent ion is expected to occur over relatively long timescales. Most fragment ions stemming from the dissociation of the C_{18}^{+} monocation have kinetic energy releases close to zero. This is indeed consistent with a statistical dissociation occurring over relatively long timescales, in which the great majority of the available energy is distributed into the vibrational and rotational degrees of freedom of the product ions rather than into kinetic energy of the nascent fragments.

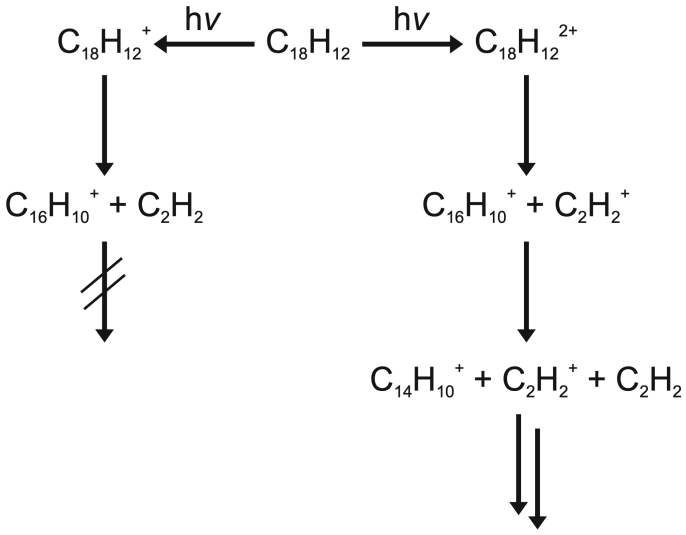

Fig. 9.5: Reaction scheme illustrating possible acetylene (C_2H_2) loss pathways following the single or double ionization of triphenylene via irradiation with the 800 nm femtosecond laser beam.

Through inspection of the relative intensities of the two components of the kinetic energy release distributions, we see that the contribution to the signal from disso-

ciation of singly and doubly charged parent ions varies for the different fragment ions. The fragment ions C_5^+, C_4^+, C_3^+, and C_2^+ have decreasing signal contributions from dissociation of singly charged parent ions and increasing contributions from doubly charged parent ions as the number of carbon atoms decreases. For fragments with six or more carbon atoms, the signal contribution from dissociation of singly charged parent ions is higher than from doubly charged parent ions. Figure 9.5 schematically illustrates the two main reasons for this observation in the example of acetylene (C_2H_2) loss from the parent ion. Firstly, the formation of light fragment ions in the primary dissociation step is more likely to occur from C_{18}^{2+} than from C_{18}^+. The dissociation of singly charged triphenylene yields a fragment ion and neutral co-fragment, with the charge residing on the heavier fragment ion in most cases. In contrast, during the dissociation of doubly charged triphenylene, both fragments are produced as ions. Hence, we are more likely to observe lighter fragment ions from the dissociation of doubly charged parent ions. Secondly, heavier daughter ions can undergo secondary dissociations to form lighter fragment ions, which is more likely to occur in fragment ions produced from doubly charged triphenylene. In our example, the C_{16}^+ fragment ions produced from C_{18}^{2+} probably have a higher internal energy than the C_{16}^+ fragment ions produced from C_{18}^+, since the dication surface very likely crosses onto the C_{16}^+ + co-fragment surface at higher internal energies than the monocation surface, making the C_{16}^+ fragment ions more likely to undergo secondary fragmentations.

The fragment ion contributions from dissociation of singly and doubly charged parent ions are spatially well-separated in the velocity-map images for ions with low m/z. However, for heavier fragment ions the separation is less clear, and signals from singly and doubly charged parent ions overlap. Covariance analysis is a powerful tool that allows the separation of the contributions to the signal from multiply and singly charged parent ion dissociation. As explained in Section 3.4,

covariance analysis determines which pairs of daughter ions are formed from the same parent ion. Therefore, covariance analysis is 'blind' to the signal stemming from singly charged parent ions, which produce only one fragment ion together with one or more neutral co-fragments.

As noted earlier, our main focus is on how the carbon framework of the molecule dissociates, so in the following discussion we will not explicitly treat the hydrogen atoms. For example, the covariance image labelled (C_n^+, C_m^+) shows the correlation between the (collective) velocity vectors of all $C_nH_x^+$ fragments and all $C_mH_y^+$ fragments. This can be thought of as showing the relative velocity distribution of the two (sets of) fragments. Figures 9.6 and 9.7 show the recoil-frame covariance maps for all possible (C_n^+, C_m^+) product pairs at laser beam intensities of $5 \cdot 10^{14}$ W cm^{-2} and $9 \cdot 10^{14}$ W cm^{-2}, respectively, with each square being a covariance map of a specific ion pair (signal ion, reference ion). The reference ion (labelled on the x-axis) is constrained to travel upwards in the image. The covariance map shows the velocity of the signal ion (labelled on the y-axis) relative to this direction in the imaging plane.

The diagonal from the top-left covariance map to the bottom-right covariance map includes all possible two-body decays, i.e. dissociation processes in which the summed number of carbon atoms of the fragment ions is equal to the total number of carbon atoms in the parent molecule. We observe covariance signals for all these ion pair combinations apart from the pair corresponding to loss of a single carbon atom. The relative intensities of the covariance maps vary significantly. Asymmetric fragmentations yielding a 'light' and a 'heavy' fragment ion (i.e. ion pairs with a large difference in mass) have a higher branching ratio than processes yielding ion pairs of similar mass.

The covariance maps appearing on the off-diagonal are the products of three (or

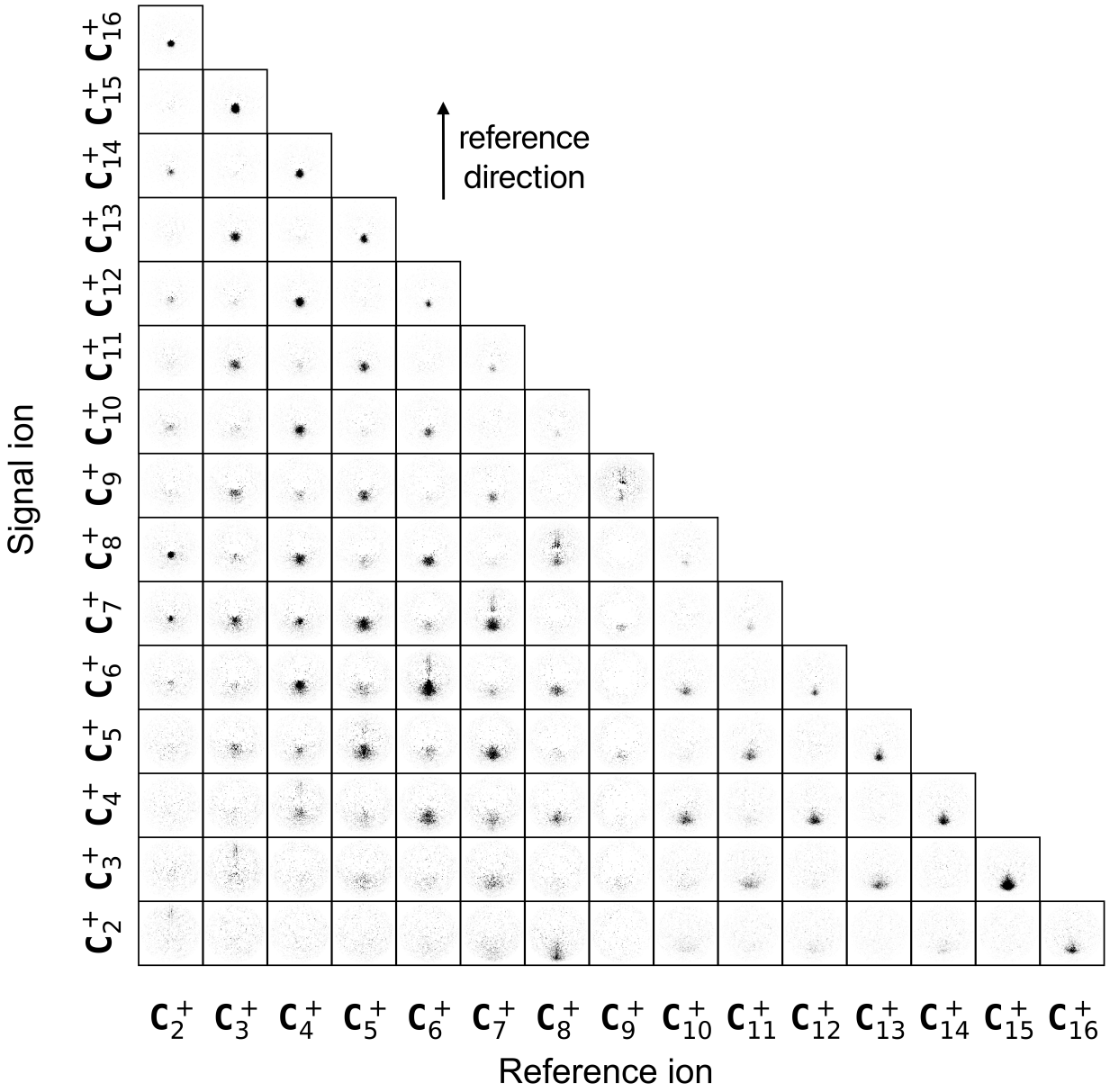

Fig. 9.6: Recoil-frame covariance maps of all possible combinations of signal and reference ions following the irradiation of triphenylene at a laser beam intensity of $5 \cdot 10^{14}$ W cm^{-2}. The reference direction is upwards in the Figure. All covariance maps are plotted with the same contrast. The fragment ion labs refer to the number of carbon atoms on the ion. As explained previously, we integrate each fragment ion peak over the hydrogen atoms. Ion pairs that exceed the number of carbon atoms on the parent molecule cannot be correlated with each other and do not show covariance. The autocovariance signal, which is the covariance of each fragment ion with itself, has been removed from the data.

higher) body decays, in which one or more neutral fragments are formed along with the detected ion pair. Many of these maps reveal intense signals, which follow the series: (C_n^+, C_m^+), (C_n^+, C_{m-2}^+), (C_n^+, C_{m-4}^+) etc. The covariance signal becomes

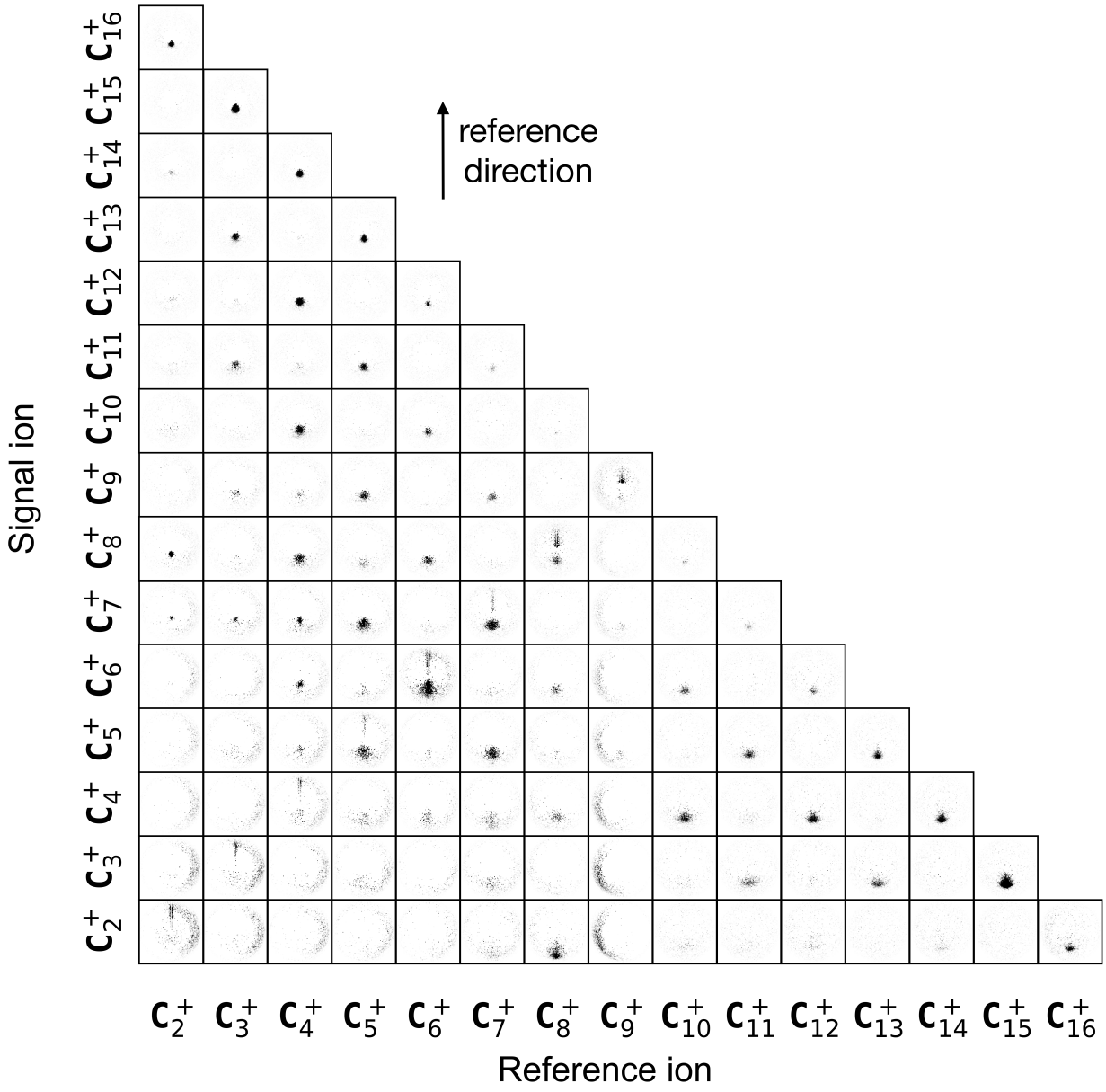

Fig. 9.7: Recoil-frame covariance maps of all possible combinations of signal and reference ions following the irradiation of triphenylene at a laser beam intensity of $9 \cdot 10^{14}$ W cm^{-2}. The reference direction is upwards in the Figure. All covariance maps are plotted with the same contrast. The fragment ion labs refer to the number of carbon atoms on the ion. As explained previously, we integrate each fragment ion peak over the hydrogen atoms. Ion pairs that exceed the number of carbon atoms on the parent molecule cannot be correlated with each other and do not show covariance. The autocovariance signal, which is the covariance of each fragment ion with itself, has been removed from the data. The edge feature in some of the covariance images is an artefact of the data and not real signal. It results from a transpose error in the covariance code. It results from a transpose error in the covariance code.

increasingly blurred as we move along such a series. We interpret this observation in terms of an initial two-body decay into the product ions C_n^+ and C_m^+, followed by

the decay of one or both primary product ions through sequential loss of neutral C_2H_2. Each C_2H_2 loss imparts a momentum 'kick' to the co-fragment ion, resulting in the blurring of the correlation with the intact primary fragment. An analogous fragmentation pattern has been observed previously by Lee and co-workers[78] in pyrene, phenanthrene, and fluorene following X-ray core ionization at 30.3 nm. The sequential loss of neutral acetylene units from the primary daughter ions is essentially the reverse of the proposed HACA mechanism for PAH growth in interstellar space, in which neutral C_2H_2 units are sequentially added to the carbon framework. The low activation barriers associated with C_2H_2 addition/ejection are consistent with it being a reversible process in PAH dications. The (C_8^+, C_2^+), (C_7^+, C_2^+), (C_7^+, C_3^+), (C_7^+, C_4^+), and (C_6^+, C_4^+) ion pairs do not fit the sequential C_2H_2 loss pattern. We will revisit these later in this Chapter.

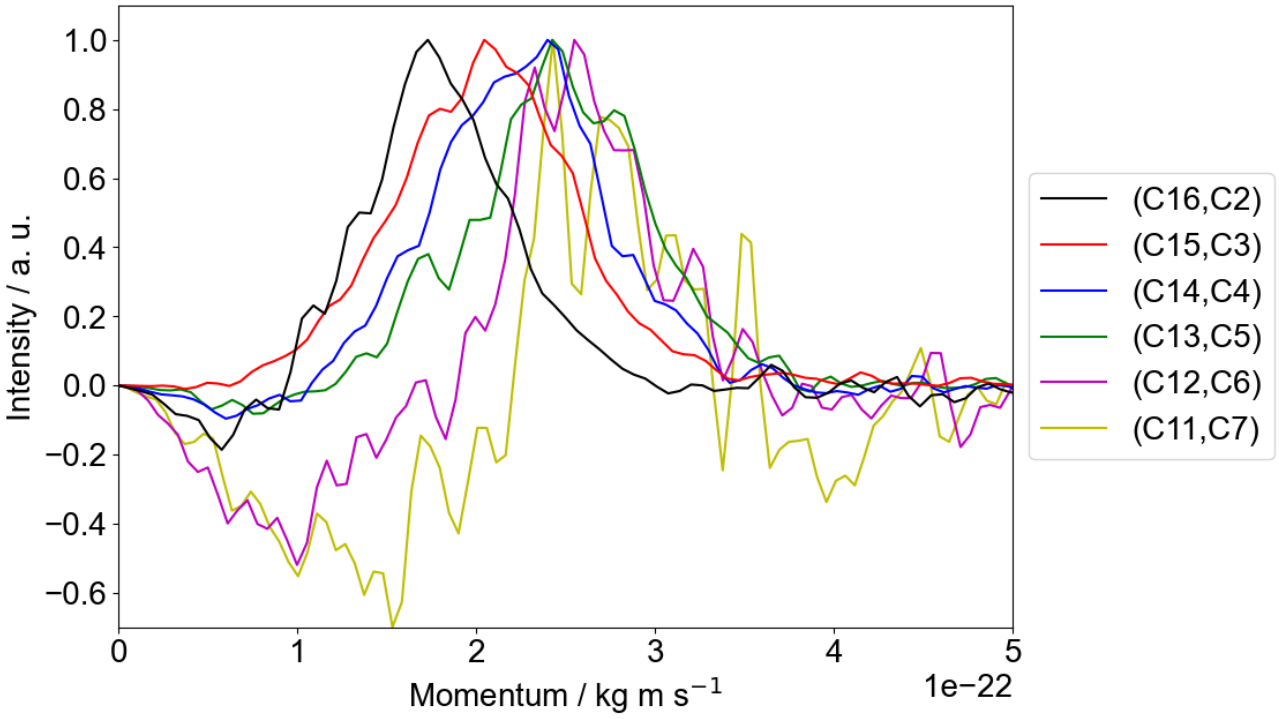

Fig. 9.8: Experimental momentum distributions of the signal ions from the (signal ion, reference ion) recoil-frame covariance images. The ion pairs are indicated in the legend. The maximum of the momentum distribution is normalized to unity.

As mentioned earlier, we observe covariance signals for all possible two-body de-

cays apart from the single carbon atom loss. A closer look at the two-body covariance maps reveals that the peak in the radial distribution of the covariance signal increases as the signal ion mass decreases. To quantify this change, we compare the momentum distributions of the signal ion in the covariance maps, which are shown in Figure 9.8. The distributions reveal a clear trend, in which for ion pairs close to each other in mass the signal ion recoils with a higher momentum than for ion pairs far apart in mass. Assuming that the total kinetic energy of the products is determined by the initial Coulomb repulsion between the charges in the doubly charged parent ion, and is therefore similar for all ion pairs, this behaviour is a direct consequence of conservation of momentum. To explore this idea further, we have calculated the Coulomb energy for a range of initial charge separations, and used this to predict the momenta for each ion pair. In a first approximation, we assume that the charges are point charges. According to Coulomb's law, the potential energy resulting from the interaction between the two charges is,

$$E = \frac{q_1 q_2}{4\pi\epsilon_0 r}, \tag{9.2}$$

where q_1 and q_2 are the two charges, ϵ_0 is the vacuum permittivity, and r is the distance between the charges. Assuming that all of the Coulomb potential E is converted into recoil kinetic energy of the products, and that the reference and signal ion are formed with equal and opposite momenta, it is straightforward to calculate the momentum of the signal ion. Figure 9.9 shows the results for initial charge separations r between 1 Å and 8 Å (for comparison, the maximum separation of any two carbon atoms in neutral triphenylene is 7.127 Å).

The curves show that the recoil momentum of the signal ion decreases monotonically with the charge distance r. Encouragingly, the simulations yield momenta with the same order of magnitude as obtained in the experiment. The vertical lines

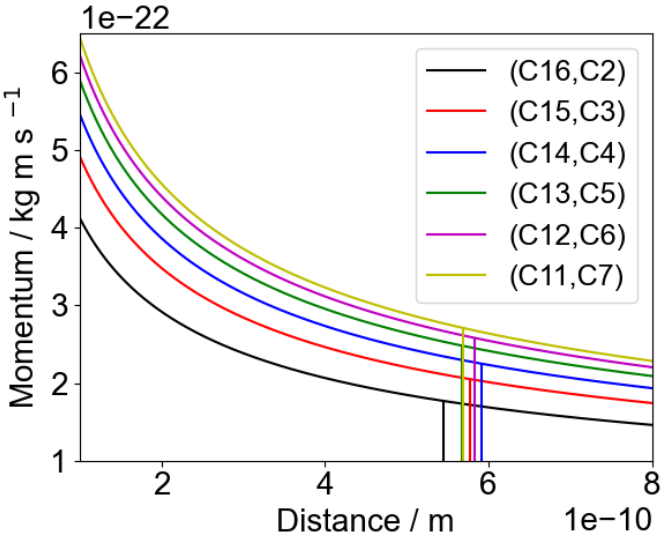

Fig. 9.9: Simulated momentum distributions of the signal ions for various (signal ion, reference ion) ion pairs based on Coulomb's law. The ion pairs are indicated in the legend. The vertical lines indicate the charge distance r, for which the predicted momentum of the signal ion matches the central momentum obtained experimentally for each ion, respectively.

indicate the charge distance r, for which the predicted momentum of the signal ion matches the central momentum obtained experimentally for each ion, respectively. These distances are between 5.4 Å and 6.0 Å for each ion pair (for comparison, the distance between the centres of two non-central benzene rings in neutral triphenylene is 4.336 Å). Thus, the Coulombic repulsion of the two charges is very likely the main force that determines the recoil momentum of the fragment ions. The simulated curves also show that if the daughter ions are close to one another in mass, their recoil momentum is higher than if they are far apart. This is highly consistent with the momentum distributions observed experimentally. We conclude that the two-body channels can be described to a first approximation in terms of a Coulombic explosion of two point charges, even though other effects likely still play a role. The fact that the model works implies a rapid 'Coulomb-explosion like' dissociation, occurring on a very short timescale following ionization. This is in stark contrast to the much slower and more statistical dissociation processes occurring in the monocation.

As noted earlier, the patterns observed in our covariance-map images, together with the previous study by Lee *et al.*[78] are consistent with ionic fragments decaying further through sequential ejection of C_2H_2, which can occur from either or both of the two daughter ions,

$$C_{18}H_x^{2+} \longrightarrow C_mH_y^+ + C_nH_z^+ \longrightarrow C_{m-2}H_{y-2}^+ + C_nH_z^+ + C_2H_2 \tag{9.3}$$

$$C_{18}H_x^{2+} \longrightarrow C_mH_y^+ + C_nH_z^+ \longrightarrow C_mH_y^+ + C_{n-2}H_{z-2}^+ + C_2H_2, \tag{9.4}$$

or even prior to charge separation from the parent ion,

$$C_{18}H_x^{2+} \longrightarrow C_{16}H_x^{2+} + C_2H_2 \longrightarrow C_mH_y^+ + C_nH_z^+ + C_2H_2. \tag{9.5}$$

Comparing the momentum distributions of the signal ion in the recoil-frame covariance images elucidates via which of the above pathways acetylene is ejected.

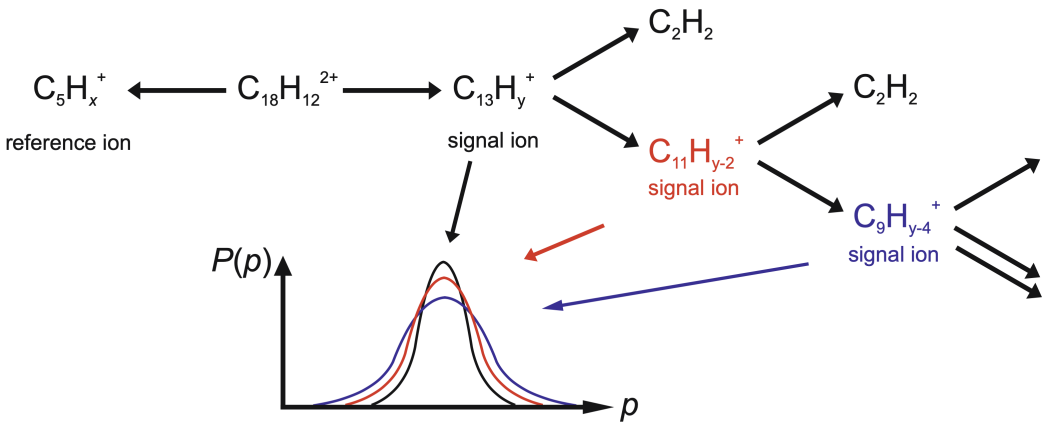

Fig. 9.10: Fragmentation pathway showing the dissociation of doubly charged triphenylene molecules into a reference and a signal ion, followed by sequential C_2H_2 ejection from the signal ion and the expected momentum distributions of the signal ion in the covariance maps.

Figure 9.10 shows the dissociation of $C_{18}H_{12}{}^{2+}$ into the $C_5H_x^+$ reference ion and $C_{13}H_y^+$ signal ion, followed by subsequent acetylene loss of the signal ion. The (C_{13}^+, C_5^+) ion pair results from the initial two-body process, in which C_{13}^+ and C_5^+ are formed with equal and opposite momenta. The covariance map reveals the mo-

mentum distribution of the C_{13}^+ ion. Now let us assume in the next step that the C_{13}^+ ion ejects C_2H_2 to form C_{11}^+, while the C_5^+ reference ion stays intact. The C_2H_2 loss imparts an additional momentum kick to the signal ion. We assume that to first approximation the acetylene is rejected in a random direction, as the C_{13}^+ ion can probably produce C_2H_2 in a variety of ways. The reference ion is not affected by this secondary decay and continues on its trajectory. As a result, the momentum distribution of the C_{11}^+ ion in the (C_{11}^+, C_5^+) covariance map is broader compared to the C_{13}^+ momentum distribution, but centred in the same position (as a results of conservation of momentum in the secondary dissociation step), as schematically illustrated in Figure 9.10. The C_{11}^+ ion can undergo another C_2H_2 loss to form the C_9^+ ion, which will broaden the signal ion momentum distribution even further.

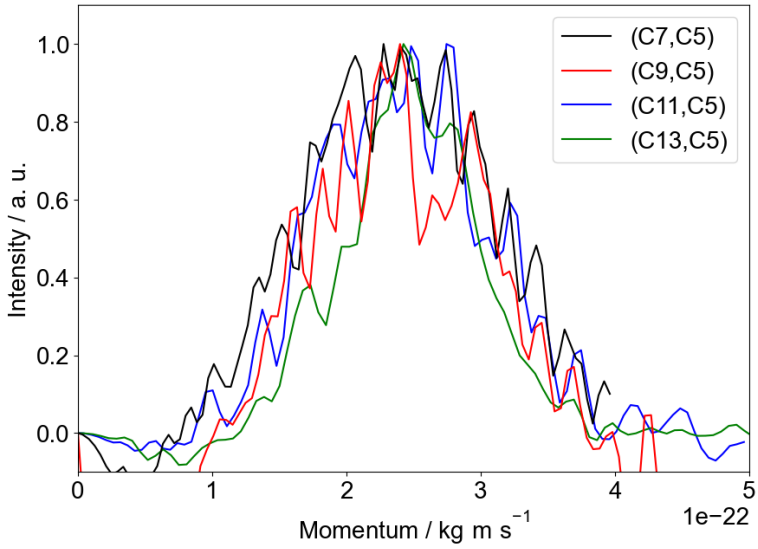

Fig. 9.11: Momentum distributions of the signal ions from the (signal ion, $C_5H_x^+$) recoil-frame covariance images. The ion pairs are indicated in the legend. The maximum of the momentum distribution is normalized to unity.

Tab. 9.1: Central momentum and full width half maximum (FWHM) of the moment distributions shown in Figure 9.11 obtained by fitting a Gaussian distribution to the curves.

(sig, ref)	momentum / kg m s^{-1}	FWHM / kg m s^{-1}
(C_{13}^+, C_5^+)	$2.48 \cdot 10^{-22}$	$1.14 \cdot 10^{-22}$
(C_{11}^+, C_5^+)	$2.41 \cdot 10^{-22}$	$1.52 \cdot 10^{-22}$
(C_9^+, C_5^+)	$2.41 \cdot 10^{-22}$	$1.39 \cdot 10^{-22}$
(C_7^+, C_5^+)	$2.39 \cdot 10^{-22}$	$1.67 \cdot 10^{-22}$

Figure 9.11 compares the momentum distributions of the signal ions for the (C_7^+, C_5^+), (C_9^+, C_5^+), (C_{11}^+, C_5^+), and (C_{13}^+, C_5^+) ion pairs. This series of ion pairs corresponds to the case introduced above, in which the initially formed signal ion, C_{13}^+, undergoes sequential C_2H_2 loss while the C_5^+ reference stays intact. The momentum distributions are similar; they peak in the same position and broaden slightly as C_2H_2 units are ejected. As explained above, we attribute this observation to the small momentum kick imparted by the departing C_2H_2 moieties to the ionic co-fragment. We note that this additional momentum contribution is small compared to the recoil momentum associated with the initial charge separation step. In order to quantify the broadening, we fitted Gaussian distributions to each momentum distribution to obtain the central momentum and FWHM of the distributions. Table 9.1 summarizes the results, showing that the central momentum does not change significantly upon C_2H_2 loss while the distributions broaden significantly. This broadening is in agreement with the covariance maps becoming increasingly blurred upon the loss of multiple C_2H_2 units.

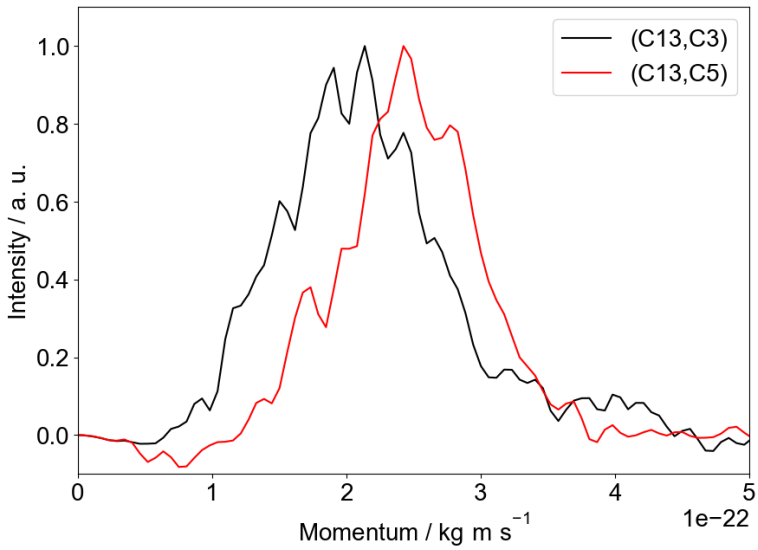

Fig. 9.12: Momentum distributions of the $C_{13}H_x^+$ signal ions from the ($C_{13}H_x^+$, reference ion) recoil-frame covariance images. The ion pairs are indicated in the legend. The maximum of the momentum distribution is normalized to unity.

So far, we have assumed the C_5^+ reference ion to stay intact. However, the C_5^+ ion

might eject C_2H_2 in a secondary decay and form the C_3^+ ion. We test this channel by comparing the momentum distributions obtained from the (C_{13}^+, C_5^+) and (C_{13}^+, C_3^+) covariance images. For both ion pairs, the C_{13}^+ ion is the signal ion and C_5^+ is the reference ion, which can in principle also eject C_2H_2, analogous to the fragmentation pathway presented in Figure 9.10. Figure 9.12 shows the momentum distributions obtained from the (C_{13}^+, C_5^+) and (C_{13}^+, C_3^+) covariance images. We observe a clear shift in the central momentum, indicating that the (C_{13}^+, C_3^+) ion pair is not predominantly formed from the (C_{13}^+, C_5^+) ion pair, but via an alternative pathway.

The results of the same analysis for other ion pairs are shown in Table C.3 in the Appendix. They exhibit the same trend, revealing that the acetylene moieties are preferably ejected from the heavier fragment ion, i.e. the fragments containing more carbon atoms, following the initial charge separation.

Earlier in this Chapter, we noted that there are some ion pairs which do not follow the sequential C_2H_2 loss pattern. Figure 9.13 is a magnified version of the relevant part of Figure 9.7 and shows the recoil-frame covariance images that fall into this category, highlighted in blue. The reference ions (labelled on the y-axis) are again restricted to travel upwards in the imaging plane, and the covariance maps visualize the velocity vector of the signal ion (labelled on the x-axis) relative to this direction. So far, all fragment ions have been assigned a charge of $+1$. However, some peaks can also contain contributions from multiply charged fragment ions. As labelled in the Figure, the resulting peak assignment is ambiguous because C_{16}^{2+}, C_{14}^{2+}, and C_{12}^{2+} yield the same m/z as C_8^+, C_7^+, and C_6^+, respectively.

We noted earlier that the sequential ejection of C_2H_2 leads to an increased blurring of the covariance maps. However, the 'anomalous' covariance maps presented here are not nearly as blurred as other covariance maps belonging to the same C_2H_2

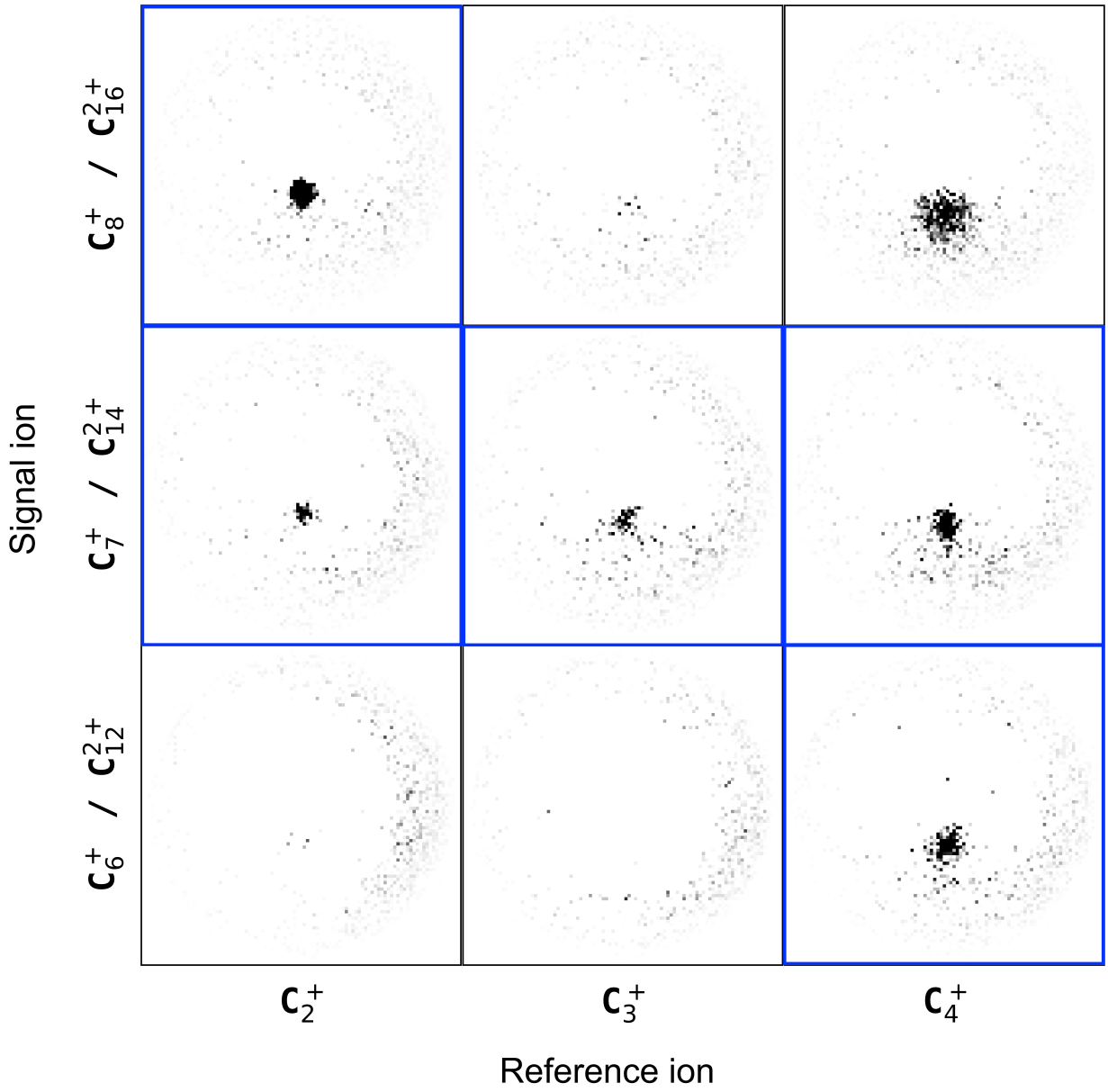

Fig. 9.13: Recoil-frame covariance maps of various combinations of signal and reference ions following the irradiation of triphenylene at a laser beam intensity of $9 \cdot 10^{14}$ W cm^{-2}. The reference direction is upwards in the Figure. All covariance maps are plotted with the same contrast. The fragment ion labels refer to the number of carbon atoms on the ion. As explained previously, we integrate each fragment ion peak over the hydrogen atoms. Ion pairs that exceed the number of carbon atoms on the parent molecule cannot be correlated with each other and do not show covariance. The autocovariance signal, which is the covariance of each fragment ion with itself, has been removed from the data. The edge feature in some of the covariance images is an artefact of the data and not real signal. It results from a transpose error in the covariance code.

loss series, and instead display a sharp signal close to the image centre. Furthermore, the (C_7^+, C_3^+) ion pair should not display signals according to the C_2H_2 loss pattern. In light of these observations, we believe that the signal in the anomalous

covariance maps highlighted in blue stems from the dissociation of triply charged parent ions, C_{18}^{3+}. Daughter ions produced from triply charged parent ions will be born with a higher kinetic energy release compared to ions stemming from doubly charged parent ions due to the increased intramolecular repulsion of the charges. We only capture the 'slow' tail of these ions, as illustrated schematically in Figure B.2 in the Appendix, which is consistent with sharp signals close to the image centre. Interestingly, the (C_{14}^{2+}, C_3^+) covariance map corresponds to a channel in which the combined number of carbon atoms within the fragment ions deviates by one from the number of carbon atoms in the parent molecule. This implies that the C_2H_2 loss fragmentation pattern may not apply to the decay of triply charged triphenylene ions.

9.4 Perylene and Benzo[a]pyrene

Figure 9.14 shows the background-subtracted, mass-calibrated TOF spectrum for the fragment ions of perylene formed following irradiation with the femtosecond laser beam at intensities between $1.4 \cdot 10^{14}$ and $3.9 \cdot 10^{15}$ W cm^{-2}. Panel (a) reveals only the perylene parent ion peak, $C_{20}H_x^+$. Hence, the LID source produces intact parent molecules. In panel (b), a second ion peak appears, which we assign to doubly charged parent ions, $C_{20}H_x^{2+}$. Increasing the laser beam intensity leads to the appearance of fragment ions, which results from the dissociation of singly and doubly charged parent ions. Similarly to the TOF spectra observed for triphenylene, the relative abundance of fragment ions peaks with m/z ratios lower than or equal to that of $C_{20}H_x^{2+}$ is higher than for heavier fragment ions. The velocity-map images and kinetic energy release distributions are qualitatively very similar to those observed triphenylene in that they contain contributions from singly and doubly charged parent ions. In the following, we focus on the dissociation pathways of

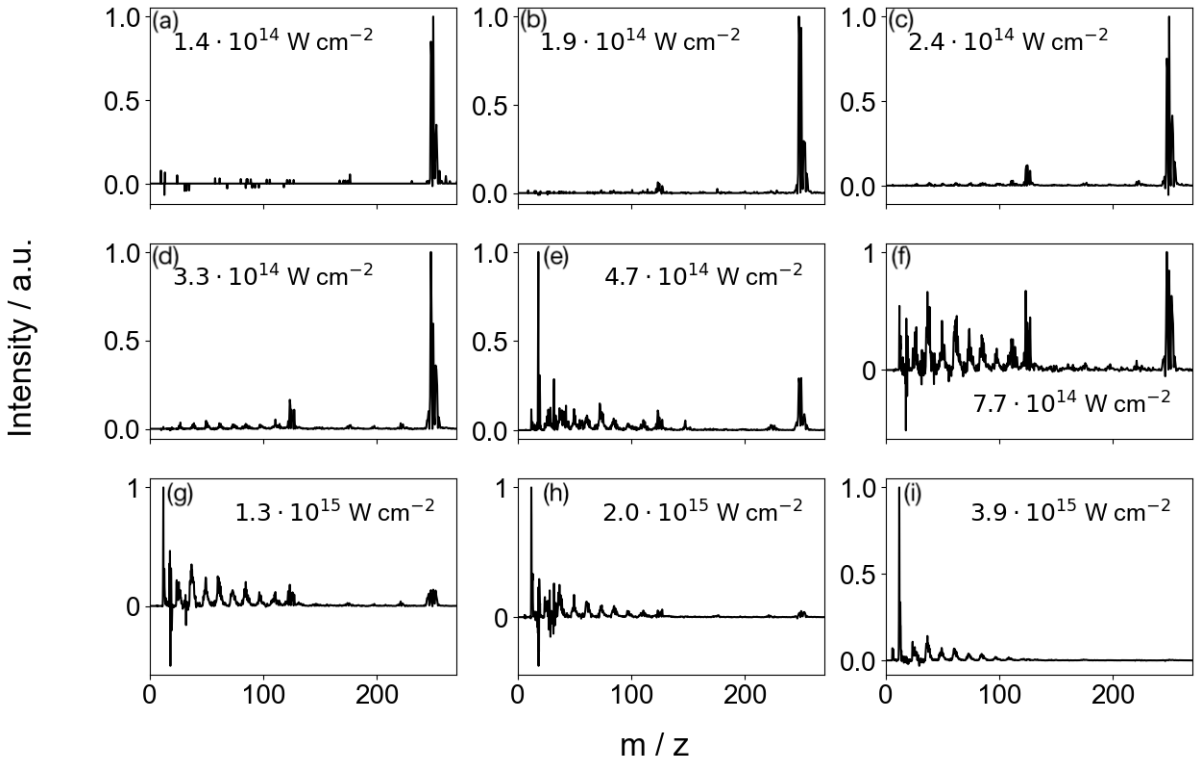

Fig. 9.14: Background-subtracted TOF spectra of perylene following the irradiation with the 800 nm femtosecond laser beam at different laser beam intensity. The intensities used are indicated in each plot.

doubly charged parent ions.

To investigate the fragmentation pattern of doubly charged parent ions, we utilize covariance analysis. Figure B.3 in the Appendix and Figure 9.15 in this Chapter show the resulting recoil-frame covariance images for all possible fragment ion combinations at irradiation laser intensities of $9 \cdot 10^{14}$ W cm^{-2} and $5 \cdot 10^{14}$ W cm^{-2}, respectively. Similarly to the analysis for triphenylene, we focus only on the carbon framework and integrate each signal over the hydrogen atoms. The recoil-frame covariance images at a laser intensity of $5 \cdot 10^{14}$ W cm^{-2} reveal the same fragmentation pattern as observed for triphenylene, in which either or both of the primary fragment ions can lose one or more C_2H_2 moieties.

At a laser beam intensity of $9 \cdot 10^{14}$ W cm^{-2}, the fragmentation pathways of doubly charged parent ions remain similar to the ones observed at $5 \cdot 10^{14}$ W cm^{-2}. How-

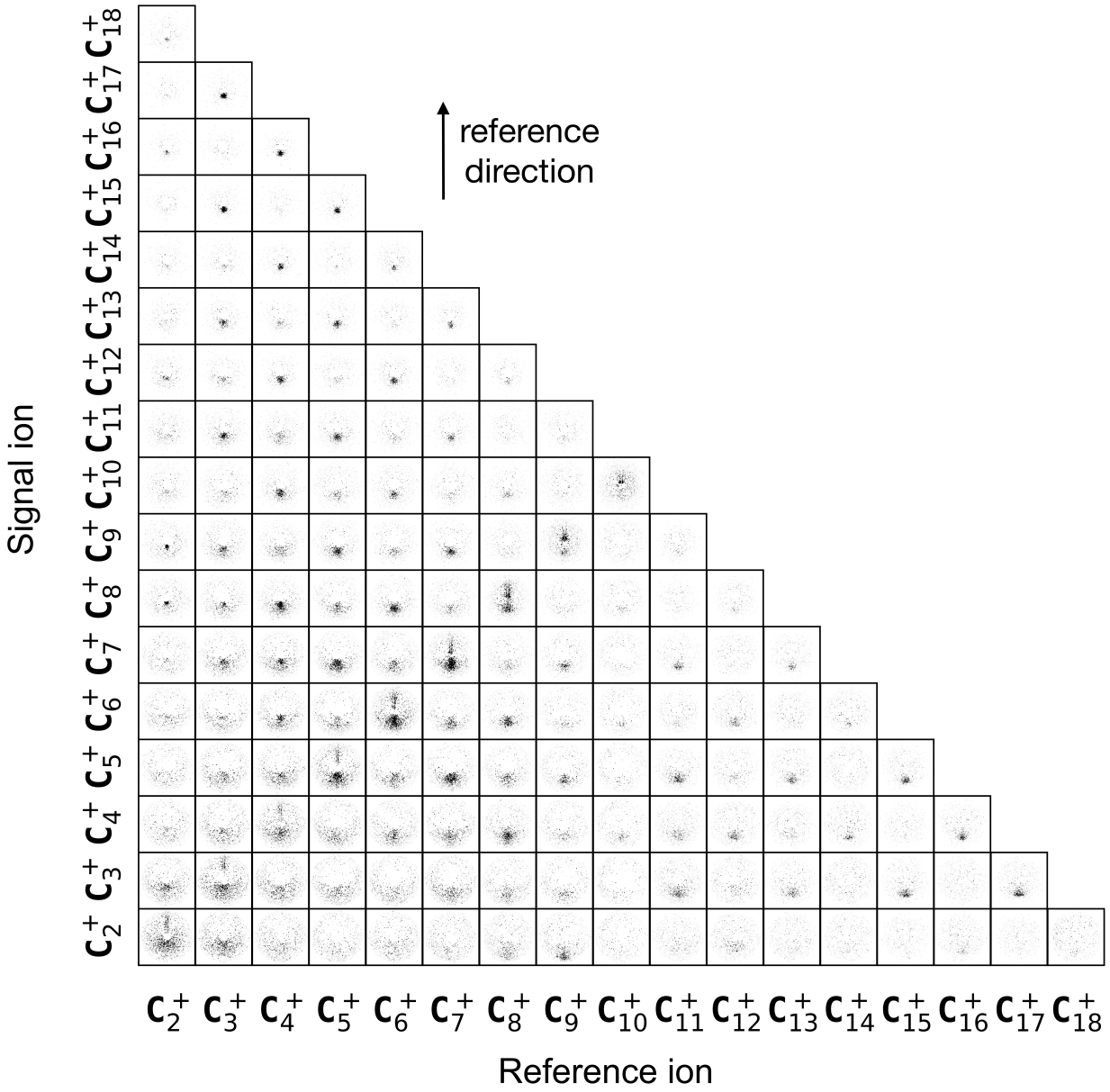

Fig. 9.15: Recoil frame covariance maps of all possible combinations of signal and reference ions following the irradiation of perylene at a laser beam intensity of $5 \cdot 10^{14}$ W cm^{-2}. The reference direction is upwards in the Figure. All covariance maps are plotted with the same contrast. The fragment ion labs refer to the number of carbon atoms on the ion. As explained previously, we integrate each fragment ion peak over the hydrogen atoms. Ion pairs that exceed the number of carbon atoms on the parent molecule cannot be correlated with each other and do not show covariance. The autocovariance signal, which is the covariance of each fragment ion with itself, has been removed from the data.

ever, the (C_6^+, C_6^+) ion pair displays a significantly more intense covariance signal, which, in contrast to the covariance images observed previously, exhibits a clear ring feature across the backward scattering angles. We will revisit this feature later

in this Chapter.

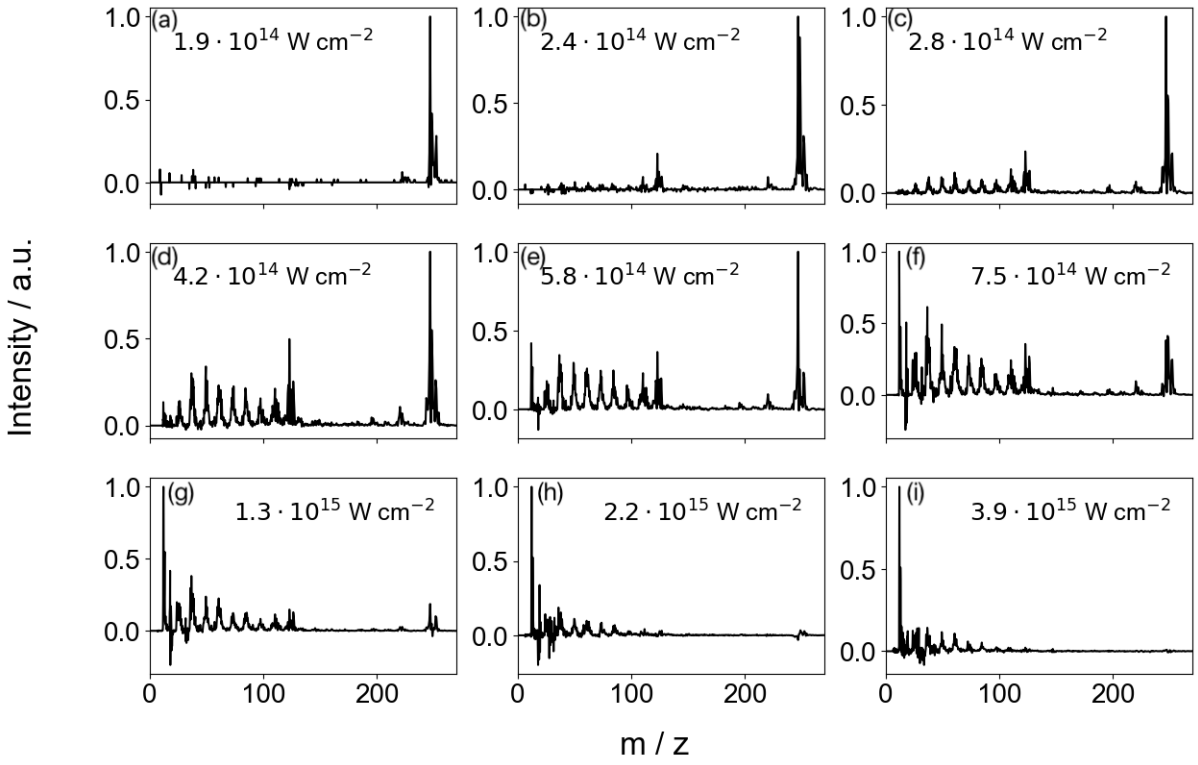

Fig. 9.16: Background-subtracted TOF spectra of benzo[a]pyrene following the irradiation with the 800 nm femtosecond laser beam at various laser beam intensity. The intensities used are indicated in each plot.

Figure 9.16 shows the mass-calibrated, background-subtracted TOF spectrum for the dissociation products of benzo[a]pyrene. The spectrum shown in panel (a), corresponding to a laser beam intensity of $1.4 \cdot 10^{14}$ W cm^{-2}, reveals two peaks. The most intense peak, appearing at high m/z, is assigned to the parent ion, $C_{20}H_x^+$, and the second significantly less intense peak at slightly lower m/z is assigned to $C_{18}H_x^+$, which is formed following acetylene loss from the parent ion,

$$C_{20}H_x^+ \longrightarrow C_2H_2 + C_{18}H_y^+. \tag{9.6}$$

Even though perylene and benzo[a]pyrene are isomers of each other, benzo[a]pyrene ions eject acetylene significantly more efficiently than perylene ions, as indicated by the $C_{18}H_x^+$ peak height at low laser beam intensities. As explained previously, small

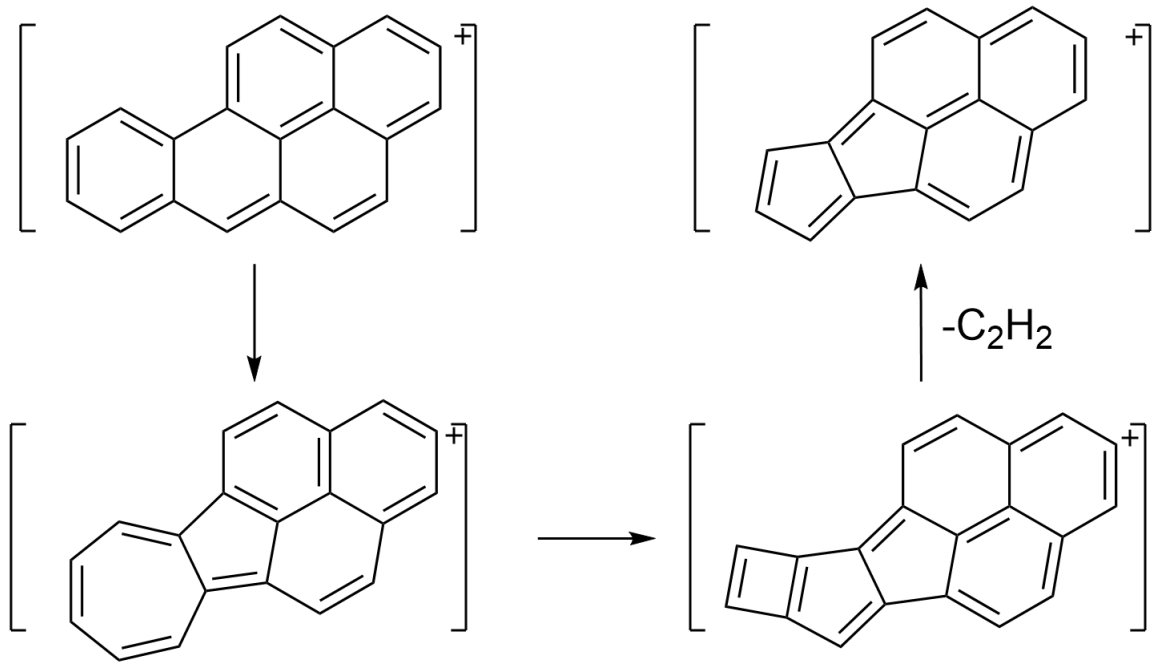

Fig. 9.17: Possible mechanism for the loss of C_2H_2 from the benzo[a]pyrene cation, in agreement with the mechanism suggested for small PAHs by West *et al.*[322]

PAHs are thought to lose acetylene via the formation of an azulene-containing intermediate followed by contraction to a five- and seven-membered ring.[322] The central benzene ring in benzo[a]pyrene has one non-bridging carbon atom, allowing the isomerization into a five-membered species. Figure 9.17 shows the mechanism for benzo[a]pyrene. However, in perylene all carbon atoms contained in the central benzene ring are bridging atoms and part of another benzene ring. Thus, it cannot rearrange into a five-membered ring. At higher laser beam intensities, the ion fragments observed for benzo[a]pyrene match the ones for perylene.

The recoil-frame covariance images for all possible fragment ion combinations are shown in Figures B.4 and B.5 in the appendix for laser beam intensities of $5 \cdot 10^{14}$ W cm^{-2} and $9 \cdot 10^{14}$ W cm^{-2}, respectively. The fragmentation pathways at both powers reveal the same pattern, as discussed previously for perylene. At $9 \cdot 10^{14}$ W cm^{-2}, the (C_6^+, C_6^+) ion pair displays a similar signal profile to the one previously observed for perylene at the same laser beam intensity. Figure 9.18

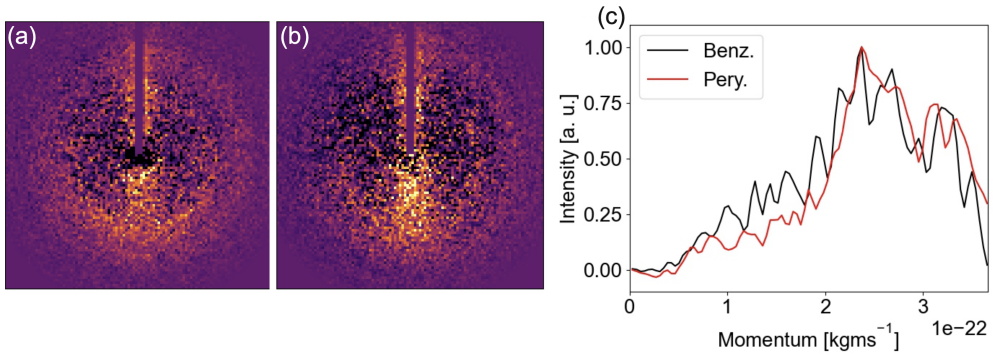

Fig. 9.18: Recoil-frame covariance images of the (C_6^+, C_6^+) ion pair resulting from the irradiation of perylene (a) and benzo[a]pyrene (b) with the 800 nm femtosecond laser beam at a laser beam intensity of $9 \cdot 10^{14}$ W cm^{-2}. The reference direction is up in the paper plane. The self-covariance along the reference direction has been manually removed for visualization purposes. Integrating the covariance images over the angle coordinate reveals the radial distribution of the C_6^+ signal ion, which is converted into momentum space using by using a SIMION calibration. Panel (c) compares the momentum distributions of the signal ion for perylene (ref) and benzo[a]pyrene (black). The maximum is normalized to one.

shows the (C_6^+, C_6^+) ion pair recoil-frame covariance images for perylene (a) and benzo[a]pyrene (b) and their momentum distributions of the signal ion (c). In contrast to the other ion pair covariance maps, the (C_6^+, C_6^+) ion pair exhibits signal in a ring that covers a large range of backwards scattered angles. The momentum distributions overlap well in the high momentum region, indicating that the dissociation mechanism might be similar for both molecules. In the future, it might be interesting to investigate what fragmentation pathway leads to this signal and why we do not observe it in triphenylene.

9.5 Conclusions

PAHs are pollutants of the environment, posing a threat to ecosystems and wildlife. Due to their large aromatic systems, they are highly durable towards decomposition. For that reason, PAHs are highly abundant in space, where they are formed from benzene via the HACA mechanism, in which acetylene units repeatedly bind to the growing PAHs. In a previous study using X-ray core ionization at the FLASH

free electron laser in Hamburg, Lee *et al.*[78] observed that small doubly charged PAHs decay via a characteristic pathway. Initially, the doubly charged parent ion fragments into two daughter ions. Afterwards, either or both of the daughter ions can sequentially eject neutral C_2H_2. In the present study, we have investigated the fragmentation dynamics of triphenylene, perylene, and benzo[a]pyrene following irradiation with the 800 nm femtosecond laser described in Chapter 7. All three molecules display the same fragmentation pattern observed by Lee and co-workers, indicating that the C_2H_2 loss pattern might be a general decay mechanism in small doubly charged PAHs, which is independent of the ionization mechanism. We have also shown that the acetylene ejection occurs preferentially from the heavier fragment ion after the initial charge separation. It remains to be seen what role the molecular geometry and especially the hydrogen atoms play in the dissociation mechanism of doubly charged PAHs. We recommend upgrades to the instrument used in this Chapter to improve the mass resolution and ensure hydrogen resolution before revisiting the above molecules. The experiment is also suitable for studying the dissociation of more highly-charged parent molecules but will need to be modified accordingly.

10 Conclusion and Outlook

10.1 Conclusion

Light-induced chemical reactions play a central role in biological systems, with photosynthesis being the most prominent example, and are part of the foundation for versatile forms of life on Earth. However, prolonged exposure to sunlight can also lead to damage to biomolecules such as DNA or enzymes, resulting in fragmentation into two or more photoproducts. Studying the fragmentation of such large molecules in the gas phase poses challenges, including experimental challenges in the introduction of the intact sample molecules into the experiment and challenges associated with analyzing the data in light of the number and complexity of possible fragmentation pathways. These challenges can be avoided to some extent by studying the key 'building blocks' of the large molecules rather than the molecules themselves.

Chapter 4 describes an investigation into the photodissociation dynamics of THF, a model compound for the DNA backbone molecule ribose, at a photolysis wavelength of 193 nm. At this wavelength, THF is electronically excited to the S_1 state via a $3s \leftarrow n$ transition, with dissociation occurring either on this state or on the electronic ground state following IC. The S_1 state is repulsive along the C−O stretch

coordinate, leading to rapid bond cleavage and formation of the diradical intermediate C_4H_8O. Following the dissociation of a C−C bond, we obtain the main product pairs OCH_2 + C_3H_6 and $HOCH_2$ + C_2H_5. The recoil anisotropy parameter decreases from zero for products formed with low velocities to limiting values of -0.75 (OCH_2 + C_3H_6) and -0.50 ($HOCH_2$ + C_2H_5) for high velocity products. We attribute this behaviour to the extent of internal excitation of the C_4H_8O diradical intermediate and the range of lifetimes over which it survives prior to cleavage of a C−C bond.

Chapter 5 describes a photodissociation study of DMF at 225 and 245 nm. DMF is the simplest tertiary amide and can be considered a model compound for the peptide bond, which forms the backbone of peptide molecules. The primary dissociation channels in DMF involve cleavage of the N−CO amide bond or the N−CH_3 methyl bond. Excitation at 225 nm or 245 nm leads predominantly to population of the S_2 $2^1A''$ state via a parallel transition. The fragmentation occurs either on this state or on S_1 following IC. Both singlet surfaces, as well as the low lying T_1 and T_2 triplet surfaces, share similar topographical features, exhibiting a barrier along the N−CO stretching coordinate, and possessing non-planar minimum-energy geometries. As a result, dissociation occurs from a variety of molecular geometries. Dissociation from planar geometries leads to little product internal excitation and correspondingly high photofragment velocities, with near-limiting values of the recoil-anisotropy parameter β. In contrast, dissociation from non-planar geometries leads to significant product internal excitation, with correspondingly lower photofragment velocities and breakdown of the axial recoil approximation to give reduced values of β.

Chapter 6 presents a photodissociation study of the DMF^+ ion at 225 nm, 245 nm, and 280 nm. The primary dissociation channel involves cleavage of the N−CO

amide bond, yielding HCO + $NC_2H_6^+$ on all low-lying ionic states, except the $3^2A'$ state, which produces HCO^+ + NC_2H_6. Interestingly, changing the photolysis wavelength from 280 nm to 225 nm does not alter the kinetic energy distribution of the $NC_2H_6^+$ ion, with virtually all the available energy being released into into internal modes of the $NC_2H_6^+$ ion and its co-product(s). In addition, N−CO bond cleavage can be accompanied by simultaneous intramolecular hydrogen transfer from the oxygen side of the molecule to the nitrogen atom, in which case NCH_4^+ can be formed. This channel is low in energy and observed efficiently at all three photolysis wavelengths. The $NC_2H_6^+$ ion has lifetimes of at least tens of microseconds and is fluxional in structure, readily isomerizing from $N(CH_3)_2^+$ to $H_2C{-}NH{-}CH_3^+$. It can dissociate via a number of different pathways to produce CH_3^+, NH_4^+, NCH_2^+, and $NC_2H_4^+$. The abundance of the various fragment ions increases with increasing photon energy, in line with the increased internal energy of the primary dissociation products. This is consistent with the velocity-map images, which look very similar in that they are fully isotropic and show little dependence on the photolysis photon energy over the range studied. The similarity of the velocity-map images could indicate that dissociation occurs from the same set of electronic states, most likely the ionic ground state ($1^2A'$) and first excited state ($2^2A'$).

The experimental capabilities determine the physical processes we can investigate and the chemical systems we can study. One major limitation is often the pulse duration of the lasers. Nanosecond lasers are suitable for initiating a chemical reaction and probing the photoproducts after a delay of tens of nanoseconds when the reaction is already over. While the product scattering distributions provide a great amount of information on the reaction mechanism, in an ideal experiment we would be able to follow the reaction in real-time, akin to recording a 'molecular movie'. For that purpose, the laser pulse duration has to be tens of femtoseconds or shorter, which is the timescale on which nuclei move. We now have access to our

own femtosecond laser beamline and use the output of a Titanium:Sapphire laser (1 kHz rate, 35 fs transform limit, 800 nm central wavelength, 60 nm bandwidth). Chapter 7 covers the laser beamline design and laser pulse characterization. The new beamline allows us to probe the molecular ground-state structure and to investigate the fragmentation dynamics of multiply charged parent ions.

Another experimental limitation regards the target molecules we can investigate. The experiments described above utilize a pulsed molecular beam. Pulsed valves are designed for the preparation of gases or high-vapour pressure liquids. However, non-volatile molecules are precluded from being studied, limiting us to the investigation of small to medium-sized molecules. Chapter 8 describes the design and characterization of a custom-built, fibre-coupled LID source capable of preparing neutral and intact parent molecules from a solid sample. The source provides a reliable and relatively low-cost way to prepare non-volatile molecules in the gas phase for laser-based VMI experiments and other gas-phase measurements.

Lastly, we investigated the fragmentation dynamics of doubly charged PAHs. PAHs are aromatic compounds consisting of two or more fused benzene rings. They are an important class of molecules on Earth and in the galaxy. A study conducted at FLASH in 2021[78] observed that small doubly charged PAHs exhibit a characteristic fragmentation pattern, in which the summed number of carbon atoms on the fragment ions differs from the carbon number of the parent molecules by a multiple of two. This was interpreted in terms of a fragmentation mechanism involving sequential loss of C_2H_2 units. Chapter 9 explores whether this pattern extends to heavier PAHs by investigating the fragmentation pattern of multiply charged triphenylene, perylene, and benzo[a]pyrene following preparation with the novel LID source and irradiation with the femtosecond laser. The fragmentation pattern observed from the parent dications matches the one observed previously, indicat-

ing that the C_2H_2 loss process is likely to be a mechanism in PAH cations and is independent of the ionization mechanism.

10.2 Outlook

10.2.1 Experimental upgrades

For various data sets in this work, the mass resolution is insufficient to distinguish clearly between fragment ions that differ by one hydrogen atom or generally by an m/z value of one. This is particularly problematic for fragment ions with large m/z values, and limits the mechanistic information we can obtain from the experiment. The mass resolution is currently limited by the detector and camera. The detector uses a P47 phosphor scintillator with an emission lifetime of 69.3 ns[180]. We plan to switch to using Exalite scintillators in the near future, which have emission lifetimes of a few nanoseconds[180] and will improve the mass resolution significantly. Another limitation is the time resolution of the camera, which is several tens of nanoseconds. In the medium to long term, we will need to switch to an alternative camera with a better time resolution. The most likely candidate is TimePix[184,185].

High femtosecond laser beam intensities in the interaction region yield very high charge states on the parent molecule, resulting in fragment ions with velocities much higher than we can currently capture in the experiment. To record these fragment ions, we can increase the repeller voltage, shorten the TOF tube, or increase the size of the detector. The repeller voltage is limited to 10 kV, which is the maximum voltage the electrical feedthrough is designed for. Hence, we will shorten the TOF tube length to about 46 cm and switch to a detector with an active diameter of 75 mm (previously 40 mm). Shortening the TOF tube will unfortunately

reduce the mass resolution, reinforcing the need for changes on the detector end.

Due to the high number of ions created by the femtosecond laser, we have observed space-charge repulsion in the interaction region and saturation effects on the detector when using high laser beam intensities. In order to avoid such issues, we need to reduce the number of molecules in the interaction region. To reduce the number of parent molecules, we have swapped the pulsed valve to an effusive nozzle. The effusive nozzle operates at significantly lower backing pressures and produces a continuous, low-density molecular beam. For the LID source, the molecular plume density in the interaction region correlates directly to the diode laser power, which should be adjusted accordingly. To reduce the background signal, we have purchased a liquid helium-cooled cryo pump, which is being installed between the imaging chamber and the turbo pump right below the interaction region. The pump will freeze out water and other background gases, significantly reducing the number of background molecules in the chamber.

10.2.2 Coulomb-explosion imaging

CEI is a technique commonly used to obtain structural information in ultrafast pump-probe experiments under the premise that the terminal velocities of the fragment ions formed in a Coulomb explosion correlate with the geometric configuration at the ionization point. However, it has not been well established to what extent quantitative information can be obtained on the nuclear geometry in terms of bond lengths and angles. With access to our femtosecond laser beamline, we can begin a set of systematic experiments on a series of carefully chosen molecules, with the goal of determining what level of quantitative information we can obtain on the molecular geometry, and how best to optimize the experimental parameters for use in structure determination measurements. The other main goal

of this project will be to determine quantitatively the boundary between the low- and high-charge regimes as introduced by Zhou *et al.*[283]

10.2.3 Laser-induced desorption source

The availability of the LID source allows access to multiple classes of molecules that we might want to study in the future. One class of molecules are peptides. We have already investigated DMF[128,135] and *N*-methylformamide (NMF)[218] at various wavelengths in the UV region. Following these studies, future experiments should investigate di- and tripeptides to see whether and how the dissociation dynamics of the peptide bonds change upon increasing the number of conjugated peptide bonds. Di- and tripeptides are solids which we should be able to prepare intact in the gas phase using the LID source.

Once the mass resolution is sufficiently improved, it would be interesting to revisit PAHs and focus not only on the carbon framework, which we already understand relatively well, but also on the hydrogen atoms. We observed that various PAHs follow a fragmentation pattern in which multiples of neutral acetylene units are ejected from the molecule. However, it is unclear what role the hydrogen atoms play in this dissociation. Is it always C_2H_2 ejected, or does the number of hydrogen atoms vary for different ion pairs? How does the number of hydrogen atoms influence the isomerization mechanism prior to dissociation? The PAH study also provides the opportunity to construct a largely unexplored theoretical framework. Some ion pairs have a higher branching ratio than others. We should be able to quantify these branching ratios experimentally using covariance analysis and correlate them with barrier heights and rate constants from theoretical calculations. Experimentally, it would also be interesting to quantify at what PAH size the fragmentation pattern observed in this work and previously by Lee *et al.*[78] breaks

down, as larger PAHs are more robust towards dissociation and better at stabilizing charge. Lastly, we hope to explore the interactions between electrons and PAHs shortly in our group, and to measure partial cross-sections and appearance energies for the various fragment ions.

One last class of potential target molecules are MALDI matrix molecules. MALDI[91,92] has been used successfully as a soft ionization technique for decades. However, there are a number of outstanding questions in relation to the charge transfer mechanism from the matrix molecules to the analyte molecules[324–326]. Investigating the interactions of the matrix molecules with light could provide insight into the charge transfer mechanism.

Light-matter interactions are ubiquitous in nature, from the human body to outer space. Depending on the light and the molecule identity one or more photons can be absorbed by the molecule, leaving it in an excited neutral or ionic state, where fragmentation is only one of the possible deactivation mechanisms. The design of experiments with well-defined observables, in our case the fragment identity and scattering distribution, allows us to obtain detailed insight into the reaction mechanism leading from photon absorption to product formation. Building on the knowledge from experiments on small molecules, the experimental reaction dynamics community will focus more attention on larger molecules in the future. This work provides an important step in this direction and has laid the groundwork for exploring larger (bio)molecules going forward.

Bibliography

[1] R. G. J. Fraser, L. F. Broadway, *Proc. R. Soc. A* **1933**, *141*, 626–633.

[2] E. H. Taylor, S. Datz, *J. Chem. Phys.* **1955**, *23*, 1711–1718.

[3] W. B. Miller, S. A. Safron, D. R. Herschbach, *Discuss. Faraday Soc.* **1967**, *44*, 108–122.

[4] C. Vallance, *Chem. Commun.* **2019**, *55*, 6336–6352.

[5] D. W. Chandler, P. L. Houston, *J. Chem. Phys.* **1987**, *87*, 1445–1447.

[6] A. T. Eppink, D. H. Parker, *Rev. Sci. Instrum.* **1997**, *68*, 3477–3484.

[7] M. Born, R. Oppenheimer, *Ann. Phys.* **1927**, *389*, 457–484.

[8] J. R. Dwyer, C. T. Hebeisen, R. Ernstorfer, M. Harb, V. B. Deyirmenjian, R. E. Jordan, R. J. Miller, *Philos. Trans. R. Soc. A* **2006**, *364*, 741–778.

[9] Y. Xiong, K. J. Wilkin, M. Centurion, *Phys. Rev. Res.* **2020**, *2*, 043064.

[10] Z. Ma, X. Zou, L. Zhao, F. Qi, T. Jiang, P. Zhu, D. Xiang, J. Zhang, *Proc. Natl. Acad. Sci. U. S. A.* **2022**, *119*, e2122793119.

[11] E. Nango, S. Iwata, *Curr. Opin. Struct. Biol.* **2023**, *81*, 102629.

[12] L. J. Butler, *Annu. Rev. Phys. Chem.* **1998**, *49*, 125–171.

[13] C. Vallance, *Philos. Trans. R. Soc. London A* **2004**, *362*, 2591–2609.

[14] J. Franck, *Trans. Faraday Soc.* **1926**, *21*, 536–542.

[15] E. Condon, *Phys. Rev.* **1926**, *28*, 1182–1201.

[16] P. Atkins, R. Friedman, *Molecular Quantum Mechanics 5th ed.*, Oxford University Press, New York, **2011**.

[17] A. Jablonski, *Nature* **1933**, *131*, 839–840.

[18] P. R. Stannard, W. M. Gelbart, *J. Phys. Chem.* **1981**, *85*, 3592–3599.

[19] V. E. Bondybey, *Annu. Rev. Phys. Chem.* **1984**, *35*, 591–612.

[20] S. Karmakar, S. Keshavamurthy, *Phys. Chem. Chem. Phys.* **2020**, *22*, 11139–11173.

[21] R. Englman, J. Jortner, *Mol. Phys.* **1970**, *18*, 145–164.

[22] M. Bixon, J. Jortner, J. Cortes, H. Heitele, M. E. Michel-Beyerle, *J. Phys. Chem.* **1994**, *98*, 7289–7299.

[23] G. G. Stokes, *Philos. Trans. R. Soc. London* **1852**, *142*, 463–562.

[24] Kasha Michael, *Discuss. Faraday Soc.* **1950**, *9*, 14–19.

[25] P. A. M. Dirac, *Proc. R. Soc. London. Ser. A* **1928**, *117*, 610–624.

[26] J. K. McCusker, *Acc. Chem. Res.* **2003**, *36*, 876–887.

[27] O. F. Mohammed, E. Vauthey, *J. Phys. Chem. A* **2008**, *112*, 3823–3830.

[28] E. Collado-Fregoso, J. S. Zugazagoitia, E. F. Plaza-Medina, J. Peon, *J. Phys. Chem. A* **2009**, *113*, 13498–13508.

[29] S. Murudkar, A. K. Mora, P. K. Singh, S. Nath, *J. Phys. Chem. A* **2011**, *115*, 10762–10766.

[30] J. P. Zobel, J. J. Nogueira, L. González, *Chem. Eur. J.* **2018**, *24*, 5379–5387.

[31] M. A. El-Sayed, *J. Chem. Phys.* **1963**, *38*, 2834–2838.

[32] F. Perrin, *Ann. Phys. (Paris).* **1929**, *10*, 169–275.

[33] P. C. Samartzis, I. Sakellariou, T. Gougousi, T. N. Kitsopoulos, *J. Chem. Phys.* **1997**, *107*, 43–48.

[34] A. S. Bracker, E. R. Wouters, A. G. Suits, Y. T. Lee, O. S. Vasyutinskii, *Phys. Rev. Lett.* **1998**, *80*, 1626–1629.

[35] R. N. Zare, D. R. Herschbach, *Proc. IEEE* **1963**, *51*, 173–182.

[36] R. N. Zare, *Mol. Photochem.* **1972**, *4*, 1–37.

[37] J. Solomon, *J. Chem. Phys.* **1967**, *47*, 889–895.

[38] B. Whitaker, *Imaging in Molecular Dynamics: Technology and Applications*, Cambridge University press, Cambridge, **2003**.

[39] C. Jonah, *J. Chem. Phys.* **1971**, *55*, 1915–1922.

[40] L. Gamer, D. Schulz, C. Enss, A. Fleischmann, L. Gastaldo, S. Kempf, C. Krantz, O. Novotný, D. Schwalm, A. Wolf, *J. Low Temp. Phys.* **2016**, *184*, 839–844.

[41] J. Mikosch, U. Frühling, S. Trippel, D. Schwalm, M. Weidemüller, R. Wester, *Phys. Chem. Chem. Phys.* **2006**, *8*, 2990–2999.

[42] G. Sarma, S. Marinakis, J. J. Ter Meulen, D. H. Parker, K. G. McKendrick, *Nat. Chem.* **2012**, *4*, 985–989.

[43] J. N. Bull, J. W. Lee, C. Vallance, *Phys. Rev. A* **2015**, *91*, 022704.

[44] J. N. Bull, J. W. Lee, C. Vallance, *Phys. Rev. A* **2017**, *96*, 042704.

[45] D. Heathcote, P. A. Robertson, A. A. Butler, C. Ridley, J. Lomas, M. Buffett, M. Bell, C. Vallance, *Faraday Discuss.* **2022**, *238*, 682–699.

[46] S. H. Gardiner, M. L. Lipciuc, C. Vallance, *J. Phys. Chem. A* **2015**, *119*, 12218–12223.

[47] S. H. Gardiner, M. L. Lipciuc, T. N. Karsili, M. N. Ashfold, C. Vallance, *Phys. Chem. Chem. Phys.* **2015**, *17*, 4096–4106.

[48] C. R. Gebhardt, T. P. Rakitzis, P. C. Samartzis, V. Ladopoulos, T. N. Kitsopoulos, *Rev. Sci. Instrum.* **2001**, *72*, 3848–3853.

[49] D. Townsend, M. P. Minitti, A. G. Suits, *Rev. Sci. Instrum.* **2003**, *74*, 2530–2539.

[50] D. Townsend, S. A. Lahankar, S. K. Lee, S. D. Chambreau, A. G. Suits, X. Zhang, J. Rheinecker, L. B. Harding, J. M. Bowman, *Science* **2004**, *306*, 1158–1161.

[51] J. W. Lee, H. Köckert, D. Heathcote, D. Popat, R. T. Chapman, G. Karras, P. Majchrzak, E. Springate, C. Vallance, *Commun. Chem.* **2020**, *3*, 72.

[52] J. L. Kinsey, *J. Chem. Phys.* **1977**, *66*, 2560–2565.

[53] R. Schmiedl, H. Dugan, W. Meier, K. H. Welge, *Zeitschrift für Phys. A Atoms Nucl.* **1982**, *304*, 137–142.

[54] W. D. Philipps, J. A. Serri, D. J. Ely, D. E. Pritchard, K. R. Way, J. L. Kinsey, *Phys. Rev. Lett.* **1978**, *41*, 937–940.

[55] T. Streibel, R. Zimmermann, *Annu. Rev. Anal. Chem.* **2014**, *7*, 361–381.

[56] M. Brouard, C. Vallance, *Tutorials in Molecular Reaction Dynamics 1st ed.*, Royal Society of Chemistry, Cambridge, UK, **2010**.

[57] M. Cardona, L. Ley, *Photoemission in Solids I: General Principles: (Topics in Applied Physics, vol.26) 3rd ed.*, Springer, Berlin, Heidelberg, New York, **1978**.

[58] S. Hüfner, *Photoelectron Spectroscopy. Principles and Applications 3rd ed.*, Springer, Berlin, Heidelberg, New York, **2003**.

[59] M. S. Scholz, W. G. Fortune, O. Tau, H. H. Fielding, *J. Phys. Chem. Lett.* **2022**, *13*, 6889–6895.

[60] W. G. Fortune, M. S. Scholz, H. H. Fielding, *Acc. Chem. Res.* **2022**, *55*, 3631–3640.

[61] O. Tau, A. Henley, A. N. Boichenko, N. N. Kleshchina, R. Riley, B. Wang, D. Winning, R. Lewin, I. P. Parkin, J. M. Ward, H. C. Hailes, A. V. Bochenkova, H. H. Fielding, *Nat. Commun.* **2022**, *13*, 507.

[62] K. Robertson, W. G. Fortune, J. A. Davies, A. Boichenko, M. S. Scholz, O. Tau, A. V. Bochenkova, H. H. Fielding, *Chem. Sci.* **2023**, *14*, 3257–3264.

[63] D. Imanbaew, Y. Nosenko, C. Kerner, K. Chevalier, F. Rupp, C. Riehn, W. R. Thiel, R. Diller, *Chem. Phys.* **2014**, *442*, 53–61.

[64] N. C. Cole-Filipiak, J. Troß, P. Schrader, L. M. McCaslin, K. Ramasesha, *J. Chem. Phys.* **2022**, *156*, 144306.

[65] R. Geneaux, H. J. Marroux, A. Guggenmos, D. M. Neumark, S. R. Leone, *Philos. Trans. R. Soc. A* **2019**, *377*, 20170463.

[66] A. D. Smith, T. Balčiu Nas, Y. P. Chang, C. Schmidt, K. Zinchenko, F. B. Nunes, E. Rossi, V. Svoboda, Z. Yin, J. P. Wolf, H. J. Wörner, *J. Phys. Chem. Lett.* **2020**, *11*, 1981–1988.

[67] Z. Hamid, A. Wadsworth, E. Rezasoltani, S. Holliday, M. Azzouzi, M. Neophytou, A. A. Guilbert, Y. Dong, M. S. Little, S. Mukherjee, A. A. Herzing,

H. Bristow, R. J. Kline, D. M. DeLongchamp, A. A. Bakulin, J. R. Durrant, J. Nelson, I. McCulloch, *Adv. Energy Mater.* **2020**, *10*, 1903248.

[68] W. R. Gentry, C. F. Giese, *Rev. Sci. Instrum.* **1978**, *49*, 595–600.

[69] D. Irimia, D. Dobrikov, R. Kortekaas, H. Voet, D. A. Van Den Ende, W. A. Groen, M. H. Janssen, *Rev. Sci. Instrum.* **2009**, *80*, 113303.

[70] M. R. Adriaens, W. Allison, B. Feuerbacher, *J. Phys. E.* **1981**, *14*, 1375–1377.

[71] O. F. Hagena, *Rev. Sci. Instrum.* **1991**, *62*, 2038–2039.

[72] D. Proch, T. Trickl, *Rev. Sci. Instrum.* **1989**, *60*, 713–716.

[73] M. Hillenkamp, S. Keinan, U. Even, *J. Chem. Phys.* **2003**, *118*, 8699–8705.

[74] W. Christen, K. Rademann, U. Even, *J. Phys. Chem. A* **2010**, *114*, 11189–11201.

[75] D. Milesevic, D. Popat, P. Gellersen, Z. Liu, J. Stimson, A. Robertson, Patrick, A. Green, C. Vallance, *Rev. Sci. Instrum.* **2023**, *94*, 114105.

[76] U. Even, *Adv. Chem.* **2014**, *2014*, 636042.

[77] U. Even, *EPJ Tech. Instrum.* **2015**, *2*, 17.

[78] J. W. Lee, D. S. Tikhonov, P. Chopra, S. Maclot, A. L. Steber, S. Gruet, F. Allum, R. Boll, X. Cheng, S. Düsterer, B. Erk, D. Garg, L. He, D. Heathcote, M. Johny, M. M. Kazemi, H. Köckert, J. Lahl, A. K. Lemmens, D. Loru, R. Mason, E. Müller, T. Mullins, P. Olshin, C. Passow, J. Peschel, D. Ramm, D. Rompotis, N. Schirmel, S. Trippel, J. Wiese, F. Ziaee, S. Bari, M. Burt, J. Küpper, A. M. Rijs, D. Rolles, S. Techert, P. Eng-Johnsson, M. Brouard, C. Vallance, B. Manschwetus, M. Schnell, *Nat. Commun.* **2021**, *12*, 6107.

[79] J. Wiese, J. Onvlee, S. Trippel, J. Küpper, *Phys. Rev. Res.* **2021**, *3*, 013089.

[80] S. Maclot, J. Lahl, J. Peschel, H. Wikmark, P. Rudawski, F. Brunner, H. Coudert-Alteirac, S. Indrajith, B. A. Huber, S. Díaz-Tendero, N. F. Aguirre, P. Rousseau, P. Johnsson, *Sci. Rep.* **2020**, *10*, 2884.

[81] A. Abdelaziz, D. H. Zaitsau, A. V. Buzyurov, S. P. Verevkin, C. Schick, *Phys. Chem. Chem. Phys.* **2020**, *22*, 838–853.

[82] G. Meijer, M. S. de Vries, H. E. Hunziker, H. R. Wendt, *Appl. Phys. B* **1990**, *51*, 395–403.

[83] A. Shachar, I. Kallos, M. S. De Vries, I. Bar, *J. Phys. B At. Mol. Opt. Phys.* **2021**, *54*, 175401.

[84] S. I. Ishiuchi, K. Yamada, H. Oba, H. Wako, M. Fujii, *Phys. Chem. Chem. Phys.* **2016**, *18*, 23277–23284.

[85] S. Bakels, M. P. Gaigeot, A. M. Rijs, *Chem. Rev.* **2020**, *120*, 3233–3260.

[86] A. Iskra, A. S. Gentleman, A. Kartouzian, M. J. Kent, A. P. Sharp, S. R. Mackenzie, *J. Phys. Chem. A* **2017**, *121*, 133–140.

[87] E. I. Brewer, A. E. Green, A. S. Gentleman, P. W. Beardsmore, P. A. Pearcy, G. Meizyte, J. Pickering, S. R. Mackenzie, *Phys. Chem. Chem. Phys.* **2022**, *24*, 22716–22723.

[88] N. Teschmit, K. Dlugolecki, D. Gusa, I. Rubinsky, D. A. Horke, J. Küpper, *J. Chem. Phys.* **2017**, *147*, 144204.

[89] J. B. Fenn, M. Mann, C. K. A. I. Meng, S. F. Wong, C. M. Whitehouse, *Science* **1989**, *246*, 64–71.

[90] M. Wilm, *Mol. Cell. Proteomics* **2011**, *10*, M111.009407.

[91] K. Tanaka, H. Waki, Y. Ido, S. Akita, Y. Yoshida, T. Yoshida, T. Matsuo, *Rapid Commun. Mass Spectrom.* **1988**, *2*, 151–153.

[92] K. Dreisewerd, *Chem. Rev.* **2003**, *103*, 395–426.

[93] B. Lindner, U. Seydel, *Anal. Chem.* **1985**, *57*, 895–899.

[94] B. Lindner, *Int. J. Mass Spectrom. Ion Process.* **1991**, *103*, 203–218.

[95] A. V. Zinovev, I. V. Veryovkin, J. F. Moore, M. J. Pellin, *Anal. Chem.* **2007**, *79*, 8232–8241.

[96] F. Calegari, A. Trabattoni, A. Palacios, D. Ayuso, M. C. Castrovilli, J. B. Greenwood, P. Decleva, F. Martín, M. Nisoli, *J. Phys. B At. Mol. Opt. Phys.* **2016**, *49*, 142001.

[97] Z. Huang, T. Ossenbrüggen, I. Rubinsky, M. Schust, D. A. Horke, J. Küpper, *Anal. Chem.* **2018**, *90*, 3920–3927.

[98] U. Sezer, L. Wörner, J. Horak, L. Felix, J. Tüxen, C. Götz, A. Vaziri, M. Mayor, M. Arndt, *Anal. Chem.* **2015**, *87*, 5614–5619.

[99] V. V. Golovlev, S. L. Allman, W. R. Garrett, N. I. Taranenko, C. H. Chen, *Int. J. Mass Spectrom. Ion Process.* **1997**, *169-170*, 69–78.

[100] W. P. Peng, Y. C. Yang, M. W. Kang, Y. K. Tzeng, Z. Nie, H. C. Chang, W. Chang, C. H. Chen, *Angew. Chem. Int. Ed.* **2006**, *45*, 1423–1426.

[101] J. C. Poully, J. Miles, S. De Camillis, A. Cassimi, J. B. Greenwood, *Phys. Chem. Chem. Phys.* **2015**, *17*, 7172–7180.

[102] O. Ghafur, S. W. Crane, M. Ryszka, J. Bockova, A. Rebelo, L. Saalbach, S. De Camillis, J. B. Greenwood, S. Eden, D. Townsend, *J. Chem. Phys.* **2018**, *149*, 034301.

[103] S. W. Crane, O. Ghafur, L. Saalbach, M. J. Paterson, D. Townsend, *Chem. Phys. Lett.* **2020**, *738*, 136870.

[104] S. W. Crane, O. Ghafur, T. Y. Cowie, A. G. Lindsay, J. O. Thompson, J. B. Greenwood, M. W. Bebbington, D. Townsend, *Phys. Chem. Chem. Phys.* **2019**, *21*, 8152–8160.

[105] P. J. van der Burgt, M. A. Brown, J. Bockova, A. Rebelo, M. Ryszka, J. C. Poully, S. Eden, *Eur. Phys. J. D* **2019**, *73*, 184.

[106] J. Bocková, A. Rebelo, M. Ryszka, R. Pandey, D. Mészáros, P. Limão-Vieira, P. Papp, N. J. Mason, D. Townsend, K. L. Nixon, V. Vizcaino, J. Poully, S. Eden, *RSC Adv.* **2021**, *11*, 20612–20621.

[107] C. Sparling, S. W. Crane, L. Ireland, R. Anderson, O. Ghafur, J. B. Greenwood, D. Townsend, *Phys. Chem. Chem. Phys.* **2023**, *25*, 6009–6015.

[108] S. Wang, Y. Dauletyarov, P. Krüger, D. A. Horke, *Phys. Chem. Chem. Phys.* **2023**, *25*, 12322–12330.

[109] Y. Dauletyarov, S. Wang, D. A. Horke, *J. Am. Soc. Mass Spectrom.* **2023**, *34*, 1538–1542.

[110] S. Wang, G. L. Abma, P. Krüger, A. van Roij, M. Balster, N. Janssen, D. A. Horke, *Eur. Phys. J. D* **2022**, *76*, 128.

[111] R. E. Blankenship, *Molecular Mechanism of Photosynthesis 3rd ed.*, Wiley, West Sussex, UK, **2021**.

[112] J. Piette, M. Paule, M. Louis, J. Decuype, *Photochem. Photobiol.* **1986**, *44*, 793–802.

[113] A. Stary, A. Sarasin, *Methods Enzymol.* **2000**, *319*, 153–165.

[114] A. P. Schuch, C. F. M. Menck, *J. Photochem. Photobiol. B Biol.* **2010**, *99*, 111–116.

[115] R. P. Rastogi, Richa, A. Kumar, M. B. Tyagi, R. P. Sinha, *J. Nucleic Acids* **2010**, *2010*, 592980.

[116] D. Milešević, J. Stimson, D. Popat, P. Robertson, C. Vallance, *Phys. Chem. Chem. Phys.* **2023**, *25*, 25322–25330.

[117] S. Tonzani, C. H. Greene, *J. Chem. Phys.* **2006**, *125*, 094504.

[118] C. J. Colyer, S. M. Bellm, B. Lohmann, G. F. Hanne, O. Al-Hagan, D. H. Madison, C. G. Ning, *J. Chem. Phys.* **2010**, *133*, 124302.

[119] X. Ren, E. Wang, A. D. Skitnevskaya, A. B. Trofimov, K. Gokhberg, A. Dorn, *Nat. Phys.* **2018**, *14*, 1062–1066.

[120] N. Y. Aouina, Z. E. A. Chaoui, *Surf. Interface Anal.* **2018**, *50*, 939–946.

[121] W. Wolff, B. Rudek, L. A. Da Silva, G. Hilgers, E. C. Montenegro, M. G. Homem, *J. Chem. Phys.* **2019**, *151*, 064304.

[122] H. J. Lüdde, M. Horbatsch, T. Kirchner, *J. Phys. B At. Mol. Opt. Phys.* **2019**, *52*, 195203.

[123] A. García-Abenza, A. I. Lozano, L. Álvarez, J. C. Oller, F. Blanco, P. Stokes, R. D. White, J. de Urquijo, P. Limão-Vieira, D. B. Jones, M. J. Brunger, G. García, *Eur. Phys. J. D* **2021**, *75*, 303.

[124] Y. Yagci, A. Ledwith, *J. Polym. Sci. Part A Polym. Chem.* **1988**, *26*, 1911–1918.

[125] M. R. Rodrigues, M. G. Neumann, *Macromol. Chem. Phys.* **2001**, *202*, 2776–2782.

[126] A. A. Scala, E. W. G. Diau, Z. H. Kim, A. H. Zewail, *J. Chem. Phys.* **1998**, *108*, 7933–7936.

[127] T. J. Wasowicz, A. Kivimäki, M. Dampc, M. Coreno, M. De Simone, M. Zubek, *Phys. Rev. A* **2011**, *83*, 033411.

[128] D. Milesevic, D. Popat, P. Robertson, C. Vallance, *Phys. Chem. Chem. Phys.* **2022**, *24*, 28343–28352.

[129] N. R. Forde, T. L. Myers, L. J. Butler, *Faraday Discuss.* **1997**, *108*, 221–242.

[130] N. R. Forde, L. J. Butler, *J. Chem. Phys.* **1999**, *110*, 8954–8968.

[131] S. Shin, A. Kurawaki, Y. Hamada, K. Shinya, K. Ohno, A. Tohara, M. Sato, *J. Mol. Struct.* **2006**, *791*, 30–40.

[132] M. Ruzi, D. T. Anderson, *J. Chem. Phys.* **2012**, *137*, 194313.

[133] X. Qiu, Z. Ding, Y. Xu, Y. Wang, B. Zhang, *Phys. Rev. A* **2014**, *89*, 033405.

[134] P. Salén, V. Yatsyna, L. Schio, R. Feifel, R. Richter, M. Alagia, S. Stranges, V. Zhaunerchyk, *J. Chem. Phys.* **2016**, *144*, 244310.

[135] M. L. Lipciuc, S. H. Gardiner, T. N. Karsili, J. W. Lee, D. Heathcote, M. N. Ashfold, C. Vallance, *J. Chem. Phys.* **2017**, *147*, 013941.

[136] D. Liu, W. Fang, Z. Lin, X. Fu, *J. Chem. Phys.* **2002**, *117*, 9241–9247.

[137] M. Eckert-Maksić, I. Antol, *J. Phys. Chem. A* **2009**, *113*, 12582–12590.

[138] M. Eckert-Maksić, M. Vazdar, M. Ruckenbauer, M. Barbatti, T. Müller, H. Lischka, *Phys. Chem. Chem. Phys.* **2010**, *12*, 12719–12726.

[139] A. Shastri, A. K. Das, S. Krishnakumar, P. J. Singh, B. N. Raja Sekhar, *J. Chem. Phys.* **2017**, *147*, 224305.

[140] M. B. Shundalau, P. S. Chybirai, A. I. Komyak, A. P. Zazhogin, M. A. Ksenofontov, D. S. Umreiko, *J. Appl. Spectrosc.* **2011**, *78*, 326–336.

[141] X. Zhou, J. A. Krauser, D. R. Tate, A. S. VanBuren, J. A. Clark, P. R. Moody, R. Liu, *J. Phys. Chem.* **1996**, *100*, 16822–16827.

[142] T. C. Jao, I. Scott, D. Steele, *J. Mol. Spectrosc.* **1982**, *92*, 1–17.

[143] V. Renugopalakrishnan, G. Madrid, G. Cuevas, A. T. Hagler, *Proc. Indian Acad. Sci. Chem. Sci.* **2000**, *112*, 35–42.

[144] R. Saladino, C. Crestini, G. Costanzo, R. Negri, E. Di Mauro, *Bioorganic Med. Chem.* **2001**, *9*, 1249–1253.

[145] R. E. Laflamme, R. A. Hites, *Geochim. Cosmochim. Acta* **1978**, *42*, 289–303.

[146] F. P. Perera, *Science* **1997**, *278*, 1068–1073.

[147] K. Ravindra, R. Sokhi, R. Van Grieken, *Atmos. Environ.* **2008**, *42*, 2895–2921.

[148] A. L. C. Lima, J. W. Farrington, C. M. Reddy, *Environ. Forensics* **2005**, *6*, 109–131.

[149] K. Kawamura, I. Suzuki, Y. Fuji, O. Watanabe, *Naturwissenschaften* **1994**, *81*, 502–505.

[150] P. Masclet, V. Hoyau, J. L. Jaffrezo, H. Cachier, *Atmos. Environ.* **2000**, *34*, 3195–3207.

[151] N. Ohkouchi, K. Kawamura, H. Kawahata, *Environ. Sci. Technol.* **1999**, *33*, 3086–3090.

[152] P. Fernández, R. M. Vilanova, J. O. Grimalt, *Environ. Sci. Technol.* **1999**, *33*, 3716–3722.

[153] Sakshi, S. K. Singh, A. K. Haritash, *Int. J. Environ. Sci. Technol.* **2019**, *16*, 6489–6512.

[154] A. B. Patel, S. Shaikh, K. R. Jain, C. Desai, D. Madamwar, *Front. Microbiol.* **2020**, *11*, 562813.

[155] J. M. Neff in *Bioaccumulation Mar. Org. Eff. Contam. from oil well Prod. water*, Elsevier, Amsterdam, **2002**, chapter 15, pp. 241–318.

[156] K. Hylland, *J. Toxicol. Environ. Heal. Part A* **2006**, *69*, 109–123.

[157] W. J. Hong, H. Jia, Y. F. Li, Y. Sun, X. Liu, L. Wang, *Ecotoxicol. Environ. Saf.* **2016**, *128*, 11–20.

[158] S. A. da Silva, E. A. S. Torres, A. P. de Almeida, G. R. Sampaio, *Food Chem.* **2018**, *245*, 798–805.

[159] L. Wang, C. Li, B. Jiao, Q. Li, H. Su, J. Wang, F. Jin, *Sci. Total Environ.* **2018**, *616-617*, 288–295.

[160] Y. Sun, S. Wu, G. Gong, *Trends Food Sci. Technol.* **2019**, *83*, 86–98.

[161] T. Rengarajan, P. Rajendran, N. Nandakumar, B. Lokeshkumar, P. Rajendran, I. Nishigaki, *Asian Pac. J. Trop. Biomed.* **2015**, *5*, 182–189.

[162] G. Lagache, H. Dole, J. Puget, P. G. Perez-Gonzalez, E. Le Floc'h, G. H. Rieke, C. Papovich, E. Egami, A. Alonso-Herrero, C. W. Engelbracht, K. D. Gordon, K. A. Misselt, J. E. Morrison, *Astrophys. J. Suppl. Ser.* **2004**, *154*, 112–117.

[163] C. Joblin, A. Tielens, *EAS Publ. Ser.* **2011**, *46*, 3–10.

[164] A. Leger, J. L. Puget, *Astron. Astrophys.* **1984**, *137*, L5–L8.

[165] L. J. Allamandola, A. G. G. M. Tielens, J. R. Baker, *Astrophys. J.* **1985**, *290*, L25–L28.

[166] A. Li, *Nat. Astron.* **2020**, *4*, 339–351.

[167] E. K. Campbell, M. Holz, D. Gerlich, J. P. Maier, *Nature* **2015**, *523*, 322–323.

[168] M. Frenklach, D. W. Clary, W. C. Gardiner, S. E. Stein, *Symp. Combust.* **1984**, *20*, 887–901.

[169] M. Frenklach, D. W. Klarry, M. K. Ramachandra, *Shock Tube Study of the Fuel Structure Effects on the Chemical Kinetic Mechanisms Responsible for Soot Formation Part II*, Tech. Rep., NASA Contractor Report, Baton Rouge, Louisiana, **1985**.

[170] E. Reizer, B. Viskolcz, B. Fiser, *Chemosphere* **2022**, *291*, 132793.

[171] J. M. Gray, J. Bossert, Y. Shyur, B. Saarel, T. C. Briles, H. J. Lewandowski, *J. Chem. Phys.* **2021**, *154*, 024201.

[172] A. H. Kung, J. F. Young, S. E. Harris, *Appl. Phys. Lett.* **1973**, *22*, 301–302.

[173] A. H. Kung, J. F. Young, S. E. Harris, *Appl. Phys. Lett.* **1976**, *28*, 239.

[174] N. P. Lockyer, J. C. Vickerman, *Laser Chem.* **1997**, *17*, 139–159.

[175] J. L. Wiza, *Nucl. Instruments Methods* **1979**, *162*, 587–601.

[176] J. Oberheide, P. Wilhelms, M. Zimmer, *Meas. Sci. Technol.* **1997**, *8*, 351–354.

[177] G. W. Fraser, *Int. J. Mass Spectrom.* **2002**, *215*, 13–30.

[178] C. D. Ertley, O. H. Siegmund, J. Hull, A. Tremsin, A. O'Mahony, C. A. Craven, M. J. Minot, *IEEE Trans. Nucl. Sci.* **2017**, *64*, 1774–1780.

[179] P. Lecoq in *Part. Phys. Ref. Libr., Vol. 2*, C. W. Fabjan, H. Schopper (Eds.), Springer, Cham, Switzerland, **2020**, p. 45.

[180] B. Winter, S. J. King, M. Brouard, C. Vallance, *Rev. Sci. Instrum.* **2014**, *85*, 023306.

[181] A. Nomerotski, M. Brouard, E. Campbell, A. Clark, J. Crooks, J. Fopma, J. J.

John, A. J. Johnsen, C. Slater, R. Turchetta, C. Vallance, E. Wilman, W. H. Yuen, *J. Instrum.* **2010**, *5*, C07007.

[182] E. S. Wilman, S. H. Gardiner, A. Nomerotski, R. Turchetta, M. Brouard, C. Vallance, *Rev. Sci. Instrum.* **2012**, *83*, 013304.

[183] A. T. Clark, J. P. Crooks, I. Sedgwick, R. Turchetta, J. W. Lee, J. J. John, E. S. Wilman, L. Hill, E. Halford, C. S. Slater, B. Winter, W. H. Yuen, S. H. Gardiner, M. L. Lipciuc, M. Brouard, A. Nomerotski, C. Vallance, *J. Phys. Chem. A* **2012**, *116*, 10897–10903.

[184] X. Llopart, R. Ballabriga, M. Campbell, L. Tlustos, W. Wong, *Nucl. Instruments Methods Phys. Res. A* **2007**, *581*, 485–494.

[185] T. Poikela, J. Plosila, T. Westerlund, M. Campbell, M. D. Gaspari, X. Llopart, V. Gromov, R. Kluit, M. V. Beuzekom, F. Zappon, V. Zivkovic, C. Brezina, K. Desch, Y. Fu, A. Kruth, *J. Instrum.* **2014**, *9*, C05013.

[186] F. Jensen, *Introduction to Computational Chemistry 2nd ed.*, Wiley, West Sussex, UK, **2007**.

[187] E. G. Lewars, *Computational Chemistry: Introduction to the Theory and Applications of Molecular and Quantum Mechanics 2nd ed., Vol. 3*, Springer, Heidelberg, **2011**.

[188] M. J. Frisch, G. W. Trucks, H. B. Schlegel, G. E. Scuseria, J. R. M. A. Robb, Cheeseman, G. Scalmani, V. Barone, G. A. Petersson, H. Nakatsuji, M. C. X. Li, A. Marenich, J. Bloino, B. G. Janesko, R. Gomperts, B. Mennucci, H. P. Hratchian, J. V. Ortiz, A. F. Izmaylov, J. L. Sonnenberg, D. Williams-Young, F. Ding, F. Lipparini, F. Egidi, J. Goings, B. Peng, A. Petrone, T. Henderson, D. Ranasinghe, V. G. Zakrzewski, J. Gao, N. Rega, G. Zheng, W. Liang, M. Hada, M. Ehara, K. Toyota, R. Fukuda, J. Hasegawa, M. Ishida, T. Nakajima, Y. Honda, O. Kitao, H. Nakai, T. Vreven, K. Throssell, J. A. Montgomery, J. E. Peralta, F. Ogliaro, M. Bearpark, J. J. Heyd, E. Brothers, K. N. Kudin, V. N. Staroverov, T. Keith, R. Kobayashi, J. Normand, K. Raghavachari, A. Rendell, J. C. Burant, S. S. Iyengar, J. Tomasi, M. Cossi, J. M. Millam, M. Klene, C. Adamo, R. Cammi, J. W. Ochterski, R. L. Martin, K. Morokuma, O. Farkas, J. B. Foresman, D. J. Fox, *Gaussian 09*, **2016**.

[189] F. Aquilante, J. Autschbach, A. Baiardi, S. Battaglia, V. A. Borin, L. F. Chibotaru, I. Conti, L. De Vico, M. Delcey, I. F. Galván, N. Ferré, L. Freitag, M. Garavelli, X. Gong, S. Knecht, E. D. Larsson, R. Lindh, M. Lundberg, P. Å. Malmqvist, A. Nenov, J. Norell, M. Odelius, M. Olivucci, T. B. Pedersen, L. Pedraza-González, Q. M. Phung, K. Pierloot, M. Reiher, I. Schapiro,

J. Segarra-Martí, F. Segatta, L. Seijo, S. Sen, D. C. Sergentu, C. J. Stein, L. Ungur, M. Vacher, A. Valentini, V. Veryazov, *J. Chem. Phys.* **2020**, *152*, 214117.

[190] B.-Y. Chang, R. C. Hoetzlein, J. A. Mueller, J. D. Geiser, P. L. Houston, *Rev. Sci. Instrum.* **1998**, *69*, 1665–1670.

[191] N. H. Abel, *J. für die Reine und Angew. Math.* **1826**, *1*, 153–157.

[192] A. J. R. Heck, D. W. Chandler, *Annu. Rev. Phys. Chem.* **1995**, *46*, 335–372.

[193] A. T. Eppink, S.-M. Wu, B. Whitaker in *Imaging Mol. Dyn. Technol. Appl.*, B. Whitaker (Ed.), Cambridge University press, Cambridge, **2003**, chapter 3, pp. 65–112.

[194] A. N. Tikhonov, *Sov. Math. Dockl* **1963**, *4*, 1035–1038.

[195] V. Dribinski, A. Ossadtchi, V. A. Mandelshtam, H. Reisler, *Rev. Sci. Instrum.* **2002**, *73*, 2634–2642.

[196] G. A. Garcia, L. Nahon, I. Powis, *Rev. Sci. Instrum.* **2004**, *75*, 4989–4996.

[197] T. Gerber, Y. Liu, G. Knopp, P. Hemberger, A. Bodi, P. Radi, Y. Sych, *Rev. Sci. Instrum.* **2013**, *84*, 033101.

[198] D. deB. Darwent, *Bond Dissociation Energies of Simple Molecules*, National Standard Reference Data System, Washington DC, **1970**.

[199] R. Micha, S. K. Wallace, D. Mozaffarian, *Circulation* **2010**, *121*, 2271–2283.

[200] L. J. Frasinski, K. Codling, P. A. Hatherly, *Science* **1989**, *246*, 1029–1031.

[201] K. E. McCulloh, T. E. Sharp, H. M. Rosenstock, *J. Chem. Phys.* **1965**, *42*, 3501–3509.

[202] C. Vallance, D. Heathcote, J. W. Lee, *J. Phys. Chem. A* **2021**, *125*, 1117–1133.

[203] D. Heathcote, Ph.D. thesis, University of Oxford, **2020**.

[204] T. Kitamura, T. Nishide, H. Shiromaru, Y. Achiba, N. Kobayashi, *J. Chem. Phys.* **2001**, *115*, 5–6.

[205] M. Pitzer, M. Kunitski, A. S. Johnson, T. Jahnke, H. Sann, F. Sturm, L. P. H. Schmidt, H. Schmidt-Böcking, R. Dörner, J. Stohner, J. Kiedrowski, M. Reggelin, S. Marquardt, A. Schießer, R. Berger, M. S. Schöffler, *Science* **2013**, *341*, 1096–1100.

[206] F. Légaré, K. F. Lee, I. V. Litvinyuk, P. W. Dooley, S. S. Wesolowski, P. R. Bunker, P. Dombi, F. Krausz, A. D. Bandrauk, D. M. Villeneuve, P. B. Corkum, *Phys. Rev. A* **2005**, *71*, 013415.

[207] C. Wu, C. Wu, Y. Fan, X. Xie, P. Wang, Y. Deng, Y. Liu, Q. Gong, *J. Chem. Phys.* **2015**, *142*, 124303.

[208] L. Chen, E. Wang, W. Zhao, M. Gong, X. Shan, X. Chen, *J. Chem. Phys.* **2023**, *158*, 054301.

[209] J. D. Pickering, K. Amini, M. Brouard, M. Burt, I. J. Bush, L. Christensen, A. Lauer, J. H. Nielsen, C. S. Slater, H. Stapelfeldt, *J. Chem. Phys.* **2016**, *144*, 161105.

[210] C. Cheng, L. J. Frasinski, G. Moğol, F. Allum, A. J. Howard, D. Rolles, P. H. Bucksbaum, M. Brouard, R. Forbes, T. Weinacht, *Phys. Rev. Lett.* **2023**, *130*, 093001.

[211] J. Rajput, T. Severt, B. Berry, B. Jochim, P. Feizollah, B. Kaderiya, M. Zohrabi, U. Ablikim, F. Ziaee, K. P. Raju, D. Rolles, A. Rudenko, K. D. Carnes, B. D. Esry, I. Ben-Itzhak, *Phys. Rev. Lett.* **2018**, *120*, 103001.

[212] J. W. McManus, T. Walmsley, K. Nagaya, J. R. Harries, Y. Kumagai, H. Iwayama, M. N. Ashfold, M. Britton, P. H. Bucksbaum, B. Downes-Ward, T. Driver, D. Heathcote, P. Hockett, A. J. Howard, E. Kukk, J. W. Lee, Y. Liu, D. Milesevic, R. S. Minns, A. Niozu, J. Niskanen, A. J. Orr-Ewing, S. Owada, D. Rolles, P. A. Robertson, A. Rudenko, K. Ueda, J. Unwin, C. Vallance, M. Burt, M. Brouard, R. Forbes, F. Allum, *Phys. Chem. Chem. Phys.* **2022**, *24*, 22699–22709.

[213] D. Heathcote, C. Vallance, *Covariance Inversion (in preparation)*, **2023**.

[214] D. Heathcote, C. Vallance, *J. Phys. Chem. A* **2021**, *125*, 7092–7098.

[215] V. Zhaunerchyk, L. J. Frasinski, J. H. Eland, R. Feifel, *Phys. Rev. A* **2014**, *89*, 053418.

[216] L. J. Frasinski, A. J. Giles, P. A. Hatherly, J. H. Posthumus, M. R. Thompson, K. Codling, *J. Electron Spectros. Relat. Phenomena* **1996**, *79*, 367–371.

[217] L. J. Frasinski, *J. Phys. B At. Mol. Opt. Phys.* **2016**, *49*, 152004.

[218] D. Popat, Ph.D. thesis, University of Oxford, **2022**.

[219] J. Stimson, *A Photofragmentation Study Of DNA Related Heterocyclic Molecules Using Velocity Map Imaging*, **2022**.

[220] B. L. W. Pickett, N. J. Hoeflich, T.-C. Liu, *J. Am. Chem. Soc.* **1951**, *73*, 4865–4869.

[221] G. J. Hernandez, *J. Chem. Phys.* **1963**, *38*, 2233–2242.

[222] J. Doucet, P. Sauvageau, C. Sandokfy, *Chem. Phys. Lett.* **1972**, *17*, 316–319.

[223] L. J. Bremner, M. G. Curtis, I. C. Walker, *J. Chem. Soc. Faraday Trans.* **1991**, *87*, 1049–1055.

[224] A. Giuliani, P. Limão-Vieira, D. Duflot, A. R. Milosavljevic, B. P. Marinkovic, S. V. Hoffmann, N. Mason, J. Delwiche, M. J. Hubin-Franskin, *Eur. Phys. J. D* **2009**, *51*, 97–108.

[225] B. Cadioli, E. Gallinella, C. Coulombeau, H. Jobic, G. Berthier, *J. Phys. Chem.* **1993**, *97*, 7844–7856.

[226] A. H. Mamleev, L. N. Gunderova, R. V. Galeev, *J. Struct. Chem.* **2001**, *42*, 365–370.

[227] D. G. Melnik, S. Gopalakrishnan, T. A. Miller, F. C. De Lucia, *J. Chem. Phys.* **2003**, *118*, 3589–3599.

[228] V. M. Rayón, J. A. Sordo, *J. Chem. Phys.* **2005**, *122*, 204303.

[229] T. Yang, G. Su, C. Ning, J. Deng, F. Wang, S. Zhang, X. Ren, Y. Huang, *J. Phys. Chem. A* **2007**, *111*, 4927–4933.

[230] P. Duffy, J. A. Sordo, F. Wang, *J. Chem. Phys.* **2008**, *128*, 125102.

[231] S. M. Park, Y. R. Lee, D. W. Kang, H. L. Kim, C. H. Kwon, *Phys. Chem. Chem. Phys.* **2017**, *19*, 30362–30369.

[232] L. Paoloni, S. Rampino, V. Barone, *J. Chem. Theory Comput.* **2019**, *15*, 4280–4294.

[233] A. Röder, A. B. Skov, A. E. Boguslavskiy, R. Lausten, A. Stolow, *Phys. Chem. Chem. Phys.* **2020**, *22*, 26241–26254.

[234] S. H. Lee, *J. Chem. Phys.* **2009**, *131*, 224309.

[235] E. Tapavicza, I. Tavernelli, U. Rothlisberger, C. Filippi, M. E. Casida, *J. Chem. Phys.* **2008**, *129*, 124108.

[236] N. Gavrilov, S. Salzmann, C. M. Marian, *Chem. Phys.* **2008**, *349*, 269–277.

[237] S. Oesterling, O. Schalk, T. Geng, R. D. Thomas, T. Hansson, R. De Vivie-Riedle, *Phys. Chem. Chem. Phys.* **2017**, *19*, 2025–2035.

[238] M. Stenrup, *Chem. Phys.* **2012**, *397*, 18–25.

[239] M. N. Ashfold, M. Bain, C. S. Hansen, R. A. Ingle, T. N. Karsili, B. Marchetti, D. Murdock, *J. Phys. Chem. Lett.* **2017**, *8*, 3440–3451.

[240] N. Kotsina, S. L. Jackson, T. Malcomson, M. J. Paterson, D. Townsend, *Phys. Chem. Chem. Phys.* **2022**, *24*, 29423–29436.

[241] B. C. Roquitte, *J. Am. Chem. Soc.* **1969**, *91*, 7664–7667.

[242] J. Kramer, *J. Phys. Chem.* **1982**, *86*, 26–35.

[243] S. W. Benson, *J. Chem. Phys.* **1964**, *40*, 105–111.

[244] S. H. Lee, *Phys. Chem. Chem. Phys.* **2010**, *12*, 2655–2663.

[245] C. H. Greene, R. N. Zare, *Annu. Rev. Phys. Chem.* **1982**, *33*, 119–150.

[246] W. S. Hopkins, M. L. Lipciuc, S. H. Gardiner, C. Vallance, *J. Chem. Phys.* **2011**, *135*, 034308.

[247] S. SenGupta, H. P. Upadhyaya, A. Kumar, P. D. Naik, P. Bajaj, *J. Chem. Phys.* **2005**, *122*, 124309.

[248] S. Pedersen, J. K.Herek, A. H.Zewail, *Science* **1994**, *266*, 1359–1364.

[249] C. Doubleday, *J. Phys. Chem.* **1996**, *100*, 3520–3526.

[250] C. E. Crespo-Hernández, B. Cohen, P. M. Hare, B. Kohler, *Chem. Rev.* **2004**, *104*, 1977–2019.

[251] C. T. Middleton, K. De La Harpe, C. Su, Y. K. Law, C. E. Crespo-Hernández, B. Kohler, *Annu. Rev. Phys. Chem.* **2009**, *60*, 217–239.

[252] T. Gustavsson, R. Improta, D. Markovitsi, *J. Phys. Chem. Lett.* **2010**, *1*, 2025–2030.

[253] B. Marchetti, T. N. Karsili, M. N. Ashfold, W. Domcke, *Phys. Chem. Chem. Phys.* **2016**, *18*, 20007–20027.

[254] H. D. Hunt, W. T. Simpson, *J. Am. Chem. Soc.* **1953**, *75*, 4540–4543.

[255] K. Kaya, S. Nagakura, *Theor. Chim. Acta* **1967**, *7*, 117–123.

[256] L. Serrano-Andrés, M. P. Fülscher, *J. Am. Chem. Soc.* **1996**, *118*, 12190–12199.

[257] H. Basch, M. B. Robin, N. A. Kuebler, *J. Chem. Phys.* **1968**, *49*, 5007–5018.

[258] J. M. Gingell, N. J. Mason, H. Zhao, I. C. Walker, M. R. Siggel, *Chem. Phys.* **1997**, *220*, 191–205.

[259] D. H. Ter Steege, C. Lagrost, W. J. Buma, D. A. Leigh, F. Zerbetto, *J. Chem. Phys.* **2002**, *117*, 8270–8280.

[260] M. A. B. Larsen, T. I. Sølling, R. Forbes, A. E. Boguslavskiy, V. Makhija, K. Veyrinas, R. Lausten, A. Stolow, M. M. Zawadzki, L. Saalbach, N. Kotsina, M. J. Paterson, D. Townsend, *J. Chem. Phys.* **2019**, *150*, 054301.

[261] M. N. R. Ashfold, G. A. King, D. Murdock, M. G. D. Nix, T. A. A. Oliver, A. G. Sage, *Phys. Chem. Chem. Phys.* **2010**, *12*, 1218–1238.

[262] G. M. Roberts, V. G. Stavros, *Chem. Sci.* **2014**, *5*, 1698–1722.

[263] M. J. Paterson, D. Townsend, *Int. Rev. Phys. Chem.* **2020**, *39*, 517–567.

[264] M. E. Jacox, *NIST Chemistry Webbook, NIST Standard Reference Database No. 69*, National Institute of Standards and Technology, Gaithersburg, MD, **2022**.

[265] G. Tsaprailis, H. Nair, Á. Somogyi, V. H. Wysocki, W. Zhong, J. H. Futrell, S. G. Summerfield, S. J. Gaskell, *J. Am. Chem. Soc.* **1999**, *121*, 5142–5154.

[266] B. Paizs, S. Suhai, *Mass Spectrom. Rev.* **2004**, *24*, 508–548.

[267] A. C. Hopkinson, *Mass Spectrom. Rev.* **2009**, *28*, 655–671.

[268] K. Biemann, S. A. Martin, *Mass Spectrom. Rev.* **1987**, *6*, 1–75.

[269] A. R. Dongré, J. L. Jones, Á. Somogyi, V. H. Wysocki, *J. Am. Chem. Soc.* **1996**, *118*, 8365–8374.

[270] A. L. McCormack, A. Somogyi, A. R. Dongré, V. H. Wysocki, *Anal. Chem.* **1993**, *65*, 2859–2872.

[271] V. H. Wysocki, G. Tsaprailis, L. L. Smith, L. A. Breci, *J. Mass Spectrom.* **2000**, *35*, 1399–1406.

[272] A. G. Harrison, *Mass Spectrom. Rev.* **1997**, *16*, 201–217.

[273] W. Cui, M. S. Thompson, J. P. Reilly, *J. Am. Soc. Mass Spectrom.* **2005**, *16*, 1384–1398.

[274] Z. Li, M. M. Dawley, I. Carmichael, S. Ptasińska, *Int. J. Mass Spectrom.* **2016**, *410*, 36–46.

[275] A. G. Loudon, K. S. Webb, *Org. Mass Spectrom.* **1977**, *12*, 283–287.

[276] F. Aquilante, J. Autschbach, R. K. Carlson, L. F. Chibotaru, M. G. Delcey, L. De Vico, I. Fdez. Galván, N. Ferré, L. M. Frutos, L. Gagliardi, M. Garavelli, A. Giussani, C. E. Hoyer, G. Li Manni, H. Lischka, D. Ma, P. Å. Malmqvist, T. Müller, A. Nenov, M. Olivucci, T. B. Pedersen, D. Peng, F. Plasser, B. Pritchard, M. Reiher, I. Rivalta, I. Schapiro, J. Segarra-Martí, M. Stenrup, D. G. Truhlar, L. Ungur, A. Valentini, S. Vancoillie, V. Veryazov, V. P. Vysotskiy, O. Weingart, F. Zapata, R. Lindh, *J. Comput. Chem.* **2016**, *37*, 506–541.

[277] K. Levsen, F. W. McLafferty, *J. Am. Chem. Soc.* **1974**, *96*, 139–144.

[278] J. Yang, X. Zhu, T. J. Wolf, Z. Li, J. F. Pedro Nunes, R. Coffee, J. P. Cryan, M. Gühr, K. Hegazy, T. F. Heinz, K. Jobe, R. Li, X. Shen, T. Veccione, S. Weathersby, K. J. Wilkin, C. Yoneda, Q. Zheng, T. J. Martinez, M. Centurion, X. Wang, *Science* **2018**, *361*, 64–67.

[279] E. T. Karamatskos, S. Raabe, T. Mullins, A. Trabattoni, P. Stammer, G. Goldsztejn, R. R. Johansen, K. Długołecki, H. Stapelfeldt, M. J. Vrakking, S. Trippel, A. Rouzée, J. Küpper, *Nat. Commun.* **2019**, *10*, 3364.

[280] M. Dantus, M. J. Rosker, A. H. Zewail, *J. Chem. Phys.* **1987**, *87*, 2395–2397.

[281] V. Engel, H. Metiu, R. Almeida, R. A. Marcus, A. H. Zewail, *Chem. Phys. Lett.* **1988**, *152*, 1–7.

[282] M. Maiuri, M. Garavelli, G. Cerullo, *J. Am. Chem. Soc.* **2020**, *142*, 3–15.

[283] W. Zhou, L. Ge, G. A. Cooper, S. W. Crane, M. H. Evans, M. N. Ashfold, C. Vallance, *J. Chem. Phys.* **2020**, *153*, 184201.

[284] J. D. Pickering, B. Shepperson, L. Christiansen, H. Stapelfeldt, *J. Chem. Phys.* **2018**, *149*, 154306.

[285] G. A. Cooper, S. T. Alavi, W. Li, S. K. Lee, A. G. Suits, *J. Phys. Chem. A* **2021**, *125*, 5481–5489.

[286] F. Allum, M. Burt, K. Amini, R. Boll, H. Köckert, P. K. Olshin, S. Bari, C. Bomme, F. Braußе, B. Cunha de Miranda, S. Düsterer, B. Erk, M. Géléoc, R. Geneaux, A. S. Gentleman, G. Goldsztejn, R. Guillemin, D. M. Holland, I. Ismail, P. Johnsson, L. Journel, J. Küpper, J. Lahl, J. W. Lee, S. Maclot, S. R. Mackenzie, B. Manschwetus, A. S. Mereshchenko, R. Mason, J. Palaudoux, M. N. Piancastelli, F. Penent, D. Rompotis, A. Rouzée, T. Ruchon, A. Rudenko, E. Savelyev, M. Simon, N. Schirmel, H. Stapelfeldt, S. Techert, O. Travnikova, S. Trippel, J. G. Underwood, C. Vallance, J. Wiese, F. Ziaee, M. Brouard, T. Marchenko, D. Rolles, *J. Chem. Phys.* **2018**, *149*, 204313.

[287] C. A. Schouder, A. S. Chatterley, J. D. Pickering, H. Stapelfeldt, *Annu. Rev. Phys. Chem.* **2022**, *73*, 323–347.

[288] C. S. Slater, S. Blake, M. Brouard, A. Lauer, C. Vallance, C. S. Bohun, L. Christensen, J. H. Nielsen, M. P. Johansson, H. Stapelfeldt, *Phys. Rev. A* **2015**, *91*, 053424.

[289] H. A. Haus, *IEEE J. Sel. Top. Quantum Electron.* **2000**, *6*, 1173–1185.

[290] M. Pessot, P. Maine, G. Mourou, *Opt. Commun.* **1987**, *62*, 419–421.

[291] P. Maine, D. Strickland, P. Bado, M. Pessot, G. Mourou, *IEEE J. Quantum Electron.* **1988**, *24*, 398–403.

[292] J. D. Pickering, *Ultrafast Lasers and Optics for Experimentalists*, IOP, Bristol, UK, **2021**.

[293] H. H. Fielding, A. D. G. Nunn in *Tutorials Mol. React. Dyn.*, M. Brouard, C. Vallance (Eds.), Royal Society of Chemistry, Cambridge, UK, **2010**, chapter 11, pp. 363–391.

[294] D. M. Riffe, A. J. Sabbah, *Rev. Sci. Instrum.* **1998**, *69*, 3099–3102.

[295] P. Wasylczyk, *Rev. Sci. Instrum.* **2001**, *72*, 2221–2223.

[296] R. Trebino, D. J. Kane, *J. Opt. Soc. Am. A* **1993**, *10*, 1101–1111.

[297] D. J. Kane, R. Trebino, *IEEE J. Quantum Electron.* **1993**, *29*, 571–579.

[298] L. Christensen, L. Christiansen, B. Shepperson, H. Stapelfeldt, *Phys. Rev. A* **2016**, *94*, 023410.

[299] H. V. S. Lam, S. Yarlagadda, A. Venkatachalam, T. N. Wangjam, R. K. Kushawaha, C. Cheng, P. Svihra, A. Nomerotski, T. Weinacht, D. Rolles, V. Kumarappan, *Phys. Rev. A* **2020**, *102*, 043119.

[300] W. Jiang, X. Wang, S. Zhang, R. Dong, Y. Guo, J. Feng, Z. Shen, T. Yan, Z. Zhu, Y. Jiang, *J. Chem. Phys.* **2022**, *157*, 084302.

[301] S. W. Crane, L. Ge, G. A. Cooper, B. P. Carwithen, M. Bain, J. A. Smith, C. S. Hansen, M. N. R. Ashfold, *J. Phys. Chem. A* **2021**, *125*, 9594–9608.

[302] S. W. Crane, J. W. L. Lee, M. N. R. Ashfold, *Phys. Chem. Chem. Phys.* **2022**, *24*, 18830–18840.

[303] L. V. Keldysh, *Sov. Phys. JETP* **1965**, *20*, 1307–1314.

[304] S. V. Popruzhenko, *J. Phys. B At. Mol. Opt. Phys.* **2014**, *47*, 204001.

[305] M. Castillejo, S. Couris, E. Koudoumas, M. Martín, *Chem. Phys. Lett.* **1998**, *289*, 303–310.

[306] M. Castillejo, S. Couris, E. Koudoumas, M. Martín, *Chem. Phys. Lett.* **1999**, *308*, 373–380.

[307] B. Yan, P. F. Claus, B. G. Van Oorschot, L. Gerritsen, A. T. Eppink, S. Y. Van De Meerakker, D. H. Parker, *Rev. Sci. Instrum.* **2013**, *84*, 023102.

[308] *NIST Chemistry Webbook, NIST Standard Reference Database Number 69*, National Institute of Standards and Technology, Gaithersburg, MD, **2023**.

[309] M. P. McCann, C. H. Chen, M. G. Payne, *J. Chem. Phys.* **1988**, *89*, 5429–5441.

[310] H. W. Jochims, M. Schwell, H. Baumgärtel, S. Leach, *Chem. Phys.* **2005**, *314*, 263–282.

[311] F. Gaie-Levrel, G. A. Garcia, M. Schwell, L. Nahon, *Phys. Chem. Chem. Phys.* **2011**, *13*, 7024–7036.

[312] R. P. Lindstedt, G. Skevis, *Symp. Combust.* **1996**, *26*, 703–709.

[313] F. Zhang, B. Jones, P. Maksyutenko, R. I. Kaiser, C. Chin, V. V. Kislov, A. M. Mebel, *J. Am. Chem. Soc.* **2010**, *132*, 2672–2683.

[314] P. M. Woods, T. J. Millar, A. A. Zijlstra, E. Herbst, *Astrophys. J.* **2002**, *574*, L167–L170.

[315] J. A. Miller, S. J. Klippenstein, *J. Phys. Chem. A* **2003**, *107*, 7783–7799.

[316] M. Frenklach, *Phys. Chem. Chem. Phys.* **2002**, *4*, 2028–2037.

[317] V. V. Kislov, A. I. Sadovnikov, A. M. Mebel, *J. Phys. Chem. A* **2013**, *117*, 4794–4816.

[318] A. Marciniak, V. Despré, T. Barillot, A. Rouzée, M. C. Galbraith, J. Klei, C. H. Yang, C. T. Smeenk, V. Loriot, S. N. Reddy, A. G. Tielens, S. Mahapatra, A. I. Kuleff, M. J. Vrakking, F. Lépine, *Nat. Commun.* **2015**, *6*, 7909.

[319] A. Marciniak, V. Despré, V. Loriot, G. Karras, M. Hervé, L. Quintard, F. Catoire, C. Joblin, E. Constant, A. I. Kuleff, F. Lépine, *Nat. Commun.* **2019**, *10*, 337.

[320] M. Hervé, V. Despré, P. Castellanos Nash, V. Loriot, A. Boyer, A. Scognamiglio, G. Karras, R. Brédy, E. Constant, A. G. Tielens, A. I. Kuleff, F. Lépine, *Nat. Phys.* **2021**, *17*, 327–331.

[321] D. Garg, J. W. Lee, D. S. Tikhonov, P. Chopra, A. L. Steber, A. K. Lemmens, B. Erk, F. Allum, R. Boll, X. Cheng, S. Düsterer, S. Gruet, L. He, D. Heathcote, M. Johny, M. M. Kazemi, H. Köckert, J. Lahl, D. Loru, S. Maclot, R. Mason, E. Müller, T. Mullins, P. Olshin, C. Passow, J. Peschel, D. Ramm, D. Rompotis, S. Trippel, J. Wiese, F. Ziaee, S. Bari, M. Burt, J. Küpper, A. M. Rijs, D. Rolles, S. Techert, P. Eng-Johnsson, M. Brouard, C. Vallance, B. Manschwetus, M. Schnell, *Front. Phys.* **2022**, *10*, 880793.

[322] B. J. West, L. Lesniak, P. M. Mayer, *J. Phys. Chem. A* **2019**, *123*, 3569–3574.

[323] A. Petrignani, M. Vala, J. R. Eyler, A. G. G. M. Tielens, G. Berden, A. F. G. van der Meer, B. Redlich, J. Oomens, *Astrophys. J.* **2016**, *826*, 33.

[324] Y. J. Bae, M. S. Kim, *Annu. Rev. Anal. Chem.* **2015**, *8*, 41–60.

[325] W. C. Chang, L. C. L. Huang, Y. S. Wang, W. P. Peng, H. C. Chang, N. Y. Hsu, W. B. Yang, C. H. Chen, *Anal. Chim. Acta* **2007**, *582*, 1–9.

[326] R. Knochenmuss, *Analyst* **2006**, *131*, 966–986.

[327] C. C. Roothaan, *Rev. Mod. Phys.* **1951**, *23*, 69–89.

[328] J. A. Pople, R. K. Nesbet, *J. Chem. Phys.* **1954**, *22*, 571–572.

[329] C. D. Sherrill, H. F. Schaefer, *Adv. Quantum Chem.* **1999**, *34*, 143–269.

[330] R. J. Bartlett, M. Musiał, *Rev. Mod. Phys.* **2007**, *79*, 291–352.

[331] R. J. Bartlett, *Annu. Rev. Phys. Chem.* **1981**, *32*, 359–401.

[332] P. G. Szalay, T. Müller, G. Gidofalvi, H. Lischka, R. Shepard, *Chem. Rev.* **2012**, *112*, 108–181.

[333] B. O. Roos in *Ab initio methods quantum Chem. 2nd ed.*, *Vol. 69*, K. P. Lawley (Ed.), Wiley, New York, USA, **1987**, pp. 399–445.

[334] W. S. Jeong, S. J. Stoneburner, D. King, R. Li, A. Walker, R. Lindh, L. Gagliardi, *J. Chem. Theory Comput.* **2020**, *16*, 2389–2399.

[335] V. Veryazov, P. A. Malmqvist, B. O. Ross, *Int. J. Quantum Chem.* **2011**, *111*, 3329–3338.

[336] S. Keller, K. Boguslawski, T. Janowski, M. Reiher, P. Pulay, *J. Chem. Phys.* **2015**, *142*, 244104.

[337] E. Brémond, M. Savarese, C. Adamo, D. Jacquemin, *J. Chem. Theory Comput.* **2018**, *14*, 3715–3727.

[338] S. Vuckovic, K. Burke, *J. Phys. Chem. Lett.* **2020**, *11*, 9957–9964.

[339] R. Send, M. Kühn, F. Furche, *J. Chem. Theory Comput.* **2011**, *7*, 2376–2386.

List of Abbreviations

BASEX	basis set expansion
BBO	beta barium borate
BNC	Bayonet Neill-Concelman
CAD	computer assisted design
CAS	Complete Active Space
CASSCF	Complete Active Space Self-Consistent Field
CC	Coupled Cluster
CEI	Coulomb explosion imaging
CI	Configuration Interaction
CW	continuous-wave
DFT	density functional theory
DMF	*N,N*-dimethylformamide
DNA	deoxyribonucleic acid
FC	Franck-Condon
FROG	frequency-resolved optical gating
FWHM	full width half maximum
GDD	group delay dispersion
HACA	hydrogen abstraction and acetylene or carbon addition
HF	Hartree-Fock
HOMO	Highest Occupied Molecular Orbital
HWP	half-wave plate
IC	internal conversion
ISC	intersystem crossing
ISM	interstellar medium
IVR	intramolecular vibrational energy redistribution
KER	kinetic energy release
LIAD	laser-induced acoustic desorption
LID	laser-induced thermal desorption
LIF	laser-induced fluorescence
MALDI	matrix-assisted laser desorption/ionization
MBPT	Many Body Perturbation Theory
MCP	microchannel plate
MCSCF	Multi-Configuration Self-Consistent Field
MO	molecular orbital
Nd:YAG	neodymium-doped yttrium aluminium garnet
NMF	*N*-methylformamide

PAH	polycyclic aromatic hydrocarbon
PEC	potential energy curve
PES	potential energy surface
PImMS	Pixel Imaging Mass Spectrometry
PMT	photo multiplier tube
REMPI	resonance-enhanced multiphoton ionization
SD	Slater determinant
SE	Schrödinger equation
SHG	second harmonic generation
SMI	spatial-map imaging
THF	tetrahydrofuran
THG	triple harmonic generation
TKER	total kinetic energy release
TOF	time-of-flight
TOF-VMI	time-of-flight velocity-map imaging
UIF	unidentified infrared emission
UV	ultraviolet
UVFS	ultra violet fused silica
VMI	velocity-map imaging
VUV	vacuum ultraviolet
XUV	extreme ultraviolet

List of Symbols

β	product recoil-anisotropy parameter
B_{if}	Einstein coefficient of stimulated absorption
c	speed of light
$\chi\left(\mathbf{R}\right)$	nuclear wavefunction
C_{p}	molar heat capacity at constant pressure
C_{v}	molar heat capacity at constant volume
d	time-of-flight length
D_0	bond dissociation energy
Δ_t	laser pulse duration
e	charge of electron
E_{rot}	rotational energy
E_{kin}	kinetic energy
E_{vib}	vibrational energy
E_{elec}	electronic energy
E_{int}	internal energy
E_{tot}	total energy
E_0	electric field amplitude
ϵ	electric vector of laser pulse
ϵ_0	vacuum permittivity
f	focal length
$\boldsymbol{F}$	force
γ	Keldysh parameter
h	Planck constant
$\hbar$	reduced Planck constant
I	intensity
I_{p}	ionization potential
k	product recoil direction
λ	wavelength
m	mass
$\hat{\boldsymbol{\mu}}$	electric dipole moment operator
$\boldsymbol{\mu}_{\mathrm{if}}$	transition dipole moment between initial and final state
N	number of nuclei in the system
∇	nabla operator
ν	frequency
ω	electric field frequency
ω_0	laser beam waist radius in interaction region

p	momentum
P	average laser power
P_2	second Legendre polynomial
P_{if}	transition probability from initial to final state
$\Phi\left(\mathbf{x}, \mathbf{R}\right)$	molecular wavefunction
ϕ, φ	polar scattering angle, azimuthal angle
P_{if}	transition probability from initial to final state
$\Psi\left(\mathbf{x}; \mathbf{R}\right)$	electronic wavefunction
r	radius
R	ideal gas constant
$\mathbf{R}$	nuclear spatial coordinates
$R_{\mathrm{A-B}}$	internuclear distance between nuclei A and B
$\rho_{\mathrm{R}}(\nu_{\mathrm{if}})$	spectral energy density at ν_{if}
σ	standard deviation
t	time
T_0	room temperature
v	velocity
V	potential energy
V_{E}	extractor potential
V_{G}	ground potential
V_{R}	repeller potential
W_{if}	transition rate from initial to final state
$\mathbf{x}$	electronic spatial and spin coordinates
x, y, z	cartesian coordinates
z	fragment charge
Z	nuclear charge

Appendix A

Appendix: electronic structure theory

A.1 Electron correlation methods

Hartree-Fock (HF)[327,328] theory yields the lowest possible energy for a given basis-set and a single Slater determinant (SD) wavefunction. For an infinitly large basis set, the resulting HF energy converges against the HF limit, the lowest total energy one can obtain using HF theory. The difference between the exact energy and the HF limit is the electron correlation energy. It can be viewed as a deviation from the mean-field interaction used in HF theory, and corresponds physically to the coupling of the motion of electrons. Electron correlation is often divided into dynamic and static (non-dynamic) contributions. Dynamic correlations are instantaneous and usually arise between to electrons that occupy the same orbital. Static correlations are found between electrons in different orbitals. Both expressions are limiting cases, as correlations transition smoothly between dynamic and static as the nuclear geometry is varied.[186]

In order to describe the electron-electron interaction better, we need to improve our

wavefunction ansatz. One intuitive approach is to add additional SDs to the HF determinant, leading to a multi-determinant wavefunction,

$$\Psi\left(\mathbf{x}\right) = a_0 \Psi_{\mathrm{HF}}^{\mathrm{SD}}\left(\mathbf{x}\right) + \sum_{i=1} a_{\mathrm{i}} \Psi_{\mathrm{i}}^{\mathrm{SD}}\left(\mathbf{x}\right) \tag{A.1}$$

where a_{i} is the weight of the i-th SD $\Psi_{\mathrm{i}}^{\mathrm{SD}}\left(\mathbf{x}\right)$. The additional SDs are excited SDs, where orbitals, that are occupied in the HF determinant are replaced by unoccupied (virtual) orbitals.[186] The determinants are labelled according to their excitation relative to the HF determinant as Singles Ψ_{S}, Doubles Ψ_{D}, Triples Ψ_{T} etc. Now, the total energy does not only depend on the basis-set size, but also on the number of SDs. The number of SDs generated depends on two factors. Firstly, the higher the number of virtual orbitals (i.e. the larger the basis-set), the higher the number of SDs that can be generated. Secondly, it also depends on the method.[186] The three main electron correlation methods are Configuration Interaction (CI)[329], Coupled Cluster (CC)[330], and Many Body Perturbation Theory (MBPT)[331] and distinguish themselves mainly by how they determine the weight coefficients a_{i}.

A.2 Multi-configuration self-consistent field

Multi-Configuration Self-Consistent Field (MCSCF)[332] is a CI method that not only optimizes the weight coefficients in equation A.1, but also the spin-orbitals in the determinants themselves. Like other CI methods, MCSCF is an iterative optimization method that makes use of the variation principle. The wavefunction ansatz consists of the HF determinant followed by a linear combination of excited SDs.

$$\Psi = a_0 \Psi_{\mathrm{HF}} + \sum_S a_S \Psi_S + \sum_D a_D \Psi_D + \sum_T a_T \Psi_T + \cdots = \sum_{i=1} a_i \Psi_i \tag{A.2}$$

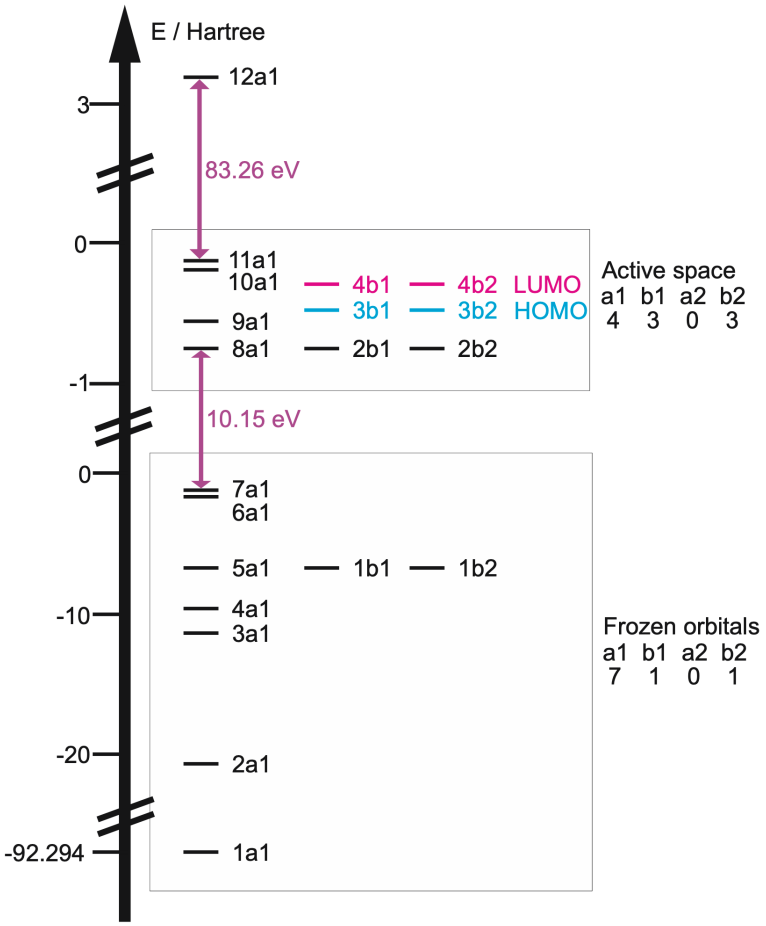

Fig. A.1: HF orbital energies for OCS and a possible way of diving them into active and inactive orbitals. The HF calculation was performed in the C_{2v} point group using the ANO-R3 basis-set. The C_{2v} point group has four irreducable representations: a1, b1, a2, and b2. In this case, the inactive space was selected to consist of 9 orbital, the active space consists of 10 orbitals. The number of active electrons is 12.

Optimization of the spin-orbitals in fact does not recover a lot of correlation energy, hence MCSCF methods are mainly used to obtain qualitatively correct wavefunctions.[186] The success of such methods depends on two factors: the selection of the active space and the initial orbitals guess.

The main challenge of MCSCF methods is to include the relevant configurations for the property of interest, i.e. to choose the correct set of occupied orbitals in the HF determinant and virtual orbitals, that are exchanged. One of the most common methods used is CASSCF[333]. In this method, orbitals are divided into sets of active and inactive orbitals, as shown in Figure A.1 for OCS. The occupancy

of inactive orbitals is 0 or 2 and remains unchanged in the calculation. The active orbitals usually consist of the highest occupied and lowest unoccupied MO. The electrons in the occupied active orbitals are called active electrons. Within the active space, a full CI is performed. That means all possible configurations and their associated weight are calculated and the linear combination corresponds to the overall wavefunction. A conventional notation for such calculations is $[n, m]$-CASSCF, where n is the number of active electrons and m is the number of active orbitals.

Although there are developments in applying machine learning to aid the active space selection[334], it is usually selected manually by the user. There are no strict rules on how to select the active space but several authors provide guidelines based on their experience.[186,335]

(1): MOs that describe the property of interest should be included. These are usually valence orbitals, which are degenerate or near-degenerate to the HOMO.

(2): We can make use of the symmetry of our system when selecting the active space. For example, in a $\mathrm{C}_{\infty\mathrm{v}}$ symmetric molecule, where the z-axis is the internuclear axis, either both p_x and p_y orbitals or none of them should be included, as they will have the same effect on the molecular system.

(3): The number of active electrons and active orbitals should be reasonably close to each other.

(4): HF orbitals on the neutral target molecule are usually good starting points for selecting the active space. However, there are traps to look out for. Firstly, the HF wavefunction may not describe the system accurately enough, if even the neutral ground state has significant multi-reference character. Secondly, if the basis-set is too large, several virtual orbitals might be found that are right above the HOMO in energy. Their order is more or less random. Hence, one might accidentally substitute important virtual orbitals for less important ones.

The initial orbital guess is usually either a set orbitals obtained from an ab-inito method of lower accuracy, e.g. HF-orbitals, or from a CASSCF calculation with a similar geometry. While Complete Active Space (CAS) methods have the potential to describe the static part of the electron correlation accurately[336] to return qualitatively correct wavefunctions, it can be combined with other techniques to also account for the dynamic correlation. One example is the addition of perturbation theory leading to the CASPT2 method. Dynamic correlation can either be inherently relevant in the system or it can become relevant upon changes of internal coordinates.

The accuracy of the level of theory depends on the system under study and the nature of the observable that is calculated. The B3LYP functional used for the geometry optimization of neutral THF has a mean absolute error $<0.05\,\text{Å}$ for a predicted bond length.[337] MP2 geometry optimizations are exceptionally good in describing covalent bonds, but become inaccurate for non-covalent interactions.[338] Thus, we assume that MP2 is very suitable for the geometry optimizations of DMF and DMF^+. Lastly, we use the B3LYP functional to calculate the excitation energies in DMF^+. B3LYP excitation energies have mean absolute errors around 0.3 eV.[339]

Appendix B

Appendix: Figures

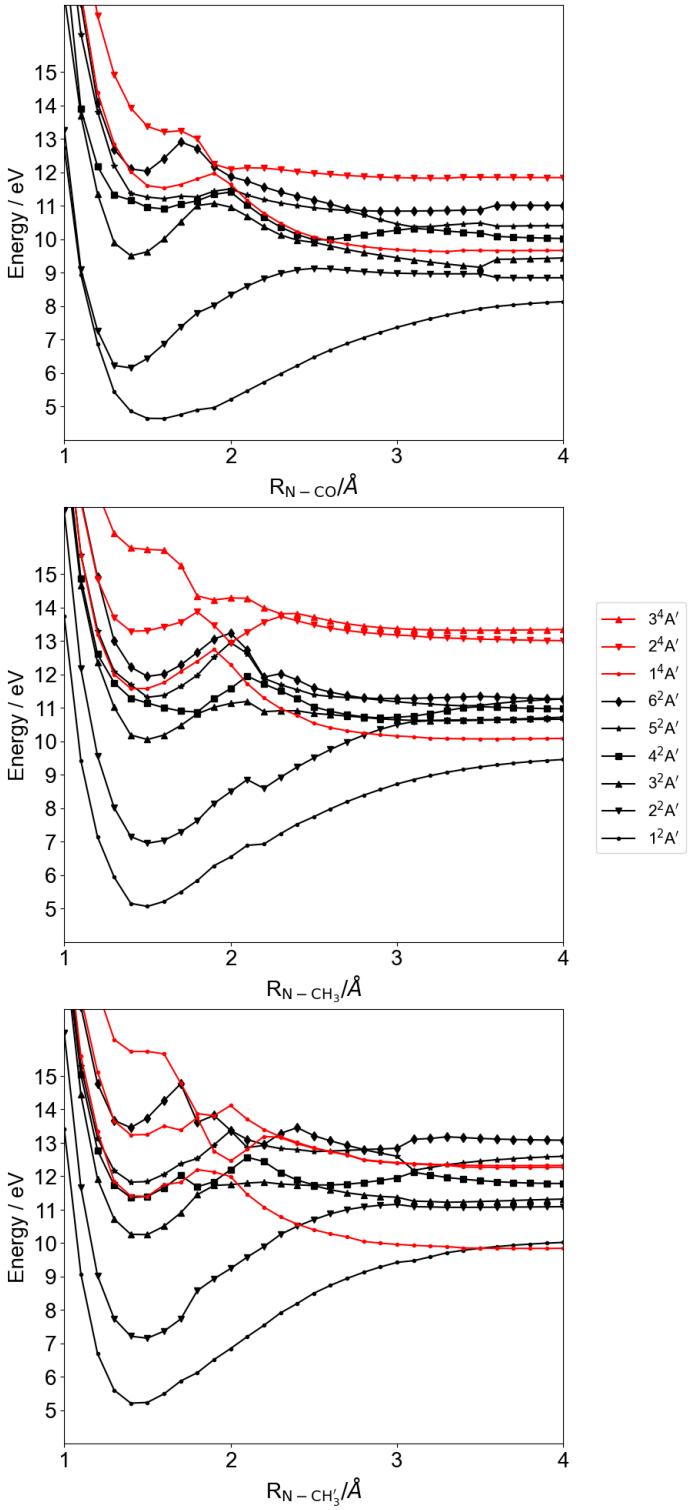

Fig. B.1: Rigid PEC of the DMF cation along the N−CO stretch coordinate (upper panel), the N−CH_3 coordinate on the side of the oxygen atom (central panel), and the remaining N−CH_3 bond (lower panel) calculated on a CASSCF(11,12) level of theory.

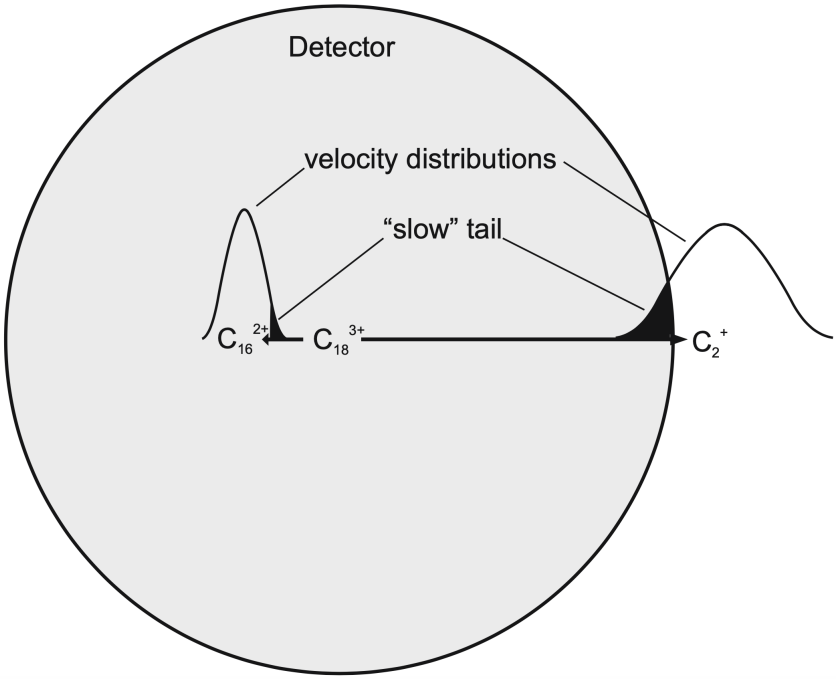

Fig. B.2: Schematic illustration of the decay of triply charged triphenylene, C_{18}^{3+} into C_{16}^{2+} + C_2^+. We only capture the ‘slow’ tail of the C_2^+ velocity distribution.

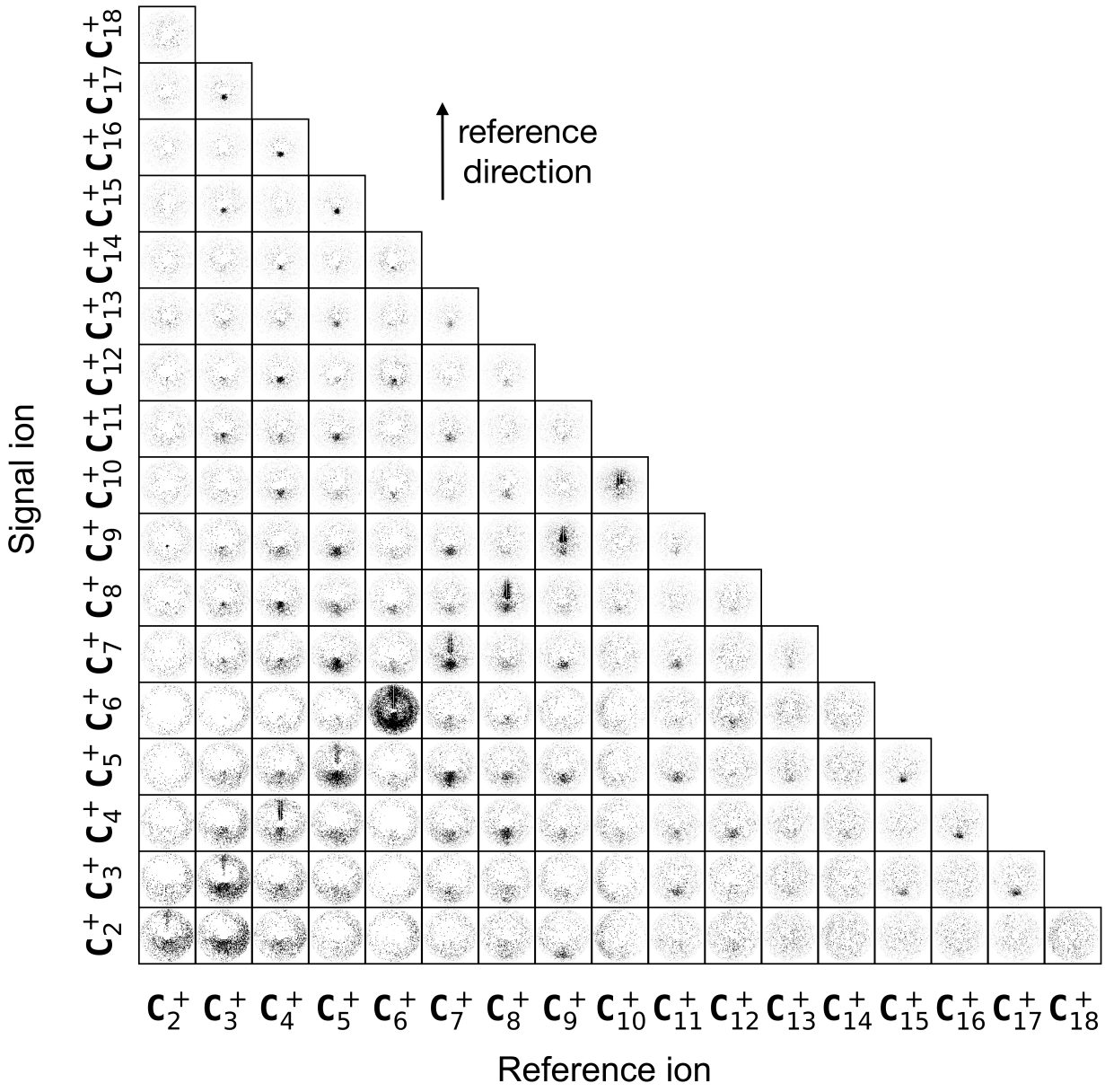

Fig. B.3: Recoil-frame covariance maps of all possible combinations of signal and reference ions following the irradiation of perylene at a laser beam intensity of $9 \cdot 10^{14}$ W cm^{-2}. The reference direction is upwards in the Figure. All covariance maps are plotted with the same contrast. The fragment ion labs refer to the number of carbon atoms on the ion. As explained previously, we integrate each fragment ion peak over the hydrogen atoms. Ion pairs that exceed the number of carbon atoms on the parent molecule cannot be correlated with each other and do not show covariance. The autocovariance signal, which is the covariance of each fragment ion with itself, has been removed from the data. The edge feature in some of the covariance images is an artefact of the data and not real signal. It results from a transpose error in the covariance code.

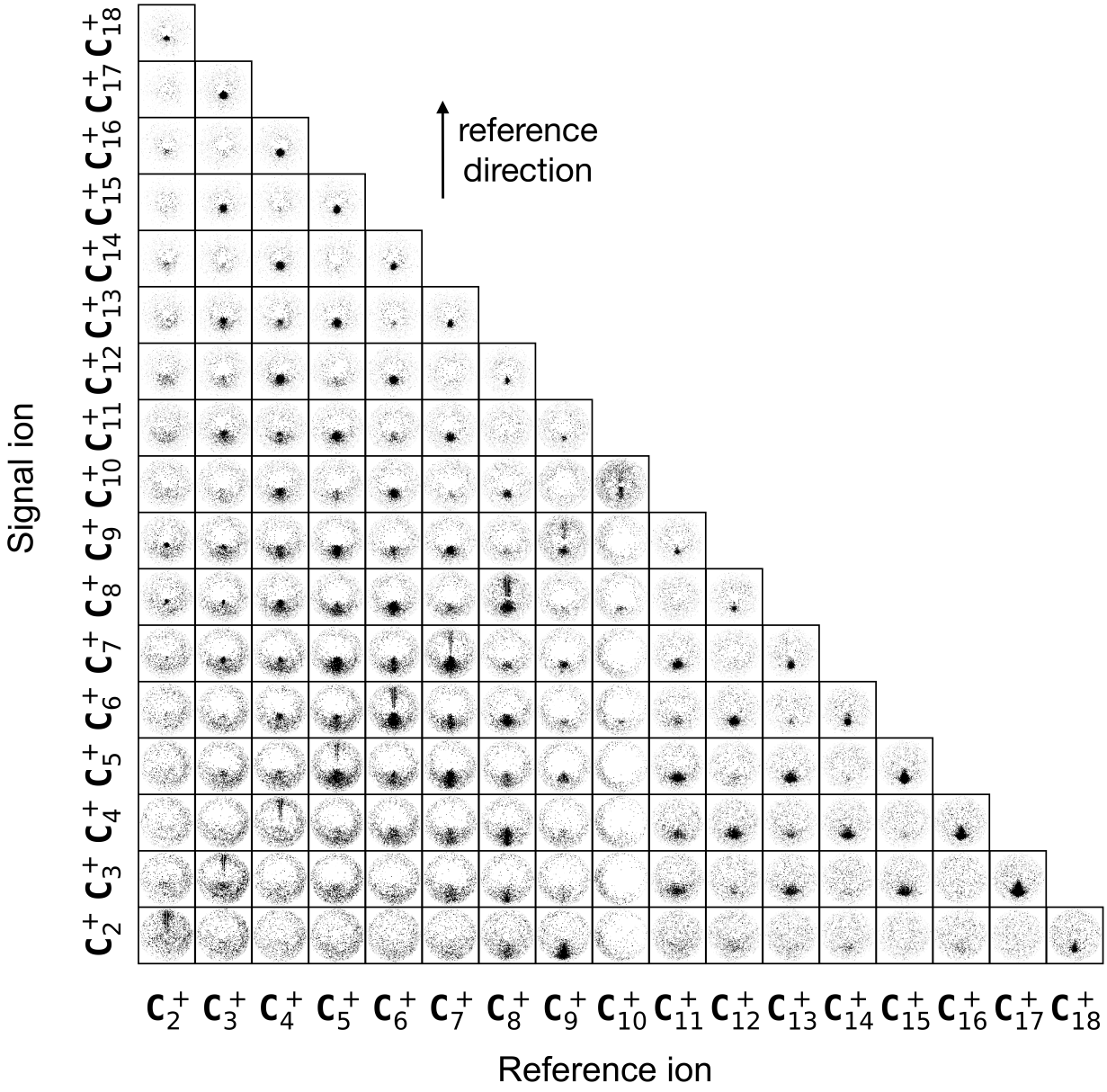

Fig. B.4: Recoil-frame covariance maps of all possible combinations of signal and reference ions following the irradiation of benzo[a]pyrene at a laser beam intensity of $5 \cdot 10^{14}$ W cm^{-2}. The reference direction is upwards in the Figure. All covariance maps are plotted with the same contrast. The fragment ion labs refer to the number of carbon atoms on the ion. As explained previously, we integrate each fragment ion peak over the hydrogen atoms. Ion pairs that exceed the number of carbon atoms on the parent molecule cannot be correlated with each other and do not show covariance. The autocovariance signal, which is the covariance of each fragment ion with itself, has been removed from the data. The edge feature in some of the covariance images is an artefact of the data and not real signal. It results from a transpose error in the covariance code.

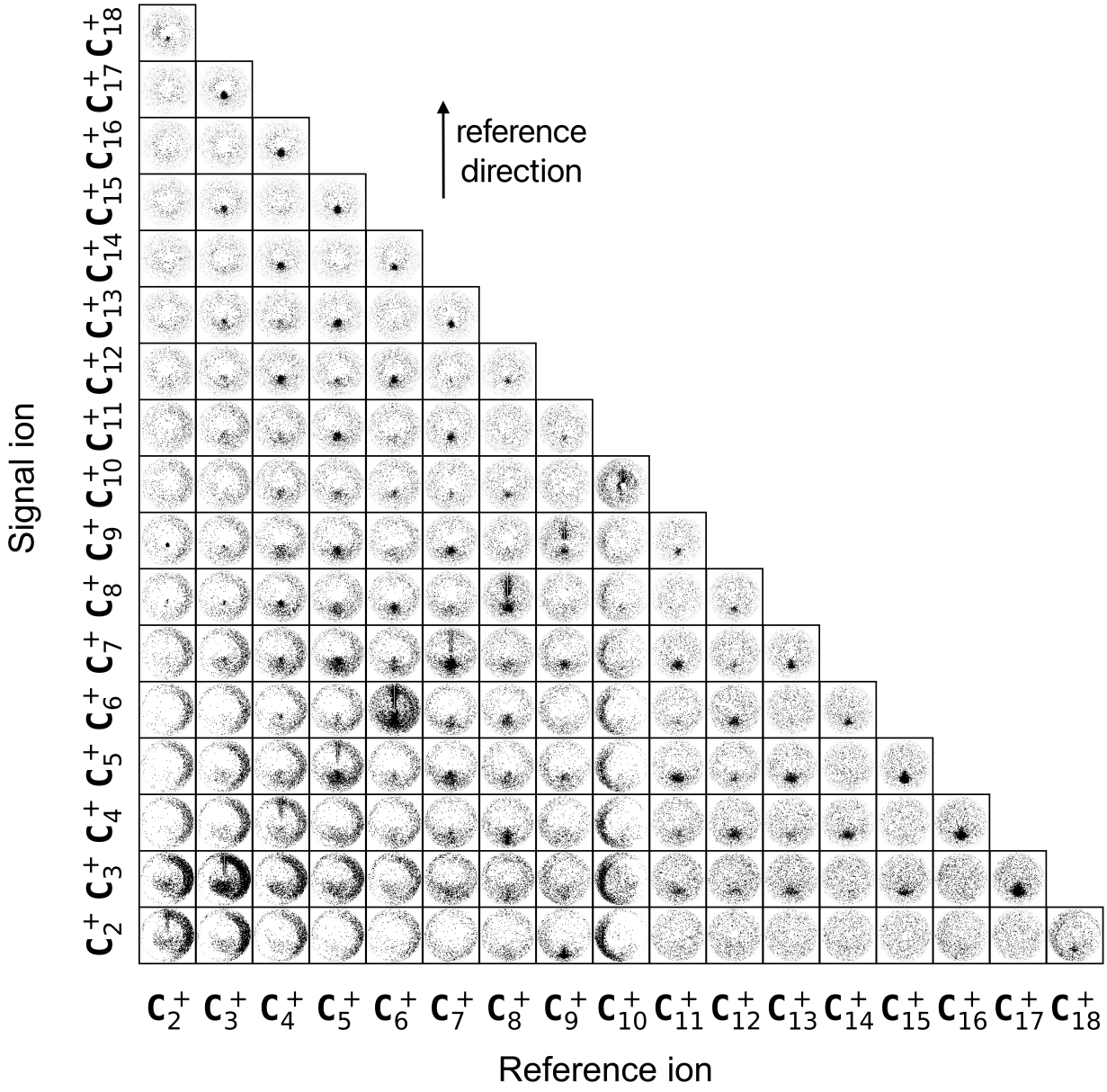

Fig. B.5: Recoil-frame covariance maps of all possible combinations of signal and reference ions following the irradiation of benzo[a]pyrene at a laser beam intensity of $9 \cdot 10^{14}$ W cm^{-2}. The reference direction is upwards in the Figure. All covariance maps are plotted with the same contrast. The fragment ion labs refer to the number of carbon atoms on the ion. As explained previously, we integrate each fragment ion peak over the hydrogen atoms. Ion pairs that exceed the number of carbon atoms on the parent molecule cannot be correlated with each other and do not show covariance. The autocovariance signal, which is the covariance of each fragment ion with itself, has been removed from the data. The edge feature in some of the covariance images is an artefact of the data and not real signal.

Appendix C

Appendix: Tables

Tab. C.1: Internal coordinates for the DMF monocation and neutral optimized on a UMP2/aug-cc-pVTZ level of theory in terms of bond lengths R (in Å), angles A (in °), and dihedral angles D (in °). The respective atom numbers are indicated by the numbers in brackets and refer to the atom numbers in Figure 6.1.

Coordinate	DMF cation	DMF neutral	Coordinate	DMF cation	DMF neutral
$R(1,2)$	1.0976	1.1011	$A(4,9,11)$	109.1043	110.7263
$R(1,3)$	1.1475	1.2233	$A(4,9,12)$	108.1716	110.7259
$R(1,4)$	1.5509	1.3574	$A(10,9,11)$	111.0178	108.6816
$R(4,5)$	1.4301	1.4463	$A(10,9,12)$	110.0943	108.6814
$R(4,9)$	1.4306	1.4433	$A(11,9,12)$	107.6591	108.4742
$R(5,6)$	1.0995	1.0913	$D(2,1,4,5)$	177.1802	179.9962
$R(5,7)$	1.0884	1.0863	$D(2,1,4,9)$	-0.7293	-0.0032
$R(5,8)$	1.0863	1.0913	$D(3,1,4,5)$	-2.5949	0.0
$R(9,10)$	1.0866	1.0882	$D(3,1,4,9)$	179.4955	179.9974
$R(9,11)$	1.0927	1.0918	$D(1,4,5,6)$	-84.5248	-119.9285
$R(9,12)$	1.0961	1.0918	$D(1,4,5,7)$	31.8484	-0.0098

Continued on next page

Tab. C.1 – continued from previous page

Coordinate	DMF cation	DMF neutral	Coordinate	DMF cation	DMF neutral
$A(2,1,3)$	131.1212	122.5368	$D(1,4,5,8)$	156.6245	119.9051
$A(2,1,4)$	109.4579	111.8751	$D(9,4,5,6)$	93.3531	60.0709
$A(3,1,4)$	119.4204	125.5882	$D(9,4,5,7)$	-150.2737	179.9896
$A(1,4,5)$	117.0621	120.4453	$D(9,4,5,8)$	-25.4976	-60.0955
$A(1,4,9)$	120.7474	121.7804	$D(1,4,9,10)$	6.4508	-0.0011
$A(5,4,9)$	122.156	117.7743	$D(1,4,9,11)$	128.9045	119.8193
$A(4,5,6)$	107.2634	110.3209	$D(1,4,9,12)$	-114.2508	-119.8210
$A(4,5,7)$	109.2958	108.2052	$D(5,4,9,10)$	-171.3502	179.9995
$A(4,5,8)$	110.0462	110.3213	$D(5,4,9,11)$	-48.8966	-60.1801
$A(6,5,7)$	107.5964	109.6224	$D(5,4,9,12)$	67.9482	60.1796
$A(6,5,8)$	109.3386	108.7417			
$A(7,5,8)$	113.1069	109.6190			
$A(4,9,10)$	110.698	109.4974			

Tab. C.2: Central momentum and full width half maximum (FWHM) of the signal ion in the recoil-frame covariance image of an ion pair obtained by fitting a Gaussian distribution to the momentum distribution.

(sig, ref)	momentum / kg m s^{-1}	FWHM / kg m s^{-1}
(C_{14}^+, C_2^+)	$1.88 \cdot 10^{-22}$	$1.04 \cdot 10^{-22}$
(C_{13}^+, C_3^+)	$2.06 \cdot 10^{-22}$	$1.34 \cdot 10^{-22}$
(C_{12}^+, C_4^+)	$2.25 \cdot 10^{-22}$	$1.43 \cdot 10^{-22}$
(C_{11}^+, C_5^+)	$2.41 \cdot 10^{-22}$	$1.52 \cdot 10^{-22}$
(C_{10}^+, C_6^+)	$2.59 \cdot 10^{-22}$	$1.24 \cdot 10^{-22}$
(C_9^+, C_7^+)	$2.61 \cdot 10^{-22}$	$0.78 \cdot 10^{-22}$
(C_{11}^+, C_3^+)	$2.08 \cdot 10^{-22}$	$1.64 \cdot 10^{-22}$
(C_{10}^+, C_4^+)	$2.19 \cdot 10^{-22}$	$1.58 \cdot 10^{-22}$
(C_9^+, C_5^+)	$2.41 \cdot 10^{-22}$	$1.39 \cdot 10^{-22}$
(C_8^+, C_6^+)	$2.50 \cdot 10^{-22}$	$1.21 \cdot 10^{-22}$
(C_7^+, C_7^+)	$2.43 \cdot 10^{-22}$	$1.41 \cdot 10^{-22}$
(C_9^+, C_3^+)	$1.76 \cdot 10^{-22}$	$0.88 \cdot 10^{-22}$
(C_8^+, C_4^+)	$2.25 \cdot 10^{-22}$	$1.50 \cdot 10^{-22}$
(C_7^+, C_5^+)	$2.39 \cdot 10^{-22}$	$1.67 \cdot 10^{-22}$
(C_6^+, C_6^+)	$2.31 \cdot 10^{-22}$	$1.80 \cdot 10^{-22}$
(C_5^+, C_7^+)	$2.19 \cdot 10^{-22}$	$1.16 \cdot 10^{-22}$

Tab. C.3: Central momentum and full width half maximum (FWHM) of the signal ion in the recoil-frame covariance image of an ion pair obtained by fitting a Gaussian distribution to the momentum distribution.

(sig, ref)	momentum / kg m s^{-1}	FWHM / kg m s^{-1}
(C_{15}^+, C_3^+)	$2.05 \cdot 10^{-22}$	$1.15 \cdot 10^{-22}$
(C_{13}^+, C_3^+)	$2.06 \cdot 10^{-22}$	$1.34 \cdot 10^{-22}$
(C_{11}^+, C_3^+)	$2.08 \cdot 10^{-22}$	$1.64 \cdot 10^{-22}$
(C_{14}^+, C_4^+)	$2.25 \cdot 10^{-22}$	$1.10 \cdot 10^{-22}$
(C_{12}^+, C_4^+)	$2.25 \cdot 10^{-22}$	$1.43 \cdot 10^{-22}$
(C_{10}^+, C_4^+)	$2.19 \cdot 10^{-22}$	$1.58 \cdot 10^{-22}$
(C_8^+, C_4^+)	$2.25 \cdot 10^{-22}$	$1.50 \cdot 10^{-22}$
(C_{14}^+, C_2^+)	$1.88 \cdot 10^{-22}$	$1.04 \cdot 10^{-22}$
(C_{12}^+, C_6^+)	$2.58 \cdot 10^{-22}$	$0.79 \cdot 10^{-22}$
(C_{10}^+, C_6^+)	$2.58 \cdot 10^{-22}$	$1.24 \cdot 10^{-22}$
(C_8^+, C_6^+)	$2.50 \cdot 10^{-22}$	$1.21 \cdot 10^{-22}$
(C_{12}^+, C_4^+)	$2.25 \cdot 10^{-22}$	$1.43 \cdot 10^{-22}$
(C_{12}^+, C_2^+)	$2.33 \cdot 10^{-22}$	$2.28 \cdot 10^{-22}$